Stony Brook University

QCD factorization and effective field theories at the LHC

A Dissertation presented

by

Mao Zeng

to

The Graduate School

in Partial Fulfillment of the

Requirements

for the Degree of

Doctor of Philosophy

in

Physics

Stony Brook University

August 2015

Stony Brook University

The Graduate School

Mao Zeng

We, the dissertation committee for the above candidate for the

Doctor of Philosophy degree, hereby recommend

acceptance of this dissertation

George Sterman - Dissertation Advisor
Distinguished Professor, Department of Physics and Astronomy

Dominik Schneble - Chairperson of Defense
Associate Professor, Department of Physics and Astronomy

Sally Dawson - Committee Member
Adjunct Professor, Department of Physics and Astronomy

Jianwei Qiu - Committee Member
Brookhaven Professor, Department of Physics and Astronomy

Frank Paige - Committee Member
Emertius Senior Scientist, Brookhaven National Laboratory

This dissertation is accepted by the Graduate School

Charles Taber
Dean of the Graduate School

Abstract of the Dissertation

QCD factorization and effective field theories at the LHC

by

Mao Zeng

Doctor of Philosophy

in

Physics

Stony Brook University

2015

Quantum Chromodynamics (QCD) is the main tool for making precise theoretical predictions for proton-proton collisions at the large hadron collider (LHC). A key lesson from QCD is that physics looks different at different energy scales, under renormalization group evolution. The simplest example is the running coupling, but more examples come from QCD factorization of hadron scattering and effective field theories. A hard scattering event in hadron collisions involves two widely separated scales: the hadron mass scale and the hard momentum transfer scale. The parton distribution functions, describing a light-cone view of the internal structure of a proton, are evolved from the hadronic scale to the hard scattering scale using the DGLAP evolution equation, to set the initial conditions for hard scattering of point-like partons.

In more complicated collider measurements, there are more than two widely-separated scales involved, and more sophisticated evolution equations are needed, forming the basis of "resummation" calculations for hadron collisions. We apply threshold resummation and p_T resummation to the production of W^+W^- boson pairs. Our results, adopted by the CMS Collaboration for experimental analysis, reduced tension between theory and experiment.

The production of a Higgs boson in association with a hadron jet is analyzed using the method of effective field theory. The largeness of the top quark mass enables us to integrate out the top quark, which is the assumption behind many theoretical calculations in the literature. But if the Higgs boson is produced with a large transverse momentum, we begin to probe the finiteness of the top quark mass, and possible novel effects beyond the Standard Model of particle physics.

To Lilian

Table of Contents

Acknowledgements

I'd like to thank my PhD advisor, George Sterman, for teaching me his many intuitive yet great insights into physics, for encouraging me to explore, and for his wisdom in pointing me in the right direction in important career decisions.

I'd like to thank Sally Dawson, who has been effectively my co-advisor, for her patience in guiding me through the techniques of my field of study, for many hours of invaluable day-to-day discussions, and for her wonderful support during every stage of my graduate study.

I'd like to thank Patrick Meade and Ian Lewis, who have mentored me in collaborated projects and broadened my horizon.

I'd like to thank Peter Van Nieuwenhuizen, who is passionately committed to teaching and has been a great source of knowledge about quantum field theory for students at the YITP.

I'd like to thank my friends at Stony Brook, Andrea, Harikrishnan, Jun, Peng, Wolfger, Xugang, Yiwen, Yachao, Yiming and Zhedong, for their companionship and generosity.

I'd like to thank my parents, who have supported me thoroughly in my pursuit of an education and career in science outside my home country, whose love I have yet to reciprocate.

I'd like to thank my wife, Lilian, who has been the greatest joy of my life, who has traveled to a different hemisphere of the globe to share our lives together, for her love and support.

This work was supported in part by the National Science Foundation grant PHY-131661.

Chapter 1

Introduction

1.1 Particle physics and hadron accelerators

The Standard Model (SM) of particle physics, built upon decades of research, is the state-of-the-art knowledge about elementary particles. The SM posits that non-gravitational interactions in nature are described by a renormalizable quantum field theory with the $SU(3) \times SU(2)_L \times U(1)_Y$ gauge group, with the matter fields being three generations of spin-1/2 quarks and leptons, and a scalar Higgs field. The $SU(3)$ sector has unbroken gauge symmetry and is known as Quantum Chromodynamics (QCD), which describes the strong nuclear force which binds quarks and gluons inside nucleons. The $SU(2)_L \times U(1)_Y$ sector is the electroweak theory. The Brout-Englert-Higgs (BEH) mechanism [1, 2, 3, 4, 5, 6] spontaneously breaks the $SU(2)_L \times U(1)_Y$ symmetry, giving rise to a massless photon responsible for quantum electrodynamics (QED), three massive gauge bosons (W^-, W^+ and Z) responsible for the weak nuclear force, and one scalar Higgs particle responsible for generating the masses of elementary particles.

The importance of the BEH mechanism comes from the fact that it is not possible to directly write down gauge-invariant mass terms for gauge bosons. For the standard model, with only left-handed fermions charged under $SU(2)_L$, it is also not possible to write down $SU(2)_L$-invariant mass terms for fermions without the BEH mechanism. Moreover, the existence of the Higgs boson is the simplest way to preserve (up to loop corrections) a well-tested relation between the weak angle and the W/Z mass ratio.

Collider and fixed-target experiments involving hadron collisions have been instrumental in verifying the SM. The smaller charge-to-mass ratio of the proton, compared with the electron, reduces synchrotron radiation and enables higher energies to be achieved in circular accelerators. A partial list of elementary particles discovered at past hadron collision experiments includes the bottom quark [7], the W and Z bosons [8, 9, 10, 11], and the top quark [12, 13]. The non-Abelian nature and flavor universality of SM couplings have also been extensively tested [14]. With all the other SM particles observed, the Large Hadron Collider (LHC) was designed to find or exclude a non-strongly coupled Higgs boson in its entire allowed mass range. Indeed, a few years after the LHC went into operation, the Higgs boson was discovered in 2012 [15, 16]. Current LHC measurements indicate that the Higgs boson has a mass of 125.09 ± 0.24 GeV [17], has expected 0 spin and even CP parity [18, 19],

and gives signal strengths consistent with SM predictions in various production and decay channels. This establishes the Standard Model (SM) as the correct theory of elementary particle physics up to an energy around several hundred giga-electron volts (GeVs).

While the SM has survived a large number of experimental tests, further exploration of particle physics is warranted, and hadron accelerators will again play a key role. First, the properties of SM particles, such as masses, mixing angles, and decay widths, deserve more precise measurements. Indeed, a primary goal of the LHC Run 2 is precision measurement of Higgs properties, such as self-couplings and Yukawa couplings to various fermion generations. Second, the Standard Model is not a complete theory of nature. There is a strong consensus that new physics will emerge at the Planck scale ($\sim 10^{19}$ GeV) or the Grand Unified Theory scale ($\sim 10^{17}$ GeV). But there are also well-motivated arguments postulating the existence of new physics at the TeV scale. For example, weak-scale supersymmetry [20] simultaneously solves the hierarchy problem and ensures precise gauge coupling unification at the GUT scale. As another example, the "WIMP miracle" [21] says that for a class of dark matter models, the dark matter particle mass should be around the TeV scale for the relic density of such particles to agree with the dark matter density observed in the universe. The LHC Run 2, and proposed future hadron colliders with an energy of up to 100 TeV, will search for TeV-scale new physics. Third, due to the difficulty of theoretical calculations in non-perturbative QCD, we have to rely on colliders to probe the internal structures of nucleons and nuclei, coded in non-perturbative objects such as collinear parton distribution functions and transverse momentum-dependent (TMD) parton distribution functions. Examples of future experiments proposed for this purpose include the Electron-Ion Collider [22] which aims to improve upon HERA, and a fixed-target experiment, AFTER@LHC [23].

1.2 Understanding hard scattering in hadron collisions

As is the case in the Rutherford scattering experiment over a century ago, hadron-hadron collisions are dominated by soft scattering events, while the rare hard scattering events serve as a microscope that probes short-distance physics. Understanding hadron-hadron collisions is made more difficult by the non-perturbative nature of the proton bound state. Fortunately, there are two simplifications from intuitive arguments. First, the effective coupling constant of QCD decreases with energy, which allows a perturbative description of physics above the energy scale of ~ 1 GeV. Second, a proton traveling at relativistic speeds is Lorentz-contracted, and looks like a flat disk traveling in a direction perpendicular to the disk surface, which means there are no initial-state interactions between the two incoming protons until the very last moment when hard scattering takes place [24]. The internal motions of partons (i.e. quarks and gluons) in the proton are effectively frozen by time dilation, during the transit of one parton from a hadron across the other hadron. The probability of undergoing a hard scattering event with a large momentum transfer Q is proportional to the probability for finding two partons, one from each proton, to be within a transverse separation of $1/Q$ of each other. Multi-parton hard scattering is suppressed because there is a small probability of finding more than two partons within a short distance of $1/Q$ when the two flat disks collide. Soft final-state interactions should not change the cross section, as long as we make sufficiently inclusive measurements that do not probe momentum scales much less than Q,

hence do not probe time scales much longer than $1/Q$ in the collision process.

With these considerations in mind, the hard scattering cross section in hadron-hadron collisions can be factorized into the product of non-perturbative parton distribution functions describing the initial configuration of the flat disk objects, and perturbatively calculable hard scattering functions describing the hard scattering of point-like partons. This is referred to as leading power (or leading twist) factorization, and corrections to this picture are of order $\Lambda_{\rm QCD}/Q$, of sub-leading power. Examples will be given below.

1.3 Proving factorization from field theory

Proving factorization at the level of rigor of theoretical physics [24, 25, 26], starting from the QCD Lagrangian, took more than a decade of work. The simplest processes can be understood via the operator product expansion in Euclidean QFT. These processes include fully inclusive electron-positron annihilation into hadrons and deeply inelastic scattering (DIS) at measured momentum transfer Q^2 via virtual photons.[1] If we make less inclusive measurements in e^+/e^- annihilation or DIS, such as the number of jets (defined via some jet algorithm), or if we study the Drell-Yan process, we will have to study QCD factorization in Minkowski space.

QCD factorization in Minkowski space is closely connected with infrared divergences in massless QCD. The hadron masses are much smaller than hard scattering scales, and the leading power contribution in the $m_{\rm hadron}/Q$ expansion is captured by infrared divergences when the partons are taken to be exactly massless. A simple but powerful technique in studying IR divergences is considering loop integrals as contour integrations in the complex plane, exploiting the full freedom to deform the integration contours. A singularity of the integrand at some point in the complex plane will not cause an IR divergence, unless the integration contour is "pinched", i.e. cannot be deformed away from that singular point. This leads to the Landau equations [27], which give a necessary condition for the appearance of IR divergences in a Feynman diagram. The set of "pinched" singular points forms sub-manifolds in the integration volume, called the *pinch singular surfaces*. Coleman and Norton re-interpreted the Landau equation as the statement that a Feynman diagram can only have pinch singularities if the diagram corresponds to classical on-shell particle propagation [28]. An immediate consequence of the Landau equation is that IR divergences only arise from particle momenta becoming soft or collinear [29].

The Landau equations determine all the diagrams which may have IR divergences, but a definite answer is only obtained after IR power-counting [29, 30], by studying the power-scaling behavior of the loop integrand as the pinch singular surface is approached. This is the analogue of UV power counting in the study of renormalization. The power-counting allows us to build a "catalog" of diagrams that contribute at leading power. We do not give a technical description of this catalog, but note that it confirms many of the intuitive results from the "flat disk" picture. For example, each collinear sub-diagram is allowed to connect to the hard sub-diagram via at most one line (gluon or quark) with a physical polarization, which suppresses multi-parton scattering and multi-parton fragmentation.

[1] To be precise, the operator product expansion predicts a set of shape variables, known as moments, of the cross section as a function of the momentum transfer.

The next task is constructing approximators to the Feynman integrand which give leading-power behavior of individual diagrams, in the vicinity of pinch singular surfaces. For example, collinear particles that enter the hard sub-diagram are approximated to be on-shell, and soft gluons connected to a collinear sub-diagram are approximated to have only polarization components in the opposite collinear direction. Just as overlapping UV divergences appear in the theory of renormalization, care must be taken to deal with the overlap between different IR-divergent momentum regions [26, 31].[2]

After constructing the leading-power approximators, one of the final steps is applying Ward identities to organize multiple diagrams into a factorized form. For example, the sum of all possible attachments of one soft gluon to a collinear sub-diagram is factorized into the product of the collinear sub-diagram itself and a soft gluon attachment via an "eikonal" vertex.

When all momentum scales, except hadron masses, are of order Q, we typically have cancellation of soft gluons, leading to "collinear factorization", with the cross section equal to a convolution of collinear functions (parton distribution functions and / or fragmentation functions) and hard scattering functions. In more complicated situations, for example the production of Drell-Yan pairs near the partonic energy threshold or with transverse momenta much less than Q, we also need soft functions.

One of the subtle issues is the so called Glauber or Coulomb gluons, which are basically soft gluons whose momenta are dominated by transverse momenta and cannot be described by eikonal couplings. The cancellation of Glauber gluons [32, 33, 34] was an essential difficulty in proving factorization for the Drell-Yan process.

1.4 DGLAP evolution equation

1.4.1 Collinear factorization and Mellin transform

Much of this dissertation will be concerned with Drell-Yan-like processes, such as the production of Higgs bosons and W^+W^- boson pairs in hadron-hadron collisions, so we will introduce collienar factorization in this context.

For a Lorentz 4-vector $v^\mu = (v^0, v^x, v^y, v^z)$, we introduce lightcone coordinates

$$v^\mu = \left(v^+, v^-, \boldsymbol{v}_T\right), \tag{1.1}$$
$$v^+ \equiv v^0 + v^z, \tag{1.2}$$
$$v^- \equiv v^0 - v^z. \tag{1.3}$$

The Lorentz 4-product becomes

$$\begin{aligned} v.w &= \frac{1}{2}v^+w^- + \frac{1}{2}v^-w^+ - \boldsymbol{v}_T.\boldsymbol{w}_T, \\ v^2 &= v^+v^- - \left|\boldsymbol{v}_T\right|^2. \end{aligned} \tag{1.4}$$

[2]For example, a diagram may develop a leading-power IR divergence when one of the gluons becomes either soft or collinear, or simultaneously soft and collinear.

For the production of a system of a large mass M by electroweak annihilation, from the scattering of two hadrons at center-of-mass energy

$$S = M^2/\tau, \tag{1.5}$$

the cross section is given in factorized form by [24]

$$\begin{aligned} s\frac{d\sigma_{AB\to M}\left(\tau, M^2\right)}{dM^2} &= \sum_{\text{partons } a,b} \int dx_a dx_b \, f_{a/A}\left(x_a, \mu_f\right) f_{b/B}\left(x_b, \mu_f\right) \\ &\quad \times \hat{\sigma}_{ab\to M}\left(M^2, \hat{s}, M^2/\mu_f^2, \alpha_s\left(\mu_f\right)\right) \qquad (1.6) \\ &= \sum_{\text{partons } a,b} \sigma_0 \int \frac{dx_a}{x_a}\frac{dx_b}{x_b} \, f_{a/A}\left(x_a, \mu_f\right) f_{b/B}\left(x_b, \mu_f\right) \\ &\quad \times C_{ab\to M}\left(z, M^2/\mu_f^2, \alpha_s\left(\mu_f\right)\right). \qquad (1.7) \end{aligned}$$

Eq. (1.6) describes a hard scattering initiated by a parton of species a from the hadron A and a parton of species b from the hadron B. $f_{a/A}$ is the parton distribution function (PDF) which can be intuitively understood as the probability of finding a parton a, with a longitudinal fraction x_a of the hadron's momentum, inside the hadron A (and similarly for $f_{b/B}$). μ_f is the factorization scale, which is, loosely speaking, the transverse-momentum scale that separates the definition of collinear and hard momenta. $\hat{s} \equiv x_a x_b S$ is the center-of-mass squared energy of the two partons, which we assume to be comparable with M^2. $\hat{\sigma}_{ab\to M}$ is the partonic cross section.[3]

In Eq. (1.7), we factor out $\sigma_0 = \sigma_0\left(M^2, \alpha_s\left(M^2\right)\right)$, which is defined by the leading order cross section of massless parton-parton scattering,

$$M^2\frac{d\sigma_{AB\to M}\left(\hat{s}, M^2\right)}{dM^2} = \sigma_0\left(M^2, \alpha_s\left(M^2\right)\right)\delta\left(1 - \frac{M^2}{\hat{s}}\right), \tag{1.8}$$

and we are left with the dimensionless "hard scattering function" or "coefficient function" $C_{ab\to M}$ depending on the variable

$$z \equiv \frac{M^2}{\hat{s}} = \frac{\tau}{x_a x_b}. \tag{1.9}$$

The parton distribution function for a quark of species a, with longitudinal momentum fraction $x > 0$, from a hadron state $|A\rangle$ traveling with momentum $P = (P^0, 0, 0, P^z)$, is defined as the matrix element

$$f_{a/A}(x, \mu_f) \equiv \int \frac{dw^-}{2\pi} e^{-ixP^+w^-/2} \langle A| \, \bar{\psi}_a\left(0, w^-, \mathbf{0}_T\right) W\left(w^-, 0\right) \frac{\gamma^+}{4} \psi_a(0) |A\rangle, \tag{1.10}$$

where we used the lightcone coordinate notations defined in Eq. (1.1)-(1.3), and $W\left(w^-, 0\right)$ is a straight Wilson line from $(0, 0, \mathbf{0}_T)$ to $(0, w^-, \mathbf{0}_T)$, to ensure gauge invariance. The plus

[3] At leading order in α_s, the partonic cross section is directly obtained from Feynman diagrams with on-shell incoming partons, but at higher orders is only obtained after appropriate subtraction of IR singularities of the diagrams.

component of the gamma matrices γ^μ is used in the above equation to project out the larger Dirac spin component. The parton distribution function defined in Eq. (1.10) needs UV renormalization besides the usual renormalization of the QCD Lagrangian itself, and μ_f is the UV renormalization scale.

It is worth noticing that in Eq. (1.7), the hard scattering function $\hat{\sigma}$ is independent of IR physics, such as the hadron species and light quark masses. Meanwhile, the collinear functions, in this case parton distribution functions, are independent of UV physics, such as the hard processes involved, which is referred to as the universality of parton distribution functions (for example, the parton distribution functions are the same for Z boson production as for W boson production). This structure of factorization is constraining enough, as will be shown in the next section, to tell us how parton distribution functions evolves with respect to μ_f.

In Eq. (1.7), the LHS depends on τ, whereas on the RHS, $f_{a/A}$, $f_{b/B}$, and $C_{ab\to M}$ depend on x_a, x_b, and z, respectively, satisfying $\tau = x_a x_b z$ or $-\ln\tau = -\ln x_a - \ln x_b - \ln z$. Therefore, if we take the Laplace transform with respect to these logarithms, the moment of the LHS becomes the product of the moments of the three functions on RHS. Generally, for any function $f(x)$ defined on $0 \le x \le 1$, its Mellin transform $\tilde{f}(N)$ is defined as the Laplace transform w.r.t. $(-\ln x)$,

$$\tilde{f}(N) \equiv \int_0^\infty d(-\ln x)\, e^{-N(-\ln x)} f(x) \tag{1.11}$$

$$= \int_0^1 dx\, x^{N-1} f(x). \tag{1.12}$$

Eq. (1.7) is thus expressed, in Mellin moment space, as a product rather than convolution,

$$\begin{aligned}\int_0^1 d\tau\, \tau^{N-1} s \frac{d\tilde{\sigma}_{AB\to M}(\tau, M^2)}{dM^2} &= \sigma_0 \sum_{\text{partons } a,b} \tilde{f}_{a/A}(N,\mu_f)\, \tilde{f}_{b/B}(N,\mu_f) \\ &\quad \times \tilde{C}_{ab\to M}\left(N, M^2/\mu_f^2, \alpha_s(\mu_f)\right) \\ &= \sigma_0 \left[\tilde{\boldsymbol{f}}_A(N,\mu_f)\right]^T \cdot \tilde{\boldsymbol{C}}\left(N, M^2/\mu_f^2, \alpha_s(\mu_f)\right) \cdot \tilde{\boldsymbol{f}}_B(N,\mu_f),\end{aligned} \tag{1.13}$$

where we absorbed partonic indices into matrix notations in the last line.

1.4.2 DGLAP evolution from consistency of factorization

The parton distribution function defined in Eq. (1.10) depends on the UV renormalization scale μ_f. The evolution of the PDFs with respect to μ_f is governed by the Dokshitzer-Gribov-Lipatov-Altarelli-Parisi (DGLAP) evolution equation [35, 36, 37], as we will derive. If we trivially rearrange Eq. (1.10) as

$$f_{a/A}(x,\mu_f) \equiv \langle A| \int \frac{dw^-}{2\pi} e^{-ixP^+w^-/2}\, \bar{\psi}_a\left(0, w^-, \mathbf{0}_T\right) W\left(w^-, 0\right) \frac{\gamma^+}{4} \psi_a(0)\, |A\rangle, \tag{1.14}$$

it is possible to derive the renormalization of $f_{a/A}$ by studying the renormalization properties of the composite non-local operator that is sandwiched between $\langle A|$ and $|A\rangle$ [26]. However,

in the risk of running into a cyclic argument, with the benefit of hindsight that the collinear factorization theorem in Eq. (1.7) is valid, we can derive DGLAP evolution simply from the consistency of Eq. (1.7).

In Eq. (1.13), the cross section on the LHS must be formally independent of μ_f, which is an artificial scale introduced to separate collinear and hard regions. Therefore, the μ_f-dependence of the parton distribution function and the hard scattering on the RHS must cancel each other. We *define*, without prior knowledge about how the hard scattering $\tilde{\boldsymbol{C}}$ depends on μ_f,

$$\frac{d}{d\ln\mu_f}\ln\tilde{\boldsymbol{C}}\left(N, M^2/\mu_f^2, \alpha_s\left(\mu_f\right)\right) = 2\tilde{\boldsymbol{\gamma}}\left(N, M^2/\mu_f^2, \alpha_s\left(\mu_f\right)\right), \tag{1.15}$$

where $\ln\tilde{C}$ is the matrix logarithm, i.e. the inverse of matrix exponentiation, and α_s is the QCD coupling constant. This implies

$$\begin{aligned}\frac{d}{d\ln\mu_f}\tilde{\boldsymbol{C}}\left(N, M^2/\mu_f^2, \alpha_s\left(\mu_f\right)\right) = {}& \tilde{\boldsymbol{\gamma}}\left(N, M^2/\mu_f^2, \alpha_s\left(\mu_f\right)\right)\cdot\tilde{\boldsymbol{C}}\left(N, M^2/\mu_f^2, \alpha_s\left(\mu_f\right)\right)\\ &+ \tilde{\boldsymbol{C}}\left(N, M^2/\mu_f^2, \alpha_s\left(\mu_f\right)\right)\cdot\tilde{\boldsymbol{\gamma}}\left(N, M^2/\mu_f^2, \alpha_s\left(\mu_f\right)\right).\end{aligned} \tag{1.16}$$

For the sake of argument, let us consider $A = B$, i.e. the collision of two hadrons of the same species. For the LHS of Eq. (1.13) to be independent of $\ln\mu_f$, we must have

$$\begin{aligned}&\left[\tilde{\boldsymbol{f}}_A\left(N,\mu_f\right)\right]^T\cdot\tilde{\boldsymbol{C}}\left(N, M^2/\mu_f^2, \alpha_s\left(\mu_f\right)\right)\cdot\left[\tilde{\boldsymbol{\gamma}}\cdot\tilde{\boldsymbol{f}}_A\left(N,\mu_f\right) + \frac{d}{d\ln\mu_f}\tilde{\boldsymbol{f}}_A\left(N,\mu_f\right)\right]\\ &+\left[\tilde{\boldsymbol{\gamma}}\cdot\tilde{\boldsymbol{f}}_A\left(N,\mu_f\right) + \frac{d}{d\ln\mu_f}\tilde{\boldsymbol{f}}_A\left(N,\mu_f\right)\right]^T\cdot\tilde{\boldsymbol{C}}\left(N, M^2/\mu_f^2, \alpha_s\left(\mu_f\right)\right)\cdot\tilde{\boldsymbol{f}}_A\left(N,\mu_f\right) = 0,\end{aligned} \tag{1.17}$$

where we have suppressed the functional arguments of $\tilde{\boldsymbol{\gamma}}$. The two lines of on the LHS of Eq. (1.17) are equal, which implies

$$\frac{d}{d\ln\mu_f}\tilde{\boldsymbol{f}}_A\left(N,\mu_f\right) = -\tilde{\boldsymbol{\gamma}}\left(N, M^2/\mu_f^2, \alpha_s\left(\mu_f\right)\right)\cdot\tilde{\boldsymbol{f}}_A\left(N,\mu_f\right), \tag{1.18}$$

Since the parton distribution function does not depend on M^2/μ_f^2, $\tilde{\boldsymbol{\gamma}}$ must have no dependence on M^2/μ_f^2, either, which allows us to simplify Eqs. (1.18) to

$$\frac{d}{d\ln\mu_f}\tilde{\boldsymbol{f}}_A\left(N,\mu_f\right) = -\tilde{\boldsymbol{\gamma}}\left(N, \alpha_s\left(\mu_f\right)\right)\cdot\tilde{\boldsymbol{f}}_A\left(N,\mu_f\right), \tag{1.19}$$

Since $\tilde{\boldsymbol{\gamma}}$ is defined by the scale dependence of the hard scattering function which does not depend on the species of the colliding hadrons, $\tilde{\boldsymbol{\gamma}}$ has no dependence on the hadron species, either.

By performing an inverse Mellin transform, the DGLAP evolution equation is written as, in the more common form,

$$\frac{d}{d\ln\mu_f}f_{a/A}\left(x,\mu_f\right) = -\sum_b\int_x^1\frac{dy}{y}\,\gamma_{ab}\left(\frac{x}{y}, \alpha_s\left(\mu_f\right)\right)f_{b/A}\left(y,\mu_f\right), \tag{1.20}$$

where the matrix γ_{ab} is referred to as the DGLAP splitting kernel.

In practical applications to hadron colliders, the scale μ_f is chosen to be comparable with the hard momentum transfer, e.g. the invariant mass of the Drell-Yan pair, in order to avoid large logarithms that spoil the convergence of the perturbation series for the hard scattering functions. PDFs, obtained from experimental fitting, are typically tabulated at some low scale ~ 1 GeV, and are evolved to the high scale using the DGLAP equation.

1.5 Effective field theories

A recurring concept in physics is that long distance phenomenon can be described without knowledge of the details of short-distance physics. For example, the proton inside the hydrogen atom can be treated as an ideal point charge in non-relativistic quantum mechanics, despite the complicated nature of the proton bound state. In quantum field theories, heavy particles with masses much greater than the collision energy can be omitted from an effective field theory, when we consider scattering light particles. In the path integral language, the heavy field is "integrated out" from the quantum action, leaving an "effective" action built only from light particle fields. Since the heavy field corresponds to quantum fluctuations at short time and length scales, it leaves an imprint as local interaction vertices in the coupling between light fields. The coupling constants that multiply effective interaction terms are referred to as "matching coefficients", which are determined by requiring the EFT to give the same prediction for low-energy scattering as the underlying theory does.

Integrating out the heavy field will produce interaction terms of arbitrarily high dimensions. Following RG flow from the heavy particle scale to the lower energy scale at which experiments are conducted, only the interaction terms with dimension less than or equal to 4, i.e. super-renormalizable and renormalizable couplings, will have undiminished strengths. Interaction terms of dimension greater than 4 will lose importance at lower scales, suffering suppression by a factor of $(\mu/\Lambda)^{d-4}$, where μ is the scale at which the low energy effective field theory is defined, and Λ is the heavy particle mass scale. Formally speaking, the low-energy scattering amplitudes can be written as an asymptotic expansion in μ/Λ, with the coefficients of the expansion obtained from successively higher-dimensional operators.

The symmetries of an EFT may be different from the underlying QFT. On the one hand, symmetries in the UV theory may be spontaneously broken and missing from the low-energy EFT. An example is chiral symmetry of massless QCD, which is missing from the low-energy chiral perturbation theory [38], due to the non-perturbative non-zero vacuum expectation value of the quark condensate $\langle \bar{q}q \rangle$. On the other hand, accidental symmetries, not present in the UV theory, could appear in the renormalizable part of the low-energy EFT, only to be broken by higher-dimensional interaction terms. An example is the $SU(2N_f)$ symmetry of heavy quark effective theory [39], which says that the coupling of the heavy quark to light fields in independent of both heavy quark flavor and spin.

An EFT generally contains all interaction terms which are compatible with the symmetries. The symmetries can be used to determine all possible forms of interaction terms in the EFT, even when we lack the ability to derive the EFT, in a reductionist sense, from the underlying theory, e.g., in the case of chiral perturbation theory. In other situations, we can directly derive the EFT interaction terms from the underlying theory, but it may be sim-

pler to use the symmetries of the EFT to fix the interaction terms. For example, "collinear gauge invariance" [40] of soft collinear effective theory implies that the attachment of scalar-polarized collinear gluons to the hard scattering vertex is described by Wilson lines, without the need for a diagrammatic matching calculation.

To construct an EFT, it is necessary to find a minimal basis of independent operators at a particular dimension. We first need to write down all such operators that are compatible with the symmetries. Next, we need to eliminate redundant operators that can be written as linear superpositions of other operators, either due to equations that hold at the operator level (from Fierz rearrangements, Jacobi identities etc.), or due to equations of motion.

An EFT generally has worse UV behavior than the underlying theory, and needs extra UV renormalization. To calculate matching coefficients without encountering large logarithms that slow down the convergence of perturbation theory, it is necessary to choose the EFT renormalization scale to be comparable with the UV-completion scale Λ. However, when applying the EFT to calculate low-energy scattering processes, the natural renormalization scale is set by the transferred momentum, which is generally much smaller than Λ. RG running of the EFT relates matching coefficients at the two widely separated renormalization scales, and resums large logarithms of the ratio of the two scales.

Effective field theories have had a tremendous impact on how quantum field theories are viewed in general. The modern view is that all QFTs, including the Standard Model, are effective field theories of some underlying UV-finite theory, e.g. a string theory. Combined with the Wilsonian view of renormalization, this largely eliminated unease about the soundness of removing infinities via renormalization, which was prevalent in the early days of QED. Another widespread view coming from the study of EFTs is that a quantum field theory must contain all interaction terms that are compatible with the symmetries of the theory, and moreover, such interaction terms should have coupling strengths that are "natural". The extreme smallness of the Higgs mass compared with the GUT scale and the undetectably small θ term of QCD are considered to be extremely improbable if the SM describes all physics up to the GUT scale, and serve as motivation for looking for new physics.

1.6 Soft collinear effective theory

1.6.1 Generalities

Soft collinear effective theory (SCET) [41, 42, 40, 43, 44, 45, 46] is an EFT formulation of QCD factorization and resummation, with a root in the earlier study of heavy quark effective theory. SCET is an EFT within perturbative QCD, and does not address non-perturbative physics; non-perturbative information, such as parton distribution functions, is used as external input.

SCET is obtained from QCD by integrating out hard momentum modes, leaving soft modes and collinear modes as low-energy effective degrees of freedom. When there are multiple collinear groups, each group is considered as a separate collinear field. The hard sub-diagram in full QCD is turned into an effective interaction vertex which couples SCET collinear fields from different collinear groups. The matching coefficient for the effective interaction vertex is the IR-insensitive hard function.

A collinear particle in SCET has a large momentum in one lightcone direction, and small momentum fluctuations in the opposite lightcone direction and the two transverse directions. This is very different from conventional EFTs whose effective modes have all momentum components small. As a result, even at leading power, the SCET collinear Lagrangian is non-local in a particular lightcone direction.

IR power counting, a necessary step in deriving QCD factorization, is performed at the Lagrangian level in SCET. For example, in the vast majority of phenomenological applications, only leading-power terms are kept in the effective Lagrangian, in which case the Feynman diagrams that result from the Lagrangian are automatically the ones that contribute at leading power. The Ward identity argument for factorizing soft gluons from collinear particles in the conventional treatment of QCD factorization [24] is replaced by the Bauer-Pirjol-Stewart field redefinition [43] in SCET. The re-defined collinear field has no leading-power coupling to the soft field, therefore soft-collinear factorization becomes manifest at the Lagrangian level.

As is the case in the conventional treatment of QCD factorization, the overlap between momentum regions needs to be treated carefully. One approach is explicitly subtracting the soft-collinear overlap from the collinear function. This is referred to as "zero-bin" subtraction [47], which is physically the same [48, 49, 50] as how soft-collinear overlap is treated in the CSS formalism. Another approach is treating SCET as a Lagrangian formulation of the Beneke-Smirnov strategy of regions [51], with analytic regulators chosen to ensure that all overlap contributions vanish as dimensionless integrals. In this approach, overlap can be ignored completely, as long as we are willing to forfeit the ability to distinguish UV and IR poles in intermediate results. This somewhat obscures the physics, but simplifies practical calculations.

1.6.2 Power counting and the effective Lagrangian

We will start constructing SCET for pure Yang-Mill theory. Using the lightcone notations in Eq. (1.1)-(1.3), we define three momentum regions,

$$\text{Collinear: } Q(1, \lambda^2, \boldsymbol{\lambda}), \tag{1.21}$$

$$\text{Anti-collinear: } Q(\lambda^2, 1, \boldsymbol{\lambda}), \tag{1.22}$$

$$\text{ultrasoft: } Q(\lambda^2, \lambda^2, \boldsymbol{\lambda}^2), \tag{1.23}$$

where λ is a small parameter. The effective field theory for these IR momentum modes is called SCET$_I$. In other situations, a soft mode $Q \sim (\lambda, \lambda, \boldsymbol{\lambda})$, instead of an ultrasoft mode, is present, and the effective field theory is called SCET$_{II}$.

The effective gluon fields are A^c, $A^{\bar{c}}$, and A^{us}, whose momenta have collinear, anti-collinear, and ultrasoft scalings, respectively. Working in covariant gauges, we examine the gluon propagator

$$\langle 0|\mathcal{T} A^\mu(0) A^\nu(x)|0\rangle = \int \frac{d^4p}{(2\pi)^4} e^{ip\cdot x} \frac{i}{p^2 + i0^+} \left(-g^{\mu\nu} + (1-\xi)\frac{p^\mu p^\nu}{p^2} \right), \tag{1.24}$$

whose power counting behavior is

$$\int \frac{d^4p}{(p^2)^2} p^\mu p^\nu \sim p^\mu p^\nu. \tag{1.25}$$

Therefore, we should assign the power counting $A^\mu \sim p^\mu$. In other words, the collinear, anti-collinear, and ultrasoft gluon fields have the following power counting, in terms of powers of λ,

$$\left(A^{c+}, A^{c-}, \boldsymbol{A}^{cT}\right) \sim \left(1, \lambda^2, \lambda\right), \tag{1.26}$$

$$\left(A^{\bar{c}+}, A^{\bar{c}-}, \boldsymbol{A}^{\bar{c}T}\right) \sim \left(\lambda^2, 1, \lambda\right), \tag{1.27}$$

$$\left(A^{us+}, A^{us-}, \boldsymbol{A}^{usT}\right) \sim \left(\lambda^2, \lambda^2, \lambda^2\right). \tag{1.28}$$

The effective Lagrangian for the ultrasoft gluon field A_s is simply

$$\mathcal{L}_{us} = \int d^4x \, (-1)\frac{1}{4}\left(F^{s,a}_{\mu\nu}\right)^2, \tag{1.29}$$

where

$$\begin{aligned} F^s_{\mu\nu} &= -\frac{1}{ig}\left[D^s_\mu, D^s_\nu\right] \\ &= -\frac{1}{ig}\left[\partial_\mu - igA^s_\mu, \partial_\nu - igA^s_\nu\right]. \end{aligned} \tag{1.30}$$

We show that this action is of leading power, i.e. $\mathcal{O}\left(\lambda^0\right)$. The power counting of D_μ behaves as p_μ. So $F^s_{\mu\nu}$ behaves as $p^\mu p^\nu$, and $\left(F^s_{\mu\nu}\right)^2$ behaves as $\left(p^2\right)^2 \sim \lambda^8$ according to the ultrasoft momentum scaling, Eq. (1.23). Meanwhile, d^4x behaves as $1/\left(p^+p^-\boldsymbol{p}_T^2\right) \sim 1/\lambda^8$. It follows that the action behaves as λ^0.

We move on the the collinear gluon field A_c. In the absence of the ultrasoft gluons, the effective action for A_c alone is simply

$$\mathcal{L}_c = \int d^4x \, (-1)\frac{1}{4}\left(F^{c,a}_{\mu\nu}\right)^2, \tag{1.31}$$

where

$$\begin{aligned} F^c_{\mu\nu} &= -\frac{1}{ig}\left[D^c_\mu, D^c_\nu\right] \\ &= -\frac{1}{ig}\left[\partial_\mu - igA^c_\mu, \partial_\nu - igA^c_\nu\right]. \end{aligned} \tag{1.32}$$

Now d^4x behaves as $1/\lambda^4$ and $\left(F^c_{\mu\nu}\right)^2$ behaves as λ^4, so the action again behaves as λ^0.

Now we derive the leading-power Lagrangian for the interaction between collinear and ultrasoft gluons. A naive attempt is making the following replacement in Eq. (1.32),

$$\begin{aligned} & D^{c\,\mu}(x) = \partial^\mu - igA^{c\,\mu}(x) \\ \longrightarrow\ & D^\mu(x) = \partial^\mu - igA^{c\,\mu}(x) - igA^{s\,\mu}(x), \qquad \text{(wrong)} \end{aligned} \tag{1.33}$$

which, unfortunately, does not have a consistent leading-power behavior. Two fixes are needed. First, the power counting in Eq. (1.26) and (1.27) tells us that only A^{s-} is of the same power as A^{c-}, while all other Lorentz components A^s are sub-leading compared with the corresponding Lorentz components of A^c, and should therefore be removed from the

leading-power Lagrangian. Second, all the momentum components of the ultrasoft field, Eq. (1.23), with the exception of the "−" component, are much smaller than the corresponding momentum components of the collinear field, Eq. (1.21). Therefore, the ultrasoft field is much more slowly varying in the "−" and transverse *coordinate* directions than the collinear field, and at leading power, the collinear field cannot resolve the dependence of the ultrasoft field on these coordinate directions. With the above two points in mind, Eq. (1.33) is corrected to

$$D^\mu\left(x^+,x^-,\boldsymbol{x}\right)=\partial^\mu-igA^{c\,\mu}\left(x^+,x^-,\boldsymbol{x}\right)-ig\delta_-^\mu A^{s\,-}\left(x^+,0,\mathbf{0}\right), \tag{1.34}$$

and the Lagrangian that extends Eq. (1.31) to include collinear-ultrasoft interactions is

$$\mathcal{L}_{c+c\cdot us}=\int d^4x\,(-1)\frac{1}{4}\left(F^a_{\mu\nu}\right)^2, \tag{1.35}$$

where

$$F_{\mu\nu}=-\frac{1}{ig}\left[D_\mu,D_\nu\right]. \tag{1.36}$$

To obtain the Lagrangian that couples the anti-collinear field with the ultrasoft field, the same procedure should be carried out, except the roles of "+" and "−" indices are interchanged.

1.6.3 Factorization of ultrasoft gluons by field redefinition

Consider the identity

$$\begin{aligned}&\left[\partial^\mu-ig\delta_-^\mu A^{s\,-}\left(x^+,0,\mathbf{0}\right),A^{c\,\nu}(x)\right]\\&=\left[\partial^\mu,W^{us}\left(x^+,0,\mathbf{0}\right)A^{c\,\nu}(x)W^{us\,\dagger}\left(x^+,0,\mathbf{0}\right)\right],\end{aligned} \tag{1.37}$$

where we defined the "ultrasoft Wilson line"

$$W^{us}\left(x^+,0,\mathbf{0}\right)=\mathcal{P}\exp\int_{-\infty}^0\frac{dy^+}{2}igA^-\left(x^++y^+,0,0\right). \tag{1.38}$$

We re-define a collinear gluon field $A^{(0)\,c}$, related to the original collinear gluon field A^c by

$$\begin{aligned}A^{(0)\,c}&=W^{us}\left(x^+,0,\mathbf{0}\right)A^{c\,\nu}(x)W^{us}\left(x^+,0,\mathbf{0}\right)\\&=W^{us,AD}\left(x^+,0,\mathbf{0}\right)A^{c\,\nu},\end{aligned} \tag{1.39}$$

where in the second line we used the Wilson line in the adjoint representation to shorten the notation. The field strength in the Lagrangian in Eq. (1.35) can be expressed in terms of the re-defined collinear gluon field as

$$F_{\mu\nu}=-\frac{1}{ig}\left[D_\mu-igA^{(0)\,c}_\mu,D_\nu-igA^{(0)\,c}_\nu\right], \tag{1.40}$$

so Eq. (1.35) becomes the free Lagrangian for the re-defined collinear field, with no interactions with the ultrasoft field. The factorization of ultrasoft gluons from collinear gluons has become manifest at the Lagrangian level, and the Feynman rules for the ultrasoft Wilson lines give the well-known eikonal vertices for (ultra)soft gluons.

1.7 Organization of the thesis

The rest of the thesis is organized as follows. In Chapter 2 we describe the direct QCD and SCET approaches to threshold resummation, and make analytic and numerical comparisons. In Chapter 3 we apply threshold resummation to calculate the rate of inclusive production of W^+W^- boson pairs at the LHC. In Chapter 4 we perform transverse momentum resummation for the production of W^+W^- boson pairs, to improve the desription of differential distributions and jet veto efficiencies. In Chapter 5 we develop the EFT description of Higgs production via gluon fusion, via dimension-7 effective operators beyond the infinite top mass limit. In Chapter 5 we apply the dimension-7 Higgs-gluon operators to study generic BSM modifications to the Higgs transverse momentum distribution. This thesis is mainly based on the publications [52, 53, 54, 55, 56, 57]. This work was supported in part by the National Science Foundation grant PHY-131661.

Chapter 2

Threshold resummation in dQCD and SCET

This chapter is based on the publication [53].

2.1 Introduction

Threshold resummations organize singular distributions in the short distance functions of factorized inclusive hadronic cross sections to all orders in perturbation theory. This organization has been carried out in a variety of ways. Early work on the subject identified the importance of soft gluon radiation under phase space restrictions, and derived leading logarithmic corrections, including the role of the running coupling [58, 59, 60]. Threshold resummations including all logarithmic orders were based on the factorization of partonic cross sections into field-theoretic matrix elements in Ref. [61] and on direct diagrammatic analysis in Refs. [62, 63]. Since then, many developments and applications employing these approaches have appeared, including those described in Refs. [64, 65, 66, 67, 68, 69, 70], which we will have occasion to use below. These resummations were carried out directly in perturbative QCD, an approach that is sometimes referred to as "full QCD", and which we will call direct QCD (dQCD) below.

Much recent discussion has concerned the apparent contrast between dQCD threshold resummations [61, 62, 63, 64, 65, 70] and those based on effective field theory [71, 72, 73, 74], in particular on soft-collinear effective theory (SCET) [42, 43, 41]. In important analyses, Refs. [75, 76] and [71, 72, 77] confirmed the analytic equivalence of SCET and dQCD methods at various levels, and highlighted differences based on differing scale choices and treatments of non-singular behavior at threshold. Our aim here is to extend these analyses and to provide a further perspective on the relationship between direct QCD and SCET resummations, by pointing out their common basis in the factorization properties of soft gluon radiation [64]. This enables us to derive their key formulas side-by-side, and in this way to clarify their similarities and differences. We will also show that in practical terms, both approaches should give nearly identical predictions for many cross sections, even though at intermediate stages their treatments of hard-scattering functions differ markedly. For example, once the resummed cross sections are each computed in a manner that avoids extraneous differences

in nonsingular terms, their numerical predictions are essentially indistinguishable for Higgs boson production at LHC kinematics. These conclusions follow from a new expansion of the cross section based on the shape of parton luminosities, which may have further applications.

Both dQCD and SCET threshold resummations use Mellin or Laplace transforms as a tool, employing much the same all-orders analysis developed for the resummation of logarithms in transverse momentum using impact parameter space [78]. In direct QCD, the factorized cross sections are often given as integrals of products of Mellin- or Laplace-transformed hard scattering functions and parton distribution functions. In SCET, transforms may appear only as aids in solving evolution equations, and resummed cross sections are given directly in momentum space as convolutions of hard scattering functions and parton distributions. As we shall see, however, both hard-scattering functions are derived from the same evolution equation, applied to the same "soft function", the vacuum expectation value of a product of Wilson lines [66, 67, 68].

We emphasize at the outset that the specific direct QCD and SCET formalisms that we compare are by no means unique. For definiteness, we follow the presentations of [70] and [71] for dQCD and SCET respectively, but the conclusions we reach should apply to other applications of threshold resummation in QCD and SCET. Further clarifying the common and distinct features of threshold resummation in the notation of these well-known papers will lead us to a number of new results as well.[1]

Our discussion in Sec. 2.2 begins with a review to set notation for the cross sections under consideration. We go on to recall the re-factorization of soft radiation near partonic threshold [61, 71, 80], and the consequent evolution equations, common to both direct QCD and SCET. We recall the differing choices of boundary conditions in the direct QCD and effective theory formalisms, and the corresponding expressions for the resummed partonic and hadronic cross sections. No new results are derived in this section, but we believe the parallel development of the central results of the two formalisms, with an independent treatment of factorization and other scale dependences, clarifies their relationship.

Section 2.3 reformulates evolution in terms of the logarithm of the renormalized soft function. This logarithm, or "resummed exponent" has a direct interpretation in terms of diagrams called webs [81, 82, 83]. We compare treatments in moment and momentum space, applying renormalization group equations to the resummed exponent [78, 64]. We focus in particular on the non-leading resummation function commonly denoted $D(\alpha_s)$, which along with the cusp anomalous dimension determines all logarithms at partonic threshold. The function $D(\alpha_s)$ turns out to be proportional to the momentum-space sum of the web diagrams, evaluated at a specific scale.

In Sec. 2.4 we extend the results of Ref. [76], and show how the effective theory and direct QCD agree for partonic cross sections, up to subleading logarithmic differences in moment space, when the soft scale is chosen for this purpose. We will see that this agreement follows systematically at any order from the evolution equation for the sum of web diagrams, derived in Sec. 2.3. Finally, in Sec. 2.5 we find that, despite their different treatments of evolution for the soft function, it is actually natural to anticipate agreement for direct QCD and soft collinear effective theory resummations of hadronic cross sections, for most of the interesting

[1] Many of the same considerations apply to resummed event shape distributions, although based on factorizations that are different from the threshold case [79].

parameter range involved in collider experiments. We identify a natural expansion of the parton luminosity function in its logarithmic derivatives, whose first term gives dQCD and SCET resummations that agree identically for a natural choice of the SCET soft scale. We include two appendices that deal with technical developments.

2.2 Factorization, re-factorization and evolution

We begin by setting the notation for Drell-Yan-like, color-singlet inclusive cross sections, including the cases of electroweak vector boson and Higgs production. We go on to recall the factorization of soft radiation near partonic threshold, identify the resulting evolution equation, and contrast the solutions of this equation in dQCD moment-space resummation [61, 62, 63, 64, 65, 69, 70] and the soft-collinear effective theory (SCET) momentum space resummation method as developed in Refs. [71, 72].

2.2.1 Electroweak annihilation and its moments

Recall that the cross section for electroweak annihilation can be written in the factorized form, Eq. (1.7), and the Mellin moment space version, Eq. (1.13). We define the parton luminosity function $\mathcal{L}$,

$$\mathcal{L}_{ab}\left(\frac{\tau}{z},\mu_f\right) = z\int \frac{dx_a}{x_a}\frac{dx_b}{x_b} f_{a/A}\left(x_a,\mu_f\right) f_{b/B}\left(x_b,\mu_f\right)\delta\left(z-\frac{\tau}{x_a x_b}\right), \tag{2.1}$$

whose Mellin transform w.r.t. (τ/z) is the product of the Mellin transform of the two parton distribution functions. This enables us to re-write Eq. (1.7) as

$$s\frac{d\sigma_{AB\to M}\left(\tau,M^2\right)}{dM^2} = \sum_{\text{partons } a,b}\sigma_0\int_\tau^1 \mathcal{L}_{ab}\left(\frac{\tau}{z},\mu_f\right) C_{ab\to M}\left(z,M^2/\mu_f^2,\alpha_s\left(\mu_f\right)\right), \tag{2.2}$$

which can also be written in Mellin moment space,

$$\int_0^1 d\tau\,\tau^{N-1} s\frac{d\sigma_{AB\to M}\left(\tau,M^2\right)}{dM^2} = \sum_{\text{partons } a,b}\tilde{\mathcal{L}}_{ab}\left(N,\mu_f\right)\tilde{C}_{ab\to M}\left(N,M^2/\mu_f^2,\alpha_s\left(\mu_f\right)\right). \tag{2.3}$$

The hard scattering functions, $C_{ab\to M}$ in Eq. (2.2), are singular at partonic threshold $z\to 1$ if $a=\bar{a}$, where $a=q$, $\bar{a}=\bar{q}$ for γ^*/Z production, and $a=\bar{a}=g$ for Higgs production.[2] While the Mellin transform of a smooth analytic function always falls off at large N, singular behavior near $z=1$ causes $\tilde{C}$ to contain terms that are constant or growing at large N. So Eq. (2.3) becomes, in the large N limit,

$$\int_0^1 d\tau\,\tau^{N-1} s\frac{d\sigma_{AB\to M}\left(\tau,M^2\right)}{dM^2} = \sum_{a\leftrightarrow\bar{a}}\tilde{\mathcal{L}}_{a\bar{a}}\left(N,\mu_f\right)\tilde{C}_{a\bar{a}\to M}\left(N,M^2/\mu_f^2,\alpha_s\left(\mu_f\right)\right)+\mathcal{O}(1/N). \tag{2.4}$$

[2]Threshold singularities arise due to soft gluon emissions which do not change the flavor of the parton, so the parton flavor combination has to be the one that can occur at leading order in α_s.

The inverse Mellin transform from $\tilde{g}(N)$ to $g(x)$, with g being any of these functions, is given by

$$g(x) = \int_{\mathcal{C}_g} \frac{dN}{2\pi i} x^{-N} \tilde{g}(N), \tag{2.5}$$

where the contour $\mathcal{C}_g$ in the complex N plane is to the right of all the singularities of $g(N)$. This implies that $g(x) = 0$ for $x > 1$. Under the Mellin transform, or a closely-related Laplace transform introduced below, logarithmic singularities of the form $\ln^m(1-z)/(1-z)$ transform into series of logarithms in N beginning with $\ln^{m+1} N$, and similarly for the inverse transform.

2.2.2 Soft gluon re-factorization and the soft function

The essential property of the hard-scattering functions $C_{a\bar{a}}(z)$, which makes resummation possible, is a re-factorization of singular behavior for $1 - z \to 0$, [61, 66, 80, 71, 73]

$$\begin{aligned} C_{a\bar{a}\to M}\left(z, M^2/\mu^2, \alpha_s(\mu)\right) &= H_{a\bar{a}}\left(M/\mu, \alpha_s(\mu)\right) \\ &\times\ S_{a\bar{a}}\left(1-z, \frac{M(1-z)}{\mu}, \alpha_s(\mu)\right) + \mathcal{O}\left((1-z)^0\right)\ , \end{aligned} \tag{2.6}$$

where as indicated, corrections are less singular than $1/(1-z)$ or $\delta(1-z)$ as $z \to 1$. Such corrections, which may include powers of $\ln(1-z)$, contribute at order $1/N$ times logs of N [84]. The factorization scale, labelled μ here, can be chosen equal to the renormalization scale for this discussion. The quantity $S_{a\bar{a}}$ is a "soft function" whose field theoretic definition, given below, is essentially equivalent in full QCD and soft-collinear effective theory.

Once a general factorization theorem, Eq. (2.2) is established, the re-factorization, Eq. (2.6) of the hard-scattering functions follows in dQCD from the use of the Ward identities of the theory [61], or equivalently in effective field theory language, by a field redefinition for hard collinear quanta [71, 73, 43]. Singular $1/(1-z)$ behavior is only present for short-distance functions that describe annihilation, $b = \bar{a}$, because all other combinations require the emission of a soft quark or antiquark into the final state, which suppresses infrared behavior. We also notice in passing that we are using a conventional, if slightly non-intuitive, terminology in which the hard-scattering function is the product of the soft function with a short-distance function. The soft function, however, is determined by perturbative methods, as we now describe.

The soft function, $S_{a\bar{a}}$, which is termed the "eikonal hard-scattering function" in Ref. [85], is a dimensionless quantity constructed from the vacuum expectation of a Wilson loop that describes the annihilation of two lightlike Wilson (or eikonal) lines,[3]

$$S_{a\bar{a}}\left(1-z, \frac{M(1-z)}{\mu}, \alpha_s(\mu)\right) = M\, W_{a\bar{a}}\left(M(1-z), \mu, \alpha_s(\mu)\right)\ . \tag{2.7}$$

[3]This is actually not the complete definition, as collinear singularities are present and need to be removed by subtracting the eikonal parton distribution functions. This can be done easily as the eikonal parton distribution functions are pure poles after $\overline{\rm MS}$ UV renormalization, due to the dimensionless nature of the integral involved. We have chosen not to get into this technicality in the text.

The function $W_{a\bar{a}}(\omega, \mu, \alpha_s(\mu))$ in turn is defined as the Fourier transform

$$W_{a\bar{a}}\left(\omega, \mu, \alpha_s(\mu)\right) = \int_{-\infty}^{\infty} \frac{dx^0}{4\pi}\, e^{i\omega x^0/2}\, \widetilde{W}_{a\bar{a}}(x^0, \vec{x}=0, \mu)\,, \tag{2.8}$$

of a Wilson loop vacuum expectation [61, 66, 80, 71]

$$\tilde{W}_{a\bar{a}}(x,\mu) = \frac{1}{N_c}\,\langle 0|\,\mathrm{Tr}\,\bar{\mathbf{T}}\left[\Phi_n^{(a)\dagger}(x)\Phi_{\bar{n}}^{(a)}(x)\right]\mathbf{T}\left[\Phi_{\bar{n}}^{(a)\dagger}(0)\Phi_n^{(a)}(0)\right]|0\rangle\,. \tag{2.9}$$

In these matrix elements, the operators Φ_β are lightlike path-ordered exponentials in the directions β,

$$\Phi_\beta^{(a)}(x) = \mathbf{P}\,\exp\left(-ig\int_{-\infty}^{0} ds\,\beta\cdot A^{(a)}(x+s\beta)\right)\,. \tag{2.10}$$

These ordered exponentials are matrices in the representations appropriate to the partons $a\bar{a}$ that annihilate, with $\beta = n, \bar{n}$ moving in opposite directions, $n\cdot\bar{n}=1$.

The matrix elements $W_{a\bar{a}}(x_0\mu)$ can be taken as the starting point for threshold resummation. In the effective field theory treatment, $W_{a\bar{a}}$ is evaluated using the SCET ultra-soft gluon field A_s rather than the usual QCD gluon field A, but since the Feynman rules involved are the same, the two definitions are essentially identical.

For all treatments of threshold resummation, Mellin, Eq. (1.12), and/or Laplace transformations are useful, and equivalent to leading power in N or $1/(1-z)$ because $(-\ln z) \approx 1-z$ in this limit. The Laplace transform of the soft function is

$$\widetilde{S}\left(\ln\frac{M}{\bar{N}\mu}, \alpha_s(\mu)\right) = \int_0^\infty \frac{d\omega}{M}\,\exp\left[-\frac{N\omega}{M}\right] S\left(\frac{\omega}{M}, \frac{\omega}{\mu}, \alpha_s(\mu)\right) \tag{2.11}$$

$$= \int_0^1 dz\, z^{N-1} S\left(1-z, \frac{M(1-z)}{\mu}, \alpha_s(\mu)\right) \;+\; \mathcal{O}(1/N)\,, \tag{2.12}$$

where as in Eqs. (2.7) and (2.8) we identify $\omega = M(1-z)$, and define

$$\bar{N} \equiv N e^{\gamma_E}\,, \tag{2.13}$$

with γ_E Euler's constant.[4] In the second equality of (2.12) we have used $z^N = e^{-(1-z)N} + \mathcal{O}(1-z)$. Notice that the soft function, $\widetilde{S}$, is dimensionless in moment space and needs only two arguments.

2.2.3 Evolution equation for the soft function

From Eqs. (2.4), (2.6), and (2.12), we have

$$\int_0^1 d\tau\,\tau^{N-1} s\frac{d\sigma_{AB\to M}\left(\tau, M^2\right)}{dM^2} = \sum_{a\leftrightarrow\bar{a}} \tilde{\mathcal{L}}_{a\bar{a}}\left(N, \mu_f\right) H\left(\frac{M}{\mu_f}, \alpha_s\left(\mu_f\right)\right)\widetilde{S}\left(\ln\frac{M}{\tilde{N}\mu_f}, \alpha_s\left(\mu_f\right)\right) + \mathcal{O}(1/N). \tag{2.14}$$

[4] We note that the combination $\ln M/\bar{N}\mu$ is denoted by L in [71].

Now we can derive evolution equations from consistency of factorization. By demanding that the $\ln \mu_f$ derivative of the LHS of the above equation gives zero, we see that the $\ln \mu_f$ derivatives of $\mathcal{L}$, H, and $\widetilde{S}$ can have at most a linear power of $\ln \tilde{N}$, $\ln \mu_f/M$, and $\ln M/(\tilde{N}\mu_f)$, respectively, multiplied by the same (with the proper sign) coefficient called the "cusp anomalous dimension",

$$\frac{d}{d\ln\mu} \ln \widetilde{S}\left(\ln\frac{M}{\bar{N}\mu}, \alpha_s(\mu)\right) = -2\Gamma_{\rm cusp}\left(\alpha_s(\mu)\right) \ln\frac{M^2}{\bar{N}^2\mu^2} - 2\gamma_W\left(\alpha_s(\mu)\right) , \tag{2.15}$$

$$\frac{d}{d\ln\mu} \ln f_{a/A}(N,\mu) = -2\Gamma_{\rm cusp}(\alpha_s(\mu)) \ln \bar{N} + 2\gamma_a\left((\alpha_s(\mu)\right) + \mathcal{O}(1/N) , \tag{2.16}$$

$$\frac{d}{d\ln\mu} \ln H\left(\frac{M}{\mu_f}, \alpha_s\left(\mu_f\right)\right) = 2\Gamma_{\rm cusp}\left(\alpha_s(\mu)\right) \ln\frac{M^2}{\mu^2} + 2\gamma_h\left(\alpha_s(\mu)\right) \tag{2.17}$$

The special role of the function $W_{a\bar{a}}(x_0\mu)$, Eq. (2.9) for threshold resummation was identified in this context by Korchemsky and Marchesini in Refs. [66, 67]. It was evaluated at two loops by Belitsky [68], who verified that in moment space it obeys the renormalization group equation Eq. (2.15) that generates double logarithms in moments, in terms of the cusp anomalous dimension, $\Gamma_{\rm cusp}(\alpha_s)$, and another anomalous dimension, $\gamma_W(\alpha_s)$ characteristic of this annihilation matrix element.[5] Specifically, γ_W in [71] equals $-(1/2)\Gamma_{\rm DY}$ in the notation of Belitsky [68]. This equation for the soft function summarizes the moment and momentum fraction evolution equations in Refs. [61] and [64], and reappears in this form in [71], for example.

The solution to the soft function evolution equation, Eq. (2.15), is

$$\widetilde{S}\left(\ln\frac{M}{\bar{N}\mu_1}, \alpha_s(\mu_1)\right) = \widetilde{S}\left(\ln\frac{M}{\bar{N}\mu_2}, \alpha_s(\mu_2)\right) \times \exp\left\{\int_{\mu_2}^{\mu_1}\frac{d\mu'}{\mu'}\left(4\Gamma_{\rm cusp}\ln\left(\frac{\mu'\bar{N}}{M}\right) - 2\gamma_W\left(\alpha_s(\mu')\right)\right)\right\} . \tag{2.18}$$

It is only at this stage that SCET and dQCD methods part ways, in their choices of the scales, and then in their use of the inverse Laplace or Mellin transform to derive physical cross sections.

In the direct QCD resummation approach [64, 68] the evolution equation (2.15) is run from scale $\mu_2 = M/\bar{N}$ to a factorization scale $\mu \sim M$, giving

$$\begin{aligned}
&\widetilde{S}^{[dQCD]}\left(\ln\frac{M}{\bar{N}\mu}, \alpha_s(\mu)\right) \\
&= S\left(0, \alpha_s(M/\bar{N})\right) \exp\left\{\int_{M/\bar{N}}^{\mu}\frac{d\mu'}{\mu'}\left(4\Gamma_{\rm cusp}\ln\left(\frac{\mu'\bar{N}}{M}\right) - 2\gamma_W\left(\alpha_s(\mu')\right)\right)\right\} \\
&= \widetilde{S}\left(0, \alpha_s(\mu)\right) \exp\left\{\int_{M/\bar{N}}^{\mu}\frac{d\mu'}{\mu'}\left(4\Gamma_{\rm cusp}(\alpha_s(\mu'))\ln\left(\frac{\mu'\bar{N}}{M}\right) - \hat{D}\left(\alpha_s(\mu')\right)\right)\right\} .
\end{aligned} \tag{2.19}$$

The first equality is the form that appears in Ref. [68], and the second is a form given in [71] and [77] in comparing dQCD and SCET resummations. In the second equality, the function

[5] It is denoted γ^W in Ref. [71].

$\hat{D}$ is defined by

$$\hat{D}\left(\alpha_s(\mu')\right) = 2\gamma_W\left(\alpha_s(\mu')\right) + \mu'\frac{\partial}{\partial\mu'}\ln\widetilde{S}(0,\alpha_s(\mu'))\,. \tag{2.20}$$

The resummation function $\hat{D}(\alpha_s)$ is thus a hybrid object, the sum of an anomalous dimension and the logarithmic derivative of the non-local perturbative soft function. We will return to its interpretation in the following section.

With a change of variables for the $\hat{D}$ term, we can rewrite Eq. (2.19) as

$$\widetilde{S}^{[dQCD]}\left(\ln\frac{M}{N\mu},\alpha_s(\mu)\right) = \widetilde{S}\left(0,\alpha_s(M)\right) \times \exp\left\{\int_{1/\bar{N}}^{\mu/M}\frac{dy}{y}\left[4\int_{yM}^{\mu}\frac{d\mu'}{\mu'}\,\Gamma_{\rm cusp}(\alpha_s(\mu')) - \hat{D}\left(\alpha_s(yM)\right)\right]\right\}, \tag{2.21}$$

which is a commonly used form, for example in [70] if we choose $\mu = \mu_f$. We will discuss factorization scale dependence below. Using explicit forms of the running coupling, Eq. (2.21) may be evaluated analytically to give the resummed moment dependence, as in Ref. [70]. Any such expression will of course produce a Landau pole in the N plane at $\bar{N} = M/\Lambda_{\rm QCD}$. This singularity and its treatment in hadronic cross sections (see the next subsection) is sometimes cited as a motivation for the SCET treatment of resummation, to which we now turn.

For SCET, in Ref. [71] the running in Eq. (2.15) is taken directly between a short distance scale μ and a fixed, N-independent soft scale μ_s,

$$\widetilde{S}^{[SCET]}\left(\ln\frac{M}{\bar{N}\mu},\alpha_s(\mu),\mu_s\right) = \widetilde{S}\left(\ln\frac{M}{\bar{N}\mu_s},\alpha_s(\mu_s)\right) \times \exp\left\{\int_{\mu_s}^{\mu}\frac{d\mu'}{\mu'}\,\left(4\Gamma_{\rm cusp}(\alpha_s(\mu'))\,\ln\left(\frac{\mu'\bar{N}}{M}\right) - 2\gamma_W\left(\alpha_s(\mu')\right)\right)\right\}. \tag{2.22}$$

Here, N-dependence is only in the the soft function evaluated at scale μ_s and in the explicit factor of $\ln N$ that multiplies the cusp anomalous dimension in the exponent. Despite this alternative representation, it is clear that the two expressions, Eq. (2.19) and (2.22) are identically equal when taken at the same choice of scale μ and evaluated to all orders, in which case $\widetilde{S}^{[SCET]}$ is independent of μ_s. Dependence on μ_s remains in $\widetilde{S}^{[SCET]}$, however, when it is evaluated to finite order, or summed to a fixed logarithmic order. Thus, μ_s should be included as an argument of $\widetilde{S}^{[SCET]}$ in general. Even in this case, however, the SCET and dQCD soft functions will be equal if we make the choice, $\mu_s = M/\bar{N}$. We can summarize these results as

$$\begin{aligned}\widetilde{S}^{[SCET]}\left(\ln\frac{M}{\bar{N}\mu},\alpha_s(\mu)\right)_{\text{all orders}} &= \widetilde{S}^{[dQCD]}\left(\ln\frac{M}{\bar{N}\mu},\alpha_s(\mu)\right)_{\text{all orders}}\,,\\ \widetilde{S}^{[SCET]}\left(\ln\frac{M}{\bar{N}\mu},\alpha_s(\mu),\mu_s=\frac{M}{\bar{N}}\right)_{\text{fixed order}} &= \widetilde{S}^{[dQCD]}\left(\ln\frac{M}{\bar{N}\mu},\alpha_s(\mu)\right)_{\text{fixed order}}\,.\end{aligned} \tag{2.23}$$

The free choice in the dQCD treatment that corresponds to the SCET soft scale is simply the lower limit of the y integral in Eq. (2.21), where $\bar{N} = e^{\gamma_E} N$ can be replaced by an arbitrary constant times N at the same logarithmic accuracy, adjusting the function $\hat{D}$ at higher orders as necessary.

In Ref. [71], the SCET expression (2.22) is further reorganized by using the $\ln N$ dependence in the exponent as a generating function for $\ln N$-dependence in the soft function. For this purpose, we adopt a notation close to that of Ref. [71] and write (2.22) as

$$\widetilde{S}^{[SCET]}\left(\ln\frac{M}{\bar{N}\mu}, \alpha_s(\mu), \mu_s\right) = \exp\left[-4S_{\rm cusp}\left(\mu_s,\mu\right) + 2\alpha_{\gamma_W}\left(\mu_s,\mu\right) + \eta(\mu_s,\mu)\,\ln\frac{M^2}{\mu_s^2}\right] \times\ \widetilde{S}\left(\ln\frac{M^2}{\mu_s^2} + \frac{\partial}{\partial\eta(\mu)}, \mu_s\right)\ \exp\left[-\,\eta(\mu_s,\mu)\,\ln\bar{N}^2\right]\,, \tag{2.24}$$

where the various quantities in the exponents are defined by

$$\begin{aligned} S_{\rm cusp}\left(\mu_s,\mu\right) &= -\int_{\mu_s}^{\mu}\frac{d\mu'}{\mu'}\,\Gamma_{\rm cusp}(\alpha_s(\mu'))\ln\frac{\mu'}{\mu_s} \;=\; -\,\frac{1}{2}C_a\frac{\alpha_s}{\pi}\,\ln^2\frac{\mu}{\mu_s} \quad +\cdots\,, \\ \alpha_{\gamma_W}\left(\mu_s,\mu\right) &= \;-\int_{\mu_s}^{\mu}\frac{d\mu'}{\mu'}\,\gamma_W(\alpha_s(\mu')) \;=\; \mathcal{O}\left(\alpha_s^2\right)\,, \end{aligned} \tag{2.25}$$

and

$$\eta(\mu_s,\mu) = \;-\,2\alpha_\Gamma\left(\mu_s,\mu\right) = -2\int_{\mu_s}^{\mu}\frac{d\mu'}{\mu'}\,\Gamma_{\rm cusp}(\alpha(\mu')) \;=\; -\,2C_a\frac{\alpha_s}{\pi}\,\ln\frac{\mu}{\mu_s} \;+\;\cdots\,. \tag{2.26}$$

Here, for definiteness and later use, we show order α_s expressions, in which $a = q, g$, with $C_q = C_F$ and $C_g = C_A$.[6] Despite the differences in notation, every term in the resummed effective theory exponential has an exact correspondence in the direct QCD result, with differences due primarily to different choices of boundary conditions. Thus, for example, the combination $S_{\rm cusp} + \eta\ln(M^2/\mu_s^2)$ in (2.24) is precisely the $\Gamma_{\rm cusp}$ term of Eq. (2.22). Matching to fixed-order and nonsingular calculations involving all parton types is also common to both formalisms, and we shall not discuss it here.

2.2.4 Hadronic cross sections in direct QCD and SCET

To close this section, we examine how the contrasting moment-space solutions (2.21) and (2.22) are inverted and combined with parton distributions to produce physical cross sections, each with its individual estimate of higher order corrections. In principle, both the moment-based dQCD expression (2.21) and the SCET expression (2.22) can be transformed to give a hard-scattering function $C_{ab\to M}\left(z, M^2/\mu_f^2, \alpha_s(\mu_f)\right)$, Eq. (2.6), directly in terms of the

[6] In Ref. [71] the quantities in Eq. (2.25) and (2.26) are evaluated by changing variables $d\ln\mu = d\alpha/\beta(\alpha)$, the details of which are omitted here.

variable z, including all singular behavior for $z \to 1$, to an accuracy determined by the order to which the anomalous dimension $\Gamma_{\rm cusp}$ and the function $\hat{D}$, Eq. (2.20) are known [86]. The well-known "minimal" approach [87] employed in Ref. [69, 70], however, numerically inverts the product of the moment of the hard scattering function times the moment of the parton luminosity. Before reviewing approaches to moment inversion, however, we will reintroduce dependence on an independent factorization scale, μ_f in the full cross section, Eq. (2.2).

The large-N factorization scale dependence of the parton distributions is given by Eq. (2.16), which can be converted to the conventional A/B notation by the relations $A = \Gamma_{\rm cusp}$ and $B_a \equiv 2\gamma_a$ (γ_a is denoted by γ^ϕ in Ref. [71]). The solution at large N for the distributions is then

$$f_{a/A}(N,\mu_f) = f_{a/A}(N,\mu)\ \exp\left[\int_\mu^{\mu_f} \frac{d\mu'}{\mu'}\ \left(-2\Gamma_{\rm cusp}(\alpha_s(\mu'))\ln\bar{N} + 2\gamma_a(\alpha_s(\mu'))\right)\right]. \qquad (2.27)$$

Substituting this relation into Eq. (2.3) gives the factorized cross section with arbitrary factorization scale, simply by absorbing this exponential into the moments of the coefficient function $\widetilde{C}_{a\bar{a}}$, which near partonic threshold is given in momentum space by the refactorized form, Eq. (2.6). The Mellin moment of the inclusive cross section factorizes into products of moment-space parton distributions times hard-scattering functions, Eq. (2.3). Following [87], one may invert the products of these functions, choosing a contour that passes between the logarithmic branch cuts at negative real N and the running coupling branch cuts at large real N, intersecting the real axis at $\mathrm{Re}(N) = n_0 > 0$ within the specified range. The presence of the right-hand branch cut leads in general to contributions with $\tau > 1$ which, however, are exponentially suppressed in the hard scale.

The "minimal" prescription [87] just described may be represented as

$$\frac{d\sigma^{(a)}_{AB\to M}(S,M^2)}{dM^2} = \sigma_0^{a\bar{a}}(S,M^2)\ \sum_{a\leftrightarrow\bar{a}}\ \int_{n_0-i\infty}^{n_0+i\infty}\frac{dN}{2\pi i}\,\tau^{-N}\ \widetilde{\mathcal{L}}_{a\bar{a}}(N,\mu_f)$$
$$\times\ \widetilde{C}^{[dQCD]}_{a\bar{a}}\left(N,\frac{M}{\mu_f},\alpha_s(\mu_f)\right), \qquad (2.28)$$

where we exhibit only those partonic channels that require threshold resummation, and where from Eq. (2.21), taking $\mu = M$ there, we have

$$\widetilde{C}^{[dQCD]}_{a\bar{a}}\left(N,\frac{M}{\mu_f},\alpha_s(\mu_f)\right) = \hat{H}_{a\bar{a}}\left(\frac{M}{\mu_f},\alpha_s(\mu_f)\right)$$
$$\times \exp\left\{\int_{1/\bar{N}}^1 \frac{dy}{y}\left[4\int_{yM}^{\mu_f}\frac{dq}{q}\ \Gamma_{\rm cusp}(\alpha_s(q))\ -\ \hat{D}\left(\alpha_s(yM)\right)\right]\right\}$$
$$+\ \mathcal{O}(1/N)\,. \qquad (2.29)$$

In this expression we have absorbed part of the μ_f behavior into a modified hard scattering function, $\hat{H}_{a\bar{a}}$, which is simply the short distance function in Eq. (2.6) multiplied by a factor associated with the evolution of the parton distributions,

$$\hat{H}_{a\bar{a}}\left(\frac{M}{\mu_f},\alpha_s(\mu_f)\right) = \exp\left\{-\ \int_M^{\mu_f}\frac{d\mu'}{\mu'}\ 4\gamma_a(\alpha_s(\mu'))\right\}\ H_{a\bar{a}}\left(1,\alpha_s(M)\right). \qquad (2.30)$$

The exponential factor absorbs all μ_f dependence associated with the anomalous dimensions $\gamma_a = \gamma_{\bar{a}}$. The expansion of the transform of Eq. (2.29) will reproduce all leading-power singularities in $1-z$ to an order limited only by our knowledge of the anomalous dimension $\Gamma_{\rm cusp}$, the resummation function, $\hat{D}$ and the overall function $\hat{H}$. Of course, to this expression we must add terms that are nonsingular for $z \to 1$ by matching.

The effective theory approach of Ref. [71] inverts moments of the soft function directly, before combining with the parton distribution functions. The cross section at arbitrary factorization scale μ_f is just a restatement of Eq. (2.3) with the SCET coefficient function,

$$\frac{d\sigma^{(a)}_{AB\to M}(S,M^2)}{dM^2} = \sigma_0^{a\bar{a}}(S,M^2) \sum_{a\leftrightarrow\bar{a}} \int_\tau^1 \frac{dz}{z}\, \mathcal{L}_{a\bar{a}}\left(\frac{\tau}{z},\mu_f\right)\, C^{[SCET]}_{a\bar{a}\to M}\left(z,M,\mu_f,\mu_s\right) . \tag{2.31}$$

In this case, the perturbative coefficient function is given at leading power in $1-z$ by combining the coefficient at scale μ, Eq. (2.24) with the evolution factor Eq. (2.27),

$$\begin{aligned} C^{[SCET]}_{a\bar{a}\to M}\left(z,M,\mu_f,\mu_s\right) = \; & H_{a\bar{a}}\left(\frac{M}{\mu},\alpha_s(\mu)\right) \int_{n_0-i\infty}^{n_0+i\infty} \frac{dN}{2\pi i}\, z^{-N} \\ & \times \exp\left[\int_\mu^{\mu_f} \frac{d\mu'}{\mu'}\left(-4\Gamma_{\rm cusp}(\alpha_s(\mu'))\ln\bar{N} + 4\gamma_a(\alpha_s(\mu'))\right)\right] \widetilde{S}^{[SCET]}_{a\bar{a}}\left(\frac{M}{\bar{N}\mu},\alpha_s(\mu),\mu_s\right) . \end{aligned} \tag{2.32}$$

The result is formally independent of the starting factorization scale, μ, which now plays the role of the "hard [matching] scale" in the effective theory treatment of Ref. [71]. When N dependence in the boundary condition has been replaced by a series of derivatives, the inverse transform from N to $1-z$ can be done explicitly, to give

$$\begin{aligned} & C^{[SCET]}_{a\bar{a}}\left(z,M,\mu,\mu_f,\mu_s\right) = \\ & \quad H_{a\bar{a}}\left(\frac{M}{\mu},\alpha_s(\mu)\right) \exp\left[-4S_{\rm cusp}\left(\mu_s,\mu\right) + 2\alpha_{\gamma_W}\left(\mu_s,\mu\right) + 4\alpha_{\gamma_a}(\mu,\mu_f) + \eta(\mu_s,\mu_f)\,\ln\frac{M^2}{\mu_s^2}\right] \\ & \qquad \times\; \widetilde{S}_{a\bar{a}}\left(\ln\frac{M^2}{\mu_s^2} + \frac{\partial}{\partial\eta(\mu_s,\mu_f)},\mu_s\right)\, \frac{e^{-2\gamma_E\eta(\mu_s,\mu_f)}\,(1-z)^{2\eta(\mu_s,\mu_f)-1}}{\Gamma\left(2\eta(\mu_s,\mu_f)\right)} , \end{aligned} \tag{2.33}$$

where in the exponential, the functions $S_{\rm cusp}(\mu_s,\mu)$ (not to be confused with $\widetilde{S}_{a\bar{a}}$), $\alpha_{\gamma_{\rm W}}(\mu,\mu_f)$ and $\eta(\mu_s,\mu_f)$ are given in Eqs. (2.25) and (2.26). The resummed cross section is then found directly in momentum space from Eq. (2.31).

In the treatment of the effective theory described in Ref. [71], the soft scale μ_s is chosen to stabilize the hadronic cross section when $S_{a\bar{a}}$ is known to fixed order. Notice that, in contrast to the dQCD result, Eq. (2.29), the leading powers in logarithms, $\alpha_s^k \ln^{2k-1}(1-z)$, are reproduced in the SCET result, Eq. (2.33), only to the order at which the soft function has been computed. Beyond this order, leading logarithms in $1-z$ are replaced by combinations of logarithms of $1-z$ and μ_s, as observed for example in [88]. This need not be a problem, so long as the range $1-\mu_s/M < z < 1$ is not phenomenologically important for the specific parton luminosity under consideration.

To close this section, we summarize by comparing Eqs. (2.28) for dQCD and (2.31) for SCET. When expanded in powers of α_s, the dQCD minimal prescription reproduces

leading and subleading logarithms in $1-z$ at all orders in perturbation theory, without introducing explicit nonperturbative parameters. Of course the choice of Mellin inversion transform of Eq. (2.28) that makes it possible to sum these terms is itself a particular choice of nonperturbative information. The effective theory resummation avoids the potential Landau pole in its application to hadronic cross sections. It does so by replacing leading logarithms of $1-z$ beyond the lowest orders with a mixture of logarithms of $1-z$ and μ_s/M, so that it remains strictly perturbative. In Secs. 2.4 and 2.5 we will explore the consequences of these rather different choices. First, however, we relate our previous resummed exponents to exponents written in terms of inverse Mellin moments and plus distributions in the dQCD formalism.

2.3 The soft function as an exponentiated Mellin moment

We have rederived in Eq. (2.29) one of the basic dQCD forms for threshold resummation in correspondence to the effective theory treatment, but there is another form of the resummed cross section, which bears further comparison here. In this form, the coefficient function $C_{a\bar{a}}$ of Eq. (2.4) is given as the exponential of an explicit Mellin moment [61, 62],

$$\begin{aligned}\widetilde{C}_{a\bar{a}}^{[dQCD]}\left(N,\frac{M}{\mu_f},\alpha_s\left(\mu_f\right)\right) &= \hat{H}_{a\bar{a}}\left(\frac{M}{\mu_f},\alpha_s(\mu_f)\right)\ \widetilde{S}_{a\bar{a}}\left(\frac{M}{\bar{N}\mu_f},\alpha_s(\mu_f)\right)\\ &= \widetilde{H}_{a\bar{a}}\left(\frac{M}{\mu_f},\alpha_s(\mu_f)\right)\ \exp\left\{\int_0^1 dz\frac{z^{N-1}-1}{1-z}\right.\\ &\quad\left.\times\left[4\int_{\mu_f}^{(1-z)M}\frac{d\mu'}{\mu'}A\left(\alpha\left(\mu'\right)\right)+D\left(\alpha\left((1-z)M\right)\right)\right]\right\}, \qquad (2.34)\end{aligned}$$

where the factorization scale dependence of the hard scattering function, $\hat{H}_{a\bar{a}}$ is given in Eq. (2.30). In the second line we have changed $\hat{H}_{a\bar{a}}$ to $\widetilde{H}_{a\bar{a}}$ because, as we shall see below, part of the N-independent term in the soft function $S_{a\bar{a}}$ has been absorbed. All leading, as well as many non-leading, logarithms of N in Eq. (2.34) are generated by the "universal" anomalous dimension, $A(\alpha_s)=\Gamma_{\rm cusp}(\alpha_s)$, which is defined by the singular term, $2A(\alpha_s)/(1-x)_+$, in diagonal DGLAP evolution (parton a here), or alternatively the coefficient of $\ln N$ in moment space, see Eq. (2.16). The function, $D(\alpha_s)$ generates the remainder of non-leading logarithms of N. It is clearly related to the function $\hat{D}(\alpha_s)$ in Eq. (2.19), and we will rederive the rather complex expression for this relation, given in [70]. We will also rederive Eq. (2.34) below from our previous considerations. This will enable us to give a direct interpretation of $D(\alpha_s)$ in terms of the soft function, $S_{a\bar{a}}$ in z space that is as natural as the definition of $\hat{D}(\alpha_s)$ in Eq. (2.20), which is formulated in terms of the soft function, $\widetilde{S}_{a\bar{a}}$ in N-space.

2.3.1 Evolution for the exponent

To derive Eq. (2.34), we consider the logarithm of the moment space soft function,

$$\widetilde{E}\left(\ln\frac{M}{\bar{N}\mu},\alpha_s(\mu)\right) \;\equiv\; \ln\left[\;\widetilde{S}\left(\ln\frac{M}{\bar{N}\mu},\alpha_s(\mu)\right)\;\right]. \tag{2.35}$$

The function $\widetilde{E}$ can be defined as the sum of a set of modified perturbative diagrams, so-called "webs" [81, 82, 83], which are discussed in the context of resummation in Ref. [85]. We will not reproduce their explicit construction here, but only emphasize that they provide a well-defined perturbative expansion that begins at order α_s with single gluon exchange and emission.

The inverse transform of $\widetilde{E}$ to momentum space is

$$\begin{aligned} E\left(1-z,\frac{M(1-z)}{\mu},\alpha(\mu)\right) &= \int_{n_0-i\infty}^{n_0+i\infty}\frac{dN}{2\pi i}\,z^{-N}\;\widetilde{E}\left(\ln\frac{M}{\bar{N}\mu},\alpha\left(\mu\right)\right) \\ &= \int_{n_0-i\infty}^{n_0+i\infty}\frac{dN}{2\pi i}\,e^{N(1-z)}\;\widetilde{E}\left(\ln\frac{M}{\bar{N}\mu},\alpha\left(\mu\right)\right) \;+\; \mathcal{O}\left((1-z)^0\right). \end{aligned} \tag{2.36}$$

Applying the inverse Laplace transform to the evolution equation (2.15) for $\widetilde{E}=\ln\widetilde{S}$, we also derive an evolution equation for the same momentum space the web function, E, accurate to leading power in $1-z$,

$$\begin{aligned} \frac{d}{d\ln\mu}E\left(1-z,\frac{M(1-z)}{\mu},\alpha(\mu)\right) &= \left[-4\Gamma_{\rm cusp}\left(\alpha(\mu)\right)\ln\frac{M}{\mu}-2\gamma_W\left(\alpha(\mu)\right)\right]\delta(1-z) \\ &\quad -\;4\Gamma_{\rm cusp}\left(\alpha(\mu)\right)\left(\frac{1}{1-z}\right)_+. \end{aligned} \tag{2.37}$$

A general solution to this equation for $z<1$ is

$$\begin{aligned} E\left(1-z,\frac{M(1-z)}{\mu},\alpha(\mu)\right) &= E\left(1-z,1,\alpha_s((1-z)M)\right) \\ &\quad -\;\frac{4}{1-z}\int_{(1-z)M}^{\mu}\frac{d\mu'}{\mu'}\,\Gamma_{\rm cusp}\left(\alpha_s(\mu')\right), \end{aligned} \tag{2.38}$$

where we have used the natural scale $(1-z)M$ as the starting point of evolution. Setting $\mu=M$ and taking the Mellin moment of $E(1-z)$, we derive precisely the form of the exponent in Eq. (2.34) up to a constant that multiplies $\delta(1-z)$ (and to which we will return in the next subsection),

$$\frac{D\left(\alpha\left((1-z)M\right)\right)}{1-z} = \;E\left(1-z,1,\alpha_s((1-z)M)\right)\;\text{for}\;1-z>0\,. \tag{2.39}$$

We can confirm the overall factor $1/(1-z)$ in the web function, E by a simple dimensional analysis of the second equality of Eq. (2.36). Comparing Eqs. (2.39) and (2.38), we recognize $D(\alpha_s)/(1-z)$ as the remainder of the web function when the soft function is collinear-subtracted (or equivalently, UV renormalized [68]) at scale $(1-z)M$. This definition of the

D term in Eq. (2.39) reproduces the Drell-Yan $D^{(2)}$ coefficient [89] from the two-loop result for the soft function in [68].

We note that Eq. (2.39) for function $D(\alpha_s)$ is comparable in simplicity to the definition of $\hat{D}$ in Eq. (2.20), and gives a transparent interpretation of D in terms of the non-local soft function. This is to be contrasted to the relative complexity of the relationship between D and $\hat{D}$, found by comparing Eqs. (2.34) and (2.19), [70]

$$\hat{D}(\alpha_s) = e^{2\gamma_E \nabla}\Gamma\left(1+2\nabla\right) D\left(\alpha_s\right) + \frac{e^{2\gamma_E \nabla}\Gamma\left(1+2\nabla\right)-1}{\nabla} 2A\left(\alpha_s\right), \tag{2.40}$$

where following the notation of [71] we define

$$\nabla \equiv \frac{d}{d\ln\mu^2} \equiv \frac{\beta(\alpha_s(\mu))}{2}\frac{\partial}{\partial\alpha_s(\mu)}. \tag{2.41}$$

The action of the derivatives ∇ is interpreted through a Taylor expansion, keeping in mind that each derivative acts only on the running coupling and therefore promotes the order in α_s. For completeness, we re-derive Eq. (2.40) in Appendix A.1.

From Eq. (2.40) in combination with the expression for $\hat{D}$ in Eq. (2.20) we obtain the differential identity found in [71] relating the D function to the anomalous dimension γ_W and the soft function in moment space,

$$e^{2\gamma_E \nabla}\Gamma\left(1+2\nabla\right)\frac{D\left(\alpha_s\right)}{2} = \gamma_W\left(\alpha_s\right) + \nabla \ln \widetilde{S}\left(0,\alpha_s\right) - \frac{e^{2\gamma_E \nabla}\Gamma\left(1+2\nabla\right)-1}{\nabla} A\left(\alpha_s\right). \tag{2.42}$$

The complexity of this expression compared to Eq. (2.39) is precisely due to using the moment-space soft function $\widetilde{S}$ (evaluated at $\mu = M/\bar{N}$) on the right-hand side in an expression for the momentum space function $D(\alpha_s)$ on the left.

2.3.2 Order-by-order structure of the exponent

We can gain further insight into the D function and its relationship to the soft function non-leading anomalous dimension, γ_W in Eq. (2.15), by studying the order-by-order expansion of the full exponent, E, Eq. (2.35). We start by expanding E at $\mu = M$ [90, 91],

$$\begin{aligned} E(1-z,1-z,\alpha_s(M)) &= \int_{n_0-i\infty}^{n_0+i\infty}\frac{dN}{2\pi i}\, e^{N(1-z)}\ \widetilde{E}\left(\ln\frac{1}{\bar{N}},\alpha_s\left(M\right)\right) \\ &= F\left(\alpha_s\left(M\right)\right)\delta(1-z) + D\left(\alpha_s\left(M\right)\right)\left(\frac{1}{1-z}\right)_+ \\ &\quad + \sum_{k=1}^{\infty} E^{(k)}\left(\alpha_s\left(M\right)\right)\left(\frac{\ln^k(1-z)}{1-z}\right)_+ . \end{aligned} \tag{2.43}$$

We will see that the function $D(\alpha_s)$ here turns out to be the same function as above. The expansion for general choice of scale μ is found from a change of variable in the inverse

transform,

$$\begin{aligned} E\left(1-z,\frac{(1-z)M}{\mu},\alpha_s(\mu)\right) &= \int_{n_0-i\infty}^{n_0+i\infty}\frac{dN}{2\pi i}\,e^{N(1-z)}\;\widetilde{E}\left(\ln\frac{M}{\bar{N}\mu},\alpha_s\left(\mu\right)\right) \\ &= \frac{M}{\mu}\int_{n_0-i\infty}^{n_0+i\infty}\frac{dN'}{2\pi i}\,e^{N'\frac{M(1-z)}{\mu}}\;\widetilde{E}\left(\ln\frac{1}{\bar{N}'},\alpha_s\left(\mu\right)\right) \\ &= \frac{M}{\mu}\int_{n_0-i\infty}^{n_0+i\infty}\frac{dN'}{2\pi i}\,e^{N'(1-z')}\;\widetilde{E}\left(\ln\frac{1}{\bar{N}'},\alpha_s\left(\mu\right)\right), \end{aligned} \tag{2.44}$$

where in the third equality we have defined

$$1-z'\equiv\frac{(1-z)M}{\mu}\,. \tag{2.45}$$

The inverse transform in final line of (2.44) has the same form as in (2.43), but now the distributions in its expansion are in terms of $1-z'$ rather than $1-z$. In particular, the resulting plus distributions are defined to give zero when integrated from $z'=0$ to $z'=1$, rather than from $z=0$ to $z=1$. The relations between the two sets of distributions are, however, simple,

$$\begin{aligned} \delta(1-z') &= \frac{\mu}{M}\,\delta(1-z)\,, \\ \left(\frac{\ln^k(1-z')}{1-z'}\right)_+ &= \frac{\mu}{M}\left[\left(\frac{\ln^k M(1-z)/\mu}{1-z}\right)_+ + \frac{\ln^{k+1}M/\mu}{k+1}\delta(1-z)\right]. \end{aligned} \tag{2.46}$$

In these terms, the web function, Eq. (2.44) is equal to $\frac{M}{\mu}$ times Eq. (2.43), with $1-z$ replaced by $1-z'$,

$$\begin{aligned} &E\left(1-z,\frac{(1-z)M}{\mu},\alpha_s(\mu)\right) \\ &= \left[F(\alpha_s(\mu))+D(\alpha_s(\mu))\ln\frac{M}{\mu}+\sum_{k=1}^{\infty}E^{(k)}(\alpha_s(\mu))\frac{\ln^{k+1}M/\mu}{k+1}\right]\delta(1-z) \\ &\quad + D(\alpha_s(\mu))\left(\frac{1}{1-z}\right)_+ + \sum_{k=1}^{\infty}E^{(k)}(\alpha_s(\mu))\left(\frac{\ln^k M(1-z)/\mu}{1-z}\right)_+. \end{aligned} \tag{2.47}$$

Now by imposing $\mu=M(1-z)$ in (2.47) for $z\neq 1$ we rederive Eq. (2.39) in the form

$$E\left(1-z,1,\alpha_s((1-z)M)\right)=\frac{1}{1-z}\;D\left(\alpha_s(\mu)\right)\,. \tag{2.48}$$

By demanding that the μ derivative of the delta function terms in the general expansion, (2.47), coincide with the delta function part of the evolution equation for the exponent (2.37), with $\mu=M$, we immediately find as well an expression for $\gamma_W(\alpha_s)$,

$$\gamma_W(\alpha_s(\mu))=\;-\;\frac{1}{2}\;\left[\mu\frac{d}{d\mu}\,F(\alpha_s(\mu))\;-\;D(\alpha_s(\mu))\right], \tag{2.49}$$

in terms of the D function and the z-independent terms in the expansion of the exponent, Eq. (2.47). Again, the simplicity of this relation relative to Eq. (2.42) results from working consistently in z space. This relation is in fact the same as Eq. (4.4) in Ref. [91], if we apply the relation Eq. (44) in [71] and make the assumption

$$\tilde{G} = -\gamma^V. \tag{2.50}$$

By comparing explicit coefficients, we checked that Eq. (2.50) holds true up to 3-loop order.

2.4 Logarithmic accuracy in the partonic cross section

The partonic cross section is a special case of the hadronic cross section, with parton distributions replaced by delta functions. The relationship between dQCD and SCET coefficient functions has been studied in both [71] and [75], where a pattern of agreement was demonstrated, when the soft scale μ_s is chosen as $M/\bar{N}$ in moment space. Certainly, the moment space equality is already implicit in the comparison of the dQCD and SCET soft function, Eqs. (2.19) and (2.22), respectively. It will be instructive, however, to follow the lead of [75] as applied to the coefficient functions and partonic cross sections, to illustrate how the soft function evolution equation Eq. (2.15) organizes the relationship between the SCET and dQCD coefficients for all choices of scales. In this section we hope to clarify further this agreement at the partonic level, relying on the evolution equation for the exponential function, Eq. (2.37). As in Ref. [75], we shall choose $\mu_f = M = \mu$, where our μ corresponds to the SCET hard matching scale, μ_h in Ref. [71].

From the refactorized expression, Eq. (2.6) and the soft function (2.22), the hard scattering function in the effective theory treatment can be written in terms of the single hard scale, M, and the (so far arbitrary) soft scale μ_s, as

$$\begin{aligned}\widetilde{C}_{a\bar{a}}^{[SCET]}\left(N, M, \mu_s\right) = H_{a\bar{a}}\left(\alpha_s(M)\right)\ \widetilde{S}_{a\bar{a}}\left(\ln\frac{M}{\bar{N}\mu_s}, \mu_s\right) \\ \times\ \exp\int_{\mu_s}^{M}\frac{d\mu'}{\mu'}\left[-4\Gamma_{\text{cusp}}\left(\alpha(\mu')\right)\ln\frac{M}{\bar{N}\mu} - 2\gamma_W\left(\alpha(\mu')\right)\right].\end{aligned} \tag{2.51}$$

As noted in Sec. 2.2, $\widetilde{C}_{a\bar{a}}^{[SCET]}$ is in principle independent of μ_s at all orders, but since we are interested precisely in the effect of taking only finite orders in $\widetilde{S}_{a\bar{a}}$, we introduce the soft scale as an additional argument. Also, from Sec. 2.2, we may assume for this discussion that

$$\widetilde{C}_{a\bar{a}}^{[SCET]}\left(N, M, \mu_s = M/\bar{N}\right) = \widetilde{C}_{a\bar{a}}^{[dQCD]}\left(N, M\right). \tag{2.52}$$

This follows from Eq. (2.23), assuming that the hard-scattering functions $H_{a\bar{a}}$ are handled identically.

In any case, once the hard-scattering functions are treated equivalently, Eq. (2.52) holds up to $1/N$ corrections when the two sides are evaluated to all orders, and up to subleading logarithmic corrections when the two sides are truncated to finite order. However, Eq. (2.52) does not immediately imply that partonic cross sections from the two methods agree, given that the transformations back to z space are handled differently. To demonstrate their

agreement, we will follow the method of [75, 76], which investigates the difference between SCET and QCD predictions in terms of the ratio of their resummed moments.

The ratio of the QCD moment to SCET moment for arbitrary μ_s is [75]

$$\begin{aligned}\widetilde{C}_{r,(a\bar{a})}\left(\ln\frac{M}{\bar{N}\mu_s},\alpha_s(\mu_s)\right) &= \frac{\widetilde{C}_{a\bar{a}}^{[dQCD]}(N,M)}{\widetilde{C}_{a\bar{a}}^{[SCET]}(N,M,\mu_s)} \\ &= \frac{\widetilde{C}_{a\bar{a}}^{[SCET]}\left(N,M,\mu_s=M/\bar{N}\right)}{\widetilde{C}_{a\bar{a}}^{[SCET]}(N,M,\mu_s)}\,, \end{aligned} \tag{2.53}$$

where if calculated to all orders, $C_{r,(a\bar{a})}$ would equal 1 identically. The reorganization of the effective theory, however, breaks this identity, and we would like to know at what logarithmic order this begins.

Subsitituting Eq. (2.51) into Eq. (2.53) allows us to derive the explicit form,

$$\begin{aligned}\widetilde{C}_{r,(a\bar{a})}\left(\ln\frac{M}{\bar{N}\mu_s},\alpha_s(\mu_s)\right) = \exp\int_{M/\bar{N}}^{\mu_s}\frac{d\mu}{\mu}\Bigg\{&-4\Gamma_{\rm cusp}\left(\alpha(\mu)\right)\ln\frac{M}{\bar{N}\mu}-2\gamma_W\left(\alpha(\mu)\right) \\ &-\mu\frac{d}{d\mu}\ln\left[\widetilde{S}_{a\bar{a}}\left(\ln\frac{M^2}{\bar{N}^2\mu^2},\mu\right)\right]\Bigg\}\,, \end{aligned} \tag{2.54}$$

an expression that manifestly reduces to unity when $\mu_s = M/\bar{N}$. We have promoted the ratio of soft functions evaluated at scales μ_s and $M/\bar{N}$ into an integral of their logarithmic derivative between these values, in the spirit of Eq. (2.19) above. Eq. (2.54) generalizes the "master formula" of Ref. [75] beyond NNLL. Now, in Eq. (2.54), the integrand in the exponent vanishes when $\tilde{S}$, $\Gamma_{\rm cusp}$ and γ_W are evaluated to all orders, because of the evolution equation for the soft function in moment space, Eq. (2.15). However, for N^{k}LL resummation in the effective theory treatment of Ref. [71], $\Gamma_{\rm cusp}$, γ_W, and $\widetilde{S}_{a\bar{a}}$ are truncated at order α_s^{k+1}, α_s^k and α_s^{k-1}, respectively. In this case, the cancellation in the integrand for general μ_s is only exact up to order α_s^{k-1}, and the exponent becomes non-zero at order α_s^k, including leading logarithmms, $\alpha_s^k\ln^{2k}N$. This corresponds to the observation in [75] that at NNLL, C_r-1 starts at order α_s^2. For N^{k}LL resummation in the convention for dQCD resummation described in [75], we would want to use $\widetilde{S}_{a\bar{a}}$ to one higher order, α_s^k. In this case the moment ratio C_r deviates from unity beginning at order α_s^{k+1}, including leading terms that behave as $\alpha_s^{k+1}\ln^{2(k+1)}N$. This corresponds to the observation in [76] that C_r-1 starts at α_s^3 order for NNLL resummation in the dQCD convention.

It is now instructive to revisit the method that leads to the effective theory coefficient function, Eq. (2.33), using the ratio C_r defined in Eq. (2.53). We first rewrite the SCET result slightly, moving explicit $(1-z)$-dependence to the left of the soft function $\widetilde{S}_{a\bar{a}}$, Eq. (2.24), which leads to

$$\begin{aligned}C_{a\bar{a}}^{[SCET]}(z,M,\mu_s) = H_{a\bar{a}}\left(\alpha_s(M)\right)&\exp\left[-4S_{\rm cusp}\left(\mu_s,M\right)+2\alpha_{\gamma_W}\left(\mu_s,M\right)\right] \\ &\times\frac{1}{(1-z)^{1-2\eta(\mu_s,M)}}\left(\frac{M^2}{\mu_s^2}\right)^{\eta(\mu_s,M)} \\ &\times\widetilde{S}_{a\bar{a}}\left(\ln\frac{M^2(1-z)^2}{\mu_s^2}+\partial_{\eta(\mu_s,M)},\alpha\left(\mu_s\right)\right)\frac{e^{-2\gamma_E\eta(\mu_s,M)}}{\Gamma\left(2\eta(\mu_s,M)\right)}\,. \end{aligned} \tag{2.55}$$

Now, by Eq. (2.53), the QCD coefficient function is of exactly the same form as the SCET coefficient, Eq. (2.51), but with $\widetilde{S}_{a\bar{a}}$ replaced by $\widetilde{C}_r \times \widetilde{S}_{a\bar{a}}$, where both $\widetilde{C}_r$ and $\tilde{S}_{a\bar{a}}$ depend on the moment variable only through the ratio $N\mu_s/M$. As a result, the direct QCD coefficient function can be written as

$$\begin{aligned} C_{a\bar{a}}^{[dQCD]}(z,M) = {} & H_{a\bar{a}}\left(\alpha_s(M)\right) \exp\left[-4S_{\rm cusp}\left(\mu_s,M\right) + 2\alpha_{\gamma_W}\left(\mu_s,M\right)\right] \\ & \times \frac{1}{(1-z)^{1-2\eta(\mu_s,M)}} \left(\frac{M^2}{\mu_s^2}\right)^{\eta(\mu_s,M)} \widetilde{C}_{r,(a\bar{a})}\left(\ln\frac{M^2(1-z)^2}{\mu_s^2} + \partial_\eta, \alpha\left(\mu_s\right)\right) \\ & \times \ \widetilde{S}_{a\bar{a}}\left(\ln\frac{M^2(1-z)^2}{\mu_s^2} + \partial_\eta, \alpha\left(\mu_s\right)\right) \frac{e^{-2\gamma_E\eta(\mu_s,M)}}{\Gamma\left(2\eta(\mu_s,M)\right)}\,. \end{aligned} \tag{2.56}$$

For the partonic cross section, we can set $\mu_s = M(1-z)$ to eliminate logarithms in Eq. (2.55). With this scale setting, the large logarithm appearing in $\widetilde{C}_r$ in Eq. (2.56) is also eliminated. Since $\tilde{S}_{a\bar{a}}$ is evaluated to $\alpha^{k-1}\left(\mu_s\right)$, while $\widetilde{C}_r$ only deviates from 1 starting at order $\alpha^k\left(\mu_s\right)$, we conclude that with the choice $\mu_s = M(1-z)$, the SCET partonic cross section agrees with the QCD partonic cross section up to subleading logarithms in moment space.

The correspondence between dQCD and the SCET formalism in momentum space when $\mu_s = M/\bar{N}$ to next-to-next-to-leading logarithm is worked out explicitly in [75]. Even at leading logarithms, however, it is useful to illustrate the difference between the resummed results at arbitrary μ_s, and their agreement for $\mu_s = M(1-z)$. At fixed coupling and leading logarithm, the SCET resummed coefficient function is found by isolating the leading terms of the general form, Eq. (2.33), and recalling the $\mathcal{O}(\alpha_s)$ results of Eqs. (2.25) and (2.26),

$$\begin{aligned} C_{a\bar{a}}^{[SCET]}(z,M,\mu_s) = {} & \delta(1-z) + 4C_a\,\frac{\alpha_s}{\pi}\frac{\ln(\mu_s/M)}{1-z} \\ & \times \exp\left[2C_a\,\frac{\alpha_s}{\pi}\ln\frac{\mu_s}{M}\left(2\ln(1-z) - \ln\frac{\mu_s}{M}\right)\right] + \text{NLL}\,. \end{aligned} \tag{2.57}$$

For comparison, the dQCD coefficient in z space can be found directly by the inverse moment of Eq. (2.29), keeping only the lowest-order term from $\Gamma_{\rm cusp}$ (the case $k=0$), to get

$$C_{a\bar{a}}^{[dQCD]}(z,M) = \delta(1-z) + 4C_a\,\frac{\alpha_s}{\pi}\frac{\ln(1-z)}{1-z}\exp\left[2C_a\,\frac{\alpha_s}{\pi}\ln^2(1-z)\right] + \text{NLL}\,. \tag{2.58}$$

As expected, these two expressions coincide exactly for $\mu_s = M(1-z)$, and as we have observed, Eq. (2.54) shows that this result extends to arbitrary logarithmic order, when more orders are included in the exponent. In the SCET LL example of Eq. (2.57), for fixed values of μ_s, however, the $\mathcal{O}(\alpha_s)$ singular behavior $[\ln(1-z)/(1-z)]_+$ is absent, and the two expressions agree only at zeroth order. This illustrates the general pattern, that for N^kLL resummation with $k \geq 1$, the SCET resummed coefficient contains explicit leading logs of $1-z$ up to order α^{k-1}, while at higher orders leading logarithms of $1-z$ are replaced by monomials in logs of μ_s/M and $1-z$.

In summary, at the specific choice $\mu_s = M(1-z)$, the effective theory and direct QCD resummations can be regarded as essentially equivalent at the partonic level. When μ_s is taken as a fixed quantity for hadronic cross sections, however, the situation is more complex. We turn to this comparison in the next section.

2.5 Comparing resummed hadronic cross sections

In this section we explore the relationship between dQCD and SCET hadronic cross sections, and show that their difference can be quantified in terms of an expansion of the partonic luminosity function, $\mathcal{L}_{a\bar{a}}(\tau/z)$, Eq. (2.2). The leading term in this expansion turns out to be identical in dQCD and SCET for a natural choice of the soft scale, μ_s, up to other choices involving non-threshold corrections. We will see that in many practical cases corrections beyond the leading term are small, further subleading both in order of α_s and of logarithms. This can be the case for nearly the full range of the variable τ.[7]

It is already clear from Eq. (2.2) that, if the parton luminosity function $\mathcal{L}_{a\bar{a}}(\tau/z)$ is given by a single power of τ/z, the hadronic cross section is approximately proportional to a simple moment of the hard scattering function [71] (see also [92] for a similar conclusion derived from the saddle point approximation for the Mellin inversion integral). In this approximation, we know from Eq. (2.23) that the hadronic cross sections of the dQCD and SCET formalisms will be equal if the SCET soft scale is taken as $\mu_s = M/\bar{s}_1$, with s_1 the effective power. Thus, if such a criterion is adopted to determine μ_s, the resummed cross sections will agree exactly. In practice, of course, this "single power approximation" is subject to finite corrections. We will show that such corrections are rather small for a wide range of τ, and can be incorporated systematically into both dQCD and SCET formalisms. Indeed, we will also see that these corrections produce differences between dQCD and SCET resummed hadronic cross sections only at subleading logarithmic order when μ_s is chosen as above. Note that this agreement will extend beyond the resummed expression to the fully-matched cross section, because the fixed-order moments in the two formalisms will agree automatically to the level that matching has been carried out.

In the following, we first describe the consequences and test the validity of the single power approximation. We go on to describe the expansion for partonic luminosity in which the single-power approximation is the leading term. We will conclude with some tests of the expansion in realistic cases, comparing the SCET and dQCD formalisms in the process.

2.5.1 The single-power approximation

Let us imagine that the parton luminosity really is exactly power-behaved. This is our "single-power approximation", for parton a,

$$\mathcal{L}_{a\bar{a}}\left(\frac{\tau}{z}\right) \;=\; \text{const}\;\left[\frac{\tau}{z}\right]^{-s_1(\tau)} \;=\; \mathcal{L}_{a\bar{a}}(\tau)\, z^{s_1(\tau)}\,, \tag{2.59}$$

where s_1 depends in general on the parton flavor a. For the remainder of this section, we drop partonic indices. As indicated, parameter s_1 is a function of τ (and also of the factorization scale, which we suppress). For such a luminosity, $\mathcal{L}(\tau/z)$, convolution with the corresponding partonic hard scattering coefficient $C(z)$ in Eqs. (2.2) and (2.4) can be identified with the

[7] Reference [74] also studies the relation of parton distribution shapes to threshold resummation within an SCET formalism.

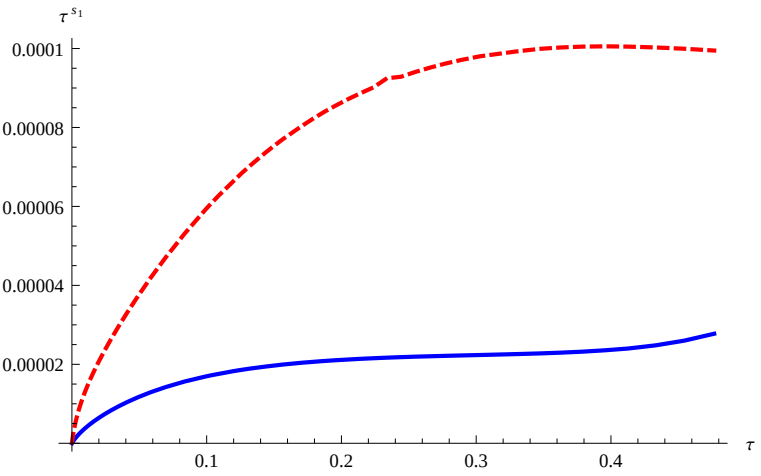

Figure 2.1: Plots of correction factors τ^{s_1} in Eq. (2.61) for gluon-gluon luminosities from Ref. [93]. The solid line represents factorization scale 126 GeV and dashed line 10 GeV.

s_1-Mellin moment of $C(z)$,

$$\begin{aligned}\frac{d\sigma(\tau)}{dM^2} &= \sigma_0 \int_\tau^1 \frac{dz}{z}\mathcal{L}\left(\frac{\tau}{z}\right) C(z) \\ &= \sigma_0\, \mathcal{L}(\tau) \int_\tau^1 \frac{dz}{z} z^{s_1(\tau)}\, C(z) \qquad (2.60) \\ &= \sigma_0\, \mathcal{L}(\tau)\, \widetilde{C}\left(s_1(\tau)\right) \;+\; \mathcal{O}\left(\tau^{s_1}\right) . \qquad (2.61)\end{aligned}$$

In the final equality we have assumed

$$1/s_1 \ll \ln\frac{1}{\tau}\,, \qquad (2.62)$$

which implies that for $z \sim \tau$, the integrand is suppressed by a factor $\tau^{s_1} \ll 1$. This ensures that the effect of the nonzero lower limit $z > \tau$ in Eq. (2.61) is negligible, so that (2.61) becomes the full Mellin moment. The property $\tau^{s_1} \ll 1$ is illustrated for a realistic gluon-gluon luminosity (which will be from the MSTW 2008 NNLO gluon distribution [93] throughout the rest of this chapter) in Fig. 2.1, with s_1 the logarithmic derivative $s_1 \equiv d\ln\mathcal{L}(y)/d\ln y$ at $y = \tau$. It can also be verified for almost the entire range of τ for realistic $q\bar{q}$ luminosities. Note that it does not by itself require s_1 to be a large number if τ is small. Correspondingly, it is natural to expect that s_1 grows as τ increases.

The argument leading to Eq. (2.61) applies to any hard-scattering function, whether derived by dQCD or effective theory. Then, if different resummations for $C(z)$ agree at the level of moments (which we have seen to be the case when we choose $\mu_s = M/\bar{s}_1$ above), they should agree phenomenologically.[8]

[8] A technical observation is that the dQCD "minimal prescription" described above in connection with Eq. (2.28), which is taken to the left of the Landau pole in N space, does not strictly speaking result in a convolution in the form of Eq. (2.61) We can, however, safely neglect such exponentially-suppressed corrections in this discussion, and we will confirm that they are negligible in the cases we consider.

To estimate corrections, we consider the Taylor expansion of $\ln \mathcal{L}(\tau/z)$, the logarithm of the luminosity, around partonic threshold, $z = 1$,

$$\ln \mathcal{L}\left(\frac{\tau}{z}\right) = \sum_{n=0}^{\infty} \frac{1}{n!} s_n(\tau) \, \ln^n z \,, \tag{2.63}$$

with

$$s_n(\tau) = (-1)^n \, \frac{d^n \ln \mathcal{L}(\tau')}{d \ln^n \tau'} \bigg|_{\tau'=\tau} . \tag{2.64}$$

Now s_1 describes the power behavior of $\mathcal{L}$ when z is close enough to $z = 1$. This single-power approximation to the luminosity will give a good approximation to the entire resummed cross section if $\mathcal{L}(\tau/z)$ becomes small by the time the higher order terms proportional to s_n, $n \geq 2$ become comparable to the first term in the expansion.

To get a more quantitative sense of the requirements for the single power approximation, we note that the luminosity $\mathcal{L}$ decreases by a factor $(1/e)^p$ when $\ln \frac{1}{z} \sim p/s_1(\tau)$. For the power z^{s_1} to dominate until $\mathcal{L}$ becomes small, we need

$$|r_n| \ll 1 \,, \quad r_n \equiv \frac{1}{n!} \frac{s_n(\tau)}{[s_1(\tau)]^n} \,, \quad n \geq 2 \,, \tag{2.65}$$

for all relevant values of n. We will argue that this is a common feature of realistic parton distributions.

A particularly simple example is a model function that reflects the steep decline of parton luminosities [94, 65, 71], as

$$\mathcal{L}(\tau') = A(1 - \tau')^{\beta}, \tag{2.66}$$

for $\beta \gg 1$. From Eq. (2.64) we have for the first logarithmic derivative

$$s_1(\tau) = \beta \, \tau/(1 - \tau) \,. \tag{2.67}$$

Clearly, the s_n remain linear in β when $n \geq 2$. Therefore r_n, the measure of convergence in Eq. (2.65), is proportional to $\beta^{-(n-1)}$, which is generically suppressed. Indeed, as long as $\beta\tau > 1$, the logarithmic expansion (2.63) of the luminosity converges, and we expect $|r_n| \ll 1$ to hold quite generally, for $\tau > 1/\beta$, not only for $\tau \to 1$. Assuming this to be the case, Eq. (2.61) is a good approximation, and $d\sigma/dM^2$ is proportional to a specific moment of the hard-scattering cross section. In the effective theory treatment, a scale choice that eliminates large logs from the soft function is $\mu_s = M/\bar{s}_1 = M(1 - \tau)/(\beta \, \tau e^{\gamma_E})$, similar to the estimate of Ref. [71] for this same luminosity.

More realistic models of parton luminosities can be constructed from model parton distributions like

$$f(x) = C \, x^{-\delta} \, (1 - x)^{\beta} \,. \tag{2.68}$$

We can test the single-power approximation explicitly in this case as well, using that the convolution of two such distributions gives a luminosity of hypergeometric form,

$$\mathcal{L}(\tau') = C^2 \, B(\beta + 1, \beta + 1) \, \tau'^{-\delta} \, (1 - \tau')^{2\beta+1} \, F_{2,1} \left(\beta + 1, \beta + 1; 2\beta + 2; 1 - \tau'\right) \,. \tag{2.69}$$

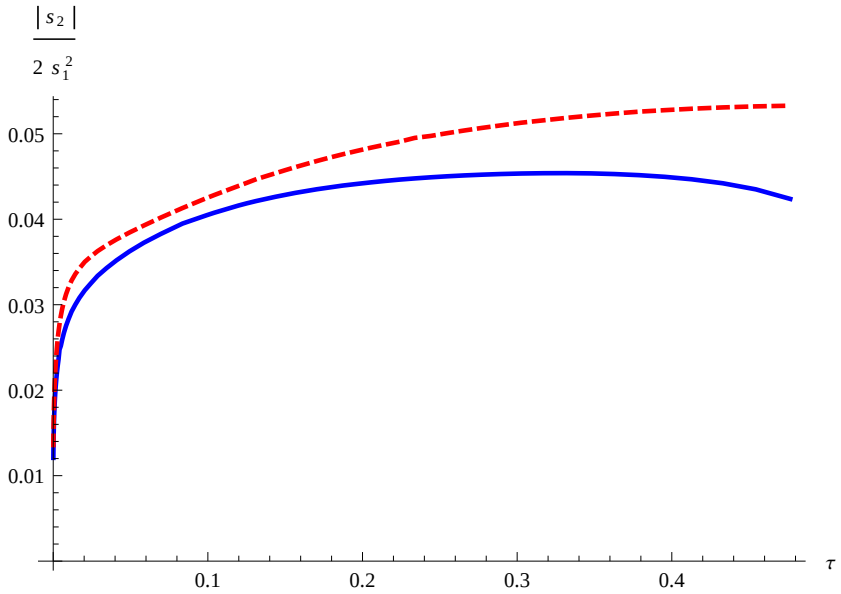

Figure 2.2: The ratio $|r_2|$, Eq. (2.65) , as a function of τ for the gluon distributions of Fig. 2.1.

We show in Appendix A.1 that this luminosity is again dominated by a single power, both for small τ, even with a moderate power, $\delta = \mathcal{O}(1)$, and for all τ when $\beta \gg 1$.

We next test condition (2.65) for $n = 2$, $|r_2| \ll 1$, for a fully realistic parton distribution. We show in Fig. 2.2 $|r_2| = |s_2|/(2s_1^2)$ for the gluon-gluon luminosity as a function of τ for $\mu_f = 10$ GeV and 126 GeV. In both cases the ratio satisfies $|r_2| \ll 1$ for all τ up to 0.5, even where s_1 is not large. The slope itself, s_1, is shown in Fig. 2.3. Luminosity functions arising from valence quark distributions, for example, the $u\bar{u}$ luminosity function, also satisfy $|r_2| \ll 1$. It is therefore natural to conclude that for many, probably most, cases of phenomenological interest, the effective power $s_1(\tau)$ determines the dominant moment, and consequently an effective soft scale, $\mu_s = M/\bar{s}_1(\tau)$.

In Fig. 2.4, which is analogous to Fig. 1 of [71], we give a logarithmic plot of the gluon-gluon luminosity versus $\ln(\tau_0/z)$, with $\tau_0 = (126\text{ GeV}/8\text{ TeV})^2 \approx (1/8)^4$, characteristic of 126 GeV ($=\mu_f$) Higgs boson production in proton-proton collisions at center-of-mass energy 8 TeV. The linear approximation is accurate while the luminosity decreases over several factors of e. In this case, the first derivative in the Taylor expansion (2.63) evidently dominates the second over an adequate region, even though the first derivative itself is not very large.

2.5.2 Corrections to the single power approximation

Having shown the equality of dQCD and SCET threshold resummations in the single-power approximation, we turn to corrections. These are associated with coefficients, s_n, $n > 1$ in

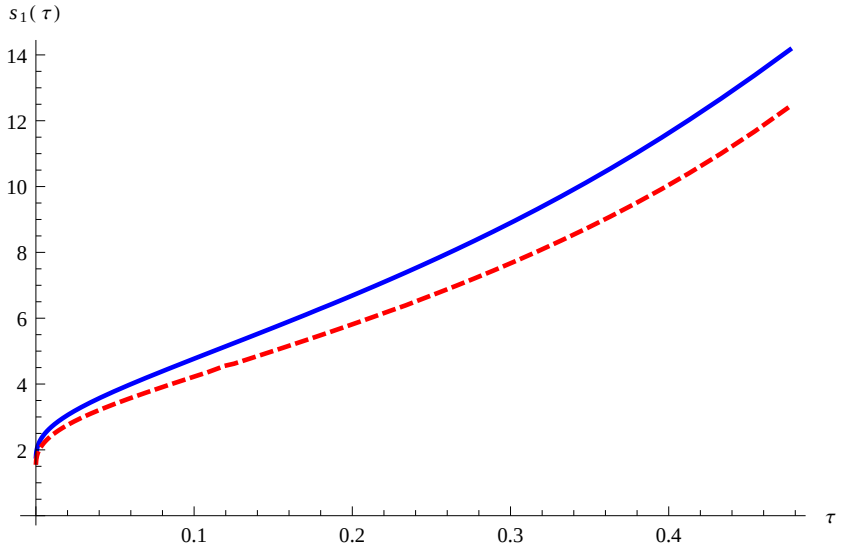

Figure 2.3: The first logarithmic derivative, s_1, Eq. (2.64), as a function of τ for the gluon distribution of Fig. 2.1.

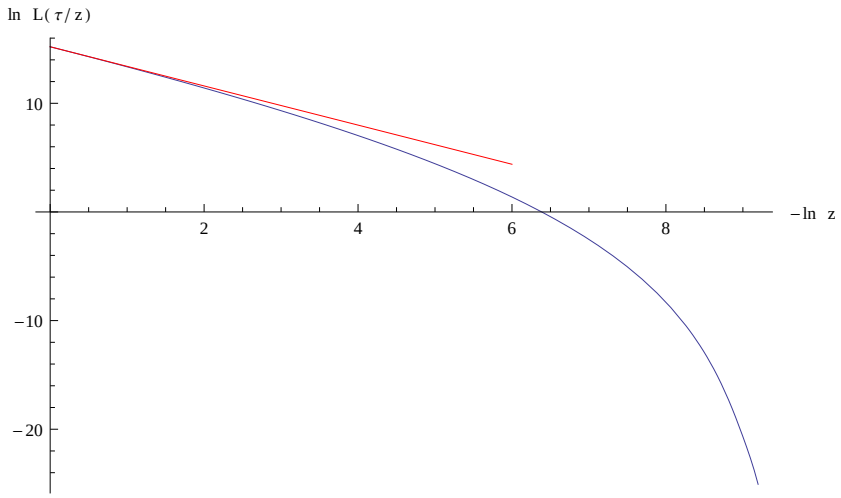

Figure 2.4: Logarithmic plot of gluon luminosity with its single-power approximation approximation

Eq. (2.63), in terms of which the luminosity function can be written as

$$\begin{aligned}\mathcal{L}\left(\frac{\tau}{z}\right) &= \mathcal{L}(\tau)\, z^{s_1}\, \exp\left[\frac{1}{2}s_2 \ln^2 z + \frac{1}{6}s_3 \ln^3 z + \frac{1}{24}s_4 \ln^4 z + \dots\right] \\ &= \mathcal{L}(\tau)\, z^{s_1}\, \left[1 + \frac{1}{2}s_2 \ln^2 z + \frac{1}{6}s_3 \ln^3 z + \left(\frac{1}{8}s_2^2 + \frac{1}{24}s_4\right)\ln^4 z + \dots\right]. \end{aligned} \tag{2.70}$$

This expansion enables us to refine the expression for the hadronic cross section in Eq. (2.61) as

$$\begin{aligned}\frac{d\sigma(\tau)}{dM^2} &= \sigma_0 \int_\tau^1 \frac{dz}{z}\mathcal{L}\left(\frac{\tau}{z}\right) C(z) \\ &= \sigma_0 \int_0^1 \frac{dz}{z}\mathcal{L}\left(\frac{\tau}{z}\right) C(z) \;+\; \mathcal{O}\left(\mathcal{L}(\tau)\tau^{s_1}\right) \\ &= \sigma_0\, \mathcal{L}(\tau) \int_0^1 \frac{dz}{z} z^{s_1}\, \left[1 + \frac{1}{2}s_2 \ln^2 z + \cdots\right] C(z) \\ &= \sigma_0\, \mathcal{L}(\tau)\left[\widetilde{C}(s_1) + \frac{1}{2}s_2\, \widetilde{C}''(s_1) + \cdots\right], \end{aligned} \tag{2.71}$$

where for simplicity we keep only s_1 and s_2 terms in the expansion. Using

$$\left(\frac{d}{ds_1}\right)^2 = \frac{1}{s_1^2}\left[\left(\frac{d}{d\ln s_1}\right)^2 - \frac{d}{d\ln s_1}\right], \tag{2.72}$$

we have

$$\frac{d\sigma(\tau)}{dM^2} = \sigma_0 \mathcal{L}(\tau)\left\{1 + r_2\left[\left(\frac{d}{d\ln s_1}\right)^2 - \frac{d}{d\ln s_1}\right] + \dots\right\}\widetilde{C}(s_1)\,, \tag{2.73}$$

where $r_2 = s_2/2s_1^2$ as in Eq. (2.65). Corrections to the single-moment approximation in Eq. (2.61) are thus suppressed by powers of $\ln s_1$ as well as by the coefficients r_n, defined in (2.65). The convergence of Eq. (2.71) as a series is thus quantifiable.

We can also test differences between SCET and dQCD in the new expansion. Applying (2.71) to the difference between SCET and dQCD resummed moments with soft scale $\mu_s = M/\bar{s}_1$ in the former, we obtain

$$\begin{aligned}&\frac{1}{\sigma_0\mathcal{L}(\tau)}\left[\frac{d\sigma(\tau)}{dM^2}^{[SCET]}\left(\tau, \mu_s = \frac{M}{\bar{s}_1}\right) - \frac{d\sigma(\tau)}{dM^2}^{[dQCD]}(\tau)\right] \\ &\quad\approx \left\{1 + r_2\left[\left(\frac{d}{d\ln s_1}\right)^2 - \frac{d}{d\ln s_1}\right]\right\}\left[\widetilde{C}^{[\mathrm{SCET}]}\left(s_1, \mu_s = \frac{M}{\bar{s}_1}\right) - \widetilde{C}^{[\mathrm{dQCD}]}(s_1)\right] \\ &\quad= \left\{1 + r_2\left[\left(\frac{d}{d\ln s_1}\right)^2 - \frac{d}{d\ln s_1}\right]\right\}\left[\widetilde{C}_r^{-1}\left(\ln\frac{M}{\bar{s}_1\mu_s}, \alpha_s(\mu_s)\right) - 1\right]\widetilde{C}^{[\mathrm{dQCD}]}(s_1)\,, \end{aligned} \tag{2.74}$$

where we have used the moment ratio Eq. (2.53) in the second equality. Recall from Sec. 2.4 that the moment ratio $\widetilde{C}_r$ deviates from unity only starting at order α_s^k in the case of N^{k}LL

resummation, when the soft function is computed to order α_s^{k-1}. We can then expand (2.74) as

$$\begin{aligned}
&\frac{1}{\sigma_0 \mathcal{L}(\tau)} \left[\frac{d\sigma(\tau)}{dM^2}^{[SCET]} \left(\tau, \mu_s = \frac{M}{\bar{s}_1} \right) - \frac{d\sigma(\tau)}{dM^2}^{[dQCD]} (\tau) \right] \\
&\quad \approx \left\{ 1 + r_2 \left[\left(\frac{d}{d \ln s_1} \right)^2 - \frac{d}{d \ln s_1} \right] \right\} \sum_{m \geq k} \sum_{1 \leq n \leq 2m} A_{mn} \alpha_s^m \ln^n \frac{M}{\bar{s}_1 \mu_s} \widetilde{C}^{[dQCD]} (s_1) \mid_{\mu_s = M/s_1} \\
&\quad = \frac{s_2}{2 s_1^2} \sum_{m \geq k} \sum_{1 \leq n \leq 2m} (2A_{m2} + A_{m1}) \, \alpha_s^k \, \widetilde{C}^{[dQCD]} (s_1) \, . \qquad (2.75)
\end{aligned}$$

In the final form, only the $n = 1, 2$ terms give non-zero contributions when $\mu_s = M/\bar{s}_1$. The leading term in Eq. (2.75) is thus of order $\mathrm{N}^{k+1}\mathrm{LL}$, that is, subleading compared to the original calculation, in addition to its suppression by r_2. This argument generalizes straightforwardly to coefficients s_n at any order. It implies that the difference between dQCD and SCET resummed hadronic cross sections is of subleading logarithmic order, and further suppressed in the luminosity expansion. This will be the case whenever the perturbation expansion Eq. (2.71) is justified by the condition Eq. (2.65), which we have verified for a variety of model and realistic parton distributions.

2.5.3 Cross section comparisons

From the discussion above, we expect that pQCD and SCET resummations should give very similar numerical results, at least when the soft scale in the latter is chosen as $M/\bar{s}_1$. To test this, we compare dQCD and SCET resummations directly in a specific case, designed to give a controlled numerical comparison between the two. To eliminate differences at non-leading powers of $1 - z$, we invert the Mellin transform numerically for both dQCD and SCET as in Eq. (**??**), after multiplying by the moment of a fitted parton luminosity function [95]. For the dQCD form, we use the contour specified by the minimal prescription.

We use Eq. (2.24) as the definition of the SCET coefficient function in moment space.[9] We then use the identity $\tilde{C}^{[dQCD]} \left(\ln \frac{1}{N}, \alpha_s(M) \right) = \tilde{C}^{[SCET]} \left(\ln \frac{1}{N}, \alpha_s(M), \mu_s = \frac{M}{N} \right)$, Eq. (2.23), as the defintion of the dQCD resummed moment, again using Eq. (2.24) to ensure that this relation is exactly satisfied in our numerical implementation, free of differences at subleading powers of $1/N$ or $1 - z$ and subleading logarithms.[10] Again, for the SCET soft scale we use $\mu_s = M/\left(s_1 e^{\gamma_E}\right)$, with s_1 determined numerically from the luminosity. Otherwise, the moment inversion here is completely independent of the single power approximation. We emphasize that with this (or indeed any) N-independent choice of μ_s, the SCET and dQCD coefficient functions are still completely different for orders beyond α_s^2 in the expansion of their corresponding NNLL resummations.

The resummations are performed to NNLL accuracy in the dQCD convention, that is, taking s_{DY}, $\hat{D}$ and γ_W in Eq. (2.24) to order α_s^2, Γ_{cusp} to order α_s^3, and using the 3-loop running coupling. The following results are evaluated with only the resummed soft function.

[9] The various functions, such as S_{cusp} and η are found in the Appendix B of [71].

[10] An example of the latter are differences between the two expressions on the right-hand side of Eq. (2.19) when γ_W and $\hat{D}$ are truncated to finite order.

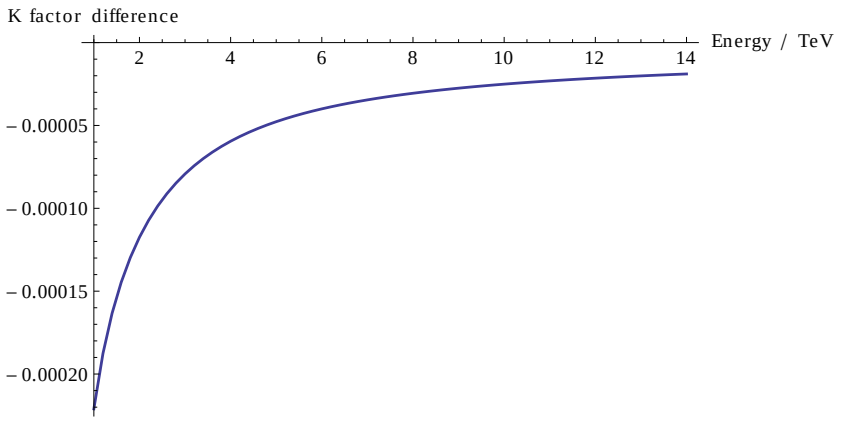

Figure 2.5: Relative difference between SCET resummation with $\mu_s = M/\bar{s}_1$ and dQCD resummation for the 126 GeV Higgs K factor, at hadronic collisin energies from 1 to 14 TeV.

We do not include constant factors such as the hard function with the effective top vertex matching coefficient, and do not perform matching to fixed order. Therefore, the plots we show are not intended as phenomenological predictions, but to serve as illustrations for the points we have made previously.

Fig. 2.5 shows the fractional difference between SCET and dQCD resummed K-factors (ratios to the Born process) for the same gluon distributions as above. We can see that the difference is tiny, below 10^{-4} for LHC energies. This can be understood because first, the ratio $r_2 = s_2/(2s_1^2)$ that characterizes corrections to the single-power approximation is quite small for small τ, as illustrated in Figs. 2.2 and 2.4, and second, its coefficient is of subleading logarithmic order ($\mathrm{N^3LL}$ in this case). This is also consistent with the observation in Ref. [72], where much of the numerical difference between dQCD and SCET resummed Higgs cross sections was traced to non-leading powers of $1 - z$ arising from the different Mellin inversion methods. Computing both dQCD and SCET cross sections numerically eliminates such differences, and the underlying difference between the two methods turns out to be very small in this case.

The consistency of dQCD and SCET results again suggests that the single power approximation should work well for either. Indeed, this turns out to be the case. Fig. 2.6a shows K-factors for the gluon fusion production of a 126 GeV Higgs, at 1-14 TeV energies. The upper, dashed curve shows the K factor from the single power approximation, that is, $\tilde{C}_{\mathrm{dQCD}}\left(N = s_1(\tau), M\right)$. The lower, solid curve shows the dQCD prediction using the full parton distribution. The full dQCD resummation agrees with the single power approximation very well, even before the corrections of Eq. (2.73) to the latter. When the correction associated with s_2 in Eq. (2.73) is taken into account, the agreement is impressive, as shown by the difference between the corrected single power and full dQCD predictions plotted in Fig. 2.6b.

In summary, for Higgs production we have verified both the usefulness of the single-power approximation, and the consequent consistency of the dQCD and SCET resummation formalisms. Of course, the full implementation of these formalisms requires the complete hard function and matching to fixed-order results, but this will not affect the conclusion that the intrinsic difference between the two resummation methods is tiny in the case of 126

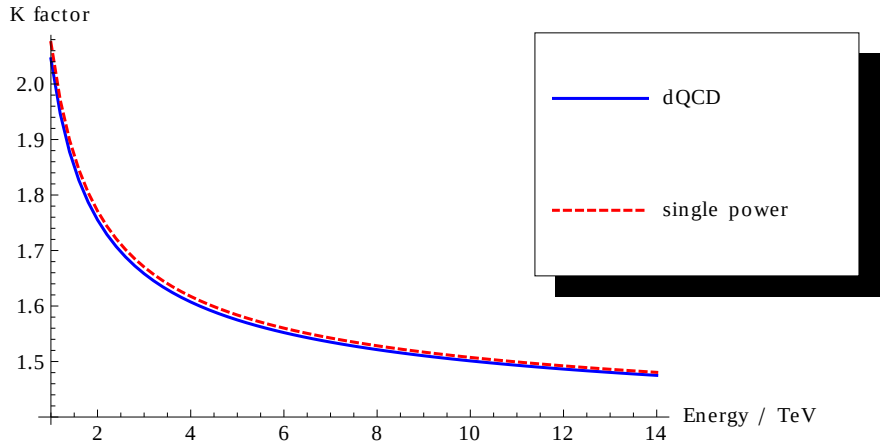

(a)

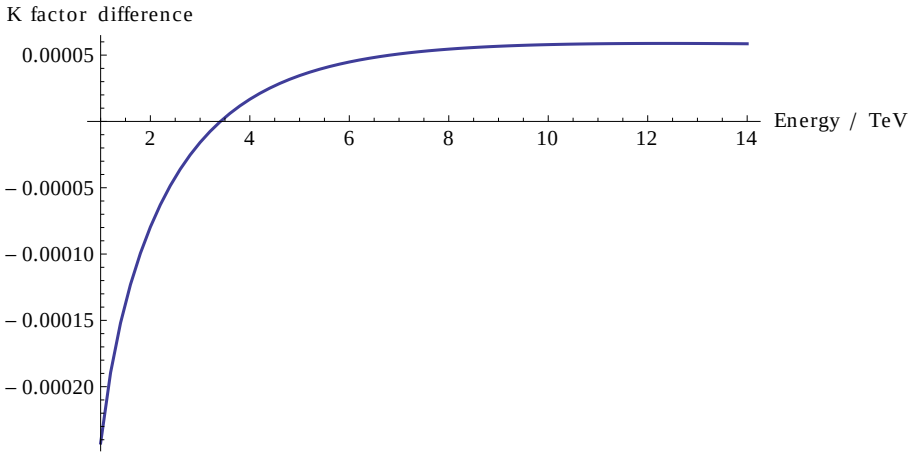

(b)

Figure 2.6: (a) Plot of 126 GeV Higgs resummed gluon fusion K factor, omitting the hard function, from dQCD and the corresponding single power approximation without s_2 correction. (b) Difference between same full resummed K factor and corresponding single power correction with its s_2 correction.

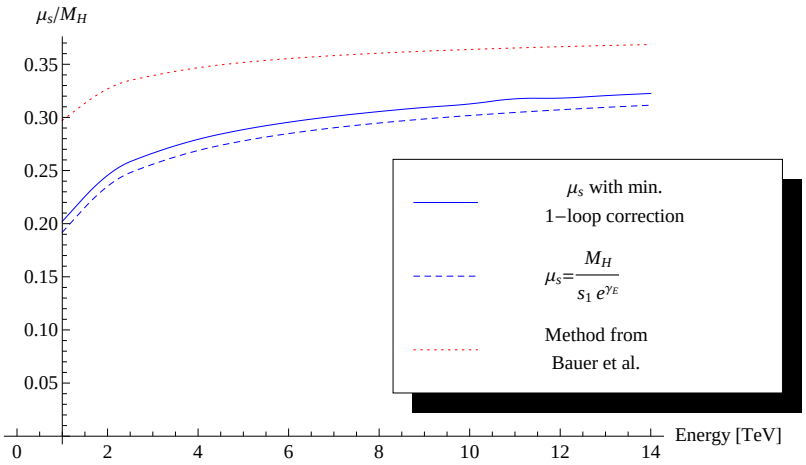

Figure 2.7: Soft scales for inclusive Higgs production obtained from minimizing the one-loop soft correction [72] (using contour Mellin inversion), from the $s_1(\tau)$ variable in the method of this chapter, and from a method proposed in [74].

GeV Higgs. Although we do not attempt a phenomenological study of other cases here, the analytic arguments and parton luminosity plots in the previous subsections seem strongly to suggest consistency between the two resummation methods over a wide kinematic range. They suggest as well that the single power approximation often may be a useful tool in its own right.

2.5.4 Soft scale comparisons

A widely used procedure in the SCET threshold resummation literature is minimizing the correction from the one-loop soft function after convoluting with the parton luminosity function [71, 96]. The method of this chapter suggests an alternative choice, $\mu_s = M/\left[s_1(\tau)e^{\gamma_E}\right]$, based directly on the shape of the parton luminosity function. A previous proposal, also based on the parton luminosity shape, in Ref. [74] suggests $\mu_s = \lambda^2 M$, where λ^2 is defined by the consistency equation

$$\lambda^2 = \frac{\int_\tau^{1-\lambda^2} \frac{dz}{z}\mathcal{L}\left(\frac{\tau}{z}\right)}{\int_{1-\lambda^2}^1 \frac{dz}{z}\mathcal{L}\left(\frac{\tau}{z}\right)}. \tag{2.76}$$

We plot in Fig. 2.7 the soft scales μ_s obtained from the three methods, for a 126 GeV Higgs produced from gluon fusion at hadronic collision energies from 1 TeV to 14 TeV. We see that the method of this chapter agrees with the method of minimizing one-loop soft corrections within a few percent, and also agrees well with the method from [74], given that, in practice, scales are varied up and down by a factor of 2, which is much larger than the differences shown in the figure.

For Higgs and Drell-Yan, the one-loop soft function is proportional to $2\ln^2[M^2/(\bar{N}^2\mu_s^2)] + \pi^2/3$ [71, 72], which is clearly minimized at $\mu_s = M/\bar{s}_1$ to the extent that the single-power approximation is valid. This explains the close agreement we observe.

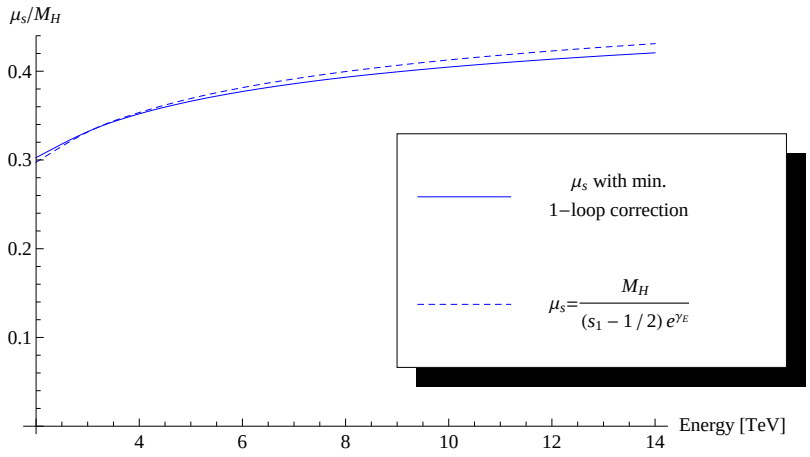

Figure 2.8: Soft scales obtained from minimizing the one-loop soft correction using the SCET inversion formula of [71], and from the $s_1(\tau) - 1/2$ variable in the method of this chapter, for the production of a 126 GeV Higgs at various energies.

2.5.5 Threshold suppressed differences

As shown in [72], the choice of $(1-z)$-suppressed terms in the widely used inversion formula in SCET differs from exact Mellin invesion, to a first approximation, by an extra factor of $1/\sqrt{z}$, accounting for more than 70% of the difference between threshold enhancements for the Higgs total cross section from dQCD and SCET threshold resummations. In the framework of the single power approximation, this replaces the power s_1 in Eq. (2.60) by $s_1 - 1/2$, giving us a result that is approximated by $\tilde{C}(s_1 - 1/2)$ instead of $\tilde{C}(s_1)$. In Fig. 2.8 we plot the comparison between the modified soft scale we predict, $\mu_s = M/\left[(s_1 - 1/2)e^{\gamma_E}\right]$, and the soft scale found by minimizing the one-loop soft correction using the widely adopted SCET inversion formula instead of contour Mellin inversion. The modified single power approximation agrees with the result of minimizing the one loop correction [72] within a few percent.

Given that s_1 is often not very large (about 1.8 for a 126 GeV Higgs from 14 TeV collisions), this downshift of s_1 by 1/2 should generally lead to milder threshold enhancement. This effect is present in Ref. [72] for Higgs production, and in Ref. [71] for the Drell-Yan process in certain parameter regions. An important dependence on threshold-suppressed factors has also been observed in the recent calculation of the gluon fusion Higgs cross-section at N^{3}LO [97] in the threshold limit.

2.6 Discussion

We have explored the similarities of dQCD and SCET threshold resummations, in the implementations of Refs. [70] and [71], respectively, and reaffirmed that they share common properties of factorization and evolution, differing primarily in the use of boundary conditions for the evolution. For the dQCD formalism, evolution starts in moment space at

scale $M/\bar{N}$, and in the SCET formalism at a soft scale, μ_s, determined by the interplay of parton luminosities and the hard scattering function. We presented a new analysis of the dQCD resummed coefficient expressed as the exponential of a Mellin transform, Eq. (2.34), showing that the non-leading resummation function $D(\alpha_s)$ is a specific sum of web diagrams computed in momentum space. We went on to extend the moment ratio method of Ref. [75], confirming that the two resummation formalisms give partonic cross sections that agree to any desired logarithmic order when the SCET boundary condition for evolution is chosen as $\mu_s = (1-z)M$.

For hadronic cross sections, we found that for a wide range of τ, the cross section is dominated by a single Mellin moment, determined by logarithmic derivatives of the luminosity function. Corrections to this approximation can be computed by an expansion of the logarithm of the luminosity around its value at threshold. We expect that for most collider scenarios, dQCD resummations, using minimal or other prescriptions, should be close to SCET threshold resummation when the soft scale of the latter is close to the value determined as above. The single-power approximation, including corrections, can provide a useful simplification in many cases, without sacrificing numerical accuracy. The approximation also simplifies the determination of the soft scale and the analysis of the effect of threshold-suppressed terms.

Chapter 3

Threshold resummation for W^+W^- production

This chapter is based on the publication [52].

3.1 Introduction

Exploring the Higgs and electroweak sector of the Standard Model is one of the primary goals of the LHC. The pair production of gauge bosons is important both as a test of the $SU(2) \times U(1)$ gauge structure and as a background for Higgs boson searches. Precise predictions for both total and differential cross sections are needed in order to understand the shape of the background to the Higgs signal and to search for anomalous three gauge boson couplings. Understanding the theoretical prediction for $pp \to W^+W^-$ is particularly important for the measurement of the Higgs decay channel, $H \to W^+W^- \to 2\ell 2\nu$, where there is no resonant structure. The W^+W^- background is estimated by a sideband analysis, where the cross section is normalized via a control region with a minimum dilepton invariant mass. Using Monte Carlo generators, the line shapes of the W^+W^- distributions are then extrapolated into the Higgs signal region [98, 99]. A change in the W^+W^- invariant mass distribution will alter the dilepton invariant mass distribution, and consequently change the extrapolation of the background estimates in the Higgs signal region.

The production of W^+W^- pairs with a subsequent leptonic decay has been studied at the Tevatron [100, 101], while both ATLAS [102, 103] and CMS [104, 105] have reported results at the LHC. The LHC results for the total W^+W^- cross section, without using resummation in data analysis, are as follows.[1]

$$\begin{aligned}
\text{ATLAS, } \sqrt{S} = 7 \text{ TeV} \quad \sigma = \;& 51.9 \pm 2.0(\text{stat}) \pm 3.9(\text{syst}) \pm 2.0(\text{lumi}) \text{ pb} \\
\text{CMS, } \sqrt{S} = 7 \text{ TeV} \quad \sigma = \;& 52.4 \pm 2.0(\text{stat}) \pm 4.5(\text{syst}) \pm 1.2(\text{lumi}) \text{ pb} \\
\text{ATLAS, } \sqrt{S} = 8 \text{ TeV} \quad \sigma = \;& 71.4 \, {}^{+1.2}_{-1.2}(\text{stat}) \, {}^{+5.0}_{-4.4}(\text{syst}) \, {}^{+2.2}_{-2.1}(\text{lumi}) \text{ pb} \\
\text{CMS, } \sqrt{S} = 8 \text{ TeV} \quad \sigma = \;& 69.9 \pm 2.8(\text{stat}) \pm 5.6(\text{syst}) \pm 3.1(\text{lumi}) \text{ pb} \,, \qquad (3.1)
\end{aligned}$$

[1] A more recent CMS analysis [106] used our transverse momentum resummation results in Chapter 4, and reported a measured total cross section that is in better agreement with theory. This will be discussed in Chapter 4.

are slightly higher than the Standard Model predictions at next-to-leading order (NLO) in QCD [107],[2]

$$\begin{aligned}\sigma(\sqrt{S} = 7 \text{ TeV})_{\text{Theory}} &= 47.04^{+2.02}_{-1.51} \text{ pb} \\ \sigma(\sqrt{S} = 8 \text{ TeV})_{\text{Theory}} &= 57.25^{+2.347}_{-1.60} \text{ pb}\,. \end{aligned} \tag{3.2}$$

The slight differences between the measured LHC values and the MCFM NLO predictions have led to speculation that the measured W^+W^- cross section is a subtle sign of new physics [108, 109, 110, 111, 112, 113, 114].

We should mention that after we finished the work covered in this chapter, the NNLO W^+W^- total cross section became available [115]. The reported results are

$$\begin{aligned}\sigma(\sqrt{S} = 7 \text{ TeV})_{\text{Theory}} &= 49.04^{+2.1\%}_{-1.8\%} \text{ pb} \\ \sigma(\sqrt{S} = 8 \text{ TeV})_{\text{Theory}} &= 59.84^{+2.2\%}_{-1.9\%} \text{ pb}\,. \end{aligned} \tag{3.3}$$

The NLO QCD corrections to $pp \to W^+W^-$ were computed in Refs. [116, 117], and then extended to include leptonic decays in Ref. [118]. The NLO predictions for the total cross section have a $3-4\%$ uncertainty at the LHC due to the choice of parton distribution functions (PDFs) and renormalization/factorization scale variation [107]. The contribution from $gg \to W^+W^-$ is formally NNLO, but numerically contributes $\sim 3\%$ at $\sqrt{S} = 7$ TeV and $\sim 4\%$ at $\sqrt{S} = 14$ TeV [119, 120, 121, 122]. The NLO results have been interfaced with a shower Monte Carlo using the formalism of the POWHEG box [123, 124, 125]. The electroweak corrections and the contribution from the $\gamma\gamma$ initial state are also known and contribute less than $1-2\%$ to the total cross section at the LHC [126, 127]. These corrections are enhanced at large values of the W^+W^- invariant mass, but have opposite signs and largely cancel.

In this chapter, we extend these results by including a resummation of threshold logarithms in the prediction of W^+W^- production. Previously, the resummation of large logarithms associated with gluon emission at low transverse momentum, p_T, in W^+W^- production was considered [128]. Unlike p_T resummation which is normalized to the NLO cross section, the emission of soft gluons near threshold can potentially enhance the rate. We consider the next-to-leading logarithmic (NLL) and next-to-next-to-leading logarithmic (NNLL) resummation of threshold corrections. To accomplish this, we utilize the formalism of soft collinear effective theory (SCET) [41, 42, 43, 44] which allows the resummation to be performed directly in momentum space [77, 129]. This formalism has been used for processes with colorless final states such as Drell-Yan [71], Higgs production [130, 72, 131], associated W/Z plus Higgs production [132], direct photon production [133] and SUSY slepton pair production [134].

The SCET formalism has also been applied to top quark pair production to resum the threshold corrections to the invariant mass distribution and to the total cross section [96, 88, 135]. The total cross section for top quark pair production using threshold resummation has

[2]The theoretical predictions have been evaluated at NLO using MCFM with MSTW2008nlo PDFs and a central scale choice of $\mu_f = M_W$. The uncertainties shown in Eq. (3.2) result from varying the scale up and down by a factor of 2. The predictions of Eq. (3.2) include the next-to-next-to-leading order (NNLO) contribution from the gg initial state [107].

been obtained using two different sets of threshold limits: one starting from the invariant mass distribution of the top quark pair (pair invariant mass kinematics) and the other beginning from the transverse momentum or rapidity distribution of the top quark[96, 88, 136]. The total cross section is then obtained by integrating over the resummed distributions. Within the theoretical uncertainties, the total cross sections for top quark pair production obtained with the different starting points are in reasonable agreement[88, 135]. The total cross section can also be obtained in the threshold limit, $\beta \to 0$, where β is the top quark velocity, and the terms of $\mathcal{O}(\alpha_s^n \ln^m \beta)$ resummed[137]. At the LHC and the Tevatron, however, the largest contributions to the total cross section for top quark pair production are not from the $\beta \to 0$ region. In this work, we will use pair invariant mass kinematics for the W^+W^- final state to obtain our resummed results.

The calculation of differential cross sections involves several scales. We consider the threshold limit $z \equiv \frac{M_{WW}^2}{s} \to 1$ which dynamically becomes important due to the fast decline of the parton luminosity function as τ increases [71], with M_{WW} the invariant mass of the W^+W^- pair and s the partonic center of mass energy. Near the partonic threshold, up to subleading powers of $(1-z)$, the cross section factorizes into a soft function which describes the soft gluon emissions and a hard function which includes the virtual corrections to the cross section. We can combine the NLO soft and hard functions with their renormalization group (RG) evolution equations to give NNLL resummed results which resum large logarithms of the form $\alpha_s^n \left(\frac{\ln^m(1-z)}{1-z} \right)_+$ with $m \leq 2n-1$. Alternatively, the RG evolution of the hard function, known to NNLO, can be matched with exact NLO results for the hard function to obtain the approximate NNLO hard function which includes the leading scale dependent contributions. Combined with the known NNLO soft function [71] for color singlet production, we are able to obtain the approximate NNLO result as an alternative to the NLO+NNLL resummed result. The advantage of the NLO+NNLL resummed results is that they contain powers of α_s to all orders, while the advantage of the approximate NNLO results is that we used the soft function to one order higher (NNLO) and the results do not contain higher orders of α_s which are sometimes not desired. In any case, the two results are extremely close to each other.

In Section 3.2, we review the formalism and SCET resummation in the threshold region. This follows closely the approach of Ref. [96]. Section 3.3 contains results for the NNLL differential and total cross sections, along with approximate results for the NNLO cross section for $pp \to W^+W^-$. Brief conclusions are presented in Section 3.4.

3.2 Basics

In this section, we review the fixed order results for $pp \to W^+W^-$ (3.2.1 and 3.2.2), the SCET formalism used to derive the RG improved NNLL results for the differential and total cross sections, including the matching to the fixed order NLO result (3.2.3), and the derivation of an approximate NNLO result(3.2.4).

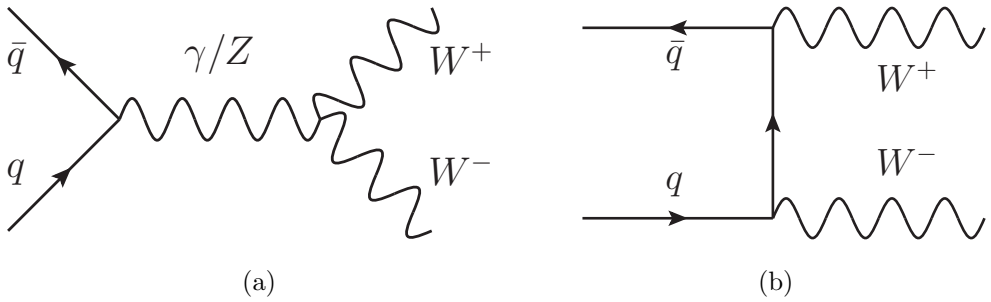

Figure 3.1: Feynman diagrams for the (a) s-channel and (b) t-channel contributions to $q\bar{q} \to W^+W^-$.

3.2.1 Born Level Result

The Born level process arises through the annihilation process

$$q(p_1) + \overline{q}(p_2) \to W^+(p_3) + W^-(p_4)\,. \tag{3.4}$$

This annihilation proceeds via s-channel γ/Z exchange and a t-channel contribution, as shown in Figs. 3.1(a) and (b), respectively. The partonic cross section is

$$\hat{\sigma}^0_{q\bar{q}} \;=\; \frac{1}{2s}\int d\Phi_2 \mid A^0_{q\bar{q}}(s,t) \mid^2, \tag{3.5}$$

where the partonic level invariants are

$$\begin{aligned} s &= (p_1+p_2)^2 \\ t &= (p_1-p_3)^2 = M_W^2 - \frac{s}{2}(1-\beta\cos\theta) \\ u &= (p_1-p_4)^2\,, \end{aligned} \tag{3.6}$$

with $s+t+u = 2M_W^2$ and $\beta = \sqrt{1-\frac{4M_W^2}{s}}$. At the Born level we have $M^2_{WW} = s$. The two body phase space is

$$d\Phi_2 \;=\; \frac{1}{8\pi s}dt = \frac{\beta}{16\pi}d\cos\theta\,. \tag{3.7}$$

Finally, the color-averaged and spin-summed and averaged matrix element squared is

$$\mid A^0_{q\bar{q}} \mid^2 = \frac{1}{4N_C}\left\{c_q^{tt}F_q^0(s,t) + c_q^{ss}(s)K_q^0(s,t) - c_q^{ts}(s)J_q^0(s,t)\right\}, \tag{3.8}$$

where $c_q^{ss}K_q^0$ is the s-channel contribution, $c_q^{tt}F_q^0$ is the t-channel contribution, and $c_q^{ts}J_q^0$ is from s- and t-channel interference. The results have been found in Ref. [116] and are given in Appendix B.1 for convenience.

Due to the collinear factorization [24, 32, 33, 34, 138], the hadronic level cross section is obtained by convolving the partonic level cross section with PDFs. In general, the hadronic cross section can be written as

$$\frac{d^2\sigma}{dM_{WW}d\cos\theta} = \sum_{ij}\frac{\beta_W}{16\pi M_{WW}S}\int_\tau^1\frac{dz}{z}\mathcal{L}_{ij}\left(\frac{\tau}{z},\mu_f\right)C_{ij}(z,M_{WW},\cos\theta,\mu_f) \tag{3.9}$$

where the sum runs over all possible initial state partons, μ_f is the factorization scale,

$$\tau = \frac{M_{WW}^2}{S}, \quad z = \frac{M_{WW}^2}{s}, \quad \text{and} \quad \beta_W = \sqrt{1 - \frac{4M_W^2}{M_{WW}^2}}\,. \tag{3.10}$$

The long-distance collinear physics is described by the parton luminosity

$$\mathcal{L}_{ij}\left(y, \mu_f\right) = \int_y^1 \frac{dx}{x} f_i(x, \mu_f) f_j\left(\frac{y}{x}, \mu_f\right), \tag{3.11}$$

where f_i is the PDF of a parton with flavor i. The coefficient functions describe the hard partonic process and can be written as a power series in α_s,

$$C_{ij} = C_{ij}^0 + \frac{\alpha_s}{4\pi} C_{ij}^1 + \dots\,. \tag{3.12}$$

We have chosen the normalization of Eq. (3.9) such that the leading order coefficient is

$$C_{ij}^0 = \delta(1-z) \mid A_{ij}^0 \mid^2, \tag{3.13}$$

and the Born level cross section is recovered.

3.2.2 NLO result

At NLO, the scattering coefficients of Eq. (3.9) receive corrections from virtual loops and real gluon emission in the $q\bar{q}$ channel, along with tree level contributions from $qg \to qW^+W^-$. In dimensional regularization with $N = 4 - 2\epsilon$, the one-loop virtual diagrams contribute

$$\sigma_{VIRT} = \frac{1}{2s} \int d\Phi_2 \mid A_{q\bar{q}}^1(s,t) \mid^2, \tag{3.14}$$

where

$$\mid A_{q\bar{q}}^1 \mid^2 = \mid A_{q\bar{q},reg}^1 \mid^2 + \mid A_{q\bar{q},div}^1 \mid^2 \tag{3.15}$$

$$\mid A_{q\bar{q},div}^1 \mid^2 = -\frac{\alpha_s}{4\pi} C_F \left(\frac{4\pi\mu^2}{s}\right)^{\epsilon} \Gamma(1+\epsilon) \left(\frac{4}{\epsilon^2} + \frac{6}{\epsilon}\right) \mid A_{q\bar{q}}^0(s,t) \mid^2$$

$$\mid A_{q\bar{q},reg}^1 \mid^2 = \frac{\alpha_s}{16\pi N_C} C_F \left\{ c_q^{tt} F_q^1(s,t) + c_q^{ss}(s) K_q^1(s,t) - c_q^{ts}(s) J_q^1(s,t) \right\}. \tag{3.16}$$

We note that since QCD does not renormalize electroweak couplings, all the UV divergences cancel leaving only IR divergences in $A_{q\bar{q},div}^1$. The one-loop corrections to the t-channel exchange are given by $c_q^{tt} F_q^1(s,t)$, to the s-channel exchange by $c_q^{ss} K_q^1(s,t)$, and the interference between the s- and t-channels by $c_q^{ts} J_q^1(s,t)$. Expressions for these terms can be found in Appendix B.1. As will be discussed in the next section, the real hard gluon emission contribution is not relevant for the resummation of the threshold logarithms and we therefore do not give it here, although it can be found in Ref. [116].

3.2.3 Threshold Resummation and Matching

We now discuss the resummation of the large logarithms in the partonic threshold limit, $z \to 1$. In this limit, since there is no phase space available for hard gluon emission, the total phase space is well described by the Born $2 \to 2$ process and Eq. (3.9) can be used. In addition to the collinear factorization, in the threshold limit the coefficient functions can be further factorized into hard, H, and soft, S, functions:[3]

$$C_{q\bar{q}}(z, M_{WW}, \cos\theta, \mu_f) \equiv H(M_{WW}, \cos\theta, \mu_f) S(\sqrt{s}(1-z), \mu_f) + \mathcal{O}(1-z)\,. \tag{3.17}$$

The soft function is given by the vacuum expectation values of soft Wilson loops [77, 71] and the hard function is calculated by matching the full QCD result onto the relevant SCET operator. It is this matching that integrates out the hard QCD modes and leaves the soft and collinear modes that comprise SCET.

The hard function is given by[4]

$$H(M_{WW}, \cos\theta, \mu) = |C_{WW}(M_{WW}, \cos\theta, \mu)\mathcal{O}_{WW}|^2\,, \tag{3.18}$$

where C_{WW} is the Wilson coefficient of the relevant SCET operator $\mathcal{O}_{WW}$. The Wilson coefficient is calculated by matching the renormalized QCD and SCET amplitudes:

$$\mathcal{M}^{\rm ren}(\epsilon, M_{WW}, \cos\theta) = Z(\epsilon, M_{WW}, \mu)\, C_{WW}(M_{WW}, \cos\theta, \mu)\mathcal{O}_{WW}, \tag{3.19}$$

where $\mathcal{M}^{\rm ren}$ is the renormalized QCD amplitude and Z is the SCET renormalization constant. In dimensional regularization, SCET loops are scaleless and vanish. This implies that the UV and IR singularities of SCET coincide and cancel. Since SCET and QCD describe the same low-scale physics and have the same IR pole structure, Z can be determined by the behavior of IR singularities in QCD [139, 140, 141, 142, 143, 144, 145]. In the $\overline{\rm MS}$ scheme, we have

$$Z(\epsilon, M_{WW}, \cos\theta, \mu) = 1 - \frac{\alpha_s C_F}{2\pi}\,(4\pi)^\epsilon\, e^{-\epsilon\gamma_E} \left\{ \frac{1}{\epsilon^2} + \frac{1}{\epsilon}\left(\ln\frac{\mu^2}{-M_{WW}^2} + \frac{3}{2} \right) \right\}. \tag{3.20}$$

The poles in Z and the NLO QCD squared amplitudes in Eq. (3.16) cancel. Hence, the one-loop contribution to the hard function is just the finite terms of Eq. (3.16) [146, 129].

Since the hard function is calculated in the perturbative region of QCD it can be expanded in powers of α_s:

$$H(M_{WW}, \cos\theta, \mu_h) = H^0(M_{WW}, \cos\theta) + \frac{\alpha_s(\mu_h)}{4\pi}\left[H^1_{reg}(M_{WW}, \cos\theta, \mu_h) + H^1_{extra}(M_{WW}, \cos\theta, \mu_h) \right], \tag{3.21}$$

where μ_h, termed the hard scale, is the scale at which QCD and SCET are matched. The normalization of the hard function is such that

$$H^0(M_{WW}, \cos\theta) = \mid A^0_{q\bar{q}} \mid^2, \tag{3.22}$$

[3] Since we are interested in a color singlet final state, the soft function S has no $\cos\theta$ dependence.

[4] In Eqs. (3.18) and (3.19), the sum over Dirac structures is implied. See Ref. [88] for an example of the relevant notation.

and

$$\begin{aligned}\frac{\alpha_s}{4\pi}H^1_{reg}(M_{WW},\cos\theta,\mu_h) &= \mid A^1_{q\bar{q},reg}\mid^2 \\ H^1_{extra}(M_{WW},\cos\theta,\mu_h) &= -C_F H^0(M_{WW},\cos\theta) \\ &\quad\times\left\{\frac{\pi^2}{3}+2\log^2\left(\frac{M^2_{WW}}{\mu_h^2}\right)-6\log\left(\frac{M^2_{WW}}{\mu_h^2}\right)\right\}. \end{aligned} \quad (3.23)$$

Now we have all the pieces to resum the threshold logarithms. As mentioned before, the hard function is calculated at the matching scale μ_h. Since the soft function describes the soft physics, it is evaluated at a soft scale, μ_s, associated with the scale of soft gluon emission. By using the RG equations (RGEs), the hard and soft functions can be evolved to the factorization scale. The RG evolution of the soft function resums logs of the form $\alpha_s^n \ln^m(\mu_s/M_{WW})$. By choosing the soft scale $\mu_s \sim M_{WW}(1-\tau)$, the RGE running resums the large threshold logarithms. In Table 3.1 we list the accuracy of the resummation at a given order. The resulting coefficient function is [71]

$$\begin{aligned} C(z,M_{WW},\cos\theta,\mu_f) &= U(M_{WW},\mu_h,\mu_s,\mu_f)\,H(M_{WW},\cos\theta,\mu_h) \\ &\quad\times\tilde{s}\left(\ln\left(\frac{M^2_{WW}}{\mu_s^2}\right)+\partial_\eta,\mu_s\right)\frac{e^{-2\gamma_E\eta}}{\Gamma(2\eta)}\frac{z^{-\eta}}{(1-z)^{1-2\eta}} \end{aligned} \quad (3.24)$$

where $\eta = 2a_\Gamma(\mu_s,\mu_f)$ and

$$U(M_{WW},\mu_h,\mu_s,\mu_f) = \left(\frac{M^2_{WW}}{\mu_h^2}\right)^{-2a_\Gamma(\mu_h,\mu_s)} \exp\left[4S(\mu_h,\mu_s)-2a_{\gamma^V}(\mu_h,\mu_s)+4a_{\gamma^\phi}(\mu_s,\mu_f)\right] \quad (3.25)$$

Finally, $\tilde{s}$ is can be expressed as a power expansion in logarithms,

$$\tilde{s}(L,\mu) = 1+\frac{\alpha_s}{4\pi}\sum_{n=0}^{2}s^{(1,n)}L^n+\left(\frac{\alpha_s}{4\pi}\right)^2\sum_{n=0}^{4}s^{(2,n)}L^n. \quad (3.26)$$

Expressions for the $s^{(i,n)}$ are given in Appendix B.2 and are identical to those found for Drell-Yan [71].

We will present results both at NLL and NNLL. The corresponding order of the needed functions is given in Table 3.1. Explicit expressions for the functions a and S, and the anomalous dimensions Γ, γ^V, and γ^ϕ can be found in the appendices of Ref. [71]. The choice of the soft scale, μ_s ,is discussed in Section 3.3.2.

The resummed results are only valid in the region $z \to 1$. To extend these results to all z, the resummed cross section needs to be matched with the full fixed order cross section. This allows the inclusion of the non-singular terms in $(1-z)$ which are present in the fixed order result but not the resummed result. For NNLL resummation, this means matching with the NLO cross section:

$$d\sigma^{NLO+NNLL} \equiv d\sigma^{NNLL}(\mu_h,\mu_f,\mu_s)+\left(d\sigma^{NLO}(\mu_f)-d\sigma^{NLO}(\mu_f)\mid_{leading\ singularity}\right) \quad (3.27)$$

where $d\sigma^{NNLL}$ is the threshold resummed cross section and $d\sigma^{NLO}\mid_{leading\ singularity}$ contains only the $\mathcal{O}(\alpha_s)$ NLO terms which are singular as $z \to 1$,

$$d\sigma^{NLO}\mid_{leading\ singularity} \equiv d\sigma^{NNLL}\mid_{\mu_h=\mu_f=\mu_s}\ . \quad (3.28)$$

Table 3.1: Accuracy of the SCET resummation at a given order and required accuracy of SCET inputs.

Order	Accuracy: $\alpha_s^n \ln^m(\mu_s/M_{WW})$	Γ_{cusp}	γ^h, γ^ϕ	$H, \tilde{s}$
NLL	$2n-1 \leq m \leq 2n$	2-loop	1-loop	tree
NNLL	$2n-3 \leq m \leq 2n$	3-loop	2-loop	1-loop

Subtracting $d\sigma^{NLO}\,|_{leading\ singularity}$ prevents double counting of terms common to the resummed and fixed order results. Also, in the limit $z \to 1$, the matched cross section corresponds to the resummed results, as desired.

3.2.4 Approximate NNLO Results

The full NNLO cross section can only be determined from a complete calculation. However, the scale dependent terms that are singular as $z \to 1$ can be determined to NNLO accuracy via the known hard and soft functions and their respective RGEs. As will be shown in the next section, most of the NLO correction comes from the leading singular piece. Hence, we expect that including the scale dependent, leading singular pieces of the NNLO cross section is a good estimate of the full NNLO result. The inclusion of these pieces is known as approximate NNLO.

The coefficient function in Eq. (3.17) can be expanded in a power series,

$$\begin{aligned} C(z, M, \cos\theta, \mu) &= C^0(z, M, \cos\theta, \mu) + \frac{\alpha_s}{4\pi} C^1(z, M, \cos\theta, \mu) \\ &\quad + \left(\frac{\alpha_s}{4\pi}\right)^2 C^2(z, M, \cos\theta, \mu)\,. \end{aligned} \tag{3.29}$$

The leading order, C^0, and NLO, C^1, contributions are fully known analytically. The NNLO contribution, C^2, can only be approximately determined from the hard and soft functions. The soft function is known fully to NNLO [71]; hence the only approximation comes from the unknown scale-independent NNLO piece of the hard function. The approximate NNLO cross section is found by calculating the scale-dependent, leading singular pieces of C^2 and adding this contribution to the full NLO result.

We expand the hard function as a power series in α_s:

$$H_{approx}(M_{WW}, \cos\theta, \mu_f) = H(M_{WW}, \cos\theta, \mu_f) + \left(\frac{\alpha_s}{4\pi}\right)^2 H^2_{approx}(M_{WW}, \cos\theta, \mu_f), \tag{3.30}$$

where the full NLO hard function, H, is given in Eq. (3.21). The NNLO hard piece, H^2_{approx}, contains only the scale dependent pieces at NNLO. We further expand H^2_{approx} in a power series of logs:

$$H^2_{approx}(M_{WW}, \cos\theta, \mu_f) = \sum_{n=1}^{3} h^{(2,n)} L^n_{WW}, \tag{3.31}$$

where $L_{WW} = \ln(M^2_{WW}/\mu^2_f)$. The coefficients $h^{(2,n)}$ can be found in Appendix B.2.

The approximate NNLO hard function in Eq. (3.30) is independent of scale to order α_s^3. Hence, scale variation only contains the $\mathcal{O}(\alpha_s^3)$ uncertainties, not taking into account the unknown NNLO scale independent and nonsingular in $(1-z)$ pieces at $\mathcal{O}(\alpha_s^2)$. Variation of the factorization scale may therefore underestimate the total uncertainty in the approximate NNLO result. However, this uncertainty can be further estimated by noting that there is an ambiguity in the logs used to expand H^2. For example, introduce a scale $Q_h \sim M_{WW}$. Then H^2 can be expanded in logs of the form $L_Q = \ln(Q_h^2/\mu_f^2)$ instead of L_{WW}. The difference between these two schemes will be order one contributions to the scale independent piece. Hence, in addition to the variation of the factorization scale, the uncertainty associated with the unknown NNLO scale independent piece is estimated by making the replacement $L_{WW} \to L_Q$ in Eq. (3.31) and varying the new scale Q_h around the central value M_{WW}, which is the natural choice from the RGEs.

We note that when including the scale independent pieces, the full NNLO hard function is independent of the scale Q_h. Similarly, since the soft function is known fully to NNLO there is no ambiguity in the choice of scales used in the log expansion.

3.3 Results

3.3.1 Soft Scale Choice

In the process of performing resummation in the SCET formalism, two additional scales are introduced: the hard scale μ_h, where the hard function is evaluated; and the soft scale, μ_s, where the soft function is evaluated. Since the hard function is calculated from matching QCD onto SCET at the scale of the hard scattering process, the central value of μ_h is naturally chosen to be the scale of the hard scattering process, $\mu_h = M_{WW}$.

The soft scale is chosen to be associated with the scale of the soft gluon emissions, such that the RG evolution resums large logs associated with soft gluon emission at threshold. Following Refs. [129, 77, 71], we choose the soft scale to be related to the hadronic energy scale, avoiding the Landau poles that plague the traditional perturbative QCD resummation [87, 129]. Hence, in the hadronic threshold limit $\tau \to 1$ we want $\mu_s \sim M_{WW}(1-\tau)$. However, at hadron colliders most of the cross section is accumulated far from $\tau = 1$ and the choice of soft scale away from this limit is less clear.

Another constraint on μ_s is that the soft function should be a well-behaved perturbative series. Hence, away from the threshold region, we choose μ_s such that the $\mathcal{O}(\alpha_s)$ piece of the soft function is minimized relative to the LO piece. Figure 3.2(a) shows the ratio of the NNLL-resummed invariant mass distribution evaluated with only the $\mathcal{O}(\alpha_s)$ piece of the soft function, $(d\sigma_{WW}^{NNLL})_{\alpha_s}$, to the NNLL-resummed distribution evaluated with only the LO piece of the soft function, $(d\sigma_{WW}^{NNLL})_0$. In both distributions, all other pieces of the resummed cross sections (aside from the soft function) are evaluated to full NNLL order. This ratio is shown for $\sqrt{S} = 8$ TeV at various values of M_{WW} with $\mu_f = \mu_h = M_{WW}$ and MSTW2008nnlo PDFs. The soft scale is chosen to correspond to the minimum of these ratios, which is found to be well described by the parameterization

$$\mu_s = M_{WW}\frac{(1-\tau)}{(a+b\sqrt{\tau})^c}. \tag{3.32}$$

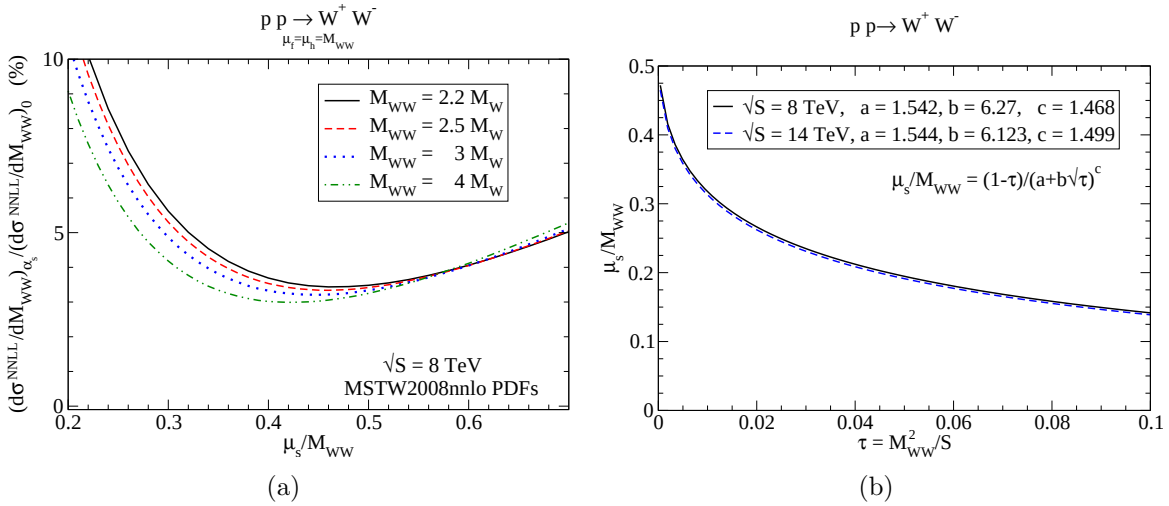

(a) (b)

Figure 3.2: (a) The ratio of the NNLL-resummed invariant mass distribution evaluated with only the $\mathcal{O}(\alpha_s)$ piece of the soft function, $(d\sigma^{NNLL}/dM_{WW})_{\alpha_s}$, to the NNLL-resummed distribution evaluated with only the LO piece of the soft function, $(d\sigma^{NNLL}/dM_{WW})_0$, at $\sqrt{S} = 8$ TeV and various values of M_{WW}. (b) The minimum value of μ_s/M_{WW} at $\sqrt{S} = 8$ TeV (solid) and $\sqrt{S} = 14$ TeV (dashed) as a function of τ.

For $\sqrt{S} = 8$ TeV, it is found that $a = 1.542$, $b = 6.27$, and $c = 1.468$. Performing a similar fit at $\sqrt{S} = 14$ TeV it is found that $a = 1.544$, $b = 6.123$, and $c = 1.499$. With this parameterization μ_s has the correct dependence on τ in the threshold region.

Figure 3.2(b) shows the minimum value of the ratio μ_s/M_{WW} at $\sqrt{S} = 8$ TeV (solid) and $\sqrt{S} = 14$ TeV (dashed) as a function of τ. As can be clearly seen, the hadronic energy makes little difference to the choice of the soft scale. For simplicity, independent of the hadronic energy scale, all results presented here use the central value of the soft scale corresponding to the 8 TeV solution:

$$\mu_s^{\min} = M_{WW} \frac{(1-\tau)}{(1.542 + 6.27\sqrt{\tau})^{1.468}}. \tag{3.33}$$

3.3.2 Differential Cross Section

We begin by considering the validity of the matching of the NNLL results to the fixed order NLO results. In order for the matching of Eq. (3.27) to be valid, the sub-leading terms in $(1-z)$ must be small. In Fig. 3.3, we show the contribution of the leading singularity to the fixed order NLO differential cross section for $\sqrt{S} = 8$ TeV and $\sqrt{S} = 14$ TeV. We fix the central scale to be $\mu_f = 2M_W$. From this figure, we see that the leading singularity captures $\sim 90\%$ of the NLO fixed order cross section. Hence, the threshold singularities contribute most of the NLO cross section and we may expect that by resumming the higher order logarithms we capture most of the higher order cross section.

In Fig. 3.4(a), we show $d\sigma/dM_{WW}$ versus M_{WW} for $\sqrt{S} = 14$ TeV, with MSTW2008 PDFs. The curves are LO, NLO, NLL (matched), and NNLL (matched), with $\mu_h = M_{WW}$, $\mu_s = \mu_s^{\min}$ and μ_f varied up and down by a factor of 2 from the central value of $\mu_f^0 = 2M_W$.

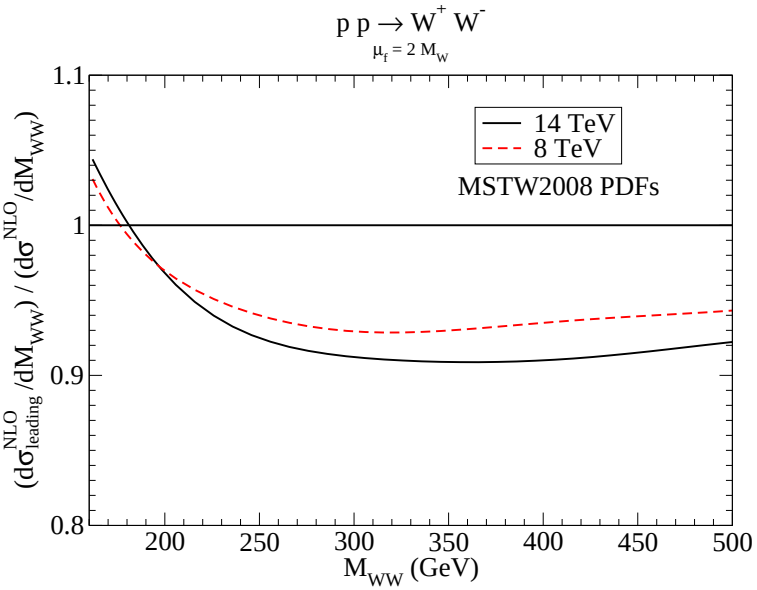

Figure 3.3: Ratio of the contribution of the leading singularity to the fixed order NLO cross section at $\sqrt{S} = 8$ and 14 TeV using MSTW2008 PDFs. NNLO (NLO) PDFs are used for the NNLL leading contribution (fixed order NLO contribution).

It is apparent that the NNLL resummation slightly increases the rate at the peak.

A change in the W^+W^- invariant mass distribution may be consequential to the analysis of the $H \to W^+W^- \to 2\ell 2\nu$ decay channel. In the zero jet bin, the major background is the SM (non-Higgs) production of W^+W^- [98, 99]. To estimate this background a sideband analysis is performed. A control region is defined with a minimum dilepton invariant mass, where the W^+W^- background strongly dominates the Higgs signal. The control region is used to normalize the cross section and then Monte Carlo is used to extrapolate the line shapes into the signal region. If higher order corrections alter the M_{WW} distribution, the dilepton invariant mass distribution will be changed and the extrapolation to the signal region will need to take this into account.

In Fig. 3.4(b) we explore the effect of higher order corrections on the invariant mass distribution by plotting the ratio of the NLO+NNLL matched and NLO M_{WW} distributions. The scales are set to be $\mu_h = M_{WW}$, $\mu_s = \mu_s^{\rm min}$, and $\mu_f = 2M_W$. For the NLO cross section evaluated with NLO PDFs (solid), the resummation increases the invariant mass distribution by $\sim 3-4\%$ in the peak region for both $\sqrt{S} = 8$ and 14 TeV and decreases it by $\sim 2\%$ and $\sim 1\%$ in the high mass region for $\sqrt{S} = 8$ and 14 TeV, respectively. However, most of this change in the M_{WW} distribution is from the different PDFs used for the resummed and NLO results, as can be seen when the NLO cross section is evaluated with NNLO PDFs (dashed). In this case, the resummation only alters the invariant mass distribution by $\lesssim 1\%$ for a wider range M_{WW}. This indicates that the calculation of the W^+W^- cross section is firmly under theoretical control.

The factorization scale dependence of the invariant mass distributions is shown in Fig. 3.5 for (a) the NNLL resummed and NLO leading, and (b) the NLO and NNLL matched results. Here we present the factorization scale dependence as a percent difference from the central

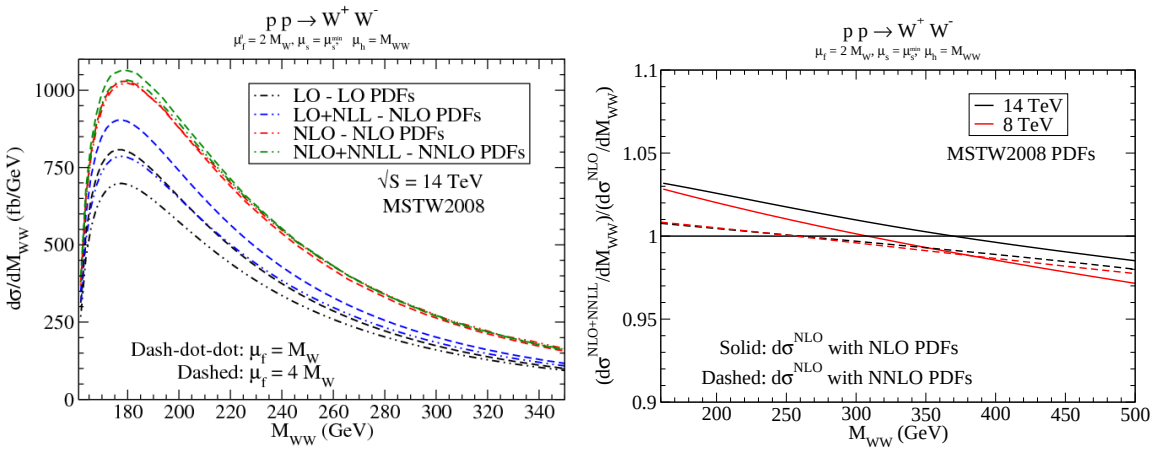

(a) (b)

Figure 3.4: (a) Invariant mass distribution and factorization scale dependence of fixed order and matched differential cross sections at $\sqrt{S} = 14$ TeV using MSTW2008 PDFs. The dash-dot-dot curves have $\mu_f = M_W$ and the dashed curves have $\mu_f = 4M_W$. (b) Ratio of the NLO+NNLL matched and NLO invariant mass distribution for $\sqrt{S} = 8$ and 14 TeV with the NLO cross section with NLO PDFs (solid) and NNLO PDFs (dashed). The factorization scale is fixed to $\mu_f = 2M_W$.

value. Using the definition of matching in Eq. (3.27), Fig. 3.5(a) indicates that there is a cancellation between the μ_f dependencies the NNLL resummed and NLO leading results for $M_{WW} \lesssim 400$ GeV. Comparing Figs. 3.5 (a) and (b), it is apparent that for $M_{WW} \gtrsim 190$ GeV the NLO μ_f dependence also cancels against the NNLL resummed dependence. Hence, although the cancellation is not as efficient at lower M_{WW}, as the invariant mass increases the μ_f dependence of the NNLL matched result is less than that of the NLO result. This can be seen in Fig. 3.5(b), where we see that that for $M_{WW} \gtrsim 220 - 230$ GeV the μ_f dependence of the NNLL matched result is lower than the NLO result. Hence, although the scale dependence of the NNLL matched result is larger than that of the NLO result at the peak of the invariant mass distribution, one can show that the resummation and matching procedure decreases the factorization scale dependence of the total cross section relative to the NLO result.

In Fig. 3.6, we show the deviation from the central scales for the NNLL resummed differential cross section, $d\sigma^{NNLL}/dM_{WW}$, versus M_{WW} for $\sqrt{S} = 14$ TeV, with MSTW2008nnlo PDFs. Again, we present the scale dependence as a percent difference from the central value. The central scales are $\mu_h^0 = M_{WW}$, $\mu_s^0 = \mu_s^{\min}$ and $\mu_f^0 = 2M_W$ and are separately varied up and down by a factor of 2. The hard and soft scale variations are of the order of $\sim 1 - 2\%$ and are relatively independent of M_{WW}. The factorization scale dependence near the peak is $\sim \pm 6\%$ and is always greater than the hard and soft scale dependencies for the invariant mass range presented.

Finally, in Fig. 3.7 we show the variation of the NNLL matched cross section with the central scale choices $\mu_h^0 = M_{WW}$, $\mu_s^0 = \mu_s^{\min}$ and $\mu_f^0 = 2M_W$ at $\sqrt{S} = 14$ TeV. The cross section varies by less than $\pm 2\%$ as the scales are varied from the central values. Again, we see that there is a large cancellation of the factorization scale when computing the matched

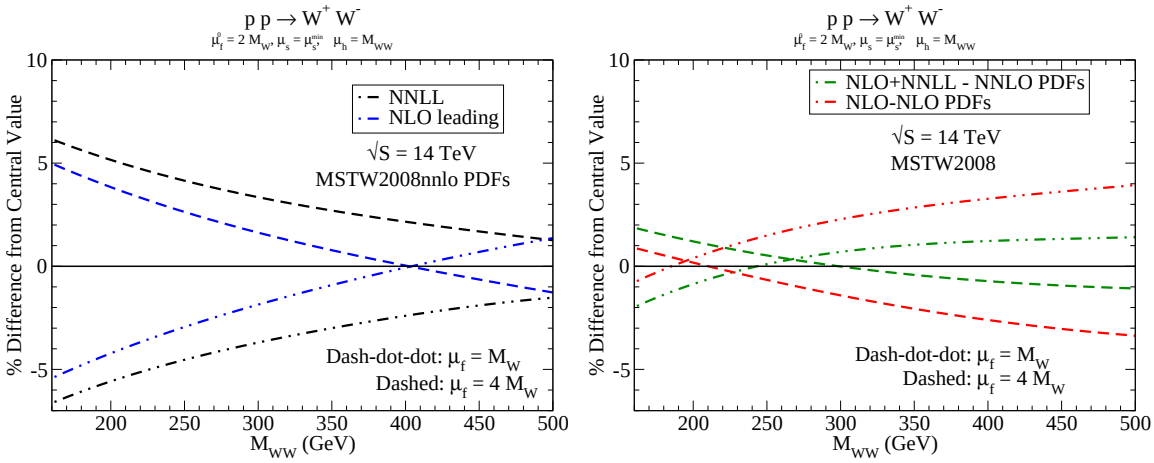

Figure 3.5: Factorization scale dependence of (a) NNLL resummed and NLO leading singularity, and (b) NLO and matched NNLL invariant mass distributions at $\sqrt{S} = 14$ TeV using MSTW2008 PDFs. The dash-dot-dot curves have $\mu_f = M_W$ and the dashed curves have $\mu_f = 4M_W$.

cross section. In contrast to the NNLL results in Fig. 3.6, the μ_f dependence of the matched result is less than (similar to) the hard and soft scale dependencies for $\mu < \mu^0$ ($\mu > \mu^0$). Also, note that unlike the soft and factorization scales, the hard scale dependence, with a minimum near the central value, actually never decreases but always increases the total cross section as it is varied from the central value. This explains why in Fig. 3.6 the effect of the hard scale variation was always to increase the differential cross section value above the central value.

3.3.3 Total Cross Section

In this section, we compile our final results for the total W^+W^- cross sections at the LHC. In Tables 3.2 and 3.3, we show successively improved results for the total cross sections using MSTW2008 PDFs. Both tables fix the central value of $\mu_h^0 = M_{WW}$ and $\mu_s^0 = \mu_s^{\min}$. Table 3.2 takes the central factorization scale to be fixed at $\mu_f^0 = 2M_W$, while Table 3.3 uses a dynamical central scale, $\mu_f^0 = M_{WW}$. The top line is the NLO result obtained from MCFM [107] (which includes the gg initial state) and is calculated using NLO PDFs. The second line of the tables is the gg contribution, σ^{gg}, calculated using MCFM, but with NNLO PDFs (as is appropriate for combining with the NNLL and approximate NNLO results). The third and fourth rows contain the NNLL matched and approximate NNLO cross sections evaluated with NNLO PDFs but without the gg contribution, $\sigma^{NLO+NNLL}$ and σ^{NLO}_{approx}, respectively. The fifth and sixth rows are the same as the third and fourth, but with the gg contribution now included. The uncertainties in the matched cross section correspond to taking the central values of the hard, soft, and factorization scales and varying each separately up and down by a factor of 2. The uncertainties in the approximate NNLO cross section correspond to varying the factorization and Q_h scales by a factor of two around

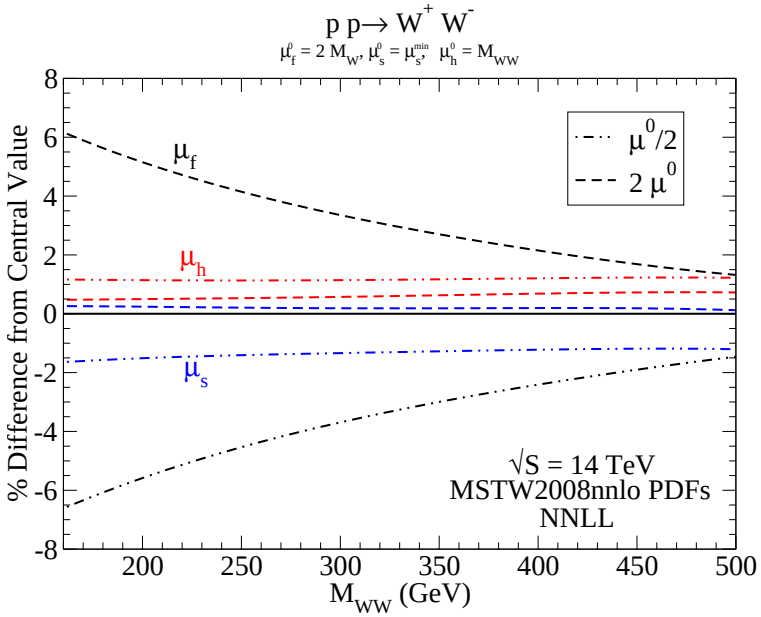

Figure 3.6: Scale dependence of the σ^{NNLL} differential cross sections at $\sqrt{S} = 14$ TeV using MSTW2008nnlo PDFs. The scales are varied by a factor of 2 up and down from the central scales, $\mu_h^0 = M_{WW}$, $\mu_s^0 = \mu_s^{\min}$ and $\mu_f^0 = 2M_W$.

their central values. The resulting uncertainties are added in quadrature.

As noted in the discussion of the previous subsection, the factorization scale dependence of the matched cross section is less than that of the NLO cross section. This cancellation is more extreme at $\sqrt{S} = 7$ and 8 TeV. Hence, even with hard and soft scale variation taken into account the scale dependence of $\sigma'^{NLO+NNLL}$ is less than that of σ^{NLO}. At $\sqrt{S} = 13$ and 14 TeV, once the uncertainties associated with hard and soft scale variation are taken into account, the scale uncertainty of $\sigma'^{NLO+NNLL}$ is similar to or greater than that of σ^{NLO}.

The scale dependence of the approximate NNLO cross sections, σ'^{NNLO}_{approx}, at $\sqrt{S} = 7$ and 8 TeV is reduced by at least a factor of three relative to the NLO cross section, while at $\sqrt{S} = 13$ and 14 TeV the uncertainties of the NLO and σ'^{NNLO}_{approx} cross sections are more similar. This is due to a cancellation of the factorization scale dependence of σ^{gg} and σ^{NNLO}_{approx} at $\sqrt{S} = 7$ and 8 TeV that is not present at $\sqrt{S} = 13$ and 14 TeV. This also explains why the scale variation of approximate NNLO cross section without gg contribution is similar to (less than) that with the gg contribution at 7 and 8 TeV (13 and 14 TeV.) Finally, with $\mu_f^0 = M_{WW}$ at $\sqrt{S} = 8$ TeV, the zero in the scale uncertainty of σ'^{NNLO}_{approx} indicates that the factor of 2 of both the factorization and Q_h scales increase the cross section.

Although there is no significant difference between the cross section prediction of σ'^{NNLO}_{approx} and $\sigma'^{NLO+NNLL}$, we consider σ'^{NNLO}_{approx} to be our best prediction for the LHC W^+W^- production cross sections, since σ'^{NNLO}_{approx} for the most part has less scale variation than $\sigma'^{NLO+NNLL}$. By comparing the NLO and approximate NNLO, σ'^{NNLO}_{approx}, cross sections, it is apparent that the effect of the higher order corrections is to increase the cross section less than ~ 1 pb at $\sqrt{S} = 8$ TeV and less than ~ 3 pb at $\sqrt{S} = 14$ TeV, while reducing the theoretical uncertainty from scale variations. The matched NNLL cross section increases the NLO cross

Table 3.2: Total cross sections for $pp \to W^+W^-$ with $\mu_f^0 = 2M_W$, $\mu_h^0 = M_{WW}$, $\mu_s^0 = \mu_s^{\min}$, and $Q_h^0 = M_{WW}$. The NLO σ^{NLO} includes the gg contribution and is evaluated with NLO PDFs and the remaining entries are evaluated with MSTW2008nnlo PDFs. The primed cross section $\sigma'^{NLO+NNLL}$ is the sum of gg contribution σ^{gg} and the matched $\sigma^{NLO+NNLL}$, while σ'^{NNLO}_{approx} is the sum of σ^{gg} and approximate NNLO, σ^{NNLO}_{approx}. The last row, σ'^{NNLO}, is our best prediction for the cross section.

σ(pb)	$\sqrt{S} = 7$ TeV	$\sqrt{S} = 8$ TeV	$\sqrt{S} = 13$ TeV	$\sqrt{S}$=14 TeV
σ^{NLO}	$45.7^{+1.5}_{-1.1}$	$55.7^{+1.7}_{-1.2}$	$110.6^{+2.5}_{-1.6}$	$122.2^{+2.5}_{-1.8}$
σ^{gg}	$1.0^{+0.3}_{-0.2}$	$1.3^{+0.4}_{-0.3}$	$3.5^{+0.9}_{-0.7}$	$4.1^{+0.9}_{-0.7}$
$\sigma^{NLO+NNLL}$	$44.9^{+0.6}_{-0.6}$	$54.8^{+0.7}_{-0.8}$	$108.2^{+1.3}_{-1.5}$	$119.5^{+1.5}_{-1.6}$
$\sigma'^{NLO+NNLL}$	$45.9^{+0.5}_{-0.6}$	$56.1^{+0.7}_{-0.8}$	$111.7^{+1.8}_{-1.6}$	$123.6^{+2.0}_{-1.8}$
σ^{NNLO}_{approx}	$45.0^{+0.4}_{-0.1}$	$54.9^{+0.5}_{-0.05}$	$108.3^{+1.0}_{-0.4}$	$119.6^{+1.2}_{-0.5}$
σ'^{NNLO}_{approx}	$46.0^{+0.4}_{-0.047}$	$56.2^{+0.6}_{-0.1}$	$111.8^{+1.7}_{-1.1}$	$123.7^{+1.8}_{-1.2}$

Table 3.3: Total cross sections for $pp \to W^+W^-$ with $\mu_f^0 = M_{WW}$, $\mu_h^0 = M_{WW}$, $\mu_s^0 = \mu_s^{\min}$, and $Q_h^0 = M_{WW}$. The NLO σ^{NLO} includes the gg contribution and is evaluated with NLO PDFs and the remaining entries are evaluated with MSTW2008nnlo PDFs. The primed cross section $\sigma'^{NLO+NNLL}$ is the sum of gg contribution σ^{gg} and the matched $\sigma^{NLO+NNLL}$, while σ'^{NNLO}_{approx} is the sum of σ^{gg} and approximate NNLO, σ^{NNLO}_{approx}. The last row, σ'^{NNLO}, is our best prediction for the cross section.

σ(pb)	$\sqrt{S} = 7$ TeV	$\sqrt{S} = 8$ TeV	$\sqrt{S} = 13$ TeV	$\sqrt{S}$=14 TeV
σ^{NLO}	$44.8^{+1.2}_{-0.9}$	$54.7^{+1.4}_{-1.0}$	$108.8^{+1.2}_{-1.3}$	$120.3^{+2.0}_{-1.3}$
σ^{gg}	$0.9^{+0.2}_{-0.2}$	$1.2^{+0.3}_{-0.1}$	$3.3^{+0.8}_{-0.6}$	$3.7^{+0.7}_{-0.6}$
$\sigma^{NLO+NNLL}$	$44.7^{+0.5}_{-0.6}$	$54.6^{+0.6}_{-0.8}$	$108.1^{+1.4}_{-1.5}$	$119.4^{+1.6}_{-1.7}$
$\sigma'^{NLO+NNLL}$	$45.6^{+0.6}_{-0.6}$	$55.8^{+0.7}_{-0.8}$	$111.4^{+2.0}_{-1.8}$	$123.1^{+2.1}_{-2.0}$
σ^{NNLO}_{approx}	$44.8^{+0.4}_{-0.1}$	$54.7^{+0.4}_{-0.04}$	$108.2^{+1.0}_{-0.4}$	$119.6^{+1.2}_{-0.6}$
σ'^{NNLO}_{approx}	$45.7^{+0.4}_{-0.04}$	$55.9^{+0.5}_{-0}$	$111.5^{+1.6}_{-1.0}$	$123.3^{+1.7}_{-1.2}$

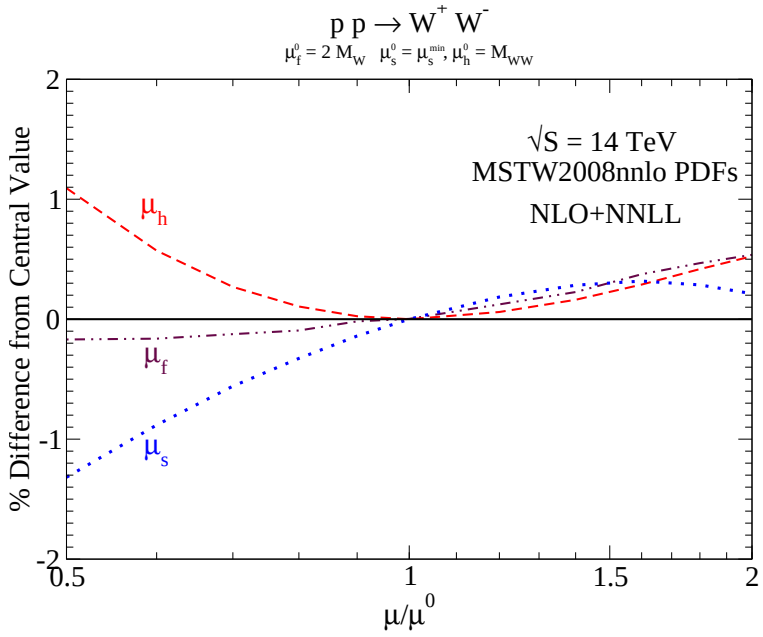

Figure 3.7: Scale dependence of the matched $\sigma^{NLO+NNLL}$ cross sections at $\sqrt{S} = 14$ TeV using MSTW2008nnlo PDFs. The scales are varied by a factor of 2 up and down from the central scales, $\mu_h^0 = M_{WW}$, $\mu_s^0 = \mu_s^{\min}$ and $\mu_f^0 = 2M_W$.

section by similar amounts, with a slightly increased scale uncertainty. There is very little difference between using a fixed factorization scale and a dynamic factorization scale. It appears that the prediction for the W^+W^- cross section is under good theoretical control.

3.4 Discussion

Now that the Higgs boson is discovered, a full exploration of the electroweak sector has begun. An important signal for this exploration is the pair production of gauge bosons, in particular W^+W^- production. This signal is a major background to $H \to W^+W^-$ and is sensitive to the electroweak gauge boson triple coupling, which directly probes the mechanism of electroweak symmetry breaking and the $SU(2) \times U(1)$ gauge structure, respectively. In order to be sensitive to new physics in the W^+W^- signal and measure the $H \to W^+W^-$ decay channel well, it is important to have accurate and precise theoretical predictions for W^+W^- production cross section and differential distributions.

In this chapter we resummed large logarithms associated with soft gluon emission at partonic threshold, $z = M_{WW}^2/s \to 1$, at NNLL order for W^+W^- pair production. This resummation was performed using the formalism of SCET [41, 42, 43, 44] which allows for the resummation directly in momentum space [77, 129]. The NNLL resummed results were then matched onto the known NLO results [116, 117]. We also calculated the approximate NNLO W^+W^- cross section. We thus obtain the most accurate cross sections and invariant mass distributions for W^+W^- production that have been calculated to date.

We found that the effect of the threshold resummation on the invariant mass distribution

was to increase the differential cross section $\sim 3-4\%$ in the peak region for both $\sqrt{S} = 8$ and 14 TeV. The matched NLO+NNLL and approximate NNLO cross section both increased the NLO cross section by $\sim 0.5 - 1.5\%$ for a factorization scale central value $\mu_f^0 = 2M_W$ and $\sim 2-3\%$ for a central scale of $\mu_f^0 = M_{WW}$, within the theoretical uncertainties. The theoretical uncertainties of the approximate NNLO cross section were generally decreased relative to those of the NLO cross section. These results indicate that the sideband analysis used for W^+W^- background estimation to $H \to W^+W^-$ signal [98, 99] is not significantly altered by higher order corrections. Also, the strong coupling constant perturbative expansion of the W^+W^- production cross section is firmly under theoretical control.

The exact NNLO cross section for $pp \to W^+W^-$ was obtained [115] after the work in this chapter was finished. The exact NNLO result is higher than the NLO result by about 5% for 7 TeV and 8 TeV collisions. Therefore, threshold terms do not account for the bulk of the NNLO corrections. This is not surprising, as Chapter 2 explained that the scale hierarchy between the hard and soft scales is controlled by how rapidly the parton luminosity function declines, quantified by the logarithmic gradient. This gradient is small at low $\tau = M^2/s$, which is especially true for the $q\bar{q}$ luminosity function. However, for the production of systems of higher invariant masses, we expect threshold resummation to serve as a more accurate approximation for higher-order terms in the cross section.

Chapter 4

p_T resummation for W^+W^- production

This chapter is based on the publication [54].

4.1 Introduction

The Standard Model (SM) of particle physics has been tested at a new energy frontier by the Large Hadron Collider (LHC). SM cross sections were measured at both 7 and 8 TeV, and the SM has passed with flying colors in almost every channel. Nevertheless there has been one channel that is consistently off at the LHC for both the ATLAS and CMS experiments, the W^+W^- cross section measured in the fully leptonic final state. This state is naively one of the most straightforward channels to measure both theoretically and experimentally as it is an electroweak final state with two hard leptons. However, at 7 and 8 TeV ATLAS [102, 147] and CMS[148, 149] have measured a discrepancy with the SM NLO calculation [116, 117] of $\mathcal{O}(20\%)$ and this extends to differential measurements not just simply an overall rescaling. At the end of this chaper, we will discuss an improved CMS analysis [106] that incorporates the results of this chapter and the recently computed NNLO total cross section [115].

This discrepancy is particularly compelling for a number of reasons. First and foremost, one of the most important channels fOr the Higgs is the W^+W^- decay channel of which SM W^+W^- is the largest background. Since this channel does not have a particular kinematic feature akin to bumps in the $\gamma\gamma$ or ZZ channels, it is important to understand the shape of the SM background quite well. CMS [150] and ATLAS[151] use data driven techniques to extrapolate and find the signal strength of the Higgs. While these data driven techniques are validated in many ways, it is often times difficult to find perfectly orthogonal control regions, and correlations may arise at higher order in theoretical calculations or because of new physics contributions. Given the shape differences observed, whether or not this is due to an insufficient SM calculation or new physics, it is important to understand that there could possibly be effects which alter the signal strength of the Higgs when the SM W^+W^- channel is understood better [152].

Another compelling reason for understanding the discrepancy is the possibility of new

sub-TeV scale physics. The dilepton + MET final state is an important background to many searches, but even more so, the large $\mathcal{O}$(pb) discrepancy currently observed still allows for the possibility of new $\mathcal{O}(100)$ GeV particles. While models of this naively would have been ruled out by previous colliders, or other searches at the LHC, in fact it turns out that there could be numerous possibilities for physics at the EW scale. These include Charginos[109], Sleptons[110], Stops[111, 112, 113] or even more exotic possibilities[114]. Remarkably, as first shown in[109], not only could new physics be present at the EW scale, it in fact can *improve* the fit to data compared to the SM significantly, because it preferentially fills in gaps in the differential distributions when new physics is at the EW scale. In particular the possibility of particles responsible for naturalness in SUSY being at the weak scale and realizing a solution of the hierarchy problem makes this particularly compelling given all the negative results in other channels.

Finally, It is particularly interesting simply from the point of QCD and the SM to understand why the W^+W^- channel has a persistently discrepant experimental result compared to SM predictions when other similar uncolored final states e.g. ZZ and WZ seem to agree quite well with experiment. There are potential theoretical reasons within the SM that could explain the difference compared to experiment and to other EW channels. One of the first points that could be addressed in the context of the W^+W^- measurement is whether or not the fixed order calculation was sufficient to describe the data. Currently the W^+W^- channel is formally known at NLO, and this is implemented in various NLO MC generators employed by ATLAS and CMS in their analyses. However, partial NNLO results are also incorporated, since $gg \to W^+W^-$ via a quark loop is included through the generator gg2VV[153, 154]. The merging of NLO WW and WWj predictions have been investigated in [155, 156, 157], while approximate calculations for higher order corrections to $gg \to W^+W^-$ are performed in [158]. Theoretically the full NNLO calculation of W^+W^- production turns out to be quite difficult, but within the past year there has been a great deal of progress; the complete NNLO calculation for ZZ total cross section has recently been completed[159]. The results of[159] are interesting, given that compared to NLO, the NNLO effect can be sizable $\mathcal{O}(10\%)$. However, when examined closely, if the full NNLO results are compared to the NLO + $gg \to ZZ$ the difference is less than $\mathcal{O}(5\%)$. Given this result for ZZ, unless there were large differences from a channel with very similar contributions, it would be highly unlikely that the full NNLO result could explain the discrepancies in the W^+W^- result.

There can be effects beyond the fixed order calculation that matter as well. As with any calculation there are additional logarithms that arise whenever there is an extra scale in the problem, for instance threshold resummation logs, or logs of the transverse momentum of the system compared to the hard scale of the system. These logarithms can either change the overall cross section as in the case of threshold resummation, or the shape of the p_T distribution in p_T resummation. In [52] the threshold resummation effects were calculated to approximate NNLL accuracy for W^+W^- production, and the effects were found to be small for the overall cross section of $\mathcal{O}(.5 - 3\%)$ compared to NLO (the NNLO calculation would largely include these logs and thus these effects should not be taken independently in magnitude). Another contribution which primarily effects the overall cross section, comes from π^2 resummation[160, 130, 72]. This has yet to be computed for W^+W^- , however it would affect other EW channels similarly, so the W^+W^- channel should not be singled out and it clearly does not explain a discrepancy of $\mathcal{O}(20\%)$ as measured in that channel.

While the aforementioned effects primarily affect the total cross-section, there are avenues that change the shape in a differential direction while keeping the total cross section constant. One such effect is p_T resummation first calculated for W^+W^- in[128, 161]. An interesting difference that arises with p_T resummation, compared to threshold resummation, is the interplay between the effects of resummation and the way that the cross section is measured for W^+W^- . Given that p_T resummation changes the shape of the p_T distribution, and the p_T distribution would be a delta function at 0 at the Born level, QCD effects are crucial for getting this distribution correct. These effects are normally sufficiently accounted for by using a Parton Shower (matched to LO or NLO fixed order) which only approaches NLL accuracy. However, in the W^+W^- channel compared to the $W^{\pm}Z$ and ZZ channels there is an additional jet veto requirement for the measurement. This requirement arises because there is an overwhelming background to W^+W^- coming from $t\bar{t}$ production and decay. The most straightforward way to reduce the $t\bar{t}$ background is to veto on extra jets to isolate the W^+W^- contribution. Given this jet veto, and the correlation between jet veto efficiency and the p_T shape of the W^+W^- system, there is an added sensitivity to the jet veto and the shape of the p_T distribution that other channels typically do not have. There is precedent for turning to p_T resummation rather than using a parton shower alone when shape differences are important, e.g. the W mass measurement at the D0[162].

In this chapter we will examine the detailed effects of p_T resummation at approximate NNLL accuracy in combination with how the experimental measurements are performed. Typically the comparison between p_T resummed processes e.g. Drell-Yan or ZZ is done at the unfolded level experimentally. However, it is the extrapolation from the fiducial cross section to the inclusive cross section that can exactly be the source of a the discrepancy and a new analysis has to be carefully performed to understand the W^+W^- channel. The difficulty in doing this of course is that in the context of p_T resummation, all radiation is inclusively summed without reference to a jet algorithm, and there is no jet-veto that can be explicitly performed. In light of this, we undertake a procedure similar to what is done for Higgs production predictions at the LHC using HqT[163] to predict the transverse momentum distribution of the Higgs. We investigate the effects of taking NLO + parton shower generated events for W^+W^- , reweighting them with the NNLL resummed p_T distribution before cuts, and then applying the cuts to find the fiducial cross section, and how the total cross section should be interpreted. We find that this leads to $\mathcal{O}(3-7\%)$ changes in the total cross section, for central choices of scales, which reduces the discrepancy.

A jet veto introduces an additional scale and thus logs related to this scale. Such logs are not identical to the logs accounted for by p_T resummation. A program of jet veto resummation [164, 165, 166, 167, 168, 169, 170, 171] would in principle be required to isolate these effects. These logs are clearly not taken account in our calculation explicitly due to the fact that there are no jets in our resummation calculation. Nevertheless, as mentioned earlier, the probability of an event passing the jet veto and the transverse momentum of the W^+W^- system is strongly correlated, therefore in the process of reweighting the parton showered events and using a jet algorithm, there is a large overlap between the logs accounted for in jet veto resummation, and the logs accounted for in our procedure. This correlation was observed for instance in [164], where for Higgs and Drell-Yan the effects of reweighting the p_T distribution agreed very well with the jet-veto efficiency coming from a jet veto resummation calculation. Given that Higgs production is dominated by gluon initial states,

we expect the agreement between reweighting and jet-veto resummation to be even better for W^+W^- . An additional motivation for performing p_T resummation and re-weighting is that we can perform detector simulations on the fully exclusive events, and predict differential observables. It would be interesting to understand the interplay of these effects even further which we leave to future work.

The rest of the chapter is structured as follows. In Section 4.2, we outline our methodology and calculation of the NNLL resummed W^+W^- p_T distribution. In Section 4.3 we explicitly describe our reweighting procedure, and demonstrate the effects on the total cross section at various energies and compared to various NLO generators and parton showers. Finally, in Section 4.4, we discuss the implications of these results both for scale choices used in resummation and the associated errors as well as how to test these effects in other channels. In particular, given the similarity in scales of W^+W^- , $W^\pm Z$ and ZZ processes, and the fact that resummation cannot tell the difference with respect to the hard matrix element, if resummation effects are responsible for even part of the discrepancy as currently measured there are distinct predictions in other channels.

4.2 W^+W^- transverse momentum resummation

4.2.1 The resummation method

For hadron collider production of electroweak bosons with invariant mass M and transverse momentum p_T, the fixed-order perturbative expansion acquires powers of large logarithms, $\alpha_s^n \log^m (M/p_T)$, with $m \leq 2n-1$, which can be resummed to all orders [172, 173, 174, 78, 175, 176, 177, 178, 179, 180]. We implement the method of Refs. [181, 182] to calculate the WW transverse momentum distribution at partial NNLL+LO.[1] Some aspects of the method are outlined below. The factorized cross section is

$$\frac{d\sigma^{WW}}{dp_T^2}(p_T, M, s) = \sum_{a,b} \int_0^1 dx_1 \int_0^1 dx_2 f_{a/h_1}\left(x_1, \mu_F^2\right) f_{b/h_2}\left(x_2, \mu_F^2\right) \frac{d\hat{\sigma}_{ab}^{WW}}{dp_T^2}\left(p_T, M, \hat{s}, \alpha_s\left(\mu_R^2\right), \mu_R^2, \mu_F^2\right), \tag{4.1}$$

where f_{a/h_1} and f_{b/h_2} are the parton distribution functions for the parton species a and b in the two colliding hadrons, $\hat{s} = s x_1 x_2$ is the partonic center of mass energy, and $d\hat{\sigma}_{ab}^{WW}/dp_T^2$ is the partonic cross section. The partonic cross section will be the sum of a resummed part and a finite part; the finite part matches resummation with fixed order calculations. In our case, we will give partial NNLL+LO results which effectively include the exact LO results at $O\left(\alpha_s\left(\mu_R^2\right)\right)$, plus partial NNLL resummation correction terms at $O\left(\alpha_s^n\left(\mu_R^2\right)\right)$, $2 \leq n \leq \infty$. The method of [181, 182] ensures that the resummation correction preserves the total cross section (which can be calculated at fixed-order reliably) while improving predictions for differential distributions, especially at low p_T.

The quantity that is resummed directly is actually the double transform of the partonic cross section,

$$\mathcal{W}_{ab,N}^{WW}\left(b, M; \alpha_s\left(\mu_R^2\right), \mu_R^2, \mu_F^2\right), \tag{4.2}$$

[1] In our convention, LO p_T distribution is at the same α_s order as the NLO total cross section.

where b, the impact parameter, is the Fourier transform moment with respect to p_T, while N is the Mellin transform moment with respect to $z = M/\hat{s}$. To invert the Mellin transform, we use the standard formula

$$\begin{aligned}&\mathcal{W}_{ab}^{WW}\left(b, M, \hat{s} = M^2/z; \alpha_s\left(\mu_R^2\right), \mu_R^2, \mu_F^2\right)\\ &= \int_{c-i\infty}^{c+i\infty} \frac{dz}{2\pi i}\, z^{-N} \mathcal{W}_{ab,\,N}^{WW}\left(b, M, \alpha_s\left(\mu_R^2\right), \mu_R^2, \mu_F^2\right)\end{aligned} \tag{4.3}$$

where c, a positive number, is the intercept between the integration contour and the real axis. In numerical implementations, the contour is deformed to the left on both the upper and lower complex planes, leaving the integral invariant but improving numerical convergence. To perform the convolution in Eq. (7.11), we fit the parton distribution functions with simple analytic functions [95] to obtain analytical Mellin transforms. We multiply the Mellin transform of the parton distribution functions with the Mellin transform of the partonic cross section, before we actually invert the transform. The error associated with fitting is less than 10^{-3}.

To invert the Fourier transform in Eq. (7.11), we use

$$\begin{aligned}\frac{d\hat{\sigma}_{ab}^{WW}}{dp_T^2}\left(p_T, M, \hat{s}, \alpha_s\left(\mu_R^2\right), \mu_R^2, \mu_F^2\right) &= \frac{M^2}{\hat{s}} \int \frac{d^2\mathbf{b}}{4\pi} e^{i\mathbf{b}\cdot p_T}\, \mathcal{W}_{ab}^{WW}\left(b, M, \hat{s}, \alpha_s\left(\mu_R^2\right), \mu_R^2, \mu_F^2\right)\\ &= \frac{M^2}{\hat{s}} \int \frac{d^2\mathbf{b}}{4\pi} \frac{b}{2} J_0\left(b p_T\right) \mathcal{W}_{ab}^{WW}\left(b, M, \hat{s}, \alpha_s\left(\mu_R^2\right), \mu_R^2, \mu_F^2\right).\end{aligned} \tag{4.4}$$

The double transform in Eq. (7.11) contains large logarithms of the form $\sim \log(M\, b)$ which correspond to $\sim \log\left(M/p_T\right)$ before the Fourier transform. Ignoring the finite term from matching to fixed-order results, the large logarithms are resummed to all order by exponentiation [181],

$$\begin{aligned}\mathcal{W}_{ab,\,N}^{WW}\left(b, M; \alpha_s\left(\mu_R^2\right), \mu_R^2, \mu_F^2\right) &= \mathcal{H}_N^{WW}\left(M, \alpha_s\left(\mu_R^2\right); M^2/\mu_F^2, M^2/Q^2\right)\\ &\quad \times \exp\left\{\mathcal{G}_N\left(\alpha_s\left(\mu_R^2\right), L; M^2/\mu_R^2, M^2/Q^2\right)\right\},\end{aligned} \tag{4.5}$$

where the $\mathcal{H}_{NN}^{WW}$ function essentially describes physics at the scale comparable with M and hence does not depend on b. To our needed accuracy, the function is deduced from the one-loop QCD virtual correction [180] for W^+W^- production calculated in [116]. On the other hand, the function $\mathcal{G}_N$ essentially describes physics at the scale of $1/b \sim p_T$ and hence does not depend on the hard process; for example, it is the same for the Drell-Yan process which is also initiated by quark-antiquarks at LO. The quantity L is defined as

$$L \equiv \ln \frac{Q^2 b^2}{b_0^2}, \quad b_0 \equiv 2e^{-\gamma_E} \approx 1.12, \tag{4.6}$$

where Q, termed the resummation scale, is chosen to be comparable in magnitude to the hard scale of the process. It is an inherent ambiguity in resummation calculations, in addition to the usual μ_R and μ_F ambiguities for fixed order calculations.

The exponent in Eq. (4.5) can be expanded in successive logarithmic orders [181, 70]

$$\begin{aligned}\mathcal{G}_N\left(\alpha_s, L; M^2/\mu_R^2, M^2/Q^2\right) = & Lg^{(1)}\left(\alpha_s L\right) + g_N^{(2)}\left(\alpha_s L; M^2/\mu_R^2, M^2/Q^2\right) \\ & + \frac{\alpha_s}{\pi} g_N^{(3)}\left(\alpha_s L; M^2/\mu_R^2, M^2/Q^2\right) \\ & + \sum_{n=4}^{+\infty}\left(\frac{\alpha_s}{\pi}\right)^{n-2} g_N^{(n)}\left(\alpha_s L; M^2/\mu_R^2, M^2/Q^2\right). \end{aligned} \tag{4.7}$$

This expansion makes sense if we regard $\alpha_s L$ as of order unity. The $g^{(1)}$ term is the leading logarithmic (LL) term, while $g^{(2)}$ and $g^{(3)}$ are the NLL and NNLL terms, and so on. The variation of Q shuffles terms between the fixed order and resummed terms and can give an estimate for as yet uncomputed higher Logs.

The necessary ingredients to perform NLL resummation can be found in [181, 180]. In addition, we also include the three-loop coefficients $A^{(3)}$ for the Sudakov form factor, calculated in [183], to achieve approximate NNLL accuracy. We re-used part of the QCD-Pegasus code [184] to calculate the NLO splitting kernel in complex moment space.

4.2.2 Numerical results

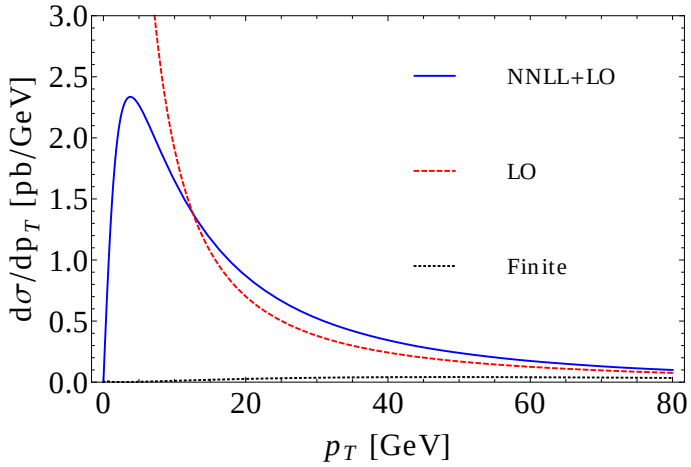

Figure 4.1: Plot of resummed, finite (matching) and fixed-order W^+W^- transverse momentum distributions from 8 TeV proton collisions.

The full details about the underlying resummation formalism, including the diagonalization of the DGLAP splitting kernel in the multi-flavor case, and the matching to fixed-order calculations, are covered in [181, 182] and will not be repeated here. We now go on to present numerical results. To make sure our numerical implementation is correct, we have reproduced the Z-boson resummed transverse momentum distribution in [182], including effects of varying the resummation scale Q.

We use the MSTW 2008 NLO parton distribution functions [93]. The central scales we use are $\mu_R = \mu_F = 2m_W$, $Q = m_W$. In fig. 4.1, we plot the resummed, fixed-order, and finite part of the W^+W^- transverse momentum distribution using central scales for 8

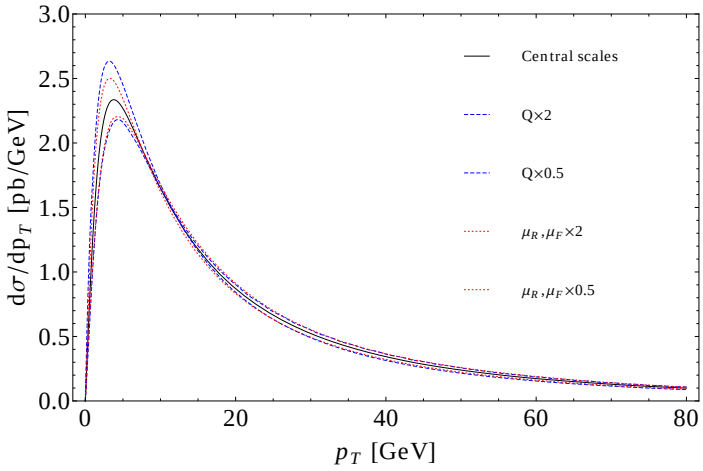

Figure 4.2: Plot of renormalization, factorization and resummation scale variations of the W^+W^- transverse momentum distribution for 8 TeV collisions.

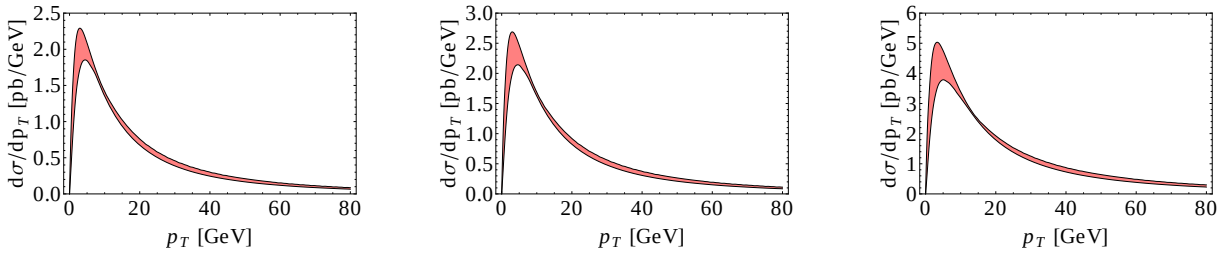

Figure 4.3: NNLO+LO predictions, with error bands, for the W^+W^- transverse momentum distribution for 7,8 and 14 TeV collisions.

TeV pp collisions. We can see that resummation cures the $p_T \to 0$ divergence of the LO distribution and generates substantial corrections. The total cross section obtained from integrating our p_T distribution agrees with exact fixed order results to better than 0.5%, which is a consistency check for our numerical accuracy.

To assess perturbative scale uncertainties, we simultaneously vary μ_R and μ_F up and down by a factor of 2, and separately vary Q up and down by a factor of 2. The resulting variations in the transverse momentum distributions are plotted in Fig. 4.2 for 8 TeV collisions. We can see that the largest scale uncertainties result from varying the resummation scale Q. By adding μ_R & μ_F variations and Q variations in quadrature, we produce the distribution with error bands, for 7, 8 and 14 TeV, shown in Fig. 4.3. The combined scale uncertainty at the peak of the distribution is around $\pm 10\%$ for each collision energy.

We now briefly mention non-perturbative effects. In Eq. (4.4) $\mathcal{W}_{ab}^{WW}$ in fact becomes singular at large b due to the divergence of the QCD running coupling below the scale $\Lambda_{\rm QCD}$. This is a non-perturbative issue and becomes important at low p_T. Many prescriptions for regulating the non-perturbative singularity exists, such as the b^* model [175, 179] and the minimal prescription [185]. We adopt a simple cutoff at $b = 2\,\mathrm{GeV}^{-1}$, and give results both with and without an additional non-perturbative Gaussian smearing factor of

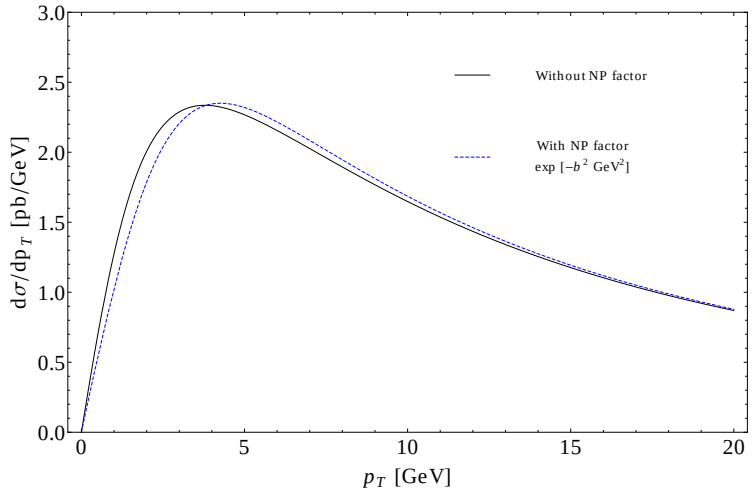

Figure 4.4: NNLL+LO prediction for the WW transverse momentum distribution at 8 TeV, with and without the non-perturbative Gaussian smearing factor exp $\left[-1\,\mathrm{GeV}^2\,b^2\right]$.

exp $\left[-g_{NP}^2\,\mathrm{GeV}^2\,b^2\right]$ with $g_{NP} = 1$. The W^+W^- fiducial cross sections after reweighting parton shower events shifts only differ by about 1% with and without the Gaussian smearing factor, much smaller than the perturbative scale uncertainties we will encounter. In Fig. 4.4 we compare the predicted WW transverse momentum distribution with and without the Gaussian smearing factor. The smearing causes the peak to shift by about 0.5 GeV to larger p_T.

Finally, we compare our p_T distribution at 8 TeV with the SCET-based resummation calculation by [161] in Fig. 4.5. The results are in good agreement, but our results show a larger error band because we varied both μ_R (with μ_F locked to be equal to μ_R) and the resummation scale Q, the latter of which indicates ambiguities in splitting contributions into the resummed part and the finite part, while the calculation by [161] only considers the variation of one scale.

4.3 Transverse Momentum Reweighting and Fiducial Cross Sections

The transverse momentum resummation shown in Section 4.2 systematically improves our understanding of the p_T distribution of the diboson system. However, the W^+W^- p_T distribution as measured by the LHC experiments is not the same as the distribution that is calculated in Section 4.2. This is because the detector only measures a certain fiducial region of phase space, there are additional cuts put on the physics objects to reduce backgrounds, and finally there are detector effects which smear the p_T distribution compared to the theoretical prediction. In very clean channels such as Drell-Yan or ZZ production, these effects can be unfolded more easily, and an unambiguous prediction for the p_T of the system can be compared to theoretical predictions. For W^+W^- the effects are more difficult to unfold and as of yet a full analysis has yet to be compared to the experimental results for the W^+W^-

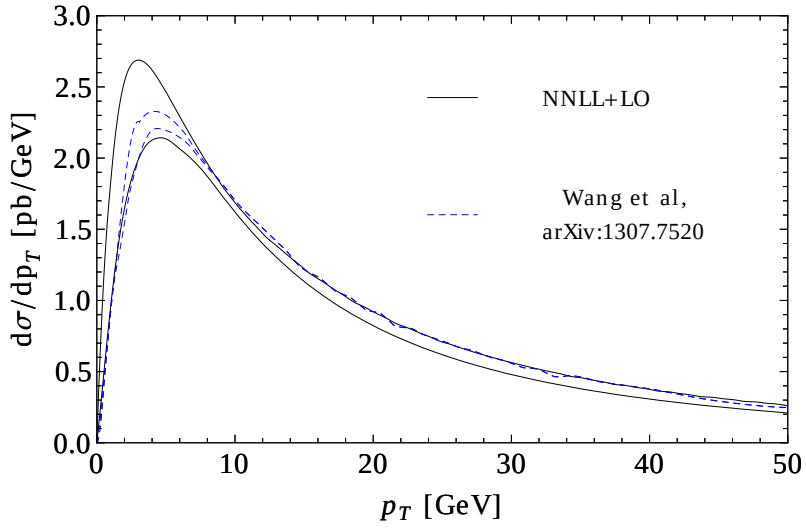

Figure 4.5: Comparision of our resummed WW p_T distribution with a SCET-based resummation calculation, with error bands shown for both.

diboson system's p_T . In fact, only ATLAS has released a distribution, the vector sum of the p_T of the leptons and MET, directly correlated to the p_T of the diboson system.

In order to compare to data, we must implement the same cuts that the experiments perform. Immediately this runs into potential problems as the distributions predicted in Section 4.2 are fully inclusive, and even at the leptonic level there are cuts that restrict the distributions to a fiducial phase space. To circumvent these difficulties we implement a reweighting procedure on generated events for the p_T of the system prior to cuts, and then perform the analysis cuts to find the effects of p_T resummation. This of course is not a perfect matching of the effects of resummation and data, but without unfolded distributions this is the closest possible comparison that can be made at this point. This procedure is akin to that used for predicting the Higgs signal at the LHC, where the transverse momentum resummed shape, taken from HqT for instance[186], is used to reweight the MC simulated events.

It is possible that a comparison between reweighted events after experimental cuts and the original Monte Carlo events *could* predict the same cross section. The formalism we use by definition does not change the total inclusive cross section. However, if the reweighted distributions that have a different shape are also cut on, then this will affect the total measured cross section. This happens because the cuts change the fiducial cross section and hence the inferred total cross section once the acceptances and efficiencies are unfolded. As we will show, there is not a direct cut on the reweighted p_T distribution, but the jet veto cut is highly correlated with it and significantly effects the extrapolated total cross section. Additionally, the cause of the correlation will also reflect that different underlying Monte Carlo generators and parton showers will have different size effects when extrapolating to the total cross section. These differences are demonstrated in Figure 4.6 where the p_T distributions predicted by resummation are compared to various Monte Carlo generators (POWHEG BOX[187, 188, 189], MadGraph/aMC@NLO and matched Madgraph 0j+1j[190]) in combi-

nation with different parton showers from Herwig++[191] and Pythia8[192]. MSTW2008 NLO pdf sets were used for all NLO event generations to be consistent with resummaton and CTEQ6 LO pdf[193] was used for the Madgraph 0+1j analysis.

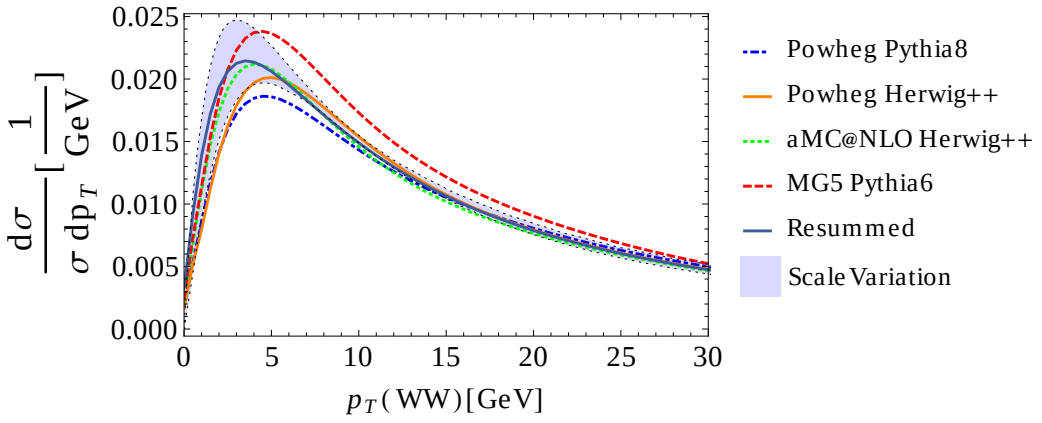

Figure 4.6: Plot of Resummation predicted and MC+shower predictions for W^+W^- transverse momentum distributions at 8 TeV. The shaded region represents the scale Q variation by a factor of 2 relative to the central scale choice $Q = m_W$ for the resummation prediction.

To perform the reweighting procedure, resummed theory curves from Section 4.2 and MC events are binned into 0.5 GeV bins along $p_{T_{WW}}$. A reweighting factor is then computed

$$F[p_T] = \frac{\text{Resummed bin}[p_T]}{\text{MC bin}[p_T]}. \tag{4.1}$$

To approximate detector effects MC events are then smeared using Delphes[194] for a fast detector simulation[1]. Finally, once detector level events are produced we apply the cuts performed by the LHC experiments. An example of the cuts implemented by the ATLAS measurement at 7 TeV is reproduced below in Table 4.1. The cuts from CMS are quite similar, the jet veto as we will show turns out to be the most important effect, and CMS has a jet veto of 30 GeV compared to 25 GeV for ATLAS. We comment on this slight difference in Section 4.4, however, since CMS has not produced a plot of the p_T of the W^+W^- system similar to ATLAS, we adopt the ATLAS cuts when demonstrating the effects of using the p_T resummed reweighted distributions. Pythia8 was used with default tuning and since all our results are shape dependent, the reweighting procedure should be performed again using our resummation-theory curves when using a non-default pythia8 tuning.

[1]The detector simulation is important to match data, as the p_T distribution of the diboson system predicted by MC@NLO[195] shown by ATLAS can not be matched without additional smearing of the MET. We demonstrated this with both PGS and Delphes. In the end however, this smearing does not effect the resummation reweighting effects shown here, because the underlying MC events and resummed reweighted events are affected in the same way. We have demonstrated this explicitly by changing the MET resolution by a factor of 2 each way, which simply shifts the peak of the p_T distribution.

Exactly two oppositely-sign leptons, $p_T > 20\,\text{GeV}, p_{T\text{leading}} > 25\,\text{GeV}$
$m_{ll'} > 15, 15, 10\,\text{GeV}$ (ee,$\mu\mu$,$e\mu$)
$\lvert m_{ll'} - m_Z \rvert > 15, 15, 0\,\text{GeV}$ (ee,$\mu\mu$,$e\mu$)
$E_{T,\text{Rel}}^{\text{miss}} > 45, 45, 25\,\text{GeV}$(ee,$\mu\mu$,$e\mu$)
Jet Veto 25 GeV
$p_{Tll'} > 30\,\text{GeV}$

Table 4.1: ATLAS cut flow for 7 TeV analysis[102]

4.3.1 Reweighting Results

We perform the reweighting as described above using a central scale $Q = m_W$ as well as varying the resummation scale Q up and down by a factor of 2 while keeping μ_R and μ_F fixed. We define the percentage difference caused by reweighting as

$$\text{percentage difference} = \frac{(\text{events}_{\text{res}} - \text{events}_{\text{MC}}) \cdot 100}{\text{events}_{\text{MC}}} \tag{4.2}$$

where

- events_{MC} is events predicted by the MC before reweighting
- events_{res} is events after reweighting the MC events.

with a positive percentage difference implying an increase in the theoretical prediction on σ_{Fid}. It is important to notice that reweighting is done with respect to $p_{T_{WW}}$ just after the shower but before detector simulation. To demonstrate the effects of other scale variations on σ_{Fid} we also varied μ_R and μ_F as well as the non-perturbative factor discussed in Section 4.2 and report the percentage differences compared to Powheg +Pythia8 (8 TeV) as an example in Table 4.2.

Scale Choice	% difference	% difference with $g_{\text{NP}} = 1$
Combined	$6.5^{+5.0}_{-3.0}$	$6.4^{+5.0}_{-3.0}$
Central scales, $Q = m_W$, $\mu_R = \mu_F = 2m_W$	6.51	6.38
$Q = 2\times$central	4.96	4.82
$Q = 0.5\times$central	10.75	10.64
$\mu_R = \mu_F = 0.5\times$central	3.89	3.76
$\mu_R = \mu_F = 2\times$central	9.16	9.04

Table 4.2: Percentage differences of reweighted theory predictions compared to Powheg+Pythia8 at 8 TeV for σ_{Fid} and various choices of scale. The 2nd column does not include the Gaussian smearing factor for non-perturbative effects, while the 3rd column includes a non-zero non-perturbative factor $g_{NP} = 1$ typical for quark dominated initial states.

We find that as observed in Section 4.2, the Q variation leads to a larger percentage difference than the μ_F or μ_R scale variation. The non-perturbative factor g_{NP} shifts the peak of the underlying p_T distributions slightly, but in the end has a minimal effect on the cross section. We show the effects of reweighting on MC generators and parton showers in Tables 4.3, 4.4, 4.5 for 7,8 and 14 TeV respectively.

MC + Parton Shower	Corrections (%)
Powheg+Pythia8	$6.4^{+4.7}_{-2.8}$
Powheg+Herwig++	$3.8^{+4.5}_{-2.6}$
aMC@NLO+Herwig++	$3.3^{+5.0}_{-3.0}$

Table 4.3: Percentage differences for σ_{Fid} of reweighted theory predictions compared to MCs+Parton Showers at 7 TeV.

MC + Parton Shower	Corrections (%)
Powheg+Pythia8	$6.5^{+5.0}_{-3.0}$
Powheg+Herwig++	$3.8^{+4.3}_{-2.5}$
aMC@NLO+Herwig++	$3.1^{+5.0}_{-3.0}$
MADGRAPH LO+Pythia6	$-9.6^{+4.4}_{-2.7}$

Table 4.4: Percentage differences for σ_{Fid} of reweighted theory predictions compared to MCs+Parton Showers at 8 TeV.

MC + Parton Shower	Corrections (%)
Powheg+Pythia8	$7.0^{+6.4}_{-5.1}$
Powheg+Herwig++	$4.4^{+5.9}_{-4.7}$
aMC@NLO+Herwig++	$4.2^{+6.5}_{-5.2}$

Table 4.5: Percentage differences for σ_{Fid} of reweighted theory predictions compared to MCs+Parton Showers at 14 TeV.

To demonstrate the effects on differential distributions, we use the ATLAS cutflows and show the predictions of p_T resummation for the 7 TeV ATLAS study[102] compared to the original MC@NLO+Herwig++ results used by ATLAS. In Figure 4.7, we plot the four distributions shown in [102]. As can be seen in Figure 4.7, p_T reweighting can improve the differential distributions somewhat, but is not capable of explaining the full discrepancy using a central choice of scales.

To demonstrate the effects at 8 TeV we show the distribution most affected, $p_T(ll+E_T^{\text{miss}})$, in Figure 4.8 using the same cutflows and different generators. This distribution is directly

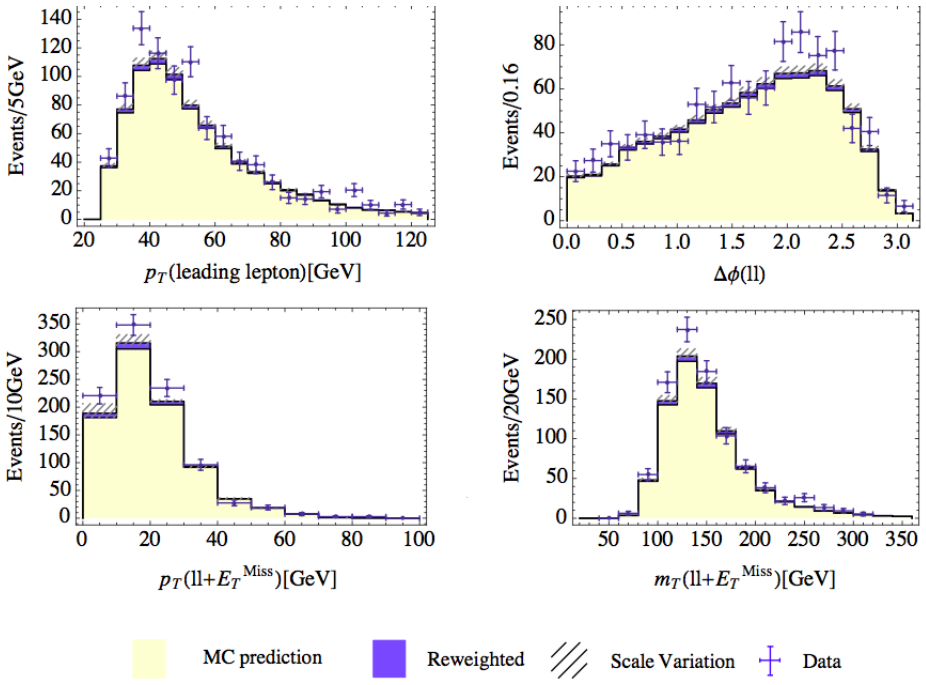

Figure 4.7: aMC@NLO+Herwig++ observables histogrammed for W^+W^- transverse momentum distribution for 7 TeV collisions and including the reweighting correction.

correlated with the p_T of the diboson system predicted by resummation, and shows the variation compared to MC generators + parton showers. The largest discrepancy compared to MC comes from the use of Powheg+Pythia8, while both Powheg and aMC@NLO are in much better agreement when Herwig++ is used as the parton shower. However, this does not mean the effects of the parton shower are the sole cause of the discrepancy. In the fractional difference shown in Figure 4.8, we see the roughly the same shape dependence for both Powheg curves, but the overall magnitude is reduced for Powheg+Herwig++ compared to Powheg+Pythia8.

4.3.2 Jet Veto

As we have shown thus far, even though the inclusive total cross-sections are the same by design, there are appreciable corrections to the fiducial cross section after reweighting. This means that some of the cuts are well correlated with the p_{TWW} variable and seem to preferentially select the low p_{TWW} region where the resummation curve dominates all the MCs except Madgraph LO. The percentage change due to reweighting at each cut level was analyzed, and as an example the effects of reweighting at each state in the cut flow is shown for Powheg-Pythia8 at 8 TeV in Table 4.6. The jet veto stage is the largest contributor to the reweighting excess. To explicitly check this, the order of the jet veto and p_{Tll} cuts was reversed and the biggest jump was found to still be the jet veto cut. In Figure 4.9 we show the correlation between 0 jet events and > 0 jet events as a function of $p_T(ll + E_T^{\text{miss}})$ before the jet veto is applied. Note that in Figure 4.9, 0-jet events primarily comprise the low p_T of

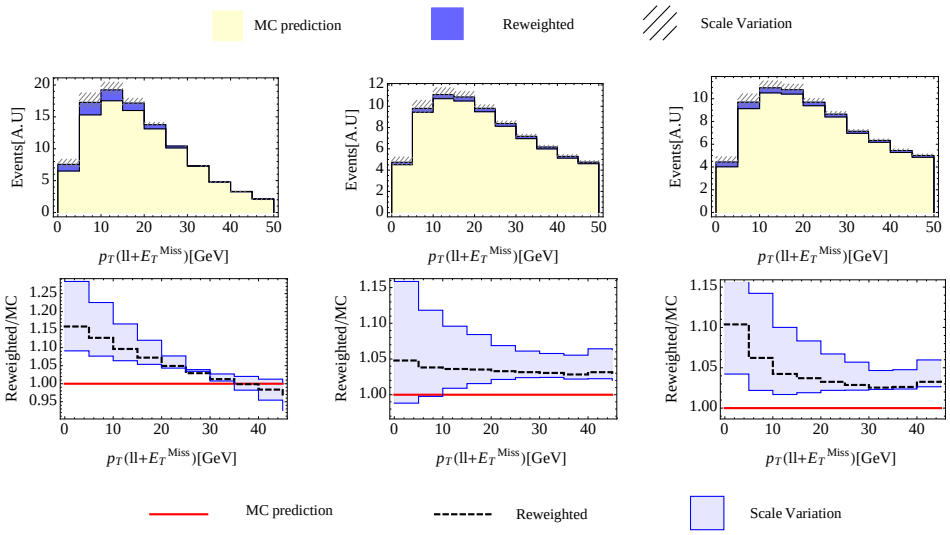

Figure 4.8: The top row shows the reweighting correction for left (Powheg+Pythia8), center (aMC@NLO+Herwig++), right (Powheg+Herwig++) to the $p_T(ll + E_T^{\text{miss}})$ observable. The bottom row has bin-by-bin percentage difference in events between reweighting and the MC + PS.

the diboson system, and as such a jet veto implies that the fiducial cross section will become more sensitive to the shape given by p_T resummation. This clearly points to the jet veto cut as the major contributor to changes in the fiducial cross section from p_T resummation reweighting. If the jet veto were increased this result would still hold, however the 0-jet cross section would then be integrated over a larger range of p_T for the diboson, and thus there would be a smaller effect on the fiducial cross section. In particular, if the jet veto were dropped entirely this would be equivalent to integrating over the entire diboson p_T which by definition would not change the measured cross section.

Cut	**% difference**
Exactly two oppositely-sign leptons, $p_T > 20\,\text{GeV}, p_{T\text{leading}} > 25\,\text{GeV}$	1.36
$m_{ll'}$ cuts	1.16
$E_{T,\text{Rel}}^{\text{miss}}$	0.83
Jet Veto	9.72
$p_{Tll'}$	10.75

Table 4.6: Percentage increase due to Resummation-Reweighting ($Q = \frac{m_W}{2}$, $\mu_R = \mu_F = 2m_W$) compared to Powheg-Pythia8 at 8 TeV for each cut stage in the cutflows listed from Table 4.1. All percentages are cumulative showing that the jet-veto is the largest effect.

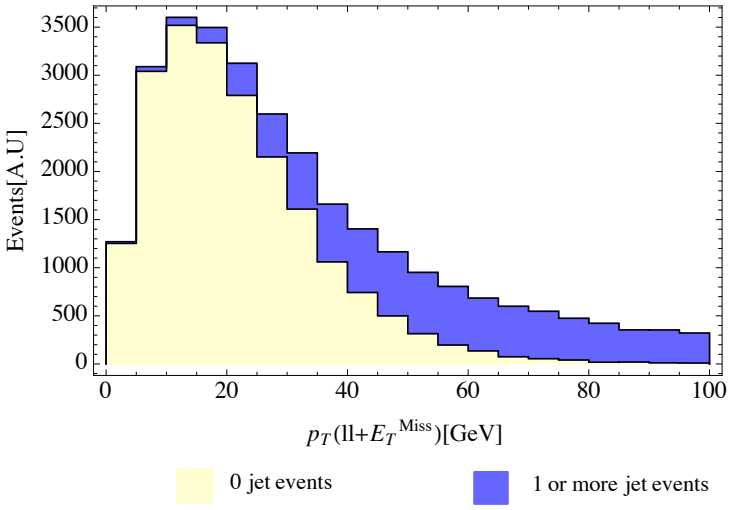

Figure 4.9: Events before the Jet veto. The number of 0 jet events or events with 1 or more jets is shown as a function of the p_T of the diboson system. Since 1 or more jet - events are vetoed, this sculpts the p_T -shape.

4.4 Discussion

As we have shown, p_T resummation, when used to reweight NLO MC distributions, can have a sizable effect on the predicted fiducial and the inferred total cross sections. The general trend in comparison with Monte Carlo generators and parton showers is to increase the predicted cross section $\sim 3-7\%$ and thus decrease the observed discrepancy compared to ATLAS and CMS. However, this statement depends on the choice of resummation scale for the W^+W^- final state. At large p_T the fixed order calculation is valid , while at small to moderate p_T the resummation calculation is most reliable. This scale in practice is analogous to the Matrix Element-Parton Shower matching scale when implementing matching procedures between the two. As discussed in Section 4.2, the resummation scale should be similar to the other hard scales in the problem. We have chosen the simple scale choice, analogous to what is done for Drell-Yan[196, 182], of $\sim M/2$, which for the W^+W^- process we have approximated as the fixed scale $Q = M_W$. We have demonstrated that the variation in this scale actually can imply quite a deal of uncertainty. For instance at 8 TeV using Powheg+Pythia8, by varying Q by a factor of 2 each we introduce a variation on the measured cross section $\sim \pm 3\%$.

The CMS Collaboration recently adopted our results for the W^+W^- transverse momentum distribution to reweight the parton shower simulation events used in the experimental analysis [106]. The total cross section deduced from the analysis is 60.1 ± 0.9 (stat.) ± 3.2 (exp.) ± 3.1 (th.) ± 1.6 (lum.) pb. The exact NNLO total cross section was recently computed [115]to be $59.84^{+2.2\%}_{-1.9\%}$ which is about 5% higher than the NLO result, and in good agreement with the experimental result cited above. The combination of the NNLO corrections and the p_T resummation study in this chapter significantly reduced tension between theory and experiment. It is worth mentioning that a recent jet veto resummation study [197] at the NLO+NNLL accuracy, with resummation of π^2 terms related to timelike Sudakov form fac-

tors, had a comparable effect on the cross section.

An important lesson reemphasized by this study is the need for further theoretical investigations of jet vetos. As we have shown p_T resummation causes a sizable effect on the total cross section because of the interplay between the jet veto and the p_T distribution. Clearly the correlation demonstrated in Section 4.3, especially Fig. 4.9, shows that the effects calculated in jet-veto resummation should be well approximated by the method employed here, similar to what was shown in [164]. Of course there are additional logs related to the jet veto which cannot be systematically improved upon within p_T resummation. It would be interesting to further investigate the interplay of these two types of resummation and the reweighting of parton showered events for more processes.

Another interesting question associated with the jet veto is how the LHC experiments can test the effects of the jet veto on the W^+W^- cross section measurement. The jet veto is a "necessary evil" in the context of measuring W^+W^- without being overwhelmed by $t\bar{t}$. However, if the jet veto were weakened significantly, then the effects demonstrated in this note would disappear both in the context of p_T resummation and jet veto resummation. If the jet-veto were varied, this could be compared to definitive predictions for the cross section as a function of the jet veto. To alleviate the issue of the $t\bar{t}$ background, we suggest that the experiments separately implement a b-jet veto and a light jet veto, of which the light jet veto should be varied to study its effects.

In this chapter we have not explicitly demonstrated the effects of resummation on the contribution of $gg \to W^+W^-$ to the W^+W^- cross section. This contribution is a small fraction of the total cross section, and as such even though resummation effects will modify its shape as well, it will not change our conclusions. However, it is important to note that the peak of the p_T spectrum for $gg \to W^+W^-$ should be at approximately 10 GeV high than for quark initiated W^+W^-, as is generic for gg initiated processes, in e.g. [181]). For a sufficiently precise measurement of the p_T distribution it would be necessary to have the shape of this distribution correct as well. A more interesting direction is the implications of understanding the correct shape of the SM W^+W^- production background for the extraction of the Higgs signal in the $H \to W^+W^-$ decay channel. Given that the W^+W^- background is extracted via data-driven methods, it is important that the shape of the distributions of the W^+W^- background is known when extrapolating from control to signal regions. While the p_T of the W^+W^- system is not a variable used for the signal/control regions, as shown in our results for the reweighted kinematic distributions at 7 TeV there is a non negligible effect on the shape of relevant variables. Future investigation is needed to study the effects of resummation on the measured signal strength of the Higgs in the W^+W^- channel.

There are other avenues for future study, for instance investigating simultaneous resummation of W^+W^- p_T with other observables, such as rapidity, to determine if any of the other cuts put on the fiducial phase space could alter the extraction of a total cross section. Regardless of future direction, this work has clearly demonstrated the importance of p_T resummation when combined with fiducial phase space cuts. Similar to how the p_T distribution of the Higgs signal is reweighted to make precise predictions for Higgs physics, it is important to use the correct p_T shape when considering processes where the W^+W^- signal is either being measured or is an important background.

Chapter 5

Higgs-gluon EFT at dimension 7

This chapter is based on the publication [55].

5.1 Introduction

The recently discovered Higgs boson has all the generic characteristics of a Standard Model Higgs boson and measurements of the production and decay rates agree to the $10-20\%$ level with Standard Model (SM) predictions [198, 199, 200, 201]. The largest contribution to Standard Model Higgs boson production comes from gluon fusion through a top quark loop and testing the nature of this Higgs-gluon interaction probes the mechanism of electroweak symmetry breaking at high scales. In models with new physics, the gluon fusion rate can be altered by new particles interacting in the loop which contribute to an effective dimension-5 operator [202, 203, 204],

$$\mathcal{L}_5 = \hat{C}_1 G^{\mu\nu,A} G^A_{\mu\nu} h \,. \tag{5.1}$$

For example, in composite models $\hat{C}_1$ is changed from its SM value by small contributions of $\mathcal{O}(v^2/f^2)$, where f is a TeV scale parameter corresponding to the composite scale [205, 206, 207]. Similarly, supersymmetric models alter the ggh coupling due to the contributions of new particles such as squarks in the loops and also by changes in the Higgs-fermion couplings [208, 209, 200, 201]. The measurement of gluon fusion by itself can only measure a combination of $\hat{C}_1$ and the top quark Yukawa coupling, but cannot distinguish between the two potential new physics effects [210, 211, 212].

The high p_T production of the Higgs boson through the process $pp \to h$+jet is particularly sensitive to new contributions to the Higgs gluon effective coupling [210, 213, 211, 214]. This is straightforward to demonstrate in top partner models where at low energy there is a cancellation between the SM top and the top partner contributions to the gluon fusion rate for Higgs production, making it extremely difficult to observe top partner physics in this channel [212, 215, 216]. The effects of top partners become apparent, however, when kinematic distributions for 2-particle final states, such as double Higgs production [217, 218], or Higgs plus jet production [219], are analyzed. The measurement of Higgs plus jet production offers the possibility to untangle new physics effects contributing to the Higgs-gluon effective interactions from beyond the SM (BSM) contributions to the Higgs-fermion Yukawa couplings.

The strong Higgs-gluon-light quark interactions can be parameterized through $SU(3)$ invariant effective dimension-5 and dimension-7 operators coupling the Higgs boson to partons, which are well known [220, 221]. The dimension -5 operator of Eq. 5.1 has been used to calculate SM Higgs production through NNLO [222, 223, 224], along with the Higgs p_T distribution [225, 226, 227]. At NLO, the total rate can be compared with an analytic result with exact top and bottom quark mass dependence [203], while at NNLO, the effective theory calculation has been compared numerically with the calculation in the full theory [228, 229]. In both instances, the dimension-5 operator gives an extremely accurate approximation to the total rate for Higgs production through gluon fusion. The Lagrangian of Eq. (5.1) corresponds to the $m_t \to \infty$ limit of the SM, and $\hat{C}_1$ has been determined to $\mathcal{O}(\alpha_s^3)$ in the SM [230, 231, 232, 233].

In this chapter, we examine the effect of both the dimension-5 and dimension -7 gluon-Higgs operators on Higgs plus jet production at NLO QCD . We present analytic formulas which can be applied to arbitrary models of new physics. The effects of these operators on the Higgs p_T distribution has been studied numerically at lowest order in Ref. [221]. The Standard Model rate for Higgs +jet is known analytically at order $\mathcal{O}(\alpha_s^3)$ [234, 235], while the NLO rate is known analytically in the $m_t \to \infty$ limit, [236, 237, 227] which corresponds to the contribution from $\hat{C}_1$. Finite top mass effects in SM NLO corrections have been obtained as a numerical expansion in $1/m_t^2$ [238, 239, 240, 241], and agree with the $m_t \to \infty$ limit only for small Higgs transverse momentum, $p_T \leq 150$ GeV. The electroweak contributions are studied in [242]. The NNLO total cross section in the $m_t \to \infty$ limit for the gg channel is known [243] while the corresponding results for other partonic channels have been obtained in the threshold approximation [244, 245, 246]. For Higgs production in association with more than one jet, exact m_t dependence is known for two and three jets at leading order [247, 248, 249], while $m_t \to \infty$ results are available at NLO for two and three jets [250, 251].

In Section 5.2, we discuss the effective Higgs-gluon effective Lagrangian, and in Section 5.3 we review the lowest order results for Higgs plus jet production in the dimension-7 effective field theory (EFT). The renormalization of the dimension-7 effective Lagrangian coefficients is discussed in Section 5.4. Sections 5.5 and 5.6 contain analytic results for Higgs plus jet production at NLO using the dimension-5 and dimension-7 contributions to the EFT, with the real emission corrections presented as heclity amplitudes using the conventions in [252, 253]. The behavior of tree amplitudes in the massless Higgs limit, $m_h^2 < (p_T^2, s, -t, -u)$, is discussed. As a by-product of our calculation, we obtain the $\mathcal{O}(1/m_t^2)$ contributions to the SM rate, modulo the non-logarithmic terms in the NLO matching coefficients in Eqs. (5.11),(5.13) which will be derived in a forthcoming work. Numerical results for the LHC are presented in Section 5.7, and some conclusions given in Section 5.8.

5.2 Effective operators

5.2.1 Higgs-gluon-quark interaction

The calculations of Higgs production from gluon fusion are greatly simplified by using an effective Lagrangian where heavy particles, such as the top quark, are integrated out. The $SU(3)$ invariant effective Lagrangian which parameterizes the CP-conserving Higgs -gluon-

light quark strong interactions is,

$$\mathcal{L}_{\rm eff} = \hat{C}_1 O_1 + \frac{1}{\Lambda^2}\Sigma_{i=2,3,4,5}\hat{C}_i O_i + \mathcal{O}\left(\frac{1}{\Lambda^4}\right). \tag{5.2}$$

For SM Higgs production, $\Lambda = m_t$ is either the $\overline{\rm MS}$ running mass or the pole mass, depending on whether the $\overline{\rm MS}$ scheme or the pole scheme is used to calculate the matching coefficients, $\hat{C}_i$. For BSM scenarios, Λ is the scale at which BSM physics generates contributions to $\hat{C}_i$.

At dimension-5, the unique operator is

$$O_1 = G^A_{\mu\nu} G^{\mu\nu,A} h\,, \tag{5.3}$$

where $G^A_{\mu\nu}$ is the gluon field strength tensor. We consider only models with a single scalar Higgs boson, although our results can be trivially generalized to the case with multiple scalars. In the SM, the coefficient, $\hat{C}_1$, is, to $\mathcal{O}\left(\alpha_s^2\right)$ [204, 203],

$$\hat{C}_1(\mu_R)^{\rm SM,\,\overline{\rm MS}} = \frac{\alpha_s(\mu_R)}{12\pi v}\left\{1 + \frac{\alpha_s(\mu_R)}{4\pi}\left[5C_A - 3C_F\right]\right\}, \tag{5.4}$$

where $C_A = N_c = 3$, $C_F = \frac{N_c^2-1}{2N_c} = \frac{4}{3}$, $v = 246$ GeV, and μ_R is an arbitrary renormalization scale of $\mathcal{O}(m_h)$.

The dimension-7 operators, needed for gluon fusion production of Higgs, are [220, 221, 254],

$$\begin{aligned}
O_2 &= D_\sigma G^A_{\mu\nu} D^\sigma G^{A,\mu\nu}\, h && (5.5)\\
O_3 &= f_{ABC} G^{A,\mu}_\nu G^{B,\nu}_\sigma G^{C,\sigma}_\mu\, h && (5.6)\\
O_4 &= g_s^2\, \Sigma_{i,j=1}^{n_{lf}} \overline{\psi}_i \gamma_\mu T^A \psi_i\, \overline{\psi}_j \gamma^\mu T^A \psi_j\, h && (5.7)\\
O_5 &= g_s \Sigma_{i=1}^{n_{lf}} G^A_{\mu\nu} D^\mu\, \overline{\psi}_i \gamma^\nu T^A \psi_i\, h\,, && (5.8)
\end{aligned}$$

where our convention for the covariant derivative is $D^\sigma = \partial^\sigma - i g_s T^A G^{A,\sigma}$, $Tr(T^A T^B) = \frac{1}{2}\delta_{AB}$ and $n_{lf} = 5$ is the number of light fermions. The operators O_1, O_2 and O_3 are the only ones that are needed in pure QCD ($n_{lf} = 0$). In the presence of light quarks, we also need O_4 and O_5 which are related by the equations of motion (eom) to gluon-Higgs operators[1]

$$\begin{aligned}
O_4\,|_{eom} &\rightarrow D^\sigma G^A_{\sigma\nu} D_\rho G^{A,\rho\nu} h \equiv O_4'\\
O_5\,|_{eom} &\rightarrow G^A_{\sigma\nu} D^\nu D^\rho G^{A,\sigma}_\rho h \equiv O_5'\,.
\end{aligned} \tag{5.9}$$

Since O_4 involves 4 light fermions, the operator contributes to Higgs plus jet production only starting at NLO, in the real-emission processes involving two incoming fermions and two outgoing fermions.

The SM coefficient, $\hat{C}_2^{\rm SM}$, can be found from the leading $\frac{1}{m_t^2}$ terms in the NLO calculation of $gg \rightarrow h$ [255], in the $\overline{MS}$ scheme,

$$\hat{C}_2^{\rm SM,\,\overline{\rm MS}}(\mu_R) = -\frac{7\alpha_s(\mu_R)}{720\pi v}\left\{1 + \frac{\alpha_s(\mu_R)}{\pi}\left[\frac{29}{84}C_A + \frac{19}{21}C_F + \frac{3}{2}C_F \ln\left(\frac{m_t^2}{\mu_R^2}\right)\right]\right\}. \tag{5.10}$$

[1] In our study, only gluons directly interact with the Higgs via a top quark loop or some BSM heavy particle, while quark-Higgs coupling is mediated by gluons.

For the remaining SM coefficients, we present only the LO contributions along with the $\alpha_s \ln(m_t^2/\mu_R^2)$ contributions which can be deduced from the renormalization group equations in Section 5.4. [2]

$$\hat{C}_3^{\mathrm{SM},\,\overline{\mathrm{MS}}}(\mu_R) = \frac{g_s(\mu_R)\alpha_s(\mu_R)}{60\pi v}\left\{1 + \frac{\alpha_s(\mu_R)}{\pi}\left[\hat{C}_3^{(1)} + \left(\frac{1}{4}C_A + \frac{3}{2}C_F\right)\ln\left(\frac{m_t^2}{\mu_R^2}\right)\right]\right\} \tag{5.11}$$

$$\hat{C}_4^{\mathrm{SM},\,\overline{\mathrm{MS}}}(\mu_R) = \frac{\alpha_s(\mu_R)}{360\pi v} + \mathcal{O}\left(\alpha_s^2(\mu_R)\right) \tag{5.12}$$

$$\hat{C}_5^{\mathrm{SM},\,\overline{\mathrm{MS}}}(\mu_R) = \frac{\alpha_s(\mu_R)}{20\pi v}\left\{1 + \frac{\alpha_s(\mu_R)}{\pi}\left[\hat{C}_5^{(1)} + \left(-\frac{121}{216}C_A + \frac{59}{54}C_F\right)\ln\left(\frac{m_t^2}{\mu_R^2}\right)\right]\right\}. \tag{5.13}$$

Because the O_4 contribution starts at NLO for Higgs plus jet production, we have only presented the LO value for $\hat{C}_4$. Since the above matching coefficients are presented in the $\overline{\mathrm{MS}}$ scheme, the top mass m_t in Eq. (5.11)-(5.13), as well as in Eq. (5.2), should be taken as the $\overline{\mathrm{MS}}$ running top mass evaluated at the renormalization scale μ_R.

To use the μ_R-independent constant parameter $1/(m_t^{\mathrm{pole}})^2$ as the EFT power expansion parameter in Eq. (5.2), in line with the usual language for EFTs, we substitute into Eq. (5.2) the relation [257],

$$m_t^{\overline{\mathrm{MS}}}(\mu_R) = m_t^{\mathrm{pole}}\left\{1 - \frac{C_F\alpha_s(\mu_R)}{\pi}\left[1 - \frac{3}{4}\ln\left(\frac{m_t^2}{\mu_R^2}\right)\right] + \mathcal{O}(\alpha_s^2)\right\}, \tag{5.14}$$

which gives,

$$\hat{C}_1^{\mathrm{SM,pole}}(\mu_R) = \hat{C}_1^{\mathrm{SM},\overline{\mathrm{MS}}}(\mu_R), \tag{5.15}$$

$$\hat{C}_2^{\mathrm{SM,pole}}(\mu_R) = -\frac{7\alpha_s(\mu_R)}{720\pi v}\left\{1 + \frac{\alpha_s(\mu_R)}{\pi}\left[\frac{29}{84}C_A + \frac{61}{21}C_F\right]\right\}, \tag{5.16}$$

$$\hat{C}_3^{\mathrm{SM,pole}}(\mu_R) = \frac{g_s(\mu_R)\alpha_s(\mu_R)}{60\pi v}\left\{1 + \frac{\alpha_s(\mu_R)}{\pi}\left[\hat{C}_3^{(1)} + 2C_F + \frac{1}{4}C_A\ln\left(\frac{m_t^2}{\mu_R^2}\right)\right]\right\} \tag{5.17}$$

$$\hat{C}_4^{\mathrm{SM,pole}}(\mu_R) = \frac{\alpha_s(\mu_R)}{360\pi v} + \mathcal{O}\left(\alpha_s^2(\mu_R)\right) \tag{5.18}$$

$$\hat{C}_5^{\mathrm{SM,pole}}(\mu_R) = \frac{\alpha_s(\mu_R)}{20\pi v}\left\{1 + \frac{\alpha_s(\mu_R)}{\pi}\left[\hat{C}_5^{(1)} + 2C_F + \left(-\frac{121}{216}C_A - \frac{11}{27}C_F\right)\ln\left(\frac{m_t^2}{\mu_R^2}\right)\right]\right\}. \tag{5.19}$$

The Feynman rules corresponding to Eq. 5.2 can be found in a straightforward manner. For most of our calculations, we will use the pure-gluon operators O_4' and O_5' in Eq. (5.9) instead of O_4 and O_5 in Eqs. (5.7) and (5.8), so that the Feynman diagrams for Higgs plus

[2] The SM matching coefficients are given in Ref. [220], but we found discrepancies at NLO. The $C_A \ln(m_t^2/\mu_R^2)$ terms in our results are one half the values in [220]. Our results are consistent with the O_3 anomalous dimension found in [256] and the O_5 anomalous dimension we calculate in Section 5.4. The non-logarithmic terms in the NLO matching coefficients, $\hat{C}_3^{(1)}$ and $\hat{C}_5^{(1)}$, will be discussed in a forthcoming work. In this study we will set $\hat{C}_3^{(1)}$ and $\hat{C}_5^{(1)}$ to zero. Also, in Ref. [220] the matching is done off-shell, so the operator equivalence relation of Eq. (5.9) cannot be used. As a result, in our convention the NLO value for $\hat{C}_5$ is different. The LO coefficients are in agreement with Refs. [220, 221], once the differing sign conventions are accounted for.

jet production from the dimension-7 operators are identical to those from the dimension-5 operator O_1. The O_3 vertices involve at least 3 gluons, while 2 gluons suffice for the other operators.

There are 2 possible tensor structures [258] for the off-shell $g^{A,\mu}(p_1)g^{B,\nu}(p_2)h(p_3)$ vertex,

$$\begin{aligned} T_1^{\mu\nu} &\equiv g^{\mu\nu}p_1\cdot p_2 - p_1^\nu p_2^\mu \\ T_2^{\mu\nu} &\equiv p_1^\mu p_2^\nu - p_2^\mu p_2^\nu \frac{p_1^2}{p_1\cdot p_2} - p_1^\mu p_1^\nu \frac{p_2^2}{p_1\cdot p_2} + p_1^\nu p_2^\mu \frac{p_1^2 p_2^2}{(p_1\cdot p_2)^2}\,. \end{aligned} \tag{5.20}$$

The Lagrangian of Eq. 5.2 has the off-shell Feynman rule,

$$\begin{aligned} ggh: &\qquad -i\delta_{AB}\left[T_1^{\mu\nu}X_1(p_1,p_2) + T_2^{\mu\nu}X_2(p_1,p_2)\right] \\ X_1(p_1,p_2) &= \left\{4\hat{C}_1 - \frac{\hat{C}_2}{\Lambda^2}4p_1\cdot p_2 - \frac{\hat{C}_4}{\Lambda^2}\left(\frac{2p_1^2p_2^2}{p_1\cdot p_2}\right) + \frac{\hat{C}_5}{\Lambda^2}(p_1^2+p_2^2)\right\} \\ X_2(p_1,p_2) &= -2p_1\cdot p_2\frac{\hat{C}_4}{\Lambda^2}\,. \end{aligned} \tag{5.21}$$

The Feynman rules for the off-shell $g(p_1^{A,\mu})g(p_2^{\nu,B})g(p_3^{\rho,C})h(p_4)$ vertex (with all momenta outgoing) are,[3]

$$\begin{aligned} O_1: &\quad -4\hat{C}_1 g_s f_{ABC}\left\{-g^{\mu\nu}(p_1-p_2)^\rho + g^{\mu\rho}(p_1-p_3)^\nu + g^{\nu\rho}(p_3-p_2)^\mu\right\} \\ O_2: &\quad -4\frac{\hat{C}_2}{\Lambda^2}g_s f_{ABC}\left\{\mathcal{A}^{\mu\nu\rho}(p_1,p_2,p_3) + \mathcal{A}^{\nu\rho\mu}(p_2,p_3,p_1) + \mathcal{A}^{\rho\mu\nu}(p_3,p_1,p_2)\right\} \\ O_3: &\quad -6\frac{\hat{C}_3}{\Lambda^2}f_{ABC}Y_0^{\mu\nu\rho}(p_1,p_2,p_3) \\ O_5: &\quad -g_s\frac{\hat{C}_5}{\Lambda^2}\left\{f_{ABC}\left[-g^{\mu\nu}p_1^\rho\left(p_1^2+p_2^2+p_3^2-2p_1\cdot p_2-4p_2\cdot p_3\right)\right.\right. \\ &\quad \left.\left. +2p_1^\nu p_2^\rho p_3^\mu + p_1^\nu p_1^\rho p_3^\mu - p_2^\mu p_2^\rho p_3^\nu\right] + 5 \text{ permutations}\right\}, \end{aligned} \tag{5.22}$$

where

$$\begin{aligned} Y_0^{\mu\nu\rho}(p_1,p_2,p_3) &= \left(p_1^\nu g^{\rho\mu} - p_1^\rho g^{\mu\nu}\right)p_2\cdot p_3 + \left(p_2^\rho g^{\mu\nu} - p_2^\mu g^{\nu\rho}\right)p_1\cdot p_3 \\ &\quad + \left(p_3^\mu g^{\nu\rho} - p_3^\nu g^{\rho\mu}\right)p_1\cdot p_2 + p_2^\mu p_3^\nu p_1^\rho - p_3^\mu p_1^\nu p_2^\rho \\ \mathcal{A}^{\mu\nu\rho}(p_1,p_2,p_3) &= (p_1-p_2)^\rho T_1^{\mu\nu}(p_1,p_2) + p_1\cdot p_2\left[X_0^{\mu\nu\rho}(p_1) - X_0^{\nu\mu\rho}(p_2)\right] \\ X_0^{\mu\nu\rho}(p) &= g^{\mu\nu}p^\rho - g^{\mu\rho}p^\nu\,. \end{aligned} \tag{5.23}$$

.

[3]We omit the $\hat{C}_4$ $gggh$ vertex because this vertex does not contribute to Higgs +jet at NLO.

5.2.2 Alternative operator basis

In the previous section, we used the basis of Eqs. (5.5)-(5.8) to describe the dimension-7 operators. Here we define another dimension- 7 operator,

$$O_6 = -D^\rho D_\rho \left(G^A_{\mu\nu} G^{\mu\nu,A}\right) h = m_h^2 O_1, \tag{5.24}$$

where the last equal sign is only valid for on-shell Higgs production, which will be assumed for the rest of this section. Using the Jacobi identities, without using the equations of motion, we have the operator identity

$$O_6 = m_h^2 O_1 = -2O_2 + 4g_s O_3 + 4O_5. \tag{5.25}$$

Therefore, we can choose $O_6 = m_h^2 O_1$, O_3, O_4, and O_5 as a complete basis for the dimension-7 Higgs-gluon-light quark operators. We can rewrite Eq. (5.2) as

$$\mathcal{L}_{\text{eff}} = C_1 O_1 + \frac{1}{\Lambda^2}\left(C_3 O_3 + C_4 O_4 + C_5 O_5\right), \tag{5.26}$$

where the re-defined matching coefficients are related to those in Eqs. (5.4),(5.10)-(5.13), (5.15)-(5.19) by,

$$C_1 \equiv \hat{C}_1 - \frac{m_h^2}{2\Lambda^2}\hat{C}_2, \tag{5.27}$$

$$C_3 \equiv 2g_s \hat{C}_2 + \hat{C}_3, \tag{5.28}$$

$$C_4 \equiv \hat{C}_4, \tag{5.29}$$

$$C_5 \equiv 2\hat{C}_2 + \hat{C}_5\,. \tag{5.30}$$

We will use the basis of Eq. 5.26 for our phenomenological studies.

In particular, for SM Higgs production, using $m_t = m_t^{\text{pole}}$ in Eq. (5.26), we have

$$C_1^{\text{SM, pole}}(\mu_R) = \frac{\alpha_s(\mu_R)}{12\pi v}\left\{1 + \frac{\alpha_s(\mu_R)}{4\pi}\left[5C_A - 3C_F\right]\right\} + \\ + \frac{7\alpha_s(\mu_R) m_h^2}{1440\pi v\, m_t^2}\left\{1 + \frac{\alpha_s(\mu_R)}{\pi}\left[\frac{29}{84}C_A + \frac{19}{21}C_F + \frac{3}{2}C_F \ln\left(\frac{m_t^2}{\mu_R^2}\right)\right]\right\}, \tag{5.31}$$

$$C_3^{\text{SM, pole}}(\mu_R) = -\frac{g_s(\mu_R)\alpha_s(\mu_R)}{360\pi v}\left\{1 + \frac{\alpha_s(\mu_R)}{\pi}\left[\frac{29}{12}C_A + \frac{25}{3}C_F - 6\hat{C}_3^{(1)} - \frac{3}{2}C_A \ln\left(\frac{m_t^2}{\mu_R^2}\right)\right]\right\}, \tag{5.32}$$

$$C_4^{\text{SM, pole}}(\mu_R) = \frac{\alpha_s(\mu_R)}{360\pi v} + \mathcal{O}\left(\alpha_s^2(\mu_R)\right), \tag{5.33}$$

$$C_5^{\text{SM, pole}}(\mu_R) = \frac{11\alpha_s(\mu_R)}{360\pi v}\left\{1 + \frac{\alpha_s(\mu_R)}{\pi}\left[-\frac{29}{132}C_A + \frac{47}{33}C_F + \frac{18}{11}\hat{C}_5^{(1)} \right.\right. \\ \left.\left. + \left(-\frac{11}{12}C_A - \frac{2}{3}C_F\right)\ln\left(\frac{m_t^2}{\mu_R^2}\right)\right]\right\}. \tag{5.34}$$

For the $gg \to h$ amplitude, O_3, O_4, and O_5 give vanishing contributions at both tree level and the one-loop level, due either to the lack of quark propagator lines or to the lack

of a scale in the diagrams. This leaves us with the operator O_1 multiplied by the matching coefficient C_1 in Eq. (5.31) which is defined to include $\mathcal{O}\left(m_h^2/m_t^2\right)$ terms. This is essentially equivalent to calculating in the $m_t \to \infty$ limit and applying a rescaling factor. For Higgs plus jet production, though, the other operators will come into play and impact differential distributions.

5.2.3 Gluon self-interaction

At $\mathcal{O}(1/m_t^2)$ in the SM, we also need the dimension-6 gluon self-interaction Lagrangian which arises from integrating out the top quark and performing Collins-Wilczek-Zee zero-momentum subtraction to obtain decoupling of the heavy top [259],

$$\begin{aligned}\mathcal{L}_{\text{eff}}^{\text{SM,self}} &= \frac{1}{m_t^2}\left(\frac{g_s\alpha_s}{720\pi}f_{ABC}G_\nu^{A,\mu}G_\sigma^{B,\nu}G_\mu^{C,\sigma} - \frac{\alpha_s}{60\pi}D^\sigma G_{\sigma\nu}^A D_\rho G^{A,\rho\nu}\right), \\ &\equiv \frac{1}{m_t^2}\left(\frac{g_s\alpha_s}{720\pi}\tilde{O}_3 - \frac{\alpha_s}{60\pi}\tilde{O}_4\right), \end{aligned} \tag{5.35}$$

where the $\tilde{O}_i$'s are defined to be identical to the O_i's in Eq. (5.5)-(5.8), but with the Higgs field, h, stripped from the operator definition. Here the matching coefficients are only given at leading order because this is sufficient for NLO Higgs plus jet production.

There is a neat way to obtain the above effective Lagrangian. Using the Higgs low-energy theorems [202], it is easy to see that at leading order matching, the $\mathcal{O}(1/m_t^2)$ terms in Eq. (5.2) and (5.35) can be packaged together in the expression,

$$\mathcal{L}^{\text{SM}}\big|_{\mathcal{O}(1/m_t^2)} = -\frac{v}{2m_t^2\left(1+\frac{h}{v}\right)^2}\sum_{i=2,3,4,5}\hat{C}_i\tilde{O}_i\,. \tag{5.36}$$

Starting from Eq. (5.36), we use the operator relation of Eq. (5.25) (which can be applied to $\tilde{O}_i$'s instead of O_i's by setting $m_h = 0$) to eliminate $\tilde{O}_2$, and further use the relation $\tilde{O}_4 = \tilde{O}_5$, valid only at zero-momentum, to eliminate $\tilde{O}_5$, to reach Eq. (5.35) which only involves $\tilde{O}_3$ and $\tilde{O}_4$. In a BSM model, the coefficients of the gluon self-interactions depend on the nature of the heavy physics which is integrated out.

5.3 Lowest Order

The lowest order amplitudes for Higgs + jet production including all fermion mass dependence (bottom and top) are given in Refs. [235, 234]. The effective Lagrangian can be used to obtain the contributions from the top quark in the infinite mass approximation, along with the SM results including terms of $\mathcal{O}(1/m_t^2)$. At the lowest order in α_s, O_3 is the only dimension-7 operator which contributes to the $gg \to gh$ channel, while O_5 is the only dimension-7 operator which contributes to channels with initial state quarks.

5.3.1 Lowest order EFT $q\bar{q}gh$ amplitude

There are 2 independent gauge invariant tensor structures for the process $0 \to q\bar{q}hg$, (where we consider all momenta outgoing) [260, 261]

$$\mathcal{T}_1^\mu \equiv i\left(p_{\bar{q}}^\mu \overline{u}(p_q)\not{p}_g v(p_{\bar{q}}) - \frac{S_{g\bar{q}}}{2}\overline{u}(p_q)\gamma^\mu v(p_{\bar{q}})\right) \tag{5.37}$$

$$\mathcal{T}_2^\mu = i\left(p_{q}^\mu \overline{u}(p_q)\not{p}_g v(p_{\bar{q}}) - \frac{S_{gq}}{2}\overline{u}(p_q)\gamma^\mu v(p_{\bar{q}})\right), \tag{5.38}$$

where $S_{q\bar{q}} = (p_q + p_{\bar{q}})^2$, $S_{gq} = (p_g + p_q)^2$, and $S_{g\bar{q}} = (p_g + p_{\bar{q}})^2$. The $0 \to q\bar{q}gh$ amplitude is given in general by,

$$M_{qqgh}^{\alpha,\mu} = \Sigma_{i=1,3-5} T^A \left(B_1^{\alpha,i}\mathcal{T}_1^\mu + B_2^{\alpha,i}\mathcal{T}_2^\mu\right), \tag{5.39}$$

where $\alpha = 0, 1$ denotes the order of the calculation (LO, NLO), and the sum is over the contributions of the different operators. The tree level amplitude to $\mathcal{O}(1/\Lambda^2)$ is,

$$M_{qqgh}^{0,\mu} = T^A(\mathcal{T}_1^\mu + \mathcal{T}_2^\mu)\left[C_1\left(\frac{-4g_s}{S_{q\bar{q}}}\right) + \frac{C_5}{\Lambda^2}(-g_s)\right], \tag{5.40}$$

i.e., the non-vanishing coefficients in Eq. 5.39 are,

$$\begin{aligned} B_1^{0,1} &= B_2^{0,1} = C_1\left(\frac{-4g_s}{S_{q\bar{q}}}\right) \\ B_1^{0,5} &= B_2^{0,5} = \frac{C_5}{\Lambda^2}(-g_s)\,. \end{aligned} \tag{5.41}$$

5.3.2 Lowest Order EFT $gggh$ amplitude

There are 4 independent gauge invariant tensor structures for the $0 \to g(p_1^\mu)g(p_2^\nu)g(p_3^\rho)h$ amplitude [234, 261, 260], assuming all momenta outgoing and $S_{ij} = 2p_i \cdot p_j$,

$$\begin{aligned} \mathcal{Y}_0^{\mu\nu\rho}(p_1,p_2,p_3) &= (p_1^\nu g^{\rho\mu} - p_1^\rho g^{\mu\nu})\frac{S_{23}}{2} + (p_2^\rho g^{\mu\nu} - p_2^\mu g^{\nu\rho})\frac{S_{31}}{2} \\ &\quad + (p_3^\mu g^{\nu\rho} - p_3^\nu g^{\rho\mu})\frac{S_{12}}{2} + p_2^\mu p_3^\nu p_1^\rho - p_3^\mu p_1^\nu p_2^\rho \end{aligned} \tag{5.42}$$

$$\mathcal{Y}_1^{\mu\nu\rho}(p_1,p_2,p_3) = p_2^\mu p_1^\nu p_1^\rho - p_2^\mu p_1^\nu p_2^\rho \frac{S_{31}}{S_{23}} - \frac{1}{2}p_1^\rho g^{\mu\nu} S_{12} + \frac{1}{2}p_2^\rho g^{\mu\nu}\frac{S_{31}S_{12}}{S_{23}} \tag{5.43}$$

$$\begin{aligned} \mathcal{Y}_2^{\mu\nu\rho}(p_1,p_2,p_3) &= \mathcal{Y}_1^{\rho\mu\nu}(p_3,p_1,p_2) \\ \mathcal{Y}_3^{\mu\nu\rho}(p_1,p_2,p_3) &= \mathcal{Y}_1^{\nu\rho,\mu}(p_2,p_3,p_1)\,. \end{aligned}$$

An arbitrary $gggh$ amplitude is written as

$$\begin{aligned} \mathcal{M}_{gggh}^{\alpha,\mu\nu\rho} = f_{ABC}\Sigma_i \Big\{ & A_0^{\alpha,i}(p_1,p_2,p_3)\mathcal{Y}_0^{\mu\nu\rho}(p_1,p_2,p_3) + \\ & \sum_{m=1,2,3} A_m^{\alpha,i}(p_1,p_2,p_3)\mathcal{Y}_m^{\mu\nu\rho}(p_1,p_2,p_3)\Big\}, \end{aligned} \tag{5.44}$$

where again $\alpha = 0{,}1$ for the lowest order (LO) and next-to-leading order (NLO) contributions, i is the contribution corresponding to O_i, and

$$\begin{aligned} A_2^{\alpha,i}(p_1,p_2,p_3) &= A_1^{\alpha,i}(p_3,p_1,p_2) \\ A_3^{\alpha,i}(p_1,p_2,p_3) &= A_1^{\alpha,i}(p_2,p_3,p_1)\,. \end{aligned} \tag{5.45}$$

The LO contributions from O_1 and O_3 are

$$\begin{aligned} A_0^{0,1}(p_1,p_2,p_3) &= 8g_sC_1\left(\frac{1}{S_{12}}+\frac{1}{S_{23}}+\frac{1}{S_{31}}\right) \\ A_1^{0,1}(p_1,p_2,p_3) &= \frac{8g_sC_1}{S_{31}} \\ A_0^{0,3}(p_1,p_2,p_3) &= \frac{C_3}{\Lambda^2}6 \\ A_1^{0,3}(p_1,p_2,p_3) &= 0\,, \end{aligned} \tag{5.46}$$

while the O_5 contribution vanishes.

5.3.3 Squared amplitudes

To obtain squared amplitudes, we need the interference between the Lorentz / Dirac tensor structures, and the interference between the color structures. For the $qg \to qh$ squared amplitude, the interferences between the tensor structures are (omitting the ones which can be obtained from $q \leftrightarrow \bar{q}$ crossing symmetry between $\mathcal{T}_1$ and $\mathcal{T}_2$).

$$\sum_A \mathrm{tr}\left(\mathrm{T^A T^A}\right) = \frac{N_c^2-1}{2}, \tag{5.47}$$

$$-\sum_{\text{spins}} \mathcal{T}_1^{\mu}\,\mathcal{T}_{1,\mu}^{\dagger} = -(1-\epsilon)S_{q\bar{q}}S_{gq}^2, \tag{5.48}$$

$$-\sum_{\text{spins}} \mathcal{T}_1^{\mu}\mathcal{T}_{2,\,u}^{\dagger} = -\epsilon S_{q\bar{q}}S_{gq}S_{g\bar{q}}\,, \tag{5.49}$$

where external fermion spinors are implicit and we work in $N = 4-2\epsilon$ dimensions. The $q\bar{q} \to gh$ squared amplitude can be obtained from crossing the $qg \to qh$ squared amplitude. For the $gg \to gh$ squared amplitude, the interferences between the tensor structures are,

$$\sum_{ABC} f^{ABC}f^{ABC} = N_c(N_c^2-1), \tag{5.50}$$

$$-\sum_{\text{spins}} \mathcal{Y}_0^{\mu\nu\rho}\mathcal{Y}_{0,\mu\nu\rho}^{\dagger} = \left(1-\frac{3}{2}\epsilon\right)S_{12}S_{23}S_{31}, \tag{5.51}$$

$$-\sum_{\text{spins}} \mathcal{Y}_1^{\mu\nu\rho}\mathcal{Y}_{0,\mu\nu\rho}^{\dagger} = \frac{1}{2}(1-\epsilon)S_{12}^2S_{31}, \tag{5.52}$$

$$-\sum_{\text{spins}} \mathcal{Y}_1^{\mu\nu\rho}\mathcal{Y}_{1,\mu\nu\rho}^{\dagger} = \frac{1}{2}(1-\epsilon)\frac{S_{12}^3S_{31}}{S_{23}}, \tag{5.53}$$

$$-\sum_{\text{spins}} \mathcal{Y}_1^{\mu\nu\rho}\mathcal{Y}_{2,\mu\nu\rho}^{\dagger} = \frac{1}{4}S_{12}S_{31}^2\,, \tag{5.54}$$

where we have omitted terms which can be obtained from cyclic permutations.

Here we present squared amplitudes, summed (but not averaged) over initial and final state spins, with $\mathcal{O}(\epsilon)$ terms omitted. For $gg \to gh$, the squared amplitude from the O_1 operator is [234]

$$\sum_{\text{spins}} \left| M^{(0)}_{gg\to gh,\, O_1} \right|^2 = 384\, C_1^2\, \frac{m_h^8 + s^4 + t^4 + u^4}{stu}, \tag{5.55}$$

while the O_1-O_3 interference contribution is

$$\sum_{\text{spins}} M^{(0)}_{gg\to gh,\, O_1} \cdot M^{(0),\dagger}_{gg\to gh,\, O_3} + \text{c.c.} = 1152\, C_1 C_3\, \frac{m_h^4}{\Lambda^2}. \tag{5.56}$$

Interestingly, the O_1 contribution, Eq. (5.55), corresponding to a rescaled $m_t \to \infty$ approximation, grows as p_T^2 for high p_T Higgs production, while the O_1-O_3 interference contribution, Eq. (5.56), remains constant and therefore diminishes in relative importance, in contrary to the generic behavior of higher-dimensional operators. This results in suppressed top mass dependence in Higgs differential distributions in the gluon channel, and will be explained by the helicity structure of the amplitudes in the soft Higgs limit, i.e. the limit $m_h^2 < (p_T^2, s, -t, -u)$, discussed in Section 5.6.

For $qg \to qh$, the squared amplitude from the O_1 operator is [234]

$$\sum_{\text{spins}} \left| M^{(0)}_{qg\to qh,\, O_1} \right|^2 = 64\, C_1^2\, \frac{s^2 + u^2}{-t}, \tag{5.57}$$

while the O_1-O_5 interference contribution is

$$\sum_{\text{spins}} M^{(0)}_{qg\to qh,\, O_1} \cdot M^{(0),\dagger}_{qg\to qh,\, O_5} + \text{c.c.} = -32\, C_1 C_5\, \frac{s^2 + u^2}{\Lambda^2} \tag{5.58}$$

The results, crossed into the $q\bar{q} \to gh$ channel, are

$$\sum_{\text{spins}} \left| M^{(0)}_{qg\to qh,\, O_1} \right|^2 = 64\, C_1^2\, \frac{t^2 + u^2}{s}, \tag{5.59}$$

$$\sum_{\text{spins}} M^{(0)}_{qg\to qh,\, O_1} \cdot M^{(0),\dagger}_{qg\to qh,\, O_5} + \text{c.c.} = 32\, C_1 C_5\, \frac{t^2 + u^2}{\Lambda^2}. \tag{5.60}$$

5.4 Renormalization of dimension-7 operators

In this section, we use the basis $O_6 \cong m_h^2 O_1$, O_3, O_4, and O_5, described in Section II.B, for the dimension-7 operators. In addition to the renormalization of the QCD coupling constant and self energies in both QCD vertices and the O_i operators, we need to renormalize the C_i matching coefficients. The renormalization of C_1 is well known [262, 263, 264], and is identical to the renormalization of α_s at one-loop. The renormalization of C_3 and C_5 are different, and they will be presented as the sum of α_s renormalization and an extra piece.

The renormalization of C_3 was found in Ref. [256]. The renormalization of C_5 is a new result.

The unrenormalized effective Lagrangian coupling the Standard Model Higgs boson to gluons is,

$$\mathcal{L}_{\text{eff}} = C_1^{\text{bare}} O_1^{\text{bare}} + \Sigma_{i=3-5} \frac{C_i^{\text{bare}}}{\Lambda^2} O_i^{\text{bare}} \,, \tag{5.61}$$

where Λ is a constant power expansion parameter that should not depend on μ_R, so in this section we will allow Λ to be equal to the top quark pole mass in the case of SM Higgs production, but not the running $\overline{\text{MS}}$ mass. The operators O_i^{bare} are defined in the same way as O_i, but with all the fields and couplings replaced by bare quantities. O_4 is needed only at LO, so we will not discuss its one-loop renormalization. In our operator basis, the one-loop mixing matrix is diagonal, so we can write

$$C_i^{\text{bare}} = C_i + \delta C_i = Z_i C_i = (1 + \delta Z_i) C_i \,. \tag{5.62}$$

The renormalization constants Z_i are found using two different methods. The first one is to calculate one-loop ggh, $gggh$, and $q\bar{q}gh$ amplitudes on-shell, and impose transverse gluon polarizations to eliminate spurious mixing into gauge non-invariant operators. The second method is to calculate these one-loop amplitudes off-shell to reduce the number of diagrams needed, and use the background field method [265] to preserve gauge-invariance. In either method, the divergences are matched to the tensor structures arising from the various operators in order to extract the renormalization of the C_i. The renormalization counterterms are given by,

$$\delta Z_1 = \delta Z_{\alpha_s}, \tag{5.63}$$

$$\delta Z_3 = \frac{3}{2} \delta Z_{\alpha_s} + \frac{\alpha_s}{2\pi\epsilon} (4\pi)^\epsilon \, r_\Gamma \, 3 C_A, \tag{5.64}$$

$$\delta Z_5 = \delta Z_{\alpha_s} + \frac{\alpha_s}{2\pi\epsilon} (4\pi)^\epsilon \, r_\Gamma \left(\frac{11}{6} C_A + \frac{4}{3} C_F \right), \tag{5.65}$$

where r_Γ is given in Eq. (5.76), and

$$\delta Z_{\alpha_s} = \frac{\alpha_s}{\pi\epsilon} (4\pi)^\epsilon r_\Gamma \, b_0, \tag{5.66}$$

$$b_0 = \left(\frac{11}{12} C_A - \frac{1}{6} n_{lf} \right) , \tag{5.67}$$

is the one-loop renormalization factor for the strong coupling α_s in an $n_{lf} = 5$ flavor theory, proportional to the beta function.

By using

$$\frac{d \ln C_i}{d \ln \mu_R} = - \frac{d \ln Z_i}{d \ln \mu_R}, \tag{5.68}$$

we have the following renormalization group running equations,

$$\frac{d}{d\ln\mu_R}\ln\left(\frac{C_1}{g_s^2}\right) = \mathcal{O}(\alpha_s^2(\mu_R)), \tag{5.69}$$

$$\frac{d}{d\ln\mu_R}\ln\left(\frac{C_3}{g_s^2}\right) = \frac{\alpha_s(\mu_R)}{\pi}\,3C_A, \tag{5.70}$$

$$\frac{d}{d\ln\mu_R}\ln\left(\frac{C_5}{g_s^2}\right) = \frac{\alpha_s(\mu_R)}{\pi}\left(\frac{11}{6}C_A + \frac{4}{3}C_F\right). \tag{5.71}$$

The leading-logarithmic solutions to the renormalization group running of Eqs. (5.69)-(5.71) are

$$C_1(\mu_R)/g_s^2(\mu_R) = C_1(\mu_0)/g_s^2(\mu_0), \tag{5.72}$$

$$C_3(\mu_R)/g_s^3(\mu_R) = \left(\frac{\alpha_s(\mu_R)}{\alpha_s(\mu_0)}\right)^{-\frac{3C_A}{2b_0}} \cdot C_3(\mu_0)/g_s^3(\mu_0), \tag{5.73}$$

$$C_5(\mu_R)/g_s^2(\mu_R) = \left(\frac{\alpha_s(\mu_R)}{\alpha_s(\mu_0)}\right)^{-\frac{1}{2b_0}\left(\frac{11}{6}C_A+\frac{4}{3}C_F\right)} \cdot C_5(\mu_0)/g_s^2(\mu_0), \tag{5.74}$$

which in principle allows us to perform matching at the new physics scale Λ, and use renormalization group running to obtain C_i at $\mu_R \sim m_h$, hence resumming large logarithms of $\Lambda/\ m_h$.

5.5 NLO virtual corrections

5.5.1 Methods

All our NLO calculations are done using O_1, O_3, and O_5 as a basis of operators, as described in Section 5.2.2, with $O(m_h^2/m_t^2)$ terms included in the C_1 matching coefficient to absorb the dimension-7 operator O_6 operator in Eq. (5.24). When calculating NLO virtual amplitudes for O_5, we exploit equations of motions to use the O_5' operator in Eq. (5.9) instead. The NLO virtual diagrams needed for O_1 are also the only ones needed for O_3 and O_5'. Our amplitude-level results, given as coefficients for the tensor structures in Eqs. (5.37),(5.38),(5.42)-(5.44), are valid in both the conventional dimensional regularization (CDR) scheme in D dimensions and the t'Hooft-Veltman scheme which has loop momenta in D dimensions and external leg momenta in 4 dimensions.

The one-loop virtual calculation is done as follows. The software FeynRules [266] is used to generate Feynman rules for each of the operators. FeynArts [267] is used to generate Feynman diagrams and produce expressions for the amplitudes by using the Feynman rules, with loop integrations unperformed. FormCalc [268] is used to perform the numerator algebra and loop integration, producing results in terms of one-loop tensor integrals (up to rank-5 box integrals). The tensor integrals are subsequently reduced to scalar integrals in D dimensions using FeynCalc [269], and combined with the explicit results for the scalar integrals [270] to produce our final analytic results for the one-loop virtual amplitudes. Alternatively, the tensor integrals can be evaluated numerically using LoopTools [268] without analytic

reduction to scalar integrals, and we have checked that the results agree numerically with our analytic formulas for the one-loop amplitudes.[4]

5.5.2 One loop $q\bar{q}gh$ amplitudes

The one-loop virtual amplitudes for $0 \to q\bar{q}gh$ and the real emission amplitudes for $0 \to q\bar{q}ggh$ are responsible for both $qg \to h + j + X$ and the $q\bar{q} \to h + j + X$, where $j = g, q$ or $\bar{q}$.

We list only the B_2 contributions for the virtual one-loop diagrams from each of the operators since B_1 can be obtained by exchanging S_{gq} and $S_{g\bar{q}}$. The virtual contribution proportional to C_4 vanishes.

The non-vanishing one-loop coefficients, $B_2^{1,i}$ defined in Eq. 5.39, from the operators O_i are,

$$\begin{aligned} B_2^{1,1} &= \frac{\alpha_s(\mu_R)}{4\pi} r_\Gamma \left(\frac{4\pi\mu_R^2}{m_h^2}\right)^\epsilon B_2^{0,1}\left[N_c V_1 + \frac{1}{N_c}V_2 + n_{lf}V_3\right] \\ B_2^{1,3} &= \frac{C_3}{m_t^2}\frac{\alpha_s(\mu_R)}{8\pi}N_c \\ B_2^{1,5} &= \frac{\alpha_s(\mu_R)}{4\pi} r_\Gamma \left(\frac{4\pi\mu^2}{m_h^2}\right)^\epsilon B_2^{0,5}\left[N_c W_1 + \frac{1}{N_c}W_2 + n_{lf}W_3\right], \end{aligned} \tag{5.75}$$

where

$$r_\Gamma \equiv \frac{\Gamma^2(1-\epsilon)\Gamma(1+\epsilon)}{\Gamma(1-2\epsilon)}\,. \tag{5.76}$$

Analytic expressions for the functions V_i and W_i are given in Appendix C.1.

The $0 \to q\bar{q}gh$ amplitude involves one ordinary QCD coupling and one EFT coupling, both of which need counterterms. The sum of the counterterms is

$$M_{q\bar{q}gh}^{CT,\mu} = \frac{3}{2}\delta Z_{\alpha_s} M_{q\bar{q}gh}^{0,\mu} - g_s(\mu_R)T^A(\mathcal{T}_1+\mathcal{T}_2)^\mu \frac{\alpha_s(\mu_R)}{2\pi\epsilon}\left(\frac{11}{6}C_A + \frac{4}{3}C_F\right)\frac{C_5}{\Lambda^2}, \tag{5.77}$$

where the renormalization for the O_1 amplitude is simply proportional to 3 times the g_s renormalization [271, 227], whereas there is an extra term for the O_5 amplitude because the C_5 renormalization in Eq. (5.65) is not proportional to δZ_{α_s}.

The renormalized one-loop virtual amplitude is then,

$$M_{q\bar{q}gh}^{V+CT,\mu} = \left(\frac{4\pi\mu_R^2}{m_h^2}\right)^\epsilon r_\Gamma \left\{\left[\frac{A_{V2}}{\epsilon^2} + \frac{A_{V1}}{\epsilon}\right]M_{q\bar{q}gh}^\mu + \left(\mathcal{T}_1+\mathcal{T}_2\right)^\mu T^A A_{V0}\right\}, \tag{5.78}$$

where

$$\begin{aligned} A_{V2} &= \frac{\alpha_s(\mu_R)}{4\pi}\left(-2N_c + \frac{1}{N_c}\right) \\ A_{V1} &= \frac{\alpha_s(\mu_R)}{4\pi}\left\{N_c \ln\left(\frac{-S_{gq}}{m_h^2}\right) + N_c \ln\left(\frac{-S_{g\bar{q}}}{m_h^2}\right) - \frac{1}{N_c}\ln\left(\frac{-S_{q\bar{q}}}{m_h^2}\right)\right]. \end{aligned} \tag{5.79}$$

[4]We find that there are some special tensor integrals which cannot be reduced to scalar integrals correctly by FeynCalc in D dimensions, but this problem has not affected our calculation, since the end results are in agreement with LoopTools.

Note that the finite contribution to the virtual amplitude, A_{V0}, is not proportional to the LO result. A_{V0} is just the contribution from the finite terms in defined in Eq. 5.75 and Appendix C.1.

5.5.3 One loop $gggh$ amplitudes

The 1-loop virtual results are,

$$\begin{aligned}
A_0^{1,1} &= \frac{\alpha_s(\mu_R)}{4\pi} r_\Gamma \left(\frac{4\pi\mu^2}{m_h^2}\right)^\epsilon N_c\, U_1\, A_0^{0,1} \\
A_1^{1,1} &= \frac{\alpha_s(\mu_R)}{4\pi} r_\Gamma \left(\frac{4\pi\mu^2}{m_h^2}\right)^\epsilon \left[N_c\, U_1\, A_1^{0,1} + \frac{8 g_s\,(N_c - N_{lf})\, S_{23}}{3 S_{12}^2}\right] \\
A_0^{1,3} &= \frac{\alpha_s(\mu_R)}{4\pi} r_\Gamma \left(\frac{4\pi\mu^2}{m_h^2}\right)^\epsilon N_c\, U_3\, A_0^{0,3} \\
A_1^{1,3} &= 0 \\
A_0^{1,5} &= 0 \\
A_1^{1,5} &= -\frac{g_s \alpha_s(\mu_R)}{4\pi} \cdot \frac{2 S_{23}}{3 S_{12}}\,.
\end{aligned} \tag{5.80}$$

Analytic expressions for the functions U_1 and U_3 are given in Appendix C.1.

The counterterm from renormalization for the QCD coupling and the EFT matching coefficients is,

$$\begin{aligned}
\mathcal{M}_{gggh}^{CT,\mu\nu\rho} &= f_{ABC}\Bigg\{\left(\delta Z_1 + \frac{1}{2}\delta Z_{\alpha_s}\right)\Bigg(A_0^{0,1}(p_1,p_2,p_3)\mathcal{Y}_0^{\mu\nu\rho}(p_1,p_2,p_3) + \\
&\quad \sum_{m=1,2,3} A_m^{0,1}(p_1,p_2,p_3)\mathcal{Y}_m^{\mu\nu\rho}(p_1,p_2,p_3)\Bigg) \\
&\quad + \delta Z_3\Bigg(A_0^{0,3}(p_1,p_2,p_3)\mathcal{Y}_0^{\mu\nu\rho}(p_1,p_2,p_3) + \\
&\quad \sum_{m=1,2,3} A_m^{0,3}(p_1,p_2,p_3)\mathcal{Y}_m^{\mu\nu\rho}(p_1,p_2,p_3)\Bigg)\Bigg\}
\end{aligned} \tag{5.81}$$

5.5.4 Soft and Collinear real contributions

Soft - qg channel

We combine the virtual and real amplitudes using the 2 cut-off phase space slicing method to regulate the soft and collinear singularities in D dimensions [272] for the $qg \to h + j + X$ and $gg \to h + j + X$ channels. The results for $q\bar{q} \to h + j + X$ can be obtained in a similar manner and are included in our numerical results.

To find the NLO cross section, we integrate the LO, NLO virtual, soft and collinear contributions over the 2-body final state phase space, and integrate the hard non-collinear

contribution over the 3-body final phase space. The total answer is finite and independent of δ_c and δ_s.

The soft contribution is defined as the contribution from real gluon emission, $qg \to qgh$, where the outgoing gluon has an energy less than a small cut-off [272],

$$E_g < \delta_s \frac{\sqrt{s}}{2}\,. \tag{5.82}$$

where δ_s is an arbitrary small number. For the qg initial state, $s = S_{g\bar{q}}$, $t = S_{q\bar{q}}$, and $u = S_{gq}$.

The soft contribution is found by integrating the eikonal approximation to the $qg \to qh + g_{\rm soft}$ amplitude-squared and integrating over the soft gluon phase space following exactly the procedure of Ref. [272]. The required integrals are found in Ref. [273]. The soft result is,

$$\mid M^{\rm soft}_{qg\to qh} \mid^2 = -\frac{\alpha_s(\mu_R)}{4\pi} r_\Gamma \left(\frac{4\pi\mu_R^2}{m_h^2}\right)^\epsilon \mid M^{(0)}_{qg\to qh} \mid^2 \left\{ A_{2S}\frac{1}{\epsilon^2} + A_{1S}\frac{1}{\epsilon} + A_{0S} \right\}, \tag{5.83}$$

where,

$$\begin{aligned}
A_{S2} &= -\frac{34}{3}, \\
A_{S1} &= \frac{68}{3}\ln\delta_s - 6\ln\left(\frac{m_h^2\beta_H}{-u}\right) - 6\ln\left(\frac{m_h^2}{s}\right) + \frac{2}{3}\ln\left(\frac{m_h^2\beta_H}{-t}\right) \\
&\quad - \ln\left(\frac{s}{m_h^2}\right) A_{S2} \\
A_{S0} &= -\frac{68}{3}\ln^2\delta_s + 12\left(\ln\frac{m_h^2\beta_h}{-u}\right)\ln\delta_s + 12\ln\left(\frac{m_h^2}{s}\right)\ln\delta_s - \frac{4}{3}\ln\left(\frac{m_h^2\beta_h}{-t}\right)\ln\delta_s \\
&\quad - 3\ln^2\left(\frac{m_h^2}{s}\right) - 3\ln^2\left(\frac{m_h^2\beta_h}{-u}\right) + \frac{1}{3}\ln^2\left(\frac{m_h^2\beta_h}{-t}\right) \\
&\quad + \left[\ln^2\left(\frac{s}{m_h^2}\right) - \frac{\pi^2}{3}\right]\frac{A_{S2}}{2}\,,
\end{aligned} \tag{5.84}$$

and $\beta_H = 1 - m_h^2/s$.

The hard contribution to the real gluon emission process $qg \to qgh$ contains collinear singularities,

$$\sigma_{\rm real} = \sigma_{\rm hard/collinear} + \sigma_{\rm hard/non-collinear}\,. \tag{5.85}$$

The hard/non-collinear terms arising from $i \to j$ parton splitting are finite and satisfy,

$$\begin{aligned}
E_g &> \delta_s\frac{\sqrt{s}}{2} \\
\mid S_{ij} \mid &> \delta_c s\,,
\end{aligned} \tag{5.86}$$

where δ_c is an arbitrary collinear cut-off and is typically $\ll \delta_s$. These terms can be integrated numerically using the amplitudes given in Appendix C.2.

Final State Collinear - qg channel

The hard collinear contribution to the partonic cross section from $q \to qg$ splitting in the final state is [272],

$$\begin{aligned}\hat{\sigma}^{HC,f}_{qg\to qgh} &= \hat{\sigma}^{LO}_{qg}\frac{\alpha_s(\mu_R)}{2\pi}r_\Gamma\left(\frac{4\pi\mu_R^2}{s}\right)^\epsilon\left\{\left(\frac{1}{\epsilon}-\ln\delta_c\right)C_F\left[2\ln\left(\frac{\delta_s}{\beta_H}\right)+\frac{3}{2}\right]\right.\\ &\left.-\frac{\pi^2}{3}-\ln^2\left(\frac{\delta_s}{\beta_H}\right)+\frac{7}{2}\right\}. \end{aligned} \tag{5.87}$$

Soft - gg channel

The contribution from soft gluon emission results from integrating the eikonal approximation to the $gg \to gh + g_{\rm soft}$ matrix-element squared over the soft gluon phase space and yields,

$$\mid M^{soft}_{gg\to gh}\mid^2 = \frac{\alpha_s(\mu_R)}{\pi}r_\Gamma\left(\frac{4\pi\mu_R^2}{m_h^2}\right)^\epsilon\left\{\frac{A_{g2}}{\epsilon^2}+\frac{A_{g1}}{\epsilon}+A_{g0}\right\}\mid M^{(0)}_{gg\to gh}\mid^2, \tag{5.88}$$

with

$$\begin{aligned} A_{g2} &= \frac{3}{2}N_c = \frac{9}{2},\\ A_{g1} &= \frac{N_c}{2}\left\{-6\log(\delta_s)+\ln\left(\frac{m_h^2}{S_{12}}\right)+\ln\left(\frac{m_h^2\beta_H}{-S_{13}}\right)+\ln\left(\frac{m_h^2\beta_H}{-S_{23}}\right)\right\}\\ &- \ln\left(\frac{S_{12}}{m_h^2}\right)A_{g2},\\ A_{g0} &= \frac{N_c}{4}\left\{12\ln^2(\delta_s)+\ln^2\left(\frac{m_h^2}{S_{12}}\right)+\ln^2\left(\frac{m_h^2\beta_H}{-S_{13}}\right)+\ln^2\left(\frac{m_h^2\beta_H}{-S_{23}}\right)\right.\\ &-4\ln\delta_s\left[\ln\left(\frac{m_h^2}{S_{12}}\right)+\ln\left(\frac{m_h^2\beta_H}{-S_{13}}\right)+\ln\left(\frac{m_h^2\beta_H}{-S_{23}}\right)\right]\\ &\left.+2Li_2\left(\frac{-S_{23}}{S_{12}\beta_H}\right)+2Li_2\left(\frac{-S_{13}}{S_{12}\beta_H}\right)\right\}\\ &+\left[\ln^2\left(\frac{S_{12}}{m_h^2}\right)-\frac{\pi^2}{3}\right]\frac{A_{g2}}{2}. \end{aligned} \tag{5.89}$$

Final State Collinear - gg channel

The hard collinear contributions from gluon splitting in the final state are [272] ,

$$\begin{aligned}\hat{\sigma}^{HC,f}_{gg\to ggh} &= \hat{\sigma}^{LO}_{gg\to gh}\frac{\alpha_s(\mu_R)}{2\pi}r_\Gamma\left(\frac{4\pi\mu_R^2}{s}\right)^\epsilon N_c\left\{\left(\frac{1}{\epsilon}-\ln\delta_c\right)\left[2\ln\left(\frac{\delta_s}{\beta_H}\right)+\frac{11}{6}\right]\right.\\ &\left.-\frac{\pi^2}{3}-\ln^2\left(\frac{\delta_s}{\beta_H}\right)+\frac{67}{18}\right\}, \end{aligned} \tag{5.90}$$

$$\hat{\sigma}^{HC,f}_{gg\to q\bar{q}h} = \hat{\sigma}^{LO}_{gg\to gh}\frac{\alpha_s(\mu_R)}{2\pi}r_\Gamma\left(\frac{4\pi\mu_R^2}{s}\right)^\epsilon n_{lf}\left\{\left(\frac{1}{\epsilon}-\ln\delta_c\right)\left(-\frac{1}{3}\right)-\frac{5}{9}\right\}, \tag{5.91}$$

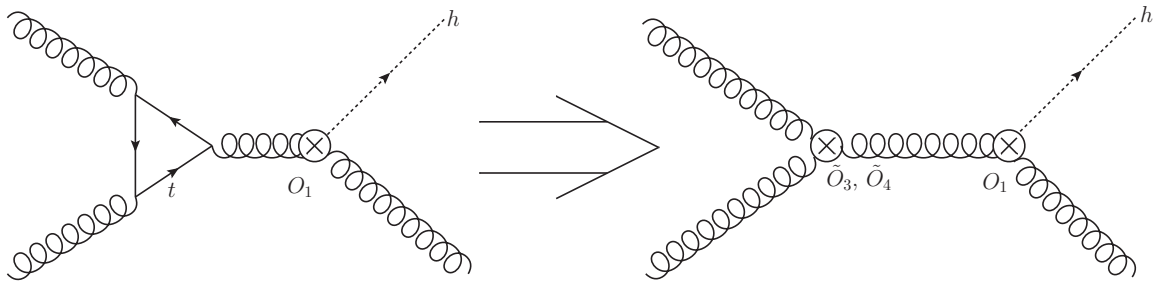

Figure 5.1: An example diagram showing the $\mathcal{O}(1/m_t^2)$ gluon self-interaction vertex from integrating out the top quark. The Higgs is produced through the O_1 operator in the $m_t \to \infty$ limit, but the overall power of this Feynman diagram is still of $\mathcal{O}(1/m_t^2)$ and should be considered on the same footing as diagrams producing the Higgs through $1/m_t^2$-suppressed dimension-7 operators.

Initial State Collinear - all channels

The contribution from collinear splitting in the initial state is combined with the renormalization of the PDFs to obtain the result given in [272], applicable to all channels,

$$d\hat{\sigma}^{\text{initial+PDF}}_{1+B\to 3+4+5} = d\hat{\sigma}^{\text{LO}}_{1+2'\to 3+4} \frac{\alpha_s(\mu_R)}{2\pi} \frac{\Gamma(1-\epsilon)}{\Gamma(1-2\epsilon)} \left[\left(\frac{4\pi\mu_R^2}{s} \right)^{\epsilon} \tilde{f}_{2'/B}(z,\mu_F) + \frac{1}{\epsilon} \left(\frac{4\pi\mu_R^2}{\mu_F^2} \right)^{\epsilon} A_1^{sc}(2\to 2'+5)\, f_{2/B}(z,\mu_F) \right], \tag{5.92}$$

where the initial state hadron B splits into a parton $2'$ which scatters with the initial state parton 1 and a parton 5 which goes into the final state. The redefined parton distribution function $\tilde{f}$ is given by [272]

$$\tilde{f}_{c/B}(x,\mu_f) = \sum_{c'} \int_x^{1-\delta_s\delta_{cc'}} \frac{dy}{y} f_{c'/B}(x/y,\mu_f) \tilde{P}_{cc'}(y), \tag{5.93}$$

$$\tilde{P}_{ij}(y) = P_{ij}(y) \ln\left(\delta_c \frac{1-y}{y} \frac{s}{\mu_f^2} \right) - P'_{ij}(y), \tag{5.94}$$

where P_{ij} and P'_{ij} are the $\mathcal{O}(\epsilon^0)$ and $\mathcal{O}(\epsilon)$ parts of the D-dimensional splitting function. The soft-collinear term A_1^{sc}, from the soft cutoff on initial state gluon emission, is given by [272]

$$A_1^{sc}(q\to qg) = C_F(2\ln\delta_s + 3/2), \tag{5.95}$$

$$A_1^{sc}(g\to gg) = 2C_A \ln\delta_s + (11C_A - 2n_{lf})/6, \tag{5.96}$$

$$A_1^{sc}(g\to q\bar{q}) = 0. \tag{5.97}$$

5.5.5 Higher-dimensional gluon self interaction contribution

In Fig. 5.1 we give an example Feynman diagram which involves Higgs coupling in the $m_t \to \infty$ limit but contains an $\mathcal{O}(1/m_t^2)$ gluon-self coupling EFT vertex. Other diagrams

of this type involve top quark loops as self-energy corrections of internal gluon propagators. These diagrams can be trivially calculated exactly, but we choose to use the EFT Lagrangian in Eq. (5.35) which gives the expansion to $\mathcal{O}(1/m_t^2)$. The contributions of these diagrams are of NLO order in α_s counting and $\mathcal{O}(1/m_t^2)$ in EFT power counting.

The contribution to the $0 \to q\bar{q}gh$ amplitude is

$$-8g_s^3\frac{1}{m_t^2}\tilde{C}_4(\mathcal{T}_1+\mathcal{T}_2)T^A = \frac{g_s^5}{30\pi^2 m_t^2}(T_1+T_2)T^A, \tag{5.98}$$

while the contribution to the $0 \to gggh$ amplitude is

$$24g_s^2 f^{ABC}\tilde{C}_3\left(\frac{S_{23}}{S_{12}}\mathcal{Y}_1^{\mu\nu\rho}+\frac{S_{12}}{S_{31}}\mathcal{Y}_2^{\mu\nu\rho}+\frac{S_{31}}{S_{23}}\mathcal{Y}_3^{\mu\nu\rho}\right) \tag{5.99}$$

$$=\frac{1}{120\pi^2}g_s^5 f^{ABC}\left(\frac{S_{23}}{S_{12}}\mathcal{Y}_1^{\mu\nu\rho}+\frac{S_{12}}{S_{31}}\mathcal{Y}_2^{\mu\nu\rho}+\frac{S_{31}}{S_{23}}\mathcal{Y}_3^{\mu\nu\rho}\right), \tag{5.100}$$

where the T_i and Y_i tensor structures are given in Eqs. (5.37),(5.38),(5.42)-(5.44).

5.6 NLO real emission helicity amplitudes

The helicity amplitudes for the production of Higgs plus two jets in the $m_t \to \infty$ limit, i.e. the O_1 contribution, was worked out long ago [274, 275]. We will calculate the amplitudes for dimension-7 operators. The all-gluon amplitudes will be given in this section, while amplitudes involving quarks will be given in Appendix C.2. The O_4 and O_5 operators, which involve quark bilinears, do not contribute to tree amplitudes without external quark legs, so only O_1 and O_3 will appear here.

Amplitudes for the G^3 operator without the Higgs, as a model for higher-dimensional modifications of the SM QCD sector, were studied in Refs. [276, 277]. These references found that the G^3 and G^2 amplitudes do not interfere with each other unless there are at least 3 jets in the final states. Our amplitudes for O_3 must reproduce these amplitudes in the limit of zero Higgs momentum, resulting in vanishing O_1-O_3 interference. The above references also proposed MHV formulas for n-gluon G^3 amplitudes involving 3 minus-helicities and $n-3$ plus helicities. We will verify that these MHV formulas hold for the O_3 $gggh$ and $ggggh$ amplitudes, i.e. G^3 amplitudes at non-zero (and non-lightlike) momentum insertion. This is expected, as Ref. [276, 277] already found MHV formulas for the G^2 operator to be valid at finite momentum, for Higgs production in the $m_t \to \infty$ limit.

For convenience, we will first give the lowest-order $gggh$ amplitude for Higgs plus jet production again, in helicity amplitude notation rather than tensor structure notation. The O_1 contributions, proportional to C_1, are

$$im^{O_1}\left(1^+,2^+,3^+,h\right) = \frac{2g_s m_h^4}{\langle 12\rangle\langle 23\rangle\langle 31\rangle}, \tag{5.101}$$

$$im^{O_1}\left(1^-,2^+,3^+,h\right) = -\frac{2g_s [23]^4}{[12][23][31]}. \tag{5.102}$$

The O_3 contributions, proportional to C_3, are

$$im^{O_3}\left(1^+,2^+,3^+,h\right) = \frac{-3[12][23][31]}{\Lambda^2}, \tag{5.103}$$

$$im^{O_3}\left(1^-,2^+,3^+,h\right) = 0, \tag{5.104}$$

in agreement with Ref. [278]. As p_T becomes large, in the Higgs rest frame, the initial and final state jets become much more energetic than the Higgs, so the $m_h \to 0$ limit of the above amplitudes, Eqs. (5.101)-(5.104), is particularly interesting. In this limit, the $--+$ amplitude is non-zero for O_1, but vanishes for O_3, so there is no interference between O_1 and O_3 for this helicity configuration. Meanwhile, the $+++$ amplitude is non-zero as $m_h \to 0$ for O_3, but vanishes as a quartic power in the $m_h \to 0$ limit for O_1, as seen in Eq. (5.101). Therefore, we expect the $gggh$ amplitude to not receive large enhancements from the dimension-7 O_3 operator at large p_T, which means the $m_t \to \infty$ approximation should work well for Higgs differential distribution even at moderately large p_T.

Now we will give the $ggggh$ tree amplitudes for O_3. They are:

$$\begin{aligned} im^{O_3}\left(1^+,2^+,3^+,4^+,h\right) = \frac{g_s}{\langle 12\rangle\langle 23\rangle\langle 34\rangle\langle 41\rangle}\Bigg(&3i\, S_{12}S_{23}S_{34} - \frac{3}{2}i\, S_{12}[31]\langle 1\not{p}_H 2]\langle 23\rangle - \\ &\frac{3}{2}iS_{12}[42]\langle 2\not{p}_H 1]\langle 14\rangle\Bigg) + 3 \text{ cyclic permutations of} \\ &(1\to 2\to 3\to 4\to 1), \end{aligned} \tag{5.105}$$

$$im^{O_3}\left(1^-,2^-,3^-,4^+,h\right) = \frac{3i\, g_s\langle 12\rangle^2\langle 23\rangle^2\langle 34\rangle^2}{\langle 12\rangle\langle 23\rangle\langle 34\rangle\langle 41\rangle}, \tag{5.106}$$

$$im^{O_3}\left(1^-,2^-,3^+,4^+,h\right) = 0. \tag{5.107}$$

We comment on the massless Higgs limit again. For the $--++$ helicity configuration, the O_3 contribution vanishes, while for the $++++$ helicity configuration, the O_1 contribution [274, 275] vanishes like a quartic power in the massless Higgs limit. However, for the $---+$ helicity configuration, neither the O_3 nor O_1 contribution vanishes in the limit $m_h \to 0$ (though the latter vanishes in the limit $p_h \to 0$), so the O_1-O_3 non-interference at high p_T is no longer true at NLO.

The amplitudes in Eqs. (5.103) and (5.106) are unchanged from the MHV formulas for G^3 at zero momentum in Ref. [276, 277]. Furthermore, Refs. [277, 279] explored the use of CSW rules [280] to build non-MHV amplitudes from MHV sub-amplitudes for the G^3 operator. We confirm that the $++++$ amplitude in Eq. (5.105) agrees with the CSW construction with G^3 inserted at non-zero momentum. The vanishing of the $--++$ amplitude in Eq. (5.107) is explained by the fact that this helicity configuration cannot be built from MHV sub-amplitudes [277, 279].

We have checked that the squared matrix elements from the helicity amplitudes, presented in this section and Appendix C.2, agree with the automated tree-level calculation by MadGraph5_aMC@NLO [190], using a UFO model file [281] for the dimension-7 operators which we created using FeynRules [266].

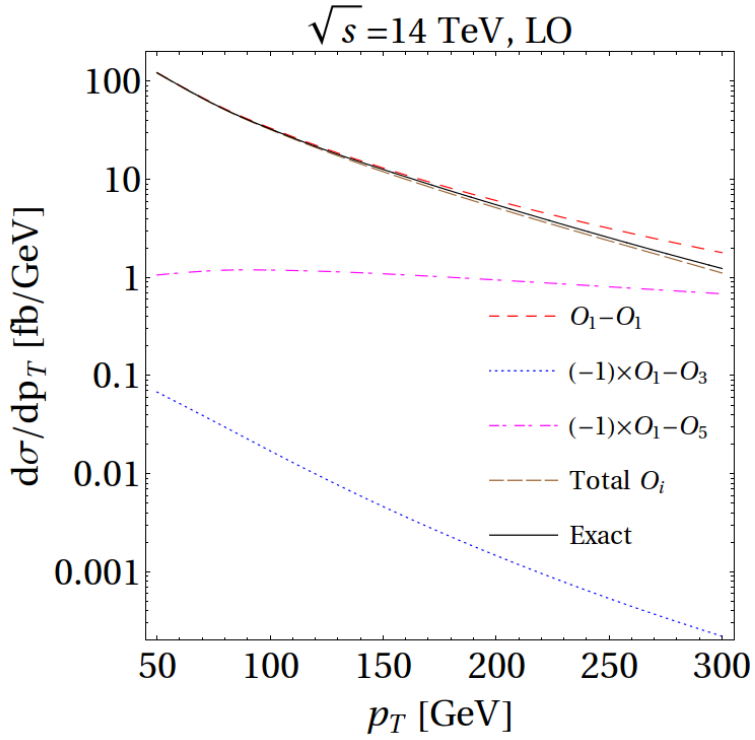

Figure 5.2: Leading order Higgs transverse momentum distributions from the dimension-5 and dimension-7 EFT operators for Higgs plus jet production at LO using CJ12 NLO PDFs with $\mu_R = \mu_F = m_h$. The curves use the $\mathcal{O}(\alpha_s)$ SM values of the C_i and include terms to $\mathcal{O}\left(1/m_t^2\right)$.

5.7 Phenomenology

In this section, we present LO, $\mathcal{O}(\alpha_s^3)$, and NLO, $\mathcal{O}(\alpha_s^4)$, results for the Higgs transverse momentum distributions resulting from the effective operators, using the basis of Eq. 5.26. All curves use NLO CJ12 PDFs [282] with $\mu_F = \mu_R = m_h = 126$ GeV, $m_t = 173$ GeV, and the 2-loop evolution of α_s, with $\alpha_s(126 \text{ GeV}) = 0.112497$. The O_1 contribution, with C_1 defined in Eq. (5.31) to include $\mathcal{O}(m_h^2/m_t^2)$ corrections, is equivalent to the $m_t \to \infty$ result rescaled by an overall correction factor. The sum of all contributions, from O_1, O_3, O_5, and the gluon self-interaction operators in Section 5.5.5, gives the full result up to $\mathcal{O}(m_h^4/m_t^4)$ corrections in the SM limit. We use the SM values for the C_i in our plots, but the individual results can be trivially rescaled for BSM coefficients.

5.7.1 LO results

At LO, O_3 does not contribute to quark channels and O_5 does not contribute to the gg channel. In Fig. 5.2, we plot the LO p_T distribution resulting from the individual operators, and in Fig. 5.3, the same plot is broken up into different partonic channels. The curves labeled as O_i-O_j are proportional to C_iC_j, where in this section we use the $\mathcal{O}(\alpha_s)$ results for the SM $C_i^{\text{SM,pole}}$. We can see that the O_1-O_1 result declines as p_T increases due to the

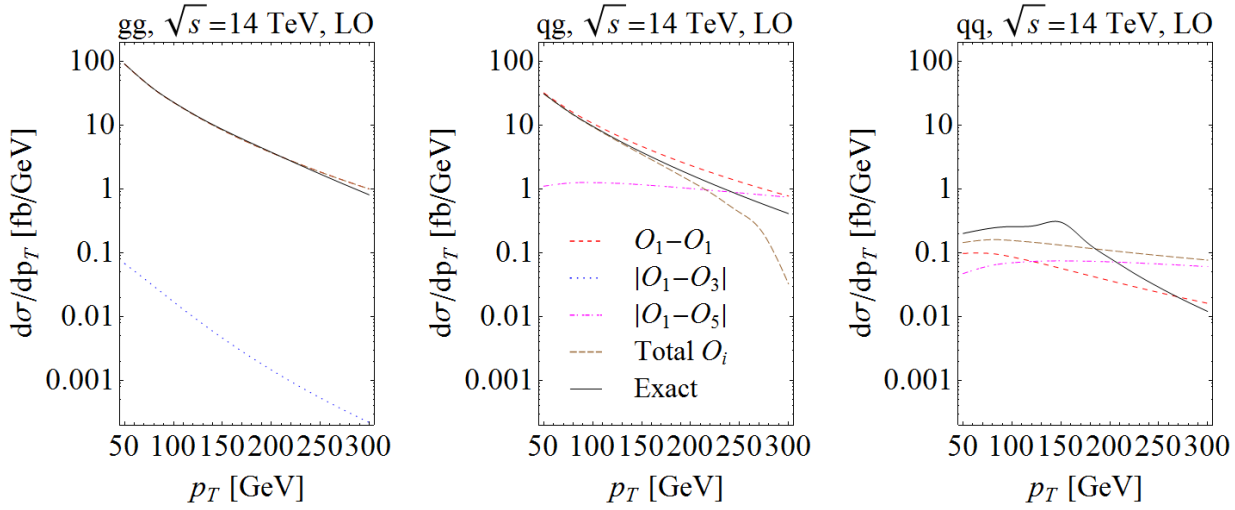

Figure 5.3: Leading order Higgs transverse momentum distributions from the dimension-5 and dimension-7 EFT operators for Higgs plus jet production at LO using CJ12 NLO PDFs with $\mu_R = \mu_F = m_h$. The curves use the $\mathcal{O}(\alpha_s)$ SM values of the C_i and include terms to $\mathcal{O}\left(1/m_t^2\right)$. Contributions from gg, qg, and qq partonic channels are shown separately.

decrease of the gg parton luminosity function, while the O_1-O_5 interference term (which is negative) grows in relative significance at large p_T due to the effects of terms of $\mathcal{O}(p_T^2/m_t^2)$ in the quark-gluon channel. The O_1-O_3 interference term declines even more rapidly than the O_1 result at high p_T, due to the non-interference of the tree-level amplitudes from O_1 and O_3 in the soft Higgs limit. As seen in the real emission section, at tree-level the two operators cannot interfere in the soft Higgs limit unless there are 3 or more jets in the final state. Also shown is the exact LO result of Ref. [234], including the effects of the top loop exactly. As made clear also in Ref. [221], the exact and the EFT results diverge for $p_T > 150$ GeV.[5]

Since for LO diagrams without external external quark lines, O_3 is the only needed operator that is not from a rescaling of the $m_t \to \infty$ limit, we have an explanation for the excellent agreement between the O_1 result and the exact result in the gg channel shown in Fig. 5.2, even at rather large p_T. For the qg-channel, on the other hand, the growing importance of O_5 explains the much worse agreement between the EFT result and the exact result at large p_T. At small p_T, though, the tree-level $qg \to qh$ amplitude factorizes into the collinear splitting $q \to qg$ and the on-shell $gg \to h$ amplitude, which explains the good agreement between the O_1 result and the exact result in the qg-channel. For the qq channel which neither enjoys the special properties of the O_3 helicity amplitudes nor factorizes into gluon sub-amplitudes, we see that the $m_t \to \infty$ approximation with scaling breaks down even at low $p_T \sim 50$ GeV. In Figs. 5.4 and 5.5 we plot the deviation of the O_1 result and the total result from the exact result. We again see the remarkably tame deviation in the

[5]After accounting for differing input parameters and basis for the dimension-7 operators, our results are in agreement with Ref. [163].

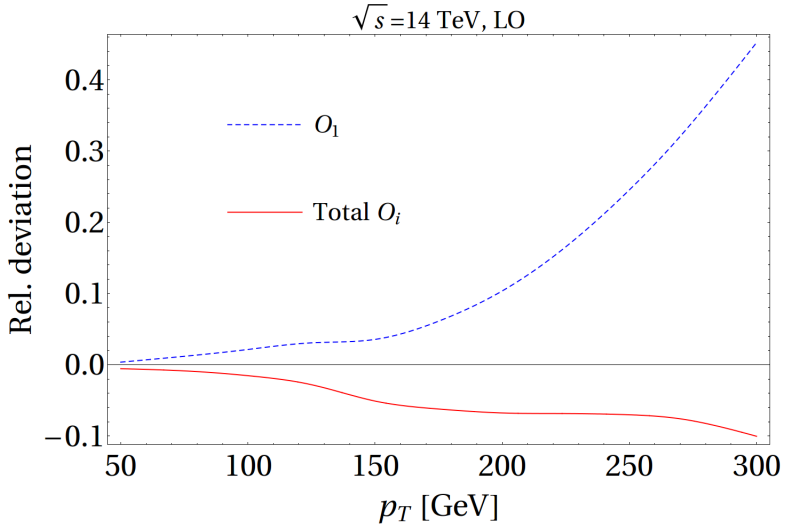

Figure 5.4: Deviations of the EFT predictions including all dimension-5 and dimension-7 operators (solid curve) from the exact result for Higgs plus jet production at LO using CJ12 NLO PDFs with $\mu_R = \mu_F = m_h$. The curves use the $\mathcal{O}(\alpha_s)$ SM values of the C_i and include terms to $\mathcal{O}\left(1/m_t^2\right)$. The dotted curve includes only the contribution from O_1.

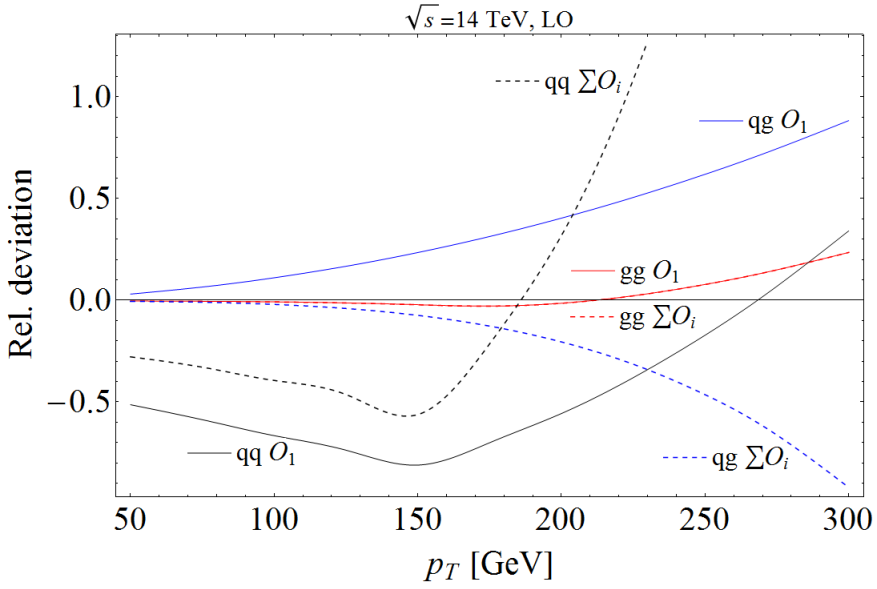

Figure 5.5: Deviations of the EFT predictions from the exact results (dotted curves) , broken up into partonic channels, for Higgs plus jet production at LO using CJ12 NLO PDFs with $\mu_R = \mu_F = m_h$. The curves use the $\mathcal{O}(\alpha_s)$ SM values of the C_i and include terms to $\mathcal{O}\left(1/m_t^2\right)$. The solid curves includes only the contribution from O_1. The red dashed and red solid curves are indistinguishable.

gg channel from the exact result, while observing that including all dimension-7 operators gives a better approximation to the exact p_T distribution than including the effects of O_1 alone, especially for $p_T < m_h$.

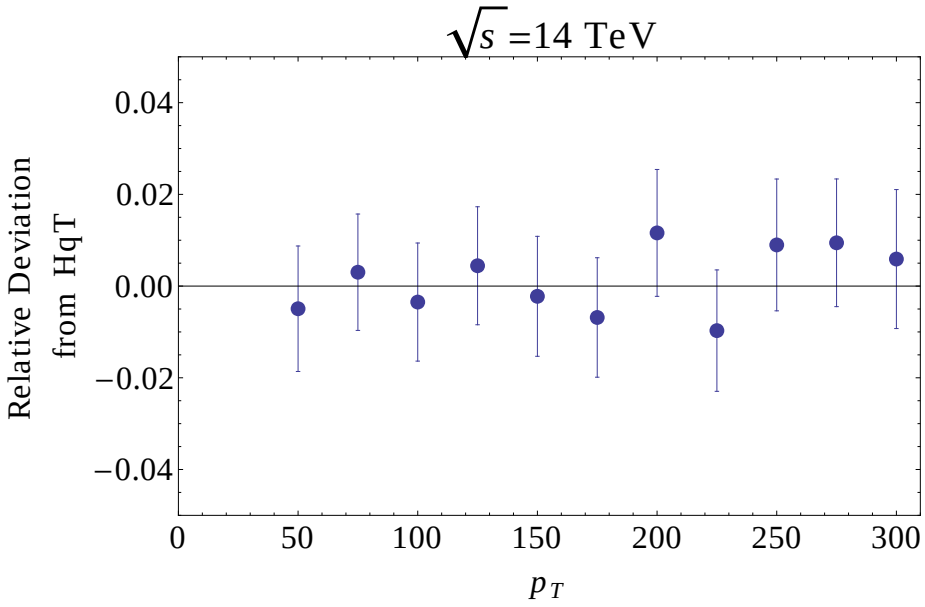

Figure 5.6: Deviation of our NLO result for the Higgs p_T distribution in the large m_t limit from the results of the HqT 2.0 program [163] using $\delta_s = 10^{-3}$, and $\delta_c = \delta_s/200$ for $p_T \geq 75$ GeV and $\delta_c = \delta_s/400$ for $p_T = 50$ GeV.

5.7.2 Numerical accuracy at NLO

Our NLO results are derived using phase space slicing with 2 cut-offs, δ_c and δ_s. To show the accuracy of our implementation of phase space slicing, in Fig. 5.6, we show the deviation of our NLO result for the $m_t \to \infty$ limit from the result produced by HqT 2.0 [163]. (The errors are statistical). We find agreement at the percent level. The variation of $d\sigma/dp_T$ with δ_s for the O_3 and O_5 operators individually (using the SM $\mathcal{O}(\alpha_s^2)$ values for the $C_i^{\rm SM,pole}$ coefficients) is plotted in Fig. 5.7 for fixed $\delta_c = 5 \times 10^{-6}$ and for $p_T = 100$ GeV. We see that at the percent level, our results are independent of the choice of soft cutoff. Similarly, we have verified the there is no dependence on the collinear cutoff when $\delta_c << \delta_s$. Our results in the following sections use $\delta_c = 5 \times 10^{-6}$ (except for the O_1 result at $p_T = 50.0$ GeV, for which we use one half this value) and $\delta_s = 10^{-3}$. All the plots are made by computing at $\delta p_T = 25$ GeV intervals, joined together by smooth curves, and it should kept in mind that an error of $\sim 1 - 2\%$ is present.

5.7.3 NLO results

In Fig. 5.8, we plot the contributions of the dimension-5 and dimension-7 EFT operators to the NLO p_T distributions. The NLO plots use the $\mathcal{O}(\alpha_s^2)$ expressions for the $C_i^{\rm SM,pole}$ and include terms only to $\mathcal{O}\left(1/m_t^2\right)$. Compared with the LO plot in Fig. 5.2, an important change is that the dimension-7 O_3 contribution no longer shows the property of declining faster than the dimension-5 O_1 contribution (because interference between O_3 and O_1 amplitudes in the soft Higgs limit starts at NLO), although O_5 is still dominant at large p_T. The curve labeled "self" is the small contribution from the $O(1/m_t^2)$ gluon self-couplings of Eq.

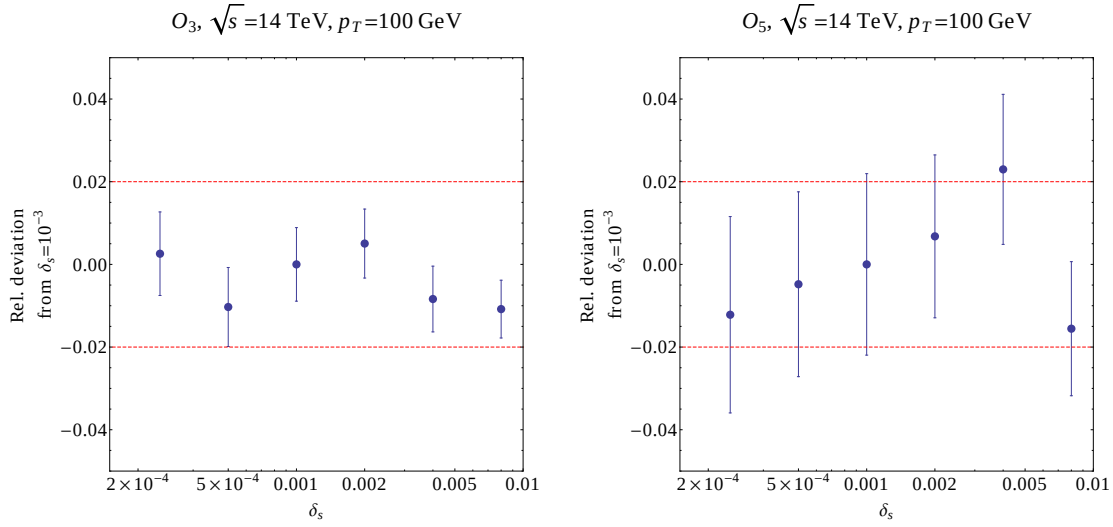

Figure 5.7: Dependence of the NLO result for the Higgs p_T distribution on the soft cutoff, δ_s, including only the interference of O_1 with O_3 (LHS) and O_1 with O_5 (RHS). The collinear cutoff is taken to be $\delta_c = 5 \times 10^{-6}$. The result with $\delta_s = 10^{-3}$ is normalized to 1.

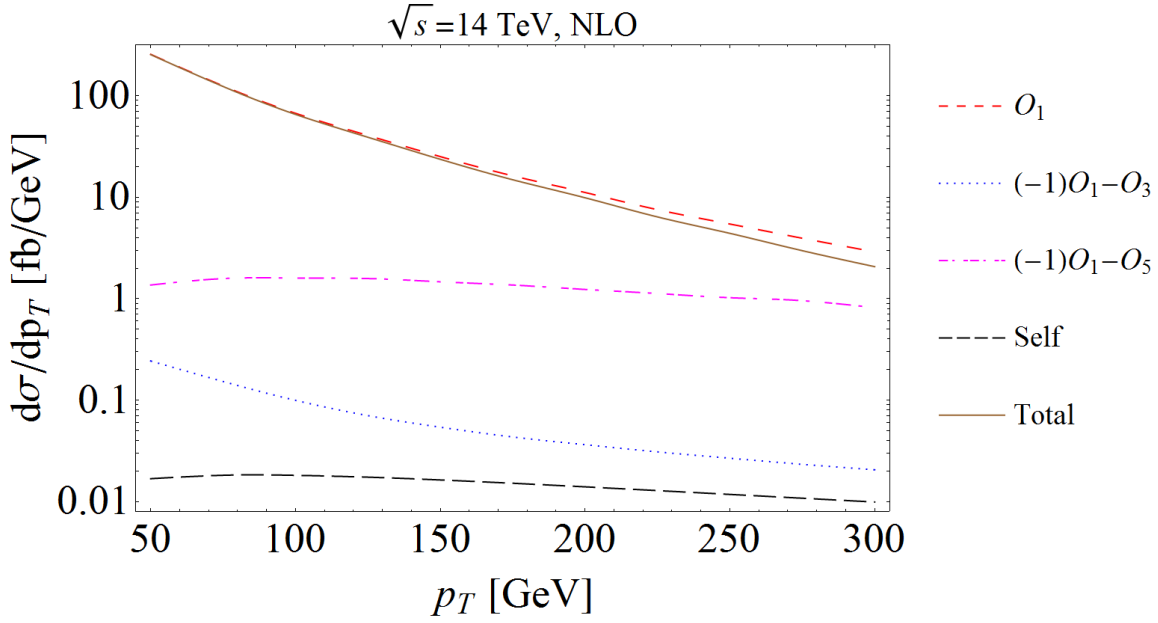

Figure 5.8: Next-to-leading order Higgs transverse momentum distributions from the EFT dimension-5 and dimension-7 operators, using the SM values of $C_i^{\rm SM,pole}$ to $\mathcal{O}(\alpha_s^2)$ and include terms only to $\mathcal{O}\left(1/m_t^2\right)$.

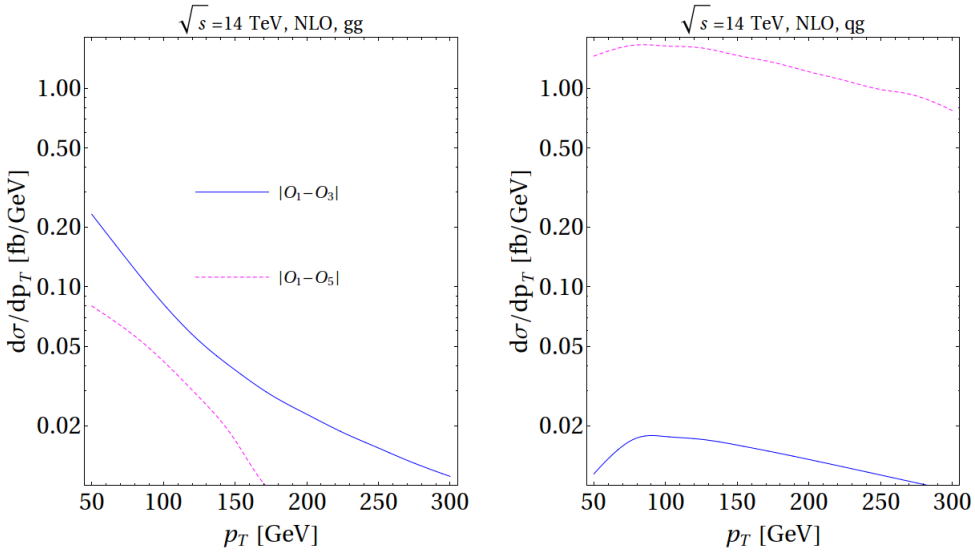

Figure 5.9: Comparison of the sizes of O_3 and O_5 contributions in the gg and qg channels at NLO.

5.35. The dimension-7 contributions to the gg and qg individual channels are shown in Fig. 5.9. In the gg channel, the O_5 operator starts to have non-vanishing contribution at NLO, but the contribution remains small compared with O_3, partly because O_5 only affects diagrams involving external quark legs or internal quark loops. In the qg channel, the O_3 operator starts to have non-vanishing contribution at NLO, but the contribution remains small compared with O_5. Therefore, we should still associate O_3 primarily with the gg channel, and O_5 primarily with channels involving initial-state quarks.

In order to quantify the size of our results, we define a p_T dependent K-factor:

$$K(p_T) = \frac{\frac{d\sigma}{dp_T}(\text{NLO})}{\frac{\mathrm{d}\sigma}{\mathrm{dp_T}}(\text{LO})}\,, \tag{5.108}$$

where in our plots both the NLO and LO curves use CJ12 PDFs with the 2-loop evolution of α_s. We plot the K factor separately for the contributions from O_1 and for the contributions from the interference of O_1 with O_3 and O_5. The results use the SM values of $C_i^{\text{SM,pole}}$, but can be rescaled appropriately for BSM models. In Fig. 5.10, we see that the NLO K-factors for O_1 and O_5 are always of order unity, while the O_3 K-factor reaches huge values at large p_T, reflecting the fact that the vanishing interference between the O_1 and O_3 helicity amplitudes in the soft Higgs limit no longer holds at one-loop level.

In Fig. 5.11, we show the NLO p_T dependent K-factors for each partonic channel. We can see that in going from the contribution of only O_1 to the sum of the contributions from all operators, the K-factor hardly changes in the gg-channel, while there are significant changes in the qg and qq channels. This is not surprising given the high p_T suppression of the O_3 contribution and the lack of an O_5 contribution in the all-gluon channel at LO, while the NLO effects are not large enough to destroy the agreement with the contribution of O_1 alone. In Fig. 5.12 we observe that when all partonic channels are summed up, the K-factor only shows modest changes [239, 238] due to the dominance of the gg channel.

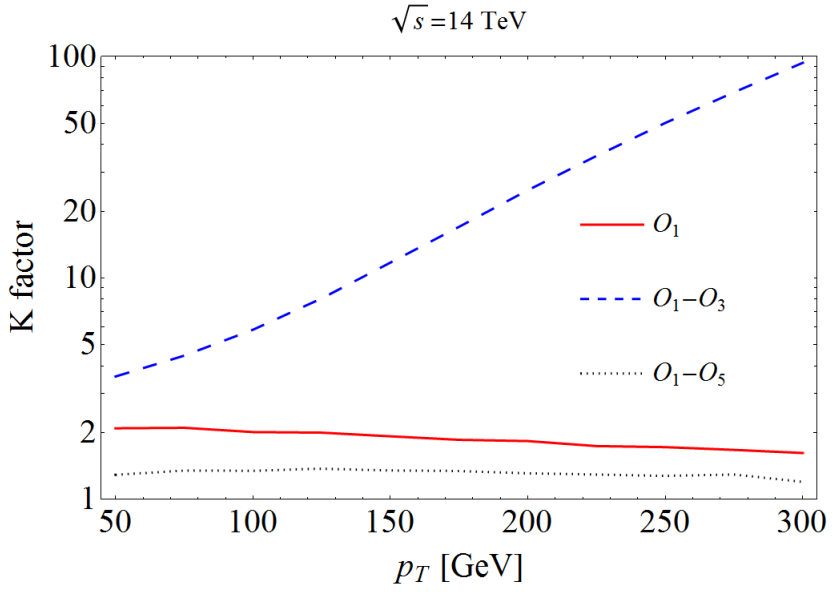

Figure 5.10: The NLO p_T-dependent K-factor for each of the operators, as defined in Eq. 5.108.

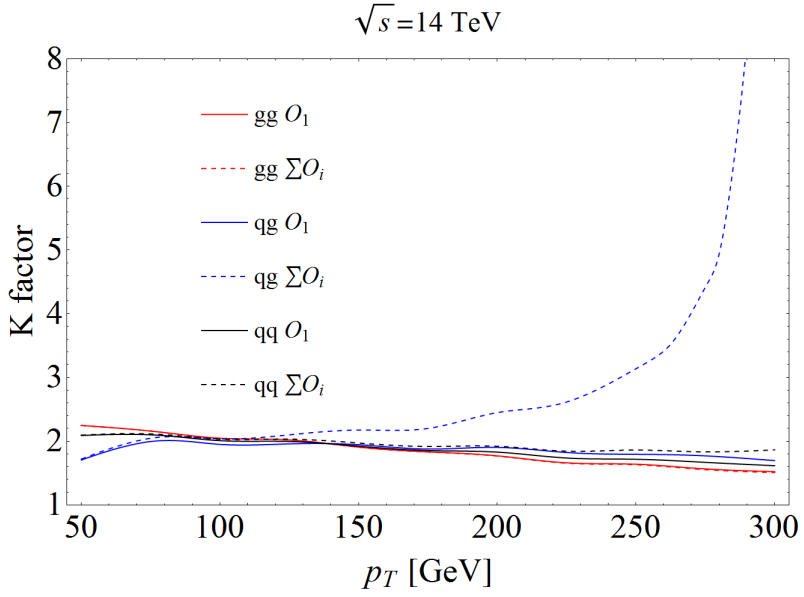

Figure 5.11: The NLO p_T-dependent K-factor, broken up into partonic channels.

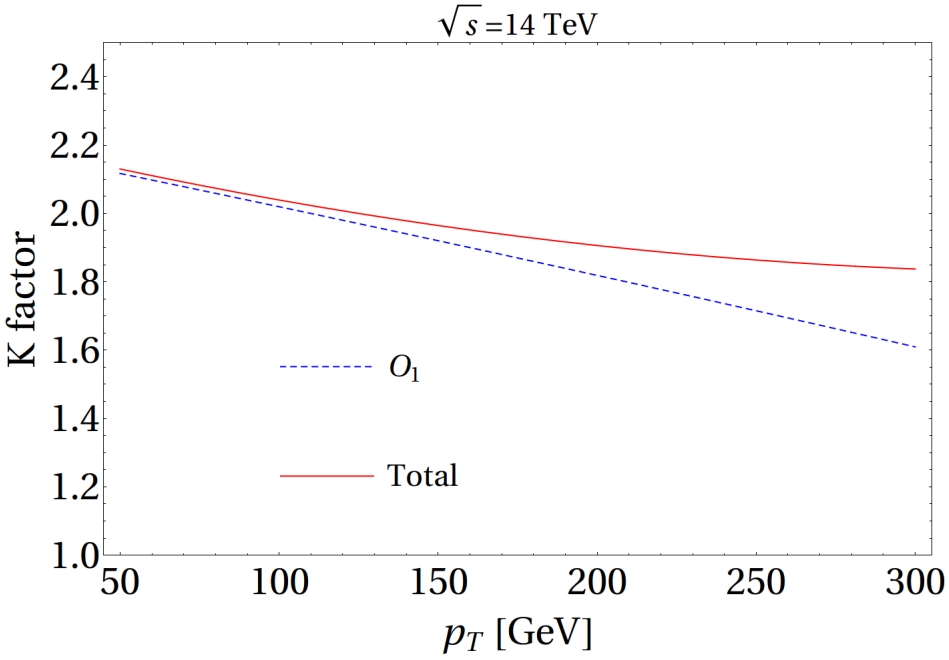

Figure 5.12: The NLO p_T-dependent K-factor, broken up into partonic channels, summed over all partonic channels.

Our K-factors plots are for SM Higgs production, with the non-logarithmic terms $\hat{C}_3^{(1)}$ and $\hat{C}_5^{(1)}$ in Eq. (5.11), (5.13) set to zero. It is straightforward to scale the K factors to reflect the effects of BSM physics. Define the K-factors corresponding to O_i as K^i, and define the expansion in α_s for SM and BSM coefficients,

$$\begin{aligned} C_i^{\rm SM} &= \alpha_s C_i^{(0,{\rm SM})} + \alpha_s^2 C_i^{(1,{\rm SM})}, \\ C_i^{\rm BSM} &= \alpha_s C_i^{(0,{\rm BSM})} + \alpha_s^2 C_i^{(1,{\rm BSM})}. \end{aligned} \tag{5.109}$$

The K-factor for a BSM model can be derived to $O(\alpha_s)$ by the rescaling,

$$\begin{aligned} \frac{K^{1,{\rm BSM}}}{K^{1,{\rm SM}}} &= 1 + 2\alpha_s \left(\frac{C_1^{(1,{\rm BSM})}}{C_1^{(0,{\rm BSM})}} - \frac{C_1^{(1,{\rm SM})}}{C_1^{(0,{\rm SM})}} \right), \\ \frac{K^{1,{\rm BSM}}}{K^{1,{\rm SM}}} &= 1 + \alpha_s \left(\frac{C_1^{(1,{\rm BSM})}}{C_1^{(0,{\rm BSM})}} - \frac{C_1^{(1,{\rm SM})}}{C_1^{(0,{\rm SM})}} + \frac{C_5^{(1,{\rm BSM})}}{C_5^{(0,{\rm BSM})}} - \frac{C_5^{(1,{\rm SM})}}{C_5^{(0,{\rm SM})}} \right), \\ \frac{K^{1,{\rm BSM}}}{K^{1,{\rm SM}}} &= 1 + \alpha_s \left(\frac{C_1^{(1,{\rm BSM})}}{C_1^{(0,{\rm BSM})}} - \frac{C_1^{(1,{\rm SM})}}{C_1^{(0,{\rm SM})}} + \frac{C_3^{(1,{\rm BSM})}}{C_3^{(0,{\rm BSM})}} - \frac{C_3^{(1,{\rm SM})}}{C_3^{(0,{\rm SM})}} \right). \end{aligned} \tag{5.110}$$

5.8 Discussion

We used an effective field theory containing strong gluon-Higgs-quark operators to dimension-7 to parameterize either non-SM couplings or the effect of a finite top mass within the SM. We calculated the NLO, $\mathcal{O}(\alpha_s^4)$, contribution to the p_T spectrum for Higgs plus jet production, including effects of $\mathcal{O}(1/\Lambda^2)$, for arbitrary values of the coefficients, C_i, of the effective Lagrangian. There are 3 dimension-7 operators which contribute to Higgs plus jet production: $O_6 \cong m_h^2 O_1$, O_3, and O_5. The operator O_6 rescales the overall gluon fusion rate for Higgs production and is constrained to be close to the SM value. The contribution from O_3, mainly in the gg channel, is suppressed at LO for large p_T since it vanishes in the soft Higgs limit, and remains numerically small at NLO, making it difficult to observe new physics in this channel, and also suppressing the dependence on the top quark mass. The contribution from O_5, which is mainly in the qg channel, is significant at large p_T. Hence, BSM physics will be most readily accessible if it contains a significant enhancement of C_5 over the SM value. We studied the renormalization of the dimension-7 operators, which makes it possible to regulate the UV divergence of the one-loop amplitudes and to use renormalization group running, from the BSM scale down to the Higgs mass scale, to resum large logarithms.

When the operator coefficients are set to their SM values, we obtain the $O(1/m_t^2)$ corrections to the NLO rate for Higgs plus jet production, modulo the non-logarithmic terms in the NLO matching coefficients in Eqs. (5.11),(5.13) to be presented shortly in a forthcoming work. These corrections are well behaved in the gg channel, but become increasingly large in the qg channel as p_T is increased above m_h. This observation is in agreement with Ref. [238]. Section 5.7 presents p_T dependent K factors which can be easily rescaled to include BSM physics.

Chapter 6

BSM applications of Higgs-gluon EFT

This chapter is based on the publication [56].

6.1 Introduction

The recently discovered Higgs boson has all the generic characteristics of a Standard Model (SM) Higgs boson and measurements of the production and decay rates agree to the $\sim$ 20% level with Standard Model predictions [198, 199, 200, 201]. Precision measurements of Higgs couplings are essential for understanding whether there exist small deviations from the Standard Model predictions which could be indications of undiscovered high scale physics. If there are no weak scale particles beyond those of the SM, then effective field theory (EFT) techniques can be used to probe the Beyond the Standard Model (BSM) physics [283, 284, 285]. The EFT is the most general description of low energy processes and new physics manifests itself as small deviations from the SM predictions. In the electroweak sector, this approach has been extensively studied [286, 287, 288, 289, 290]. The effects of BSM operators affecting Higgs production in the strong sector have been less studied [55, 291, 241].

The largest contribution to Standard Model Higgs boson production at the LHC comes from gluon fusion through a top quark loop and we examine new physics effects in this channel, along with the related Higgs + jet channel. We consider an effective Lagrangian containing the SM fermions and gauge bosons, along with a single Higgs boson, h. At dimension-4, the fermion- Higgs couplings can be altered from the SM couplings by a simple rescaling,

$$-\mathcal{L}_f = \kappa_f \left(\frac{m_f}{v}\right) \overline{f} f h + H.c.\,, \tag{6.1}$$

where $\kappa_f = 1$ in the SM. In models with new physics, the gluon fusion rate can also be altered by new heavy particles interacting with the Higgs boson at one-loop, which contribute to an effective dimension-5 operator [202, 203, 204]

$$\mathcal{L}_5 = C_1 G^{A,\mu\nu} G^A_{\mu\nu} h\,, \tag{6.2}$$

where $C_1 = \alpha_s/(12\pi v)$ for an infinitely heavy fermion with $\kappa_f = 1$. For convenience, we

define κ_g to be the ratio of C_1 to this reference value,

$$\kappa_g \equiv C_1 / \left(\frac{\alpha_s}{12\pi v}\right). \tag{6.3}$$

We compute the top quark contribution to scattering processes exactly using Eq. 6.1, (*i.e.*, not in the infinite top quark mass limit), and consider C_1 to be only the contribution from new physics. The measurement of gluon fusion by itself can determine a combination of κ_g and the top quark Yukawa coupling, κ_t, but cannot distinguish between the two for $m_t \gg m_h$ [212, 210, 211, 219]. Including the dimension-5 operator of Eq. (6.2), the cross section is generically,

$$\mu_{ggh} \equiv \frac{\sigma(gg \to h)}{\sigma(gg \to h)_{SM}} \sim \mid \kappa_t + \kappa_g \mid^2 + \mathcal{O}\left(\frac{m_h^2}{m_t^2}\right). \tag{6.4}$$

The requirement that $\mid \mu_{ggh} - 1 \mid < 10\%$ (or 5%) is shown in Fig. 6.1, where top quark mass effects are included exactly. The SM corresponds to the point $\kappa_g = 0, \kappa_t = 1$. The contribution from $b-$ quarks is small and has been neglected.

The boosted production of the Higgs boson through the process $pp \to h+$jet is sensitive to the Higgs- gluon effective coupling [219, 210, 213, 211, 214, 292] and offers the possibility of disentangling new physics effects and hence breaking the degeneracy between κ_t and κ_g. An effective Lagrangian approach is useful for studying this high p_T BSM physics and the Higgs-parton interactions can be described as a sum of higher dimension operators,

$$\mathcal{L}_{EFT} \sim \mathcal{L}_4 + \mathcal{L}_5 + \mathcal{L}_6 + \mathcal{L}_7 + \dots, \tag{6.5}$$

where $\mathcal{L}_n$ includes all dimension-n operators. At dimension-5 and assuming CP conservation, there is only the single operator of Eq. (6.2) modifying the Higgs-gluon interactions. The dimension-5 operator has been broadly used to obtain higher order QCD corrections to Higgs rates [204, 203, 222, 224, 237, 236, 223, 227, 243].

Dimension-7 operators affecting Higgs- gluon interactions from QCD interactions have received less attention [220, 221, 291]. Because their contributions are proportional to the strong coupling, g_s, these operators can have numerically significant effects. In a previous work [55], we considered the effects of dimension-7 operators affecting Higgs- gluon interactions and demonstrated the importance of including these operators along with the NLO QCD corrections in order to obtain realistic predictions of boosted Higgs spectra. The largest contribution to Higgs + jet production is from the O_1 operators in the gg initial channel. The NLO QCD corrections to this channel are relatively flat in p_T and lead to an enhancement of roughly a factor of 2 in the rate at the 14 TeV LHC. The contributions from O_3 to Higgs + jet production are suppressed at lowest order QCD (LO) for large p_T, since they vanish in the soft Higgs limit. These contributions receive large NLO corrections, but remain numerically small and are never important. The contributions from the interference of the O_1 and O_5 operators can be important for large $p_T \sim 300\ GeV$ and receive NLO QCD corrections which are again fairly p_T independent and increase the rate by a factor of ~ 1.2.

In this chapter, we examine the expected size of the coefficients of the Higgs-gluon EFT dimension-5 and dimension-7 operators in several representative UV models with heavy colored scalars and fermions. We are particularly interested in the question of whether

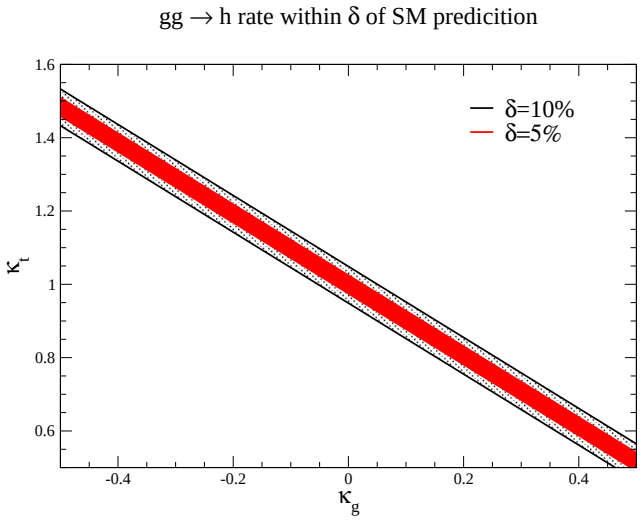

Figure 6.1: Allowed values of the EFT coefficients when the total gluon fusion rate, $gg \to h$, is within $\pm 10\%(\pm 5\%)$ of the SM prediction, $(\kappa_g \equiv 12\pi v C_1/\alpha_s)$.

the measurement of the boosted Higgs p_T distribution can distinguish the nature of the underlying UV physics, should there be any deviation from the SM. We then demonstrate how the inclusion of the dimension-7 operators affects fit to EFT Higgs parameters from gluon fusion. We work at LO QCD.

In Section 6.2, we review the EFT. The heavy colored scalar and fermion models which we study are introduced in Section 6.3 and the matching coefficients of the EFT presented. Phenomenological results at the LHC are given in Section IV and some conclusions about the usefulness of the EFT in this channel presented in Section 6.5.

6.2 Effective Lagrangian

In this section, we review the effective Lagrangian relevant for Higgs + jet production containing non-SM Higgs-gluon interactions. We consider a CP conserving Lagrangian, with no new Higgs particles,

$$\mathcal{L} = \mathcal{L}_{SM} + (\kappa_t - 1)(-1)\bar{t}th + \mathcal{L}_5 + \mathcal{L}_7 + \ldots, \tag{6.6}$$

where

$$\mathcal{L}_5 + \mathcal{L}_7 \equiv \hat{C}_1 O_1 + \Sigma_{i=2,3,4,5}\hat{C}_i O_i\,, \tag{6.7}$$

Note that there are no relevant dimension-6 operators of the type we are considering.

At dimension-5, the unique operator is

$$O_1 = G^A_{\mu\nu}G^{\mu\nu,A}h\,, \tag{6.8}$$

where $G^A_{\mu\nu}$ is the gluon field strength tensor. The dimension-7 operators needed for the gluon fusion production of Higgs are [220, 221, 254],

$$\begin{aligned}
O_2 &= D_\sigma G^A_{\mu\nu} D^\sigma G^{A,\mu\nu} h && (6.9)\\
O_3 &= f_{ABC} G^{A,\mu}_\nu G^{B,\nu}_\sigma G^{C,\sigma}_\mu h && (6.10)\\
O_4 &= g_s^2 h \Sigma_{i,j=1}^{n_{lf}} \overline{\psi}_i \gamma_\mu T^A \psi_i \, \overline{\psi}_j \gamma^\mu T^A \psi_j && (6.11)\\
O_5 &= g_s h \Sigma_{i=1}^{n_{lf}} G^A_{\mu\nu} D^\mu \, \overline{\psi}_i \gamma^\nu T^A \psi_i\,, && (6.12)
\end{aligned}$$

where our convention for the covariant derivative is $D^\sigma = \partial^\sigma - i g_s T^A G^{A,\sigma}$, $Tr(T^A T^B) = \frac{1}{2}\delta_{AB}$ and $n_{lf} = 5$ is the number of light fermions. Including light quarks, O_4 and O_5 are needed, which are related by the equations of motion (eom) to gluon-Higgs operators,

$$\begin{aligned}
O_4\,|_{eom} &\rightarrow D^\sigma G^A_{\sigma\nu} D_\rho G^{A,\rho\nu} h \equiv O_4'\\
O_5\,|_{eom} &\rightarrow G^A_{\sigma\nu} D^\nu D^\rho G^{A,\sigma}_\rho h \equiv O_5'\,. && (6.13)
\end{aligned}$$

Since O_4 involves 4 light fermions, the operator only contributes to Higgs + jet production starting at NLO.

A different dimension- 7 operator is useful,

$$O_6 = -D^\rho D_\rho \left(G^A_{\mu\nu}G^{\mu\nu,A}\right) h = -\partial^\rho \partial_\rho \left(G^A_{\mu\nu}G^{\mu\nu,A}\right) h = m_h^2 O_1, \tag{6.14}$$

where the last equal sign is only valid for on-shell Higgs production. Using the Jacobi identities,

$$O_6 = m_h^2 O_1 = -2O_2 + 4g_s O_3 + 4O_5. \tag{6.15}$$

Therefore, we can choose $O_6 = m_h^2 O_1$, O_3, O_4, and O_5 as a complete basis for the dimension-7 Higgs-gluon-light quark operators. We rewrite Eq. (6.7) as

$$\mathcal{L}_{\text{eff}} = C_1 O_1 + (C_3 O_3 + C_4 O_4 + C_5 O_5)\,. \tag{6.16}$$

The lowest order amplitudes for Higgs + jet production including all fermion mass dependence (bottom and top) are given in Refs. [235, 234]. A study of Higgs + jet production

at LO QCD in the EFT approximation involves only C_1, C_3 and C_5 [55, 278]. At the lowest order in α_s, O_3 is the only dimension-7 operator which contributes to the $gg \to gh$ channel, while O_5 is the only dimension-7 operator which contributes to channels with initial state quarks. The lowest order amplitudes in the EFT for Higgs + jet production can be found in Ref. [55], along with the NLO results including the effects of dimension-7 operators. For Higgs + jet production at NLO in BSM models, the EFT description also needs to include the higher-dimensional 3−gluon effective vertex generated at one-loop [55, 293], which could affect dijet and top quark rates [294].

6.3 UV Physics And the EFT

In this section, we discuss several prototype BSM physics models which have heavy particles contributing to Higgs + jet production and we compute the matching coefficients for the EFT in these models. This will allow us to estimate the size of BSM contributions.

6.3.1 Heavy Colored Scalars

We consider the addition of either real or complex $SU(3)$ scalars, ϕ_i [295, 296, 297, 298, 299]. Our numerical results are all derived for a complex scalar triplet. The scalar portion of the Lagrangian involving a new complex scalar, ϕ_i, and the SM-like Higgs doublet, H, is ,

$$V_{\text{complex}} = V_{SM}(H) + m_i^2 \phi_i^\dagger \phi_i + \frac{C_h}{v} \phi_i^\dagger \phi_i (H^\dagger H) - \lambda_4 (\phi_i^\dagger \phi_i)^2 \,, \tag{6.17}$$

where V_{SM} is the SM Higgs potential. For a real scalar,

$$V_{\text{real}} = V_{SM} + \frac{m_i^2}{2} (\phi_i)^2 + \frac{C_h}{2v} (\phi_i)^2 (H^\dagger H) - \lambda_4 (\phi_i)^4 \,. \tag{6.18}$$

In unitary gauge, $H \to (0, (h+v)/\sqrt{2})$.

6.3.2 Top Partner Model

Many BSM contain a charge - $\frac{2}{3}$ partner of the top quark. We consider a general case with a vector-like $SU(2)_L$ singlet fermion which is allowed to mix with the Standard Model like top quark [300, 301, 302, 303, 216]. The mass eigenstates are defined to be t and T with masses m_t and M_T and are derived from the gauge eigenstates using bi-unitary transformations involving two mixing angles θ_L and θ_R. Without loss of generality, θ_R can be removed by a redefinition of the top partner gauge eigenstate and the Higgs couplings are then modified from those of the SM [218]:

$$\begin{aligned} L_h^{top\ partner} = & -\Big\{ \cos^2\theta_L \frac{m_t}{v} \bar{t}_L t_R h + \sin^2\theta_L \frac{M_T}{v} \overline{T}_L T_R h \\ & + \frac{M_T}{2v} \sin(2\theta_L) \bar{t}_L T_R h + \frac{m_t}{2v} \sin(2\theta_L) \overline{T}_L t_R h + H.c. \Big\} \,. \end{aligned} \tag{6.19}$$

Precision electroweak fits to the oblique parameters, as well as M_W, place stringent restrictions on the product $\sin^2\theta_L M_T^2$ and for $M_T \sim 1$ TeV, $\sin\theta_L < .17$ [216, 302]. Higgs production has been investigated at NNLO for top partner models in Ref. [216] and the rate determined to be within a few % of the SM rate for allowed values of θ_L. Large effects in this channel require values of $\sin\theta_L$ that are excluded by precision measurements. ATLAS [304] and CMS [305] have searched for top singlet partners and excluded M_T below 655 GeVand 687 GeV, respectively. Similar limits on top partner masses and mixing can be obtained for different choices of top partner $SU(2)_L$ properties [302].

6.3.3 Predictions for Coefficients

The exact results for the contributions from high scale fermion [235, 234] and scalar loops [295, 296] to the rates for $q\overline{q} \to gh$ and $gg \to gh$ are well known. Matching to the EFT expressions, the coefficient functions can be extracted. The EFT amplitude for $q\overline{q} \to gh$ from virtual heavy particles with mass, m, is

$$\begin{aligned} \mid A(q\overline{q} \to gh) \mid^2 &= 64 g_s^2 \left(\frac{\hat{t}^2+\hat{u}^2}{\hat{s}}\right)\left[C_1^2 + \frac{\hat{s} C_1 C_5}{2}\right] \\ &= \lim_{m\to\infty}\left(\frac{4\alpha_s^3}{\pi}\right)\left(\frac{\hat{u}^2+\hat{t}^2}{\hat{s}v^2}\right) \mid \mathcal{A}_5(\hat{s},\hat{t},\hat{u},m^2) \mid^2 , \end{aligned} \tag{6.20}$$

while the EFT amplitude for $gg \to gh$ from virtual heavy particles with mass, m, is

$$\begin{aligned} \mid A(gg \to gh) \mid^2 &= g_s^2\left[384 C_1^2\left[\frac{m_h^8+\hat{s}^4+\hat{t}^4+\hat{u}^4}{\hat{s}\hat{t}\hat{u}}\right] + 1152 C_1 C_3 m_h^4\right] \\ &= \lim_{m\to\infty}\left(\frac{96\alpha_s^3}{\pi}\frac{m_h^8}{\hat{s}\hat{t}\hat{u}v^2}\right)\Big\{ \mid \mathcal{A}_2(\hat{s},\hat{t},\hat{u},m^2) \mid^2 + \mid \mathcal{A}_2(\hat{u},\hat{s},\hat{t},m^2) \mid^2 \\ &\quad + \mid \mathcal{A}_2(\hat{t},\hat{u},\hat{s},m^2) \mid^2 + \mid \mathcal{A}_4(\hat{s},\hat{t},\hat{u},m^2) \mid^2 \Big\} , \end{aligned} \tag{6.21}$$

where $\hat{s},\hat{t}$, and $\hat{u}$ are the usual Mandelstam variables. The coefficient functions $\mathcal{A}_2(\hat{s},\hat{t},\hat{u},m^2)$, $\mathcal{A}_4(\hat{s},\hat{t},\hat{u},m^2)$ and $\mathcal{A}_5(\hat{s},\hat{t},\hat{u},m^2)$ are given in Ref. [234] for fermion loops and in Ref. [295] for scalar loops. The C_1, C_3 and C_5 coefficients of Eqs. 6.20 and 6.21 depend in general on the parameters of the underlying UV completion of the model. By matching the EFT predictions with the heavy fermion expansions, we obtain the EFT coefficients given in Table 6.1. At LO, the dimension -7 term contributing to the $gg \to gh$ amplitude does not contain any dependence on the kinematic variables. For TeV scale masses, it is clear that the coefficients are quite small. For the top partner model, the coefficient functions for the heavier Dirac fermion contributions need to be multiplied by the factor $\sin^2\theta_L$ appearing in Eq. (6.19), while the SM top quark contribution is included exactly without using the EFT.

The matching of the EFT and the underlying UV theory are done at the high scale Λ. Using the anomalous dimensions found in Ref. [55, 256], the coefficients can be evolved to a

	Dirac Fermion	$SU(3)$ Triplet Scalar	$SU(3)$ Octet Scalar
$C_1(\Lambda)$	$\frac{\alpha_s \kappa_F}{12\pi v}\left[1+\frac{7m_h^2}{120m_F^2}\right]$	$-\frac{\alpha_s}{96\pi M_S^2}C_h\left[1+\frac{2m_h^2}{15M_S^2}\right]$	$-\frac{\alpha_s}{16\pi M_S^2}C_h\left[1+\frac{2m_h^2}{15M_S^2}\right]$
$C_3(\Lambda)$	$-\frac{g_s\alpha_s\kappa_F}{360\pi v m_F^2}$	$-\frac{g_s\alpha_s}{1440M_S^4}C_h$	$-\frac{g_s\alpha_s}{240M_S^4}C_h$
$C_5(\Lambda)$	$\frac{11\kappa_F\alpha_s}{360\pi v m_F^2}$	$-\frac{\alpha_s}{360\pi M_S^4}C_h$	$-\frac{\alpha_s}{60\pi M_S^4}C_h$

Table 6.1: The effective Lagrangian coefficient functions for heavy Dirac fermions and heavy scalars with mass, m_F and M_S, respectively. The coefficient functions, along with g_s and α_s, are evaluated at the scale $\Lambda = m_F, M_S$.

low scale, $\mu_R \sim m_h$,

$$\frac{d}{d\ln\mu_R}\ln\left(\frac{C_1(\mu_R)}{g_s^2(\mu_R)}\right) = \mathcal{O}(\alpha_s^2(\mu_R)), \tag{6.22}$$

$$\frac{d}{d\ln\mu_R}\ln\left(\frac{C_3(\mu_R)}{g_s^3(\mu_R)}\right) = \frac{\alpha_s(\mu_R)}{\pi}\,3C_A, \tag{6.23}$$

$$\frac{d}{d\ln\mu_R}\ln\left(\frac{C_5(\mu_R)}{g_s^2(\mu_R)}\right) = \frac{\alpha_s(\mu_R)}{\pi}\left(\frac{11}{6}C_A+\frac{4}{3}C_F\right), \tag{6.24}$$

where $C_A = 3$ and $C_F = \frac{4}{3}$. The one-loop electroweak RG running of C_1/g_s^2 [306] is non-zero, and its effect on the Higgs p_T distribution in the TeV range is found to be at the percent level [307].

The leading-logarithmic solutions to the renormalization group running equations Eq. (6.22)-(6.24) are

$$C_1(\mu_R)/g_s^2(\mu_R) = C_1(\mu_0)/g_s^2(\mu_0), \tag{6.25}$$

$$C_3(\mu_R)/g_s^3(\mu_R) = \left(\frac{\alpha_s(\mu_R)}{\alpha_s(\mu_0)}\right)^{-\frac{3C_A}{2b_0}}\cdot C_3(\mu_0)/g_s^3(\mu_0), \tag{6.26}$$

$$C_5(\mu_R)/g_s^2(\mu_R) = \left(\frac{\alpha_s(\mu_R)}{\alpha_s(\mu_0)}\right)^{-\frac{1}{2b_0}\left(\frac{11}{6}C_A+\frac{4}{3}C_F\right)}\cdot C_5(\mu_0)/g_s^2(\mu_0)\,, \tag{6.27}$$

where $b_0 = \frac{1}{12}(11C_A - 2n_{lf})$ and $\mu_0 \sim \Lambda$. The evolution of the coefficient functions is shown in Fig. 6.2. C_1 is increased by $\sim$ a factor of 2 when evolving from $\Lambda \sim 5$ TeV to the weak scale, while C_3 and C_5 are reduced by a similar factor.

6.4 Phenomenology

We will eventually be interested in whether measurements of the p_T spectrum can distinguish between the effects of the dimension-5 and dimension-7 operators resulting from scalars and from fermions; that is, *"Is the EFT a useful tool for disentangling the source of high scale physics?"*

Throughout this chapter, diagrams involving the SM top quark are evaluated with exact m_t dependence without using the Higgs-gluon EFT, while the contributions from heavy BSM particles, such as a color triplet scalar or a fermionic top partner, are considered both exactly and in the EFT approximation.

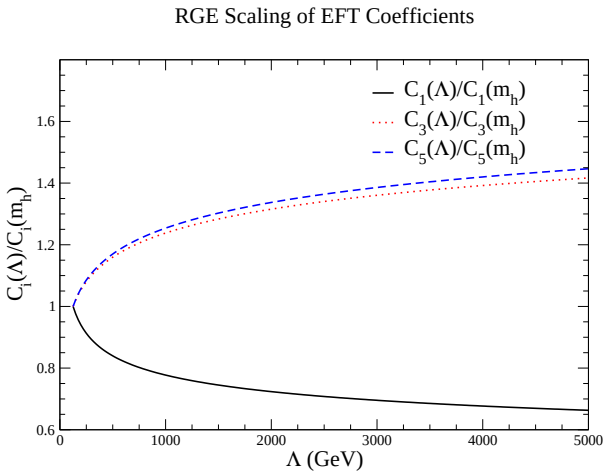

Figure 6.2: The evolution of the dimension- 5 and dimension-7 EFT coefficients from the scale of new physics, $\sim \Lambda$, to the electroweak scale.

6.4.1 Heavy Colored Scalars

We begin by considering the effect of heavy color triplet scalars on Higgs + jet production. (The case of a light colored scalar has been considered in [296].) We use CJ12 NLO PDFs [282] and $\mu_R = \mu_F = \sqrt{m_h^2 + p_T^2}$ for all curves, with $m_h = 125$ GeV, $m_t = 173$ GeV, and $m_b = 4.5$ GeV. All plots refer to Higgs + jet production at lowest order and with $\sqrt{s} = 14$ TeV. When using the EFT, the effects of heavy scalars are included using the coefficients of Table I. Since the effects are suppressed by $1/M_S^2$ in C_1 and $1/M_S^4$ in the other C_i, we expect relatively small effects unless the coefficient function C_h is large. We expect C_h to be of order the electroweak scale in a realistic model and in our plots, we take $C_h = 3M_Z$.[1] Numerically, the effects are linear in C_h for modest values of C_h/M_Z and our results can be trivially rescaled.

The exact one-loop contribution of the heavy scalars relative to the SM rate are shown in

[1] If ϕ_i corresponds to the left-handed top squark of the MSSM, then in the alignment limit ($\sin\beta = \cos\alpha$), $C_h \sim 3M_Z$, which motivates our choice. This numerical value is not important for our conclusions, as long as C_h/M_Z is not a large number.

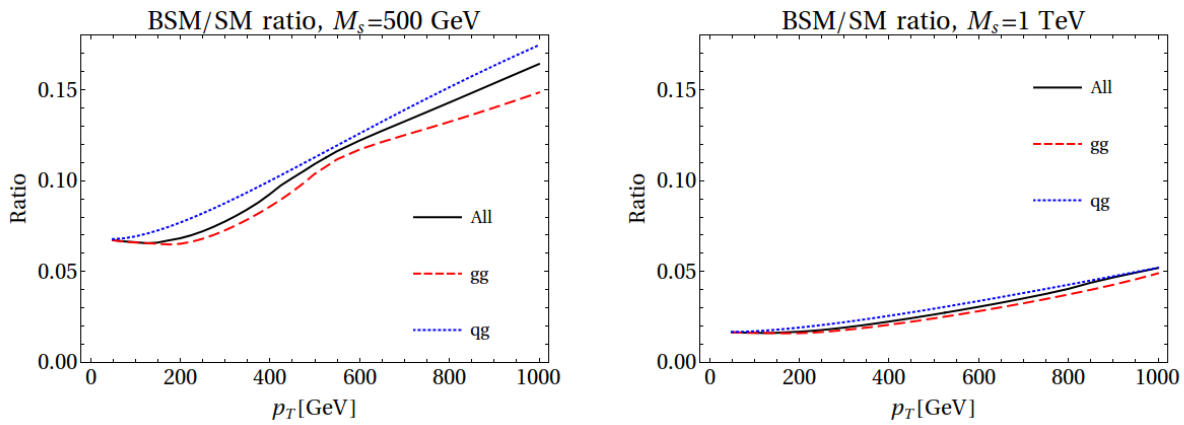

Figure 6.3: Contribution of a 500 GeV color triplet scalar (LHS) and a 1 TeV scalar (RHS), relative to the SM Higgs p_T distribution. The gg and qg partonic channels, and the sum of all partonic channels (which also includes $q\bar{q}$), are shown separately. Both the SM top and the scalar contributions are included exactly at LO.

Fig. 6.3 and as expected, they cause only a few percent deviation from the SM rate at low p_T. We define the ratio, "BSM/SM" to be the differential (or integrated) rate in the theory with the SM top quark and scalar included exactly normalized to the SM rate minus 1, i.e. it is the incremental contribution from the addition of a scalar. At large p_T, the deviation becomes significant, approaching $\sim 15\%$ for $p_T \sim 1$ TeV for a 500 GeV scalar and $\sim 5\%$ for a 1 TeV scalar. We note that the effects of a color octet scalar are a factor of $C_A/T_F = 6$ larger than those of a color triplet scalar. The integrated cross sections with a $p_{T_{cut}}$ are shown in Fig. 6.4, and a significant contribution from the scalars to the boosted Higgs signal is apparent for $p_{T_{cut}} \sim M_S$ for $M_S = 500$ GeV. For the heavier scalar, $M_S \sim$ TeV, the effects are only a few % even for very large p_{Tcut}.

Since the lowest order contribution from scalars is known exactly, we can explore the range of validity of the EFT. Fig. 6.5 shows the deviation of the EFT calculation from the exact 1-loop result when color triplet scalars are included. For a 500 GeV scalar, the EFT is accurate to within a few % below M_S and has large deviations above 500 GeV when only the dimension-5 ($\sim 1/M_S^2$) contributions are included. Including the dimension-7 contributions improves the accuracy of the EFT. Interestingly, for $M_S = 1$ TeV, the EFT becomes less accurate at large p_T when the dimension-7 effects are included. The EFT expansion clearly breaks down at a scale $p_T \sim M_S$. Fig. 6.6 demonstrates the accuracy of the EFT in the p_T integrated cross section and we observe the same behavior. (The cross section is integrated to $p_T = 1$ TeV, where the EFT is breaking down. Since the partonic results are integrated with a falling PDF spectrum, we expect the results to be reasonably reliable.) The contributions from the gg and qg initial states are shown separately in Figs. 6.7 and 6.8.

6.4.2 Heavy Fermion Top Partners

In this section we consider the effect of a top partner model on the shape of the Higgs p_T distribution. We take the top partner mass $M_T = 500$ GeV and the mixing angle

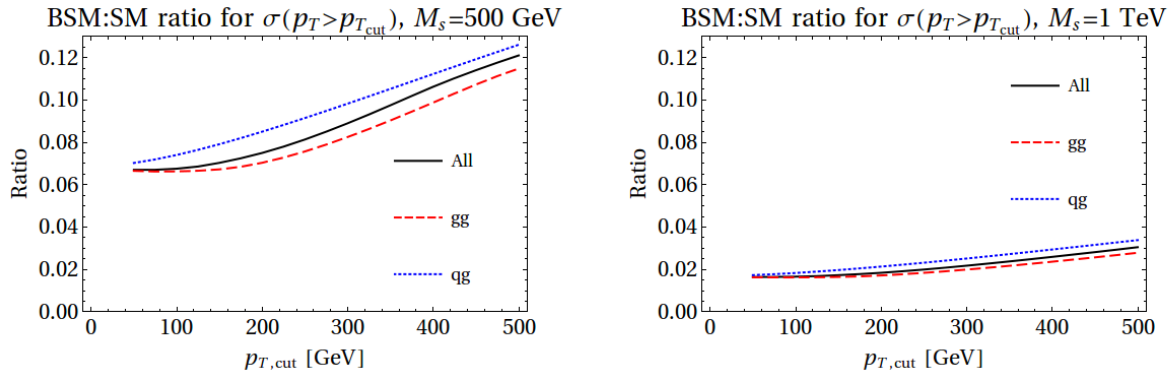

Figure 6.4: Contribution of a 500 GeV color triplet scalar and a 1 TeV scalar, relative to the SM cross section, with a cut $p_{T_{cut}}$. The gg and qg partonic channels, and the sum of all partonic channels (which also include $q\bar{q}$), are shown separately.Both the SM top and the scalar contributions are included exactly at LO.

$\cos\theta_L = 0.966$. Fig. 6.9 shows the ratio of the inclusive cross section in the top partner model to that in the SM, minus 1, evaluated with the exact dependence on the masses m_t and M_T, along with the same quantity integrated with a $P_{T_{cut}}$. We note that the results of Ref. [219] demonstrate large effects at high $p_T \sim 1$ TeV when $\sin\theta_L = 0.4$. Regretably, such large mixing angles are excluded by precision electroweak data. (We agree with the results of Ref. [219] for small $\sin\theta_L$.) Fig. 6.10 shows the accuracy of the EFT predictions for differential and integrated p_T distributions, relative to the results with exact m_t and M_T dependence.

We close this section by summarizing our results for top partners and scalars in Fig. 6.11, which dramatically demonstrates the difficulty of extracting information about the underlying UV physics.

6.4.3 EFT Fits

In this subsection, we consider the effects of a general rescaling of the EFT coefficients. As in Eq. (6.1) and Eq. (6.3), we consider the SM top quark contribution rescaled by κ_t, and the C_1 coefficients rescaled by κ_g relative to an infinitely heavy Dirac fermion whose mass comes entirely from the Higgs, i.e. $C_1 = \kappa_g \cdot \alpha_s/(12\pi v)$. For the dimension-7 operators, we vary the matching coefficients $C_i = \kappa_i C_i(M_S = 500 \text{ GeV}, C_h = 3m_Z)$ for $i = 3, 5$, where the reference values, scaled by κ_i, are $C_3(M_S, C_h) = -g_s\alpha_s C_h/(1440 M_S^4)$ and $C_5(M_S, C_h) = -\alpha_s C_h/(360\pi M_S^4)$ corresponding to the EFT coefficients from Table I for a 500 GeV scalar. The total cross section for single Higgs production is roughly unchanged from the SM, if we fix $\kappa_t + \kappa_g$ to be 1, according to Eq. (6.4). Fig. 6.12 demonstrates that excessively large values of κ_5 are required for a large effect from O_5. Fig. 6.13 shows that the inclusion of O_3 has very little effect even for huge values of κ_3, as expected from the helicity arguments in [55]. On the other hand, the effect of rescaling κ_t and κ_g separately can have a relatively large effect.

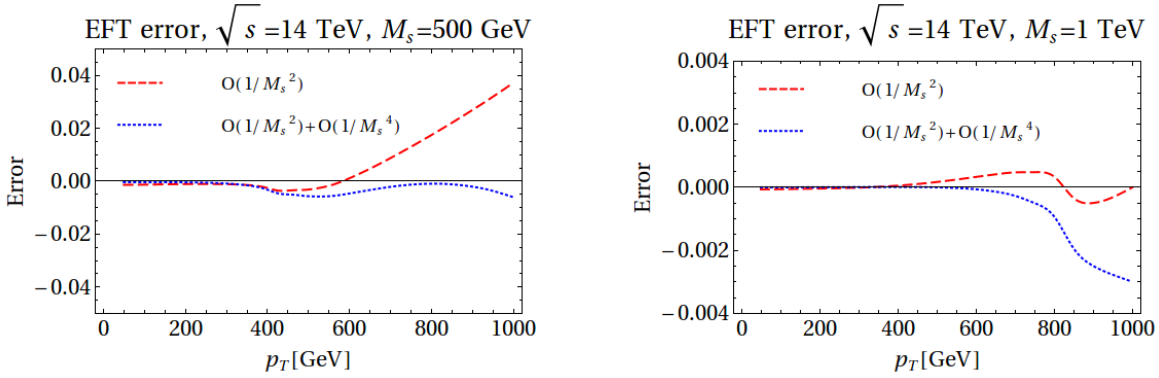

Figure 6.5: Accuracy of the effective field theory calculation of $d\sigma/dp_T$ relative to the exact calculation when including 500 GeV (LHS) and 1 TeV (RHS) color triplet scalars including all partonic initial states. The dashed lines contain only the dimension-5 contributions, while the dotted lines contain both the dimension-5 and dimension-7 contributions. The SM top quark contribution is always included exactly.

6.5 Discussion

The process Higgs + jet has been proposed as a useful channel for studying BSM physics and for disentangling the effects of a modification of the dimension-4 $t\bar{t}h$ Yukawa coupling from a non-SM dimension-5 Higgs-gluon effective vertex. We further include dimension-7 effective Higgs-gluon operators and compute the EFT coefficient functions in two representative models with heavy colored scalars and fermions. The coefficient functions are suppressed by inverse powers of the heavy mass scales, m, and are therefore quite small.

At lowest order, the effects of colored scalars and fermions can be computed exactly and the accuracy of the EFT determined. Typically, better accuracy is obtained in the gg channel than in the qg channel, and the EFT is accurate to a few percent for $p_T < m$. Our results illustrate the dilemma of the EFT approach: large effects are only obtained at high p_T and the contribution from the dimension -7 operators is small for $p_T < m$. On the other hand, Fig. 6.12 demonstrates a modest sensitivity to C_1, independent of κ_t. If any deviation is found in the Higgs transverse momentum distribution up to 1 TeV, the deviation is unlikely to provide information about the UV physics beyond the single parameter C_1. Our results support the validity of an approach using only the dimension-5 Higgs-gluon operator. Inclusion of the NLO QCD corrections is unlikely to change this conclusion, since the NLO corrections to the C_1^2 contribution do not have a large p_T dependence in the region where the EFT is valid.

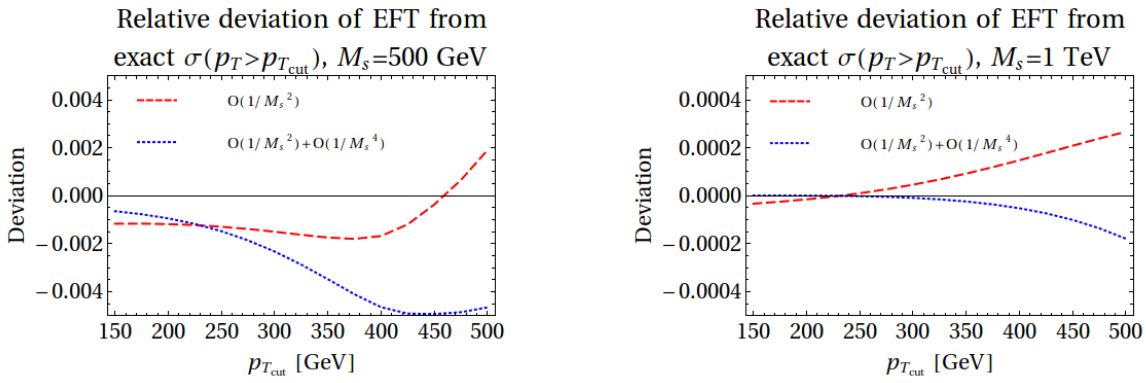

Figure 6.6: Accuracy of the effective field theory calculation of the total cross section subject to a $p_{T_{cut}}$, relative to the exact calculation when including 500 GeV (LHS) and 1 TeV (RHS) color triplet scalars including all partonic initial states. The dashed lines contain only the dimension-5 contributions, while the dotted lines contain both the dimension-5 and dimension-7 contributions. The SM top quark contribution is included exactly.

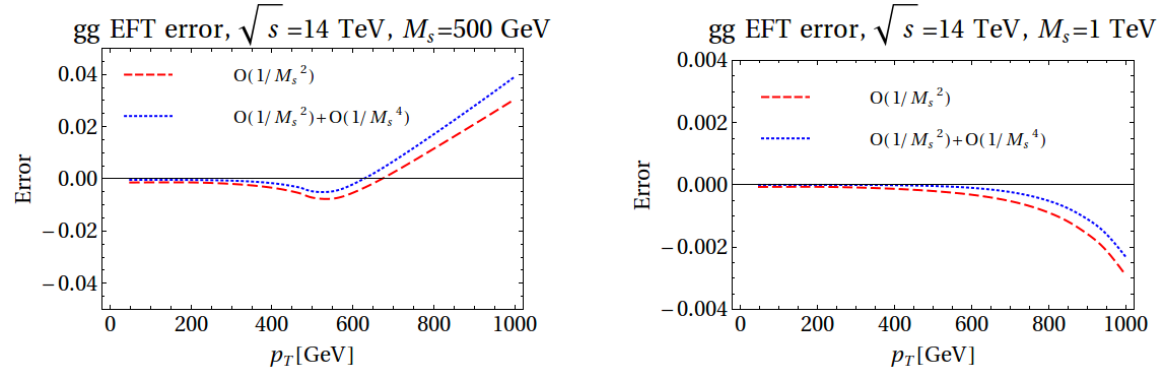

Figure 6.7: Accuracy of the effective field theory calculation of $d\sigma/dp_T$ relative to the exact calculation when including 500 GeV (LHS) and 1 TeV (RHS) color triplet scalars and including only the gg initial state. The dashed lines contain only the dimension-5 contributions, while the dotted lines contain both the dimension-5 and dimension-7 contributions. The SM top quark contribution is included exactly.

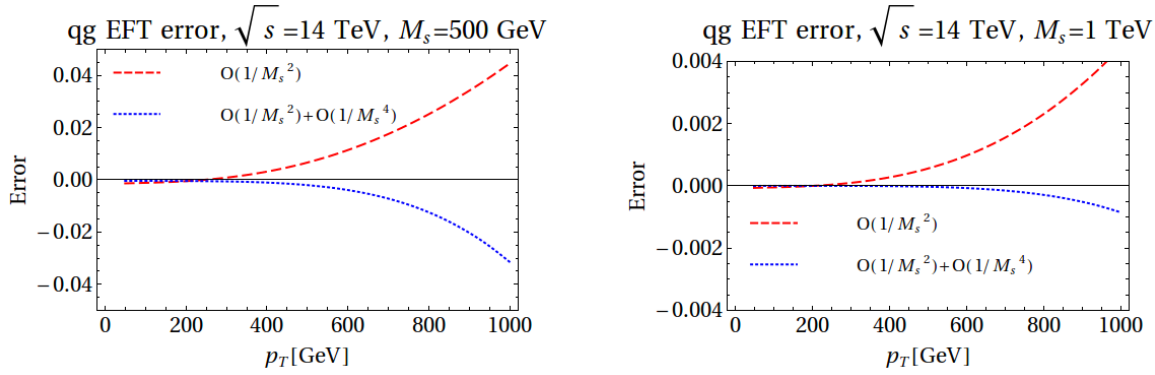

Figure 6.8: Accuracy of the effective field theory calculation of $d\sigma/dp_T$ relative to the exact calculation when including 500 GeV (LHS) and 1 TeV (RHS) color triplet scalars and including only the qg initial state. The dashed lines contain only the dimension-5 contributions, while the dotted lines contain both the dimension-5 and dimension-7 contributions. The SM top quark contribution is included exactly.

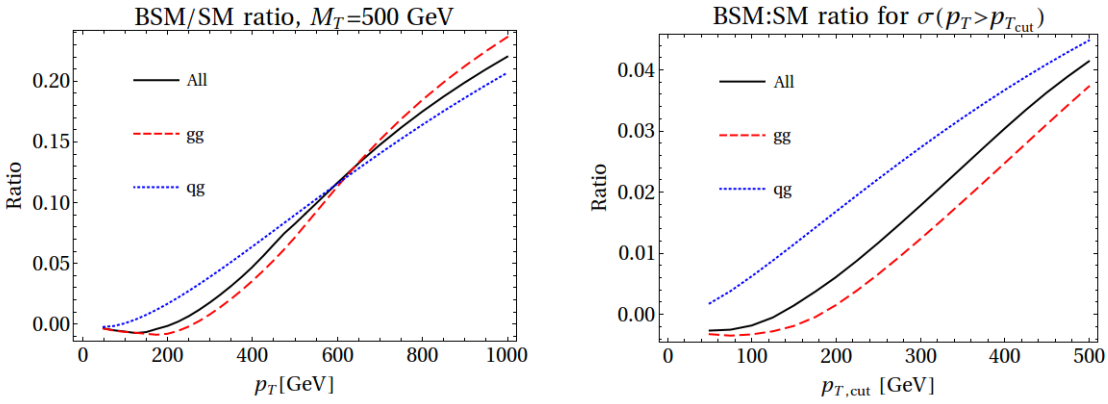

Figure 6.9: The BSM contribution, relative to the SM contribution, to the differential (LHS) and integrated Higgs p_T distribution (RHS). The gg and qg partonic channels, and the sum of all partonic channels (which also include $q\bar{q}$), are shown separately. Both the top partner and top quark contributions are included exactly at LO.

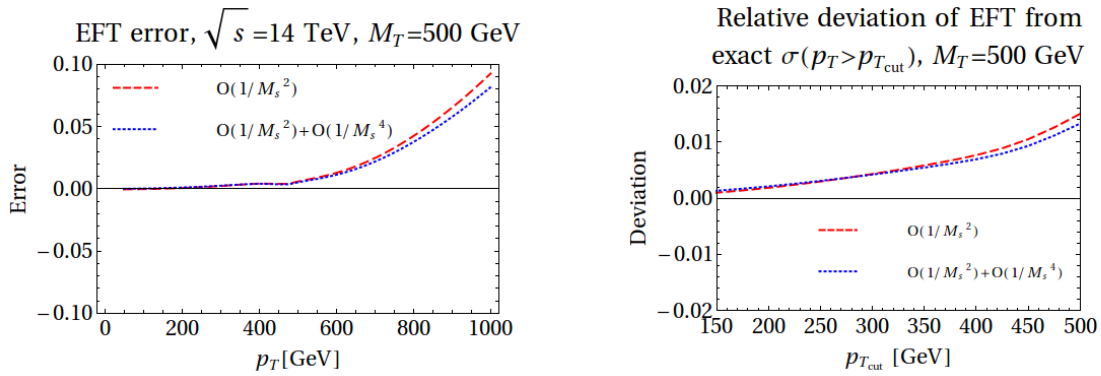

Figure 6.10: Accuracy of the effective field theory calculation of the differential (LHS) and integrated (RHS) p_T distribution, relative to the exact calculation, for a 500 GeV fermionic top partner with $\theta = \pi/12$.

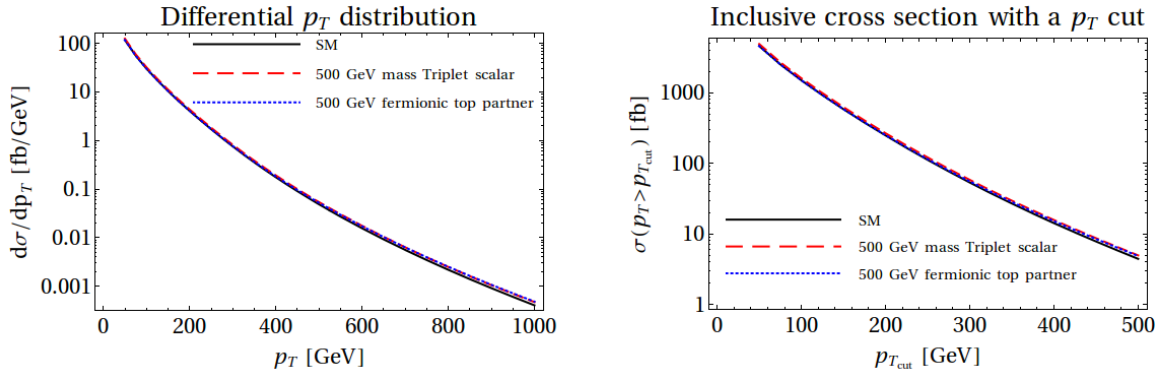

Figure 6.11: Cross sections including the SM result and a 500 GeV color triplet scalar , the SM result and a 500 GeV top partner, compared with the SM predictions.

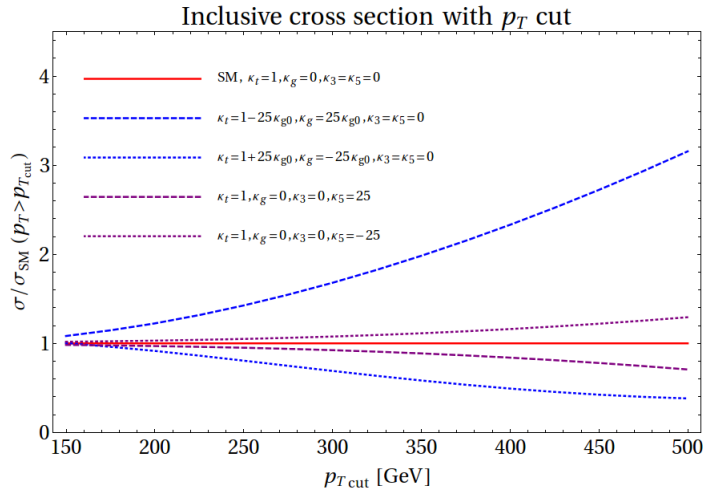

Figure 6.12: Inclusive cross section with a p_T cut at $\sqrt{s} = 14$ TeV, normalized to the SM rate. In our parameterization of BSM effects, the SM rate is rescaled by κ_t, while C_1, C_3, and C_5 are rescaled by κ_g, κ_3, and κ_5, respectively, with the model in Subsection 6.4.1 corresponding to $|\kappa_g|/\kappa_{g0} = \kappa_3 = \kappa_5 = 1$, $\kappa_{g0} \approx 0.0337$. We have fixed $\kappa_t + \kappa_g = 1$ to approximately conserve the total cross section. κ_3 is fixed to zero in this plot to highlight the effects of κ_g and κ_5.

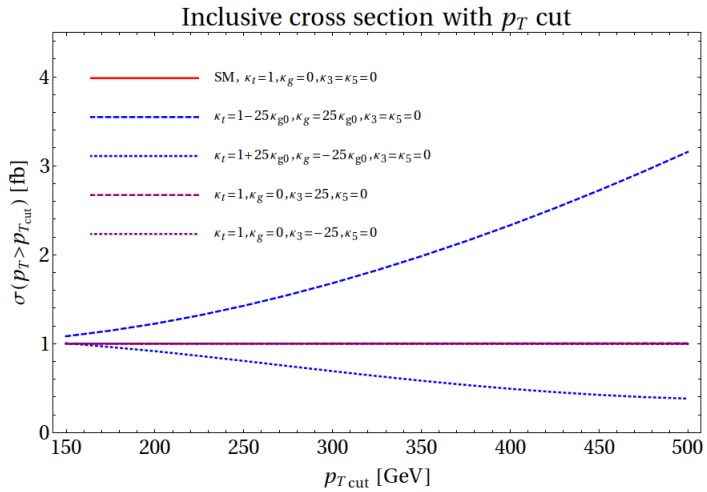

Figure 6.13: Inclusive cross section with a p_T cut at $\sqrt{s} = 14$ TeV, normalized to the SM rate. In our parameterization of BSM effects, the SM rate is rescaled by κ_t, while C_1, C_3, and C_5 are rescaled by κ_g, κ_3, and κ_5, respectively, with the model in Subsection 6.4.1 corresponding to $|\kappa_g|/\kappa_{g0} = \kappa_3 = \kappa_5 = 1$, $\kappa_{g0} \approx 0.0337$. We have fixed $\kappa_t + \kappa_g = 1$ to approximately conserve the total cross section. κ_5 is fixed to zero in this plot to highlight the effects of κ_g and κ_3. The effect of κ_3 can be seen to be extremely small.

Chapter 7

Violation of factorization in jet veto resummation

This chapter is based on the publication [57].

7.1 Introduction

For the Drell-Yan (DY) process, the cancellation of Glauber gluons was a major difficulty in proving factorization [32, 33, 34]. In QCD factorization at leading power, by the Collins-Soper-Sterman (CSS) formalism [24, 25, 26] or soft collinear effective theory (SCET) [41, 42, 40, 43], soft gluons decouple from the dynamics of collinear particles through the eikonal approximation. However, the eikonal approximation is not applicable to soft gluons whose momenta are dominated by transverse components, called Glauber / Coulomb gluons. This issue is of direct relevance for the resummation of jet veto logarithms at hadron colliders [164, 165, 167, 168, 169, 170], which requires re-factorization of the Drell-Yan cross section when the jet veto scale is much lower than the hard scale.

In the simpler cases of the Sudakov form factor and semi-inclusive deeply inelastic scattering (SIDIS), cancellation of Glauber gluons is achieved at the amplitude level, by deforming integration contours [308] away from the Glauber region. In such cases, if the Glauber region is included in the calculation, the cancellation happens between the Glauber region and the subtraction of overlap between the Glauber region and other regions [309, 26, 310]. Such cancellation is by no means automatic; it places strong constraints [26, 311] on the choice of Wilson lines in the definition of the soft and collinear functions, including the directions (past-pointing / incoming versus future-pointing / outgoing) and possible rapidity regularization.[1]

For the Drell-Yan process, the cancellation is more involved, due to the presence of both initial-state and final-state poles, in both collinear sectors. Incoming Wilson lines are chosen, to be compatible with contour deformation away from initial-state poles (which is responsible

[1] The compatibility between contour deformation and rapidity regularization by off-lightcone Wilson lines [26] has been studied in the aforementioned references, but it should be possible to extend the studies to other rapidity regulators [312, 313] used in the SCET literature, which bear more resemblance to dimensional regularization.

for the sign flip of the Sivers function between DY and SIDIS [314]), while final-state poles that obstruct contour deformation are canceled after summing over cuts and integrating over certain momentum components. While there are earlier proofs of cancellation of Glauber gluons, the CSS proof in [34], based on both plus- and minus- lightcone ordered perturbation theory (LCOPT), is the most powerful one, because its applicability extends beyond leading-twist massless parton scattering [315], with important phenomenological applications to, e.g. subleading-twist quarkonium production [316].

The CSS proof originally required integrating over the transverse momenta of the partons, but it was subsequently realized that in the Feynman gauge, the proof carries through [85, 26] for transverse momentum dependent (TMD) factorization for the Drell-Yan process. However, for factorization of "isolated" Drell-Yan production with measured hadronic event shape variables such as transverse energy [317, 167, 318] and beam thrust [319, 320] (see also [321]), the existing proofs are not applicable, as shown in [322] which explored connections with multi-parton interactions.

In fact, one of the crucial last steps of the CSS proof is integrating over the virtuality of the active partons (after summing over cuts in LCOPT). This step is directly broken by a measurement of the beam thrust variable, as the factorization proposed in [319] involves the virtuality-dependent PDF, also called the beam function.

We will borrow the terminology "generalized factorization" for hadron-hadron collisions proposed in a slightly different context, TMD factorization. Generalized factorization is to be distinguished from "standard factorization" for hadron-hadron collisions, the latter of which assumes cancellation of Glauber gluons and always defines soft and collinear functions using past-pointing / incoming Wilson lines carrying the color charges of the active partons. For example, the factorization of beam thrust in [319] using SCET should be characterized as standard factorization.[2] Generalized factorization, in a narrow sense, involves modification of Wilson lines in collinear and soft functions [323, 324, 325, 326], but in a general sense, can be any factorization with a sensible spin structure [327].[3] In the model field theory considered in this chapter, the colored active partons and the produced heavy uncolored particles are scalars carrying no spin indices, and generalized factorization is liberally defined as any factorization of the cross section into a product / convolution of scalar hard, collinear, anti-collinear, and possibly soft functions We will make the definition precise in Section 7.3.1.

To disprove a leading-power factorization statement, it is sufficient to demonstrate, at some fixed order in α_s, that the leading-power part of the cross section contradicts the prediction from factorization. Since QCD factorization relies on arguments that are applicable to *all* unbroken gauge theories, irrespective of e.g. gauge groups and matter contents, it is sufficient to find a contradiction in a model field theory that allows easy calculation. Model field theories involving polarized scattering, again in the slightly different context of TMD factorization, have been used to show the violation of both standard factorization and generalized factorization for hadron production at small transverse momentum [328, 329, 330, 327].

In this chapter, we will consider Drell-Yan-like scattering in a model field theory, and

[2]The equivalence of leading-power soft collinear factorization derived from traditional QCD methods and from SCET, for sufficiently inclusive observables that guarantee the cancellation of Glauber gluons, has been demonstrated extensively, for example in [48, 49, 50, 53, 79]

[3]For example, the large component of the Dirac spinor of a collinear quark should be projected out, and gluons that enter the hard scattering should carry two possible transverse polarizations.

study spin asymmetries in the doubly-differential beam thrust distribution. For this special model and observable, the vast majority of diagrams vanish, allowing a clean calculation of factorization-violating effects. The goal of the study is two fold. First, we would like to give an explicit demonstration that standard factorization is violated, which was shown by [322] to be extremely likely. Second, we would like to show that it is not possible for a generalized factorization theorem to hold, since decoupling of the two collinear sectors necessarily leads to zero spin asymmetry, while the calculations in this chapter find a non-zero spin asymmetry. The non-cancellation of Glauber gluons found in this chapter only happens above the jet veto scale, so collinear factorization is still valid if the jet veto scale is perturbative, but our ability to resum large logarithms in the hard scattering function will be compromised.

Ref. [331] introduced new jet algorithm-based observables, such as the "jet beam thrust", which are designed to be less sensitive to Glauber effects, while preserving the rapidity-dependent nature of the beam thrust variable. Other recent research [328, 329, 330, 327, 332, 333, 334, 335] investigated the violation of QCD factorization in contexts other than, or wider than, the Drell-Yan process. For perturbative resummation, the logarithmic order at which factorization-violating effects start has been discussed for top quark pair production at low transverse momentum [336, 337] and dijet event shapes [338].

This chapter is organized as follows. In Section 7.2 we give a description of the model field theory and the observable measured in our thought experiment. In Section 7.3 we explain why a non-zero spin asymmetry would contradict both standard factorization and generalized factorization. In Section 7.4 we check that up to $\mathcal{O}(\alpha_s^2)$, factorizable diagrams, as well as the vast majority non-factorizable diagrams, do not contribute, due to cancellations associated with this special observable. In Section 7.5 we evaluate the only $\mathcal{O}(\alpha_s^2)$ cut diagram left, which involves one Glauber gluon exchanged on each side of the cut. The evaluation gives a non-zero spin asymmetry, which is the desired result. Some discussions are given in Section 7.6.

7.2 The model for showing factorization breaking

7.2.1 Model field theory

We consider QCD with a hypothetical massless complex scalar quark ϕ (instead of a Dirac fermion quark as in real QCD) under the fundamental representation of $SU(3)$. The scalar quark also carries an electric charge of $+e$. The produced heavy particle Φ (analogous to γ^* and Z^0 in the real Drell-Yan process) is a neutral color-singlet scalar with mass M, and couples to the light scalar quarks via the interaction Lagrangian $-g_\Phi \Phi \phi^* \phi$. The photon γ serves the role as a "hadron" which can split into an active scalar quark that participates in hard scattering, and a spectator scalar quark going down the beam pipe. We consider the Drell-Yan process $\gamma + \gamma \to \Phi + X$. The lowest-order diagram is $\gamma + \gamma \to \Phi + \phi + \phi^*$, shown in Fig.7.1.

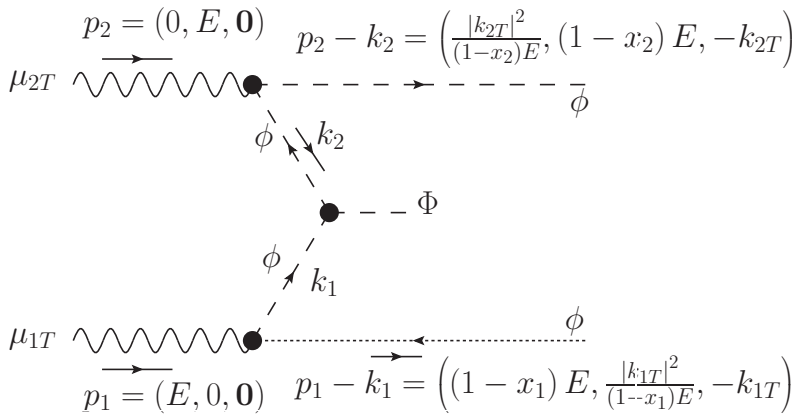

Figure 7.1: The leading-order Feynman diagram for $\gamma + \gamma \to \Phi + X$ in the model theory. Here $X = \phi + \phi^*$.

7.2.2 Observable - spin asymmetry in doubly differential beam thrust

We will use the beam thrust variable [339, 319]

$$\tau_B \equiv \frac{1}{M} \sum_i |p_{T_i}| e^{-|y_i - y|}, \tag{7.1}$$

where y and M are the rapidity and invariant mass of the Drell-Yan pair (actually a heavy scalar in our model), and the index i runs over every detected hadron. Requiring $\tau_B \ll 1$ strongly restricts hadronic activity, especially in the central rapidity region. It is useful to consider the *doubly-differential distribution* [319] in (τ_R, τ_L), where τ_R receives contribution from only the right hemisphere ($y_i > y$) and τ_L receives contribution from only the left hemisphere ($y_i < y$).

Even though the arguments in this paper also apply to jet algorithm-based vetoes, for concreteness we will consider the doubly-differential beam thrust distribution from the scattering of two photons. Our thought experiment involves incoming photons with several polarization configurations, from which we obtain the double spin asymmetry in the distribution. We will do the calculation for a heavy scalar Φ produced at rapidity $y = 0$, and with the left and right hemispheres having the same beam thrust $\tau_R = \tau_L = \frac{1}{2}\tau_B \ll 1$. The phase space integral for the square of the amplitude in Fig. 7.1 is, in the approximation that k_1 is plus-collinar and k_2 is minus-collinear,

$$\begin{aligned}
&\left.\frac{d^3\sigma}{d\tau_R d\tau_L dy}\right|_{y=0,\,\tau_R=\tau_L=\tau_B/2} \\
&= \frac{1}{2E^2} \int \frac{dx_1}{2(2\pi)\,(1-x_1)} \int \frac{dx_2}{2(2\pi)\,(1-x_2)} \int \frac{d^2k_{1T}}{(2\pi)^2} \int \frac{d^2k_{2T}}{(2\pi)^2} \,|\mathcal{M}|^2 \\
&\quad 2\pi\delta\left(x_1 x_2 E^2 - M^2\right) \delta\left(\frac{1}{2}\ln\frac{x_1}{x_2}\right) \delta\left(\frac{\tau_B}{2} - \frac{|k_{1T}|^2}{M\,(1-x_1)\,E}\right) \delta\left(\frac{\tau_B}{2} - \frac{|k_{2T}|^2}{M\,(1-x_2)\,E}\right)
\end{aligned} \tag{7.2}$$

The delta functions in Eq. (7.2) force

$$x_1 = x_2 = \frac{M}{E} \equiv x, \tag{7.3}$$

$$|k_{1T}| = |k_{2T}| = \sqrt{\frac{\tau_B(1-x)}{2}} \equiv |k_{0T}|\,, \tag{7.4}$$

and Eq. (7.2) simplifies to

$$\begin{aligned}&\left.\frac{d^3\sigma}{d\tau_R d\tau_L dy}\right|_{y=0,\,\tau_R=\tau_L=\tau_B/2}\\ &= \frac{M^2}{16\pi E^2}\int\frac{d^2k_{1T}}{(2\pi)^2}\int\frac{d^2k_{2T}}{(2\pi)^2}\delta\left(|k_{1T}|^2-|k_{0T}|^2\right)\delta\left(|k_{2T}|^2-|k_{0T}|^2\right)|\mathcal{M}|^2\,.\end{aligned} \tag{7.5}$$

For the scattering of two photons, we define the *absolute* double spin asymmetry as

$$\sigma_{\rm asym} = \left(\sigma_{\uparrow\downarrow}+\sigma_{\downarrow\uparrow}-\sigma_{\uparrow\uparrow}-\sigma_{\downarrow\downarrow}\right)/4, \tag{7.6}$$

where up and down arrows denote right and left polarizations. The *relative* double spin asymmetry is defined as the above expression divided by the unpolarized cross section

$$\sigma_{\rm unpol} = \left(\sigma_{\uparrow\downarrow}+\sigma_{\downarrow\uparrow}+\sigma_{\uparrow\uparrow}+\sigma_{\downarrow\downarrow}\right)/4. \tag{7.7}$$

When a photon traveling in the z direction is right polarized the polarization vector is $\epsilon_\uparrow = \left(\epsilon^0_\uparrow, \epsilon^x_\uparrow, \epsilon^y_\uparrow, \epsilon^z_\uparrow\right) = (0,1,i,0)/\sqrt{2}$. So $\epsilon^\mu_\uparrow \epsilon^{*\nu}_\uparrow = \left(-g^{\mu_T\nu_T} - i\epsilon^{\mu_T\nu_T}\right)/2$, where $\epsilon^{xy} = -\epsilon^{yx} = 1$. Similarly, for a left-polarized photon, $\epsilon^\mu_\downarrow \epsilon^{*\nu}_\downarrow = \left(-g^{\mu_T\nu_T} + i\epsilon^{\mu_T\nu_T}\right)/2$. The half difference between the polarization sums is

$$\frac{1}{2}\left(\epsilon^\mu_\downarrow\epsilon^{*\nu}_\downarrow - \epsilon^\mu_\uparrow\epsilon^{*\nu}_\uparrow\right) = \frac{1}{2}i\epsilon^{\mu_T\nu_T}, \tag{7.8}$$

To obtain the (absolute) double spin asymmetry in the distribution, we can replace $|M|^2$ in Eq.(7.5) by

$$|\mathcal{M}|^2_{\rm asym} = \frac{1}{4}\epsilon_{\mu_{1T}\,\nu_{1T}}\epsilon_{\mu_{2T}\,\nu_{2T}}\mathcal{M}^{\mu_{1T}\,\mu_{2T}}\mathcal{M}^{\nu_{1T}\,\nu_{2T}}, \tag{7.9}$$

while to obtain the unpolarized cross section, we use the averaged squared matrix element

$$|\mathcal{M}|^2_{\rm unpol} = \frac{1}{4}g_{\mu_{1T}\,\nu_{1T}}g_{\mu_{2T}\,\nu_{2T}}\mathcal{M}^{\mu_{1T}\,\mu_{2T}}\mathcal{M}^{\nu_{1T}\,\nu_{2T}}, \tag{7.10}$$

7.3 Outline of the proof by contradiction

7.3.1 Definitions of standard and generalized factorization

By standard factorization, we mean factorization derived by assuming the cancellation of spectator-spectator Glauber gluon exchanges. For the doubly differential beam thrust distribution (in the left and right hemispheres) in Drell-Yan production of a system of invariant

mass M, at hadronic c.o.m.collision energy E, the factorization formula in double Laplace moment space is [319, 166]

$$\begin{aligned}
&\int_0^\infty d\tau_R e^{-N_R\,\tau_R} \int_0^\infty d\tau_L e^{-N_L\,\tau_L} \frac{d^3\sigma\left(H_1+H_2\to\Phi+X\right)}{d\tau_R d\tau_L dy}\bigg|_{y=0} \\
&= H\left(\frac{M^2}{\mu_f^2},\alpha_s\left(\mu_f\right)\right)\tilde{B}_1\left(\frac{M^2}{N_R\,\mu_f^2},x,\alpha_s\left(\mu_f\right)\right)\tilde{B}_2\left(\frac{M^2}{N_L\,\mu_f^2},x,\alpha_s\left(\mu_f\right)\right) \\
&\times\tilde{S}\left(\frac{M^2}{N_R^2\,\mu_f^2},\frac{M^2}{N_L^2\,\mu_f^2},\alpha_s\left(\mu_f\right)\right)+\mathcal{O}\left(\frac{1}{N_R},\frac{1}{N_L}\right),
\end{aligned} \tag{7.11}$$

where $x = M/E$ is the Bjorken variable for both collinear sectors, as we imposed $y = 0$. H is the hard function. $\tilde{B}_1$ and $\tilde{B}_2$ are the two moment-space collinear functions, also called beam functions in the literature, for the collinear sectors initiated by the incoming hadrons H_1 and H_2, respectively. $\tilde{S}$ is the moment-space soft function. The beam function is the "virtuality-dependent PDF" [319], originally defined using SCET fields with implicit zero-bin subtraction [47]. In Appendix D we define the beam function using the scalar QCD fields used in this paper.

We now define generalized factorization by the following criteria. The differential cross section is written in the factorized form, Eq. (7.11), but we allow the hard, collinear, and soft functions to be defined as arbitrary functions that generally differ from how they are defined in standard factorization. Since our model involves perturbative hadron-parton coupling, we require the (7.11) to match the differential cross section order-by-order in α_s. The only dependence on the incoming state H_1, including the species of the hadron and the polarization, should be contained in $\tilde{B}_1$, and the same condition is imposed on H_2 and $\tilde{B}_2$.

Under either standard or generalized factorization, the double longitudinal spin asymmetry in the factorized differential cross section is, in schematic moment-space factorized form,

$$-\frac{1}{4}H\left(\tilde{B}_1^{\uparrow}-\tilde{B}_1^{\downarrow}\right)\left(\tilde{B}_2^{\uparrow}-\tilde{B}_2^{\downarrow}\right)\tilde{S}, \tag{7.12}$$

while the corresponding expression for single longitudinal spin asymmetry is

$$\frac{1}{2}H\left(\tilde{B}_1^{\uparrow}-\tilde{B}_1^{\downarrow}\right)\tilde{B}_2^{\text{unpol}}\tilde{S}. \tag{7.13}$$

In Eqs.(7.12) and (7.13), we used "↑", "↓", and "unpol" to denote right polarization, left polarization, and no polarization, respectively.

7.3.2 Violation of standard factorization

Since the model theory is parity-conserving, and since the active parton is a scalar that cannot carry longitudinal polarization, we can check from the definition of the beam function that $\tilde{B}_1$ and $\tilde{B}_2$ do not depend on the polarizations of the hadrons. This implies that the double spin asymmetry, given in the schematic factorized form Eq.(7.12), must vanish at leading power to all orders in α_s. But we need to consider additional contributions from the Glauber region in spectator-spectator interaction, and its overlap with other regions (to be

subtracted); if the sum of these contributions is non-zero, as we will find in the subsequent sections, we obtain a contradiction to standard factorization.[4]

7.3.3 Violation of generalized factorization

Suppose that the generalized collinear function, unlike the standard collinear function, has dependence on the polarization of the hadron. This may appear strange but is perfectly allowed by our broad definition of generalized factorization. Then we cannot yet rule out generalized factorization just from the non-zero value of the double spin asymmetry. An additional input is needed. It is an immediate consequence of parity conservation of our model theory that there must be vanishing single spin asymmetry in the doubly differential beam thrust distribution. Since the unpolarized scattering cross section is non-zero, the unpolarized beam function $\tilde{B}_2$ in Eq.(7.13) cannot be vanishing (except at isolated points, assuming the function is analytic). So $\tilde{B}_1^{\uparrow} - \tilde{B}_1^{\downarrow}$ must be almost everywhere zero, which means everywhere zero if the function is analytic. This again leads to a vanishing double spin asymmetry in Eq.(7.12). Therefore the non-zero result of the subsequent sections contradicts not only standard factorization but also generalized factorization with decoupled collinear sectors.

7.4 Vanishing diagrams

7.4.1 Vanishing LO diagram

We known that factorizable diagrams give a vanishing contribution to the double spin asymmetry in our model, but we will explicitly verify that the LO contribution from squaring the diagram in Fig.7.1 vanishes, to introduce notations and demonstrate cancellations that are also applicable to some non-factorizable diagrams. For brevity, we write

$$D\left(p\right) \equiv \frac{i}{p^2 + i\epsilon}, \tag{7.14}$$

$$\epsilon\left(p_1, p_2\right) \equiv \epsilon_{\mu_{1T}\,\mu_{2T}}\, p_1^{\mu_{1T}} p_2^{\mu_{2T}}. \tag{7.15}$$

The diagram evaluates to, given that p_1 and p_2 have no transverse components,

$$\begin{aligned} i\mathcal{M}_{\text{LO}}^{\mu_{1T}\,\mu_{2T}} &= (-i) g_\Phi 2ie\, k_1^{\mu_{1T}} (-2ie)\, k_2^{\mu_{2T}} D\left(k_1\right) D\left(k_2\right) \\ &= -4ie^2 g_\Phi\, k_1^{\mu_{1T}}\, k_2^{\mu_{2T}} D\left(k_1\right) D\left(k_2\right). \end{aligned} \tag{7.16}$$

In this expression we omitted the color factor δ_{ab}, with a and b being the color indices for the scalar / anti-scalar pair in the final state. Using Eq.(7.9), the resulting double spin asymmetry in the squared matrix element is,

$$\frac{1}{4}\epsilon_{\mu_{1T}\,\nu_{1T}}\epsilon_{\mu_{2T}\,\nu_{2T}}\mathcal{M}_{\text{LO}}^{\mu_{1T}\,\mu_{2T}}\left(\mathcal{M}_{\text{LO}}^{\nu_{1T}\,\nu_{2T}}\right)^* \propto \epsilon\left(k_1^T, k_1^T\right)\epsilon\left(k_2^T, k_2^T\right) = 0. \tag{7.17}$$

[4] We will actually show that the distribution is non-zero at some (τ_B, τ_L), but this is sufficient to imply that the distribution cannot be an identically vanishing function in moment space.

In contrast, the unpolarized spin-summed squared matrix element is, using Eqs.(7.3) for zero rapidity,

$$|\mathcal{M}_{\rm LO}|^2_{\rm unpol} = 2C_A \cdot \frac{1}{4} g_{\mu_{1T}\,\nu_{1T}} g_{\mu_{2T}\,\nu_{2T}} \mathcal{M}_{\rm LO}^{\mu_{1T}\,\mu_{2T}} \left(\mathcal{M}_{\rm LO}^{\nu_{1T}\,\nu_{2T}}\right)^* = 2C_A \cdot 4e^4 g_\Phi^2 \frac{(1-x)^4}{|k_{1T}|^2\,|k_{2T}|^2}, \quad (7.18)$$

In this expression we include the color factor C_A from the final-state color sum, and an overall factor of 2 to account for the possibility of reversing the complex scalar arrow (i.e.swapping scalar and anti-scalar). The explicit momentum components in Fig.7.1 have been used to evaluate $D(k_1)$ and $D(k_2)$. Using Eq. (7.18) as the squared matrix element in the phase space integral Eq. (7.5), we obtain the LO unpolarized beam thrust distribution

$$\left.\frac{d^3\sigma_{\rm LO}}{d\tau_R d\tau_L dy}\right|_{y=0,\tau_R=\tau_L=\tau_B/2} = \frac{M^2}{16\pi E^2} 2C_A \cdot 4e^4 g \Phi^2 (1-x)^4 I_{\rm LO}, \quad (7.19)$$

where we defined

$$\begin{aligned} I_{\rm LO} &= \int \frac{d^2k_{1T}}{(2\pi)^2} \int \frac{d^2k_{2T}}{(2\pi)^2} \delta\left(|k_{1T}|^2 - |k_{0T}|^2\right) \delta\left(|k_{2T}|^2 - |k_{0T}|^2\right) \frac{1}{|k_{1T}|^2\,|k_{2T}|^2} \\ &= \frac{1}{(4\pi)^2\,|k_{0T}|^4}. \end{aligned} \quad (7.20)$$

7.4.2 Vanishing one-loop cut diagram

Consider the diagram Fig.7.2 in which the two spectator lines are connected by one gluon that is either a Glauber gluon or a normal soft gluon, *in interference* with the complex conjugate of the LO diagram. We will show that the resulting contribution to the spin asymmetry has vanishing real and imaginary parts. For more general models and observables, the contribution is purely imaginary when the gluon has Glauber-like momentum, and cancels with the complex conjugate cut diagram [32, 322].[5] But in our special model theory, even the imaginary contribution vanishes. Fig.7.2 evaluates to, again noticing $p_1^T = p_2^T = 0$ and omitting the color factor $C_F\delta_{ab}$,

$$\begin{aligned} i\mathcal{M}_1^{\mu_{1T}\,\mu_{2T}} = -ig_\Phi \int \frac{d^4l}{(2\pi)^4} 4e^2 g_s^2 \, &\left(k_1^{\mu_{1T}} - l^{\mu_{1T}}\right) \left(k_2^{\mu_{2T}} + l^{\mu_{2T}}\right) (2p_1 - 2k_1 + l)\cdot(2p_2 - 2k_2 - l) \\ &D(l)\, D(p_1 - k_1 + l)\, D(p_2 - k_2 - l)\, D(k_1 - l)\, D(k_2 + l) \quad (7.21) \\ \approx -8ie^2 g_\Phi\, g_s^2 \left(p_1^+ - k_1^+\right)\left(p_2^- - k_2^-\right) &\int d^4l \, \left(k_1^{\mu_{1T}} - l^{\mu_{1T}}\right) \left(k_2^{\mu_{2T}} + l^{\mu_{2T}}\right) \\ &D(l)\, D(p_1 - k_1 + l)\, D(p_2 - k_2 - l)\, D(k_1 - l)\, D(k_2 + l), \quad (7.22) \end{aligned}$$

where we used approximation $l^+, l^- \ll Q$, applicable to both the Glauber and the normal soft region, after the "$\approx$" sign. Therefore, the interference between the diagram in Fig.7.2

[5] A rare exception is single transverse spin asymmetry, for which factorization can be violated by the exchange of only one Glauber gluon, because the resulting imaginary contribution is multiplied by another imaginary factor from the Dirac trace with γ^5, to give a real contribution [328].

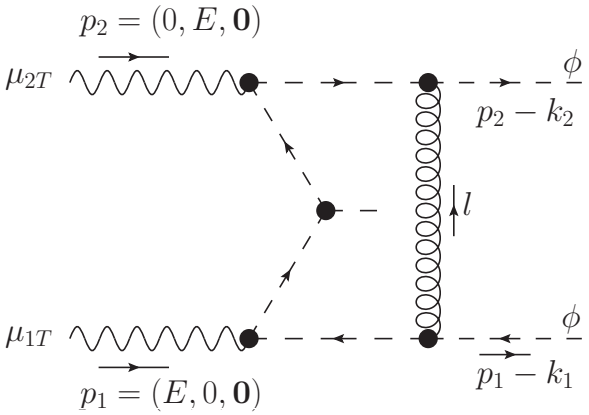

Figure 7.2: The one-Glauber exchange diagram in the model field theory.

and the complex conjugate of the LO diagram in Fig.7.1 is

$$\begin{aligned}&\epsilon_{\mu_{1T}\,\nu_{1T}}\epsilon_{\mu_{2T}\,\nu_{2T}}\mathcal{M}_1^{\mu_{1T}\,\mu_{2T}}\left(\mathcal{M}_{\rm LO}^{\nu_{1T}\,\nu_{2T}}\right)^*\\ &\propto \int d^4l\,\epsilon\left(k_1^T, l^T\right)\epsilon\left(k_2^T, l^T\right) D\left(l\right) D\left(p_1 - k_1 + l\right) D\left(p_2 - k_2 - l\right) D\left(k_1 - l\right) D\left(k_2 + l\right),\end{aligned} \tag{7.23}$$

where only l_T-dependent terms are shown after the proportional sign "$\propto$". Recall that we would like to measure the doubly-differential beam thrust distribution at some $\tau_L = \tau_R$, with the heavy particle Φ produced at zero rapidity. We still need to integrate the squared matrix element Eq.(7.23) over the phase space of k_1 and k_2 with appropriate measurement functions. Consider a particular point in the l-integration volume in Eq.(7.23), for example, a point with $l_x \neq 0$, $l_y = 0$ without loss of generality. Then we can flip the sign of the y component of k_1 without changing any terms in the integrand in Eq.(7.23) except for flipping the sign of $\epsilon\left(k_1^T, l^T\right)$. Since jet veto observables are azimutally symmetric and do not generate a preferred y-direction for k_1, Eq.(7.23) gives a vanishing contribution to the doubly differential beam thrust distribution. At some general value of l, the needed change of variable is

$$k_1^T \to R_{l^T} \circ k_1^T = (k_1^x, k_1^y) - 2\frac{l^x k_1^y - l^y k_1^x}{|l^T|^2}\left(-l^y, l^x\right), \tag{7.24}$$

denoting a reflection of k_1 in the line through the origin in the $\pm l_T$ direction. The squared matrix element in Eq.(7.23) has odd parity under this transformation, while the beam thrust variables (τ_R, τ_L) are invariant. Therefore the contribution vanishes after phase space integration.

7.4.3 Vanishing two-loop cut diagrams

Consider any cut diagram whose lower spectator line has only one gluon attachment, with the gluon being either soft or Glauber-like, such as the diagrams shown in Fig.7.3. As is the case for the one-gluon diagram in Fig.7.2, the lower collinear sector only depends on the following three momenta, p_1, k_1, and l. It is also easily checked that, again, at leading

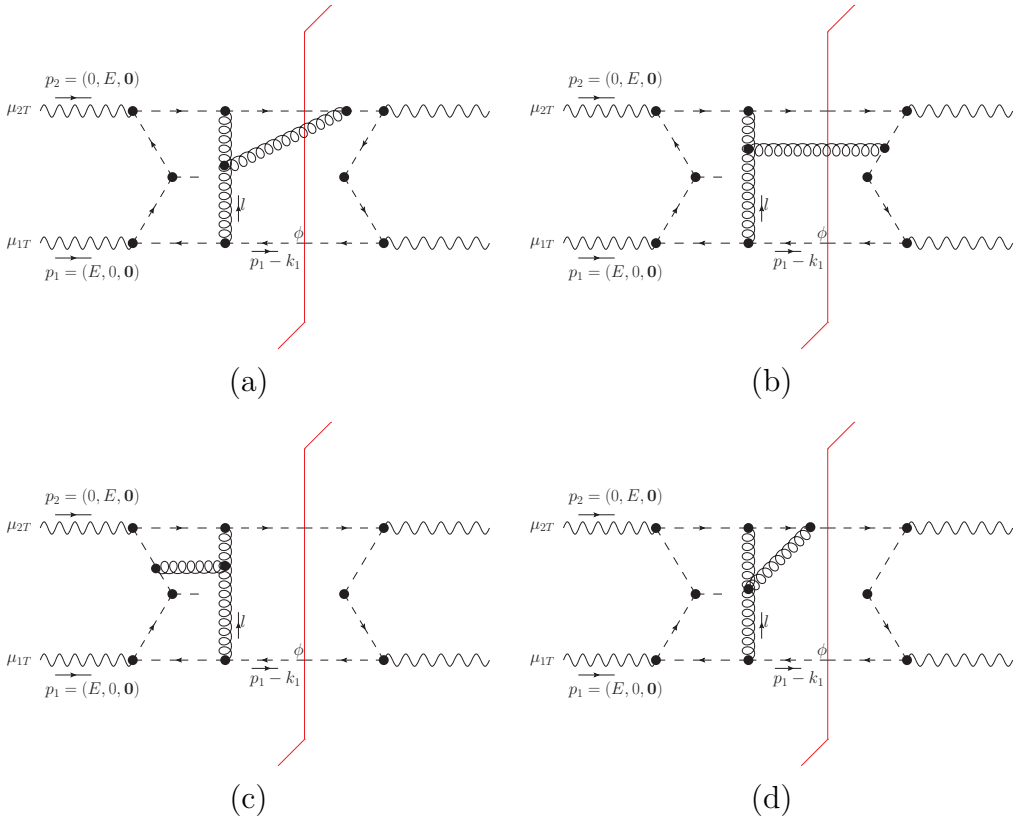

Figure 7.3: Example cut diagrams, each with only one gluon attached to the spectator line on the lower half of the graph, while more than one gluons may attach to the upper spectator line.

power, the only numerator factors that depends on l_T (or the other unlabeled transverse loop momenta) are the photon-scalar vertices.

Therefore, exactly the same transformation as in Sec. 7.4.1, Eq.(7.24), reverses the sign of the cut amplitude, and proves that the contribution is zero after phase space integration for k_1 and k_2.

To prove that the cut diagram in Fig.7.4, i.e. a 2-loop diagram with a box in interference with the complex conjugate of the LO diagram, vanishes, we need a little more work. Recall that a "pinch" in the Glauber region arises when both the active parton and spectator lines depend on the Glauber-like exchanged momentum. Since the active quark line in Fig.7.4 depends on l, but not l_1, only the overall exchanged momentum l can be pinched in the Glauber region $\sim (\lambda^2, \lambda^2, \lambda)$, to produce a potentially non-factorizable contribution. Meanwhile, it can be checked by IR power counting that the individual momenta l_1 and $l - l_1$ can be both Glauber-like, or both soft $\sim (\lambda, \lambda, \lambda)$, for the diagram to give a leading-power contribution.[6]

[6]If l is Glauber-like, l_1 and $l - l_1$ can also be both plus-collinear or both minus-collinear for the diagram to contribute at leading power. But it is not necessary to consider this situation, because the sum of diagrams involving a secondary hard vertex is suppressed by Ward identities, as shown by Labastida and Sterman [340].

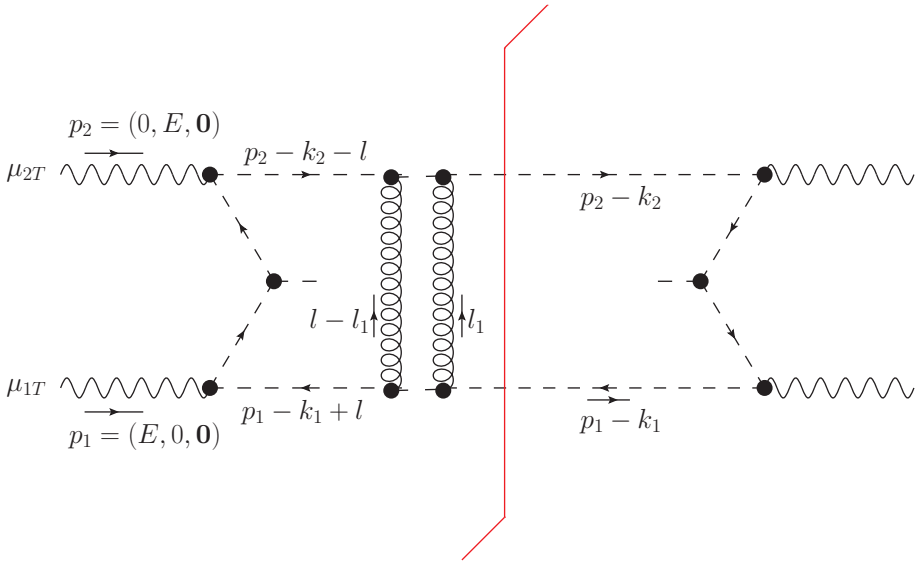

Figure 7.4: Two Glauber gluons exchanged on the same side of the cut, in the model field theory.

As is the case for diagram Fig.7.2, the only leading-power dependence of numerator factors on l_T is from the photon-scalar vertices. Here these vertices only depend on l_T but not l_{1T}. So the leading-power cut-amplitude is, omitting the color factor C_F^2 and other constant factors,

$$\begin{aligned}
&\epsilon_{\mu_{1T}\,\nu_{1T}}\epsilon_{\mu_{2T}\,\nu_{2T}}\mathcal{M}_2^{\mu_{1T}\,\mu_{2T}}\left(\mathcal{M}_{\rm LO}^{\nu_{1T}\,\nu_{2T}}\right)^* \\
\propto &\int d^4l\,\epsilon\left(k_1^T, l^T\right)\epsilon\left(k_2^T, l^T\right) D\left(k_1 - l\right) D\left(k_2 + l\right) D\left(p_1 - k_1 + l\right) D\left(p_2 - k_2 - l\right) \\
&\int d^4l_1\, D\left(l_1\right) D\left(l - l_1\right) D\left(p_1 - k_1 + l_1\right) D\left(p_2 - k_2 - l_1\right),
\end{aligned} \tag{7.25}$$

where we have collected all the l_1-dependent terms in the third line.

We briefly comment on the "Glauber-II" region discussed in [319], which has momentum scaling $(\lambda^4, \lambda^4, \lambda^2)$ instead of the usual Glauber scaling $(\lambda^2, \lambda^2, \lambda)$. The factor $\epsilon\left(k_1^T, l^T\right)\epsilon\left(k_2^T, l^T\right)$ in Eq.(7.25) and Eq.(7.23), absent in unpolarized scattering, gives a suppression when l_T is smaller than the usual Glauber transverse momentum. Therefore, even if the "Glauber-II" region is relevant for leading-power unpolarized scattering, it is not relevant here. Also there will be no singularity from $l_T \to 0$, which is important because the next step is analyzing the cut diagram at fixed l_T, assuming that the subsequent integration over l_T causes no complication.

With l being Glauber-like and l_1 being either Glauber-like or soft, the only propagators that have leading-power dependence on l^- are the two lines immediately connected to the lower incoming hadron p_1, and the only propagators that have leading-power dependence on l^+ are the two lines immediately connected to the upper incoming hadron p_2. So at any fixed l_T, we can perform the l^+ and l^- integrals by contour integration [32, 26], picking up

the poles by cutting the lines $p_2 - k_2 - l$ and $p_1 - k_1 + l$ in Fig.7.4, producing an imaginary contribution multiplied by a one-loop box diagram initiated by the on-shell lines $p_2 - k_2 - l$ and $p_1 - k_1 + l$. To obtain a real contribution that is not canceled by the complex conjugate cut diagram, we need another imaginary contribution from the one-loop box diagram, which can be obtained from the Glauber region of l_1.[7] Now with both l and l_1 being Glauber-like, we can make the following approximations for the l_1-dependent terms,

$$D(l_1) \approx \frac{i}{-|l_{1T}|^2 + i0}, \tag{7.26}$$

$$D(l - 1_1) \approx \frac{i}{-|l_T - l_{1T}|^2 + i0}, \tag{7.27}$$

$$D(p_1 - k_1 + l_1) \approx \frac{i}{(1-x)Q\left(\frac{|k_{1T}|^2}{(1-x)Q} + l_1^-\right) - |k_{1T} - l_{1T}|^2 + i0}, \tag{7.28}$$

$$D(p_2 - k_2 - l_1) \approx \frac{i}{(1-x)Q\left(\frac{|k_{2T}|^2}{(1-x)Q} - l_1^+\right) - |k_{2T} - l_{1T}|^2 + i0} \tag{7.29}$$

Therefore, integrating $D(p_1 - k_1 + l_1)$ and $D(p_2 - k_2 - l_1)$ over l_1^- and l_1^+, respectively, we obtain the constant factor $(-1)\pi^2/\left[(1-x)Q\right]^2$. We are left with just the two-dimensional $\int d^2 l_{1T}$ integral over $D(l_1)$ and $D(l - l_1)$. At this point, we can re-use the strategy for showing the vanishing of the interference between Fig.7.2 and the LO graph, and replace both k_1^T and l_1^T by their mirror images in the line through the origin in the direction of $\pm l^T$. The integrand reverses sign, and since this transformation does not affect the doubly differential beam thrust distribution, the final contribution from the cut diagram Fig.7.4 is zero. The diagram with a"cross box", in interference with the complex conjugate of the LO diagram, gives a vanishing contribution for exactly the same reason.

7.5 Non-zero two-Glauber diagram

We have excluded all cut diagrams whose lower (or upper) spectator line is attached by only one soft gluon (normal soft gluon or Glauber gluon) in Section 7.4.3. We have also excluded the diagram involving two Glauber gluons on the same side of the cut, including the diagram with a box, Fig.7.4, and an unshown diagram with a cross box. This leaves us, at the order α_s^2 relative to LO, the only possible contribution from the cut diagram in Fig.7.5, showing the interference of Fig.7.2 with its own complex conjugate. Out of the two soft gluons exchanged on the two sides of the cut, one has to be a Glauber gluon to produce factorization-violating effects, and then the other one also has to be a Glauber gluon to produce a real contribution that is not canceled by the complex conjugate cut diagram [32, 322].

[7] As shown in [310] for the scalar ϕ^3 theory, the Glauber region alone gives the correct imaginary part of the one-loop box diagram, while other regions, after being "unitarized" by removing the overlap with the Glauber region, do not contribute.

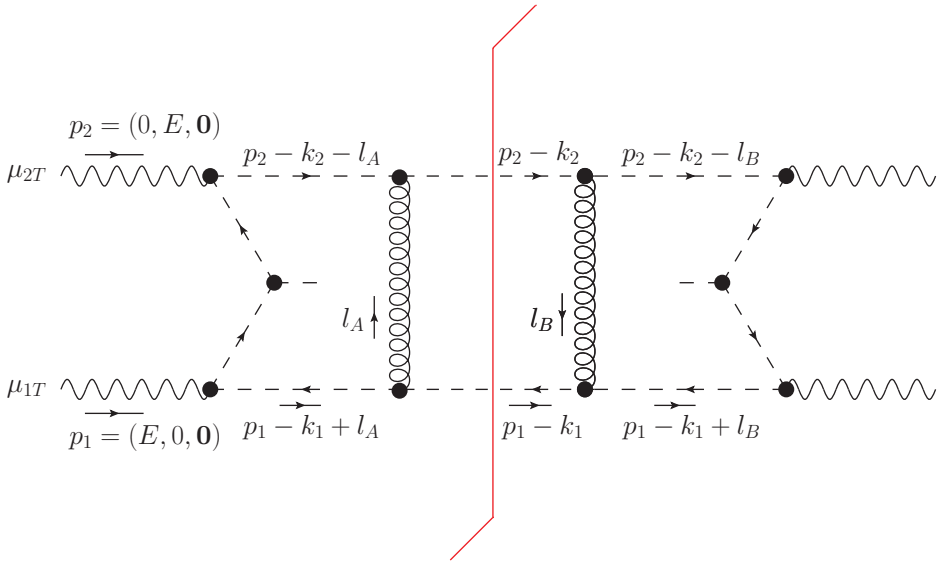

Figure 7.5: The cut diagram with one Glauber gluon exchanged on either side of the cut, i.e.the square of Fig.7.2.

7.5.1 Reducing to 2D integrals by contour integration

We show that the cut diagram Fig.7.5, from squaring the amplitude in Fig.7.2, gives a non-zero contribution to the double longitudinal spin asymmetry.

As above, we fix the heavy particle Φ to have zero rapidity, so that in Fig.7.5, $x_1 = x_2 = x$, $k_1^+ = k_2^- = xQ$, and the amplitude Eq.(7.22) can be re-written as

$$i\mathcal{M}_1^{\mu_{1T}\,\mu_{2T}} = -4ie^2 g_\Phi\, g_s^2 (1-x)^2 Q^2 \int \frac{dl^+ dl^- d^2 l_T}{(2\pi)^4}\, \left(k_1^{\mu_{1T}} - l^{\mu_{1T}}\right) \left(k_2^{\mu_{2T}} + l^{\mu_{2T}}\right) \\ D\left(l\right) D\left(p_1 - k_1 + l\right) D\left(p_2 - k_2 - l\right) D\left(k_1 - l\right) D\left(k_2 + l\right), \tag{7.30}$$

In this expression, with l lying in the Glauber region, the relevant leading-power approximations are

$$D(l) \approx \frac{i}{-l_T^2 + i0}, \tag{7.31}$$

$$D(p_1 - k_1 + l) \approx \frac{i}{(1-x)Q\left(\frac{|k_{1T}|^2}{(1-x)Q} + l^-\right) - |k_{1T} - l_T|^2 + i0}, \tag{7.32}$$

$$D(k_1 - l) \approx \frac{i}{xQ\left(-\frac{|k_{1T}|^2}{(1-x)Q} - l^-\right) - |k_{1T} - l_T|^2 + i0}, \tag{7.33}$$

$$D(p_2 - k_2 - l) \approx \frac{i}{(1-x)Q\left(\frac{|k_{2T}|^2}{(1-x)Q} - l^+\right) - |k_{2T} - l_T|^2 + i0}, \tag{7.34}$$

$$D(k_2 - l) \approx \frac{i}{xQ\left(-\frac{|k_{2T}|^2}{(1-x)Q} - l^+\right) - |k_{2T} - l_T|^2 + i0}, \tag{7.35}$$

We first integrate over l^+ and l^- using contour integration, picking up the poles from the vanishing of $D(p_1 - k_1 + l)$ and $D(p_2 - k_2 - l)$. We are left with the l_T integral,

$$i\mathcal{M}_1^{\mu_{1T}\,\mu_{2T}} = 4e^2 g_\Phi\, g_s^2 (1-x)^2 \int \frac{d^2 l_T}{(2\pi)^2}\, \left(k_1^{\mu_{1T}} - l^{\mu_{1T}}\right)\, \left(k_2^{\mu_{2T}} + l^{\mu_{2T}}\right) \frac{1}{|l_T|^2}\, \frac{1}{|k_{1T} - l_T|^2}\, \frac{1}{|k_{2T} + l_T|^2}, \tag{7.36}$$

So the asymmetry from the cut diagram Fig.7.5, using the spin sum formula Eq. (7.9), is

$$\begin{aligned} |\mathcal{M}_1|^2_{\text{asym}} &= 2C_F^2 C_A \int \frac{d^2 l_A}{(2\pi)^2} \int \frac{d^2 l_B}{(2\pi)^2} \frac{1}{4} \epsilon_{\mu_{1T}\,\nu_{1T}} \epsilon_{\mu_{2T}\,\nu_{2T}} \mathcal{M}_1^{\mu_{1T}\,\mu_{2T}} \left(\mathcal{M}_1^{\mu_{1T}\,\mu_{2T}}\right)^* \\ &= 2C_F^2 C_A \cdot 4e^4 g_\Phi^2\, g_s^4 (1-x)^4 \int \frac{d^2 l_A}{(2\pi)^2} \int \frac{d^2 l_B}{(2\pi)^2} \mathcal{I}_{\text{asym}}\left(k_{1T}, k_{2T}, l_A, l_B\right), \end{aligned} \tag{7.37}$$

where, using the notation in Eq.(7.15),

$$\begin{aligned} \mathcal{I}_{\text{asym}}\left(k_{1T}, k_{2T}, l_A, l_B\right) &= \epsilon\left(k_1 - l_A, k_1 - l_B\right) \epsilon\left(k_2 + l_A, k_2 + l_B\right) \\ &\times \frac{1}{|l_A|^2} \frac{1}{|k_{1T} - l_A|^2} \frac{1}{|k_{2T} + l_A|^2} \frac{1}{|l_B|^2} \frac{1}{|k_{1T} - l_B|^2} \frac{1}{|k_{2T} + l_B|^2}. \end{aligned} \tag{7.38}$$

In Eq.(7.37), the previously ignored color factor $C_F^2 C_A$ is shown, and an overall factor of 2 is present to account for the possibility of reversing the complex scalar arrow (i.e.swapping scalar and anti-scalar) in Fig.7.2. Using Eq. (7.37) as $|\mathcal{M}|^2$ in Eq. (7.5), we obtain

$$\left.\frac{d^3\sigma_{\text{asym}}}{d\tau_R d\tau_L dy}\right|_{y=0, \tau_R=\tau_L=\tau_B/2} = \frac{M^2}{16\pi E^2} 2C_F^2 C_A \cdot 4e^4 g \Phi^2\, g_s^4 (1-x)^4 I_{\text{asym}}, \tag{7.39}$$

where we defined I_{asym} as the loop and phase space integral over the integrand, Eq. (7.38),

$$\begin{aligned} I_{\text{asym}} = \int \frac{d^2 l_A}{(2\pi)^2} \int \frac{d^2 l_B}{(2\pi)^2} \int \frac{d^2 k_{1T}}{(2\pi)^2} \int \frac{d^2 k_{2T}}{(2\pi)^2} \\ \delta\left(|k_{1T}|^2 - |k_{0T}|^2\right) \delta\left(|k_{2T}|^2 - |k_{0T}|^2\right) \mathcal{I}_{\text{asym}}\left(k_{1T}, k_{2T}, l_A, l_B\right). \end{aligned} \tag{7.40}$$

7.5.2 Cancellation of IR divergences and numerical evaluation

Consider the l_A and l_B integrals in Eq.(7.40). Possible IR divergences may arise from the vanishing of any of the denominators in Eq.(7.38), if the singularities are not integrable. The singularities at $l_{A,B} = k_{1T}$ and $l_{A,B} = -k_{2T}$ are integrable, because the numerator factors on the 2nd line of Eq.(7.38) vanish at these points. However, there seems to be logarithmic singularities when l_A or l_B approaches zero. We show that this is not the case, because there is a linear suppression when l_A or l_B, becomes small, turning the singularities into integrable ones. The subsequent argument will be similar to Section 7.4.1, where we used the reflection of k_1 to show that the one-Glauber diagram vanishes. This suppression also implies that there is no leading power contribution from any regions with much smaller

transverse momenta, such as the ultra-soft region and the "Glauber-II" region discussed in [319], or from the overlap between these regions and the regular Glauber region.

We use $R_p \circ q$, defined in Eq.(7.24), to denote the reflection of the two-vector q with respect to to the line through the origin in the direction of the two-vector p. We then re-write Eq.(7.40) as

$$\begin{aligned} I_{\text{asym}} = \frac{1}{2} \int \frac{d^2k_{1T}}{(2\pi)^2} \int \frac{d^2k_{2T}}{(2\pi)^2} \, \delta\left(|k_{1T}|^2 - |k_{0T}|^2\right) \delta\left(|k_{2T}|^2 - |k_{0T}|^2\right) \\ \times \int \frac{d^2l_A}{(2\pi)^2} \int \frac{d^2l_B}{(2\pi)^2} \big[\mathcal{I}_{\text{asym}}\left(k_{1T}, k_{2T}, l_A, l_B\right) + \mathcal{I}_{\text{asym}}\left(R_{l_A} \circ k_{1T}, k_{2T}, l_A, l_B\right)\big]. \end{aligned} \tag{7.41}$$

In this form, the last line can be readily checked to vanish when l_B=0, and linearly suppressed when l_B is small. The Jacobian factor from the reflection is 1, so we simply need to put a factor of 1/2 at the start of Eq.(7.41). We go one step further by reflecting k_{2T} with respect to the line through l_B, recasting Eq.(7.40) into

$$\begin{aligned} I_{\text{asym}} = \frac{1}{4} \int \frac{d^2k_{1T}}{(2\pi)^2} \int \frac{d^2k_{2T}}{(2\pi)^2} \, \delta\left(|k_{1T}|^2 - |k_{0T}|^2\right) \delta\left(|k_{2T}|^2 - |k_{0T}|^2\right) \\ \times \int \frac{d^2l_A}{(2\pi)^2} \int \frac{d^2l_B}{(2\pi)^2} \big[\mathcal{I}_{\text{asym}}\left(k_{1T}, k_{2T}, l_A, l_B\right) + \mathcal{I}_{\text{asym}}\left(R_{l_A} \circ k_{1T}, k_{2T}, l_A, l_B\right) \\ \mathcal{I}_{\text{asym}}\left(k_{1T}, R_{l_B} \circ k_{2T}, l_A, l_B\right) + \mathcal{I}_{\text{asym}}\left(R_{l_A} \circ k_{1T}, R_{l_B} \circ k_{2T}, l_A, l_B\right)\big], \end{aligned} \tag{7.42}$$

where the sum inside the square bracket receive a linear suppression when either l_A or l_B become small, and a quadratic suppression when both l_A and l_B are made small simultaneously. This makes both the points $l_A,\ l_B = 0$ integrable singularities despite the quadratic denominators in Eq.(7.38). So the expression Eq.(7.42) is IR finite. UV finiteness is also clear by power counting. With both IR and UV divergences absent, Eq.(7.42) can be evaluated by straightforward Monte Carlo integration without regularization or subtraction. Using the Vegas algorithm implemented by the CUBA library [341], with 4.2 million points sampled, we obtain

$$I_{\text{asym}} = (1.58 \pm 0.02) \frac{1}{(4\pi)^4 \left|k_{0T}\right|^4} \tag{7.43}$$

Dividing the absolute asymmetry given by Eqs.(7.39) and (7.43) by the LO unpolarized differential cross section given by Eqs.(7.19) and (7.20), we obtain the relative spin asymmetry

$$\begin{aligned} \left(\frac{d^3\sigma_{\text{asym}}}{d\tau_R d\tau_L dy} \Big/ \frac{d^3\sigma_{\text{LO}}}{d\tau_R d\tau_L dy}\right)\Bigg|_{y=0, \tau_R=\tau_L=\tau_B/2} &= C_F^2 g_s^4 \cdot I_{\text{asym}}/I_{\text{LO}} \\ &= (1.58 \pm 0.02) C_F^2 \alpha_s^2. \end{aligned} \tag{7.44}$$

We have shown that the asymmetry is non-zero, proving that Glauber gluons break factorization for the doubly differential beam thrust distribution.

7.6 Discussion

We have performed a calculation of factorization-violating effects in the beam thrust distribution from Drell-Yan-like scattering in a simple model field theory. Any factorization in the

limit of small beam thrust (corresponding to a stringent jet veto), standard or generalized, would predict a vanishing double longitudinal spin asymmetry, due to the scalar nature of the active quarks in this parity-conserving model. The non-zero result found in our calculation is in contradiction to any generalized factorization that separates beam-thrust dependence into universal functions. The non-factoring contribution, Eq. (7.44), is in fact infrared safe, which shows that collinear factorization is respected to this order, but with factorization scale $\mu_F = \mathcal{O}(\sqrt{\tau_B s})$. Logarithms of beam thrust are thus contained in the hard-scattering function of collinear factorization, and standard resummation methods do not reply. The breakdown of generalized factorization would eventually lead to corrections to the existing predictions of jet veto resummation calculations [164, 165, 168, 167, 169, 170].

The question remains, *"At which logarithmic order do such corrections start?"* The lowest-order factorization-violating diagram in this study involves two spectator lines and two virtual Glauber gluons, producing a non-zero result. This would be of order α_s^4 if we were studying massless parton scattering instead of photon-photon scattering. This result contains no large logarithms for two reasons. First, the intrinsic virtuality of collinear particles, anti-collinear particles, and Glauber gluons are all of the order $Q^2\tau_B$ [319]. Second, the order of the diagram is too low to acquire Regge-type rapidity logarithms, which will show up at higher orders in ladder-type diagrams. But we still need to multiply the result by the hard function (which always factorizes, though collinear and soft functions can be entangled by Glauber gluons), with double logarithms $\sim \alpha_s^n \ln^{2n} \tau_B$ due to running from the scale Q^2 to $Q^2\tau_B$. We end up with $\alpha_s^{n+4} \ln^{2n} \tau_B$. In unpolarized scattering, there can also be a non-zero contribution when two soft / Glauber gluons are exchanged on the same side of the cut, which potentially gives one power of a Regge-type logarithm, resulting in $\alpha_s^{n+4} \ln^{2n+1} \tau_B$. This suggests a breakdown of naive jet veto resummation at no later than $\mathrm{N^4LL}$.

A corollary of the study is that a proper description of the Drell-Yan process with stringent jet vetoes must include entanglement between the two collinear sectors. It should be noted that our study only demonstrates the inevitability of entangling the two collinear sectors, while soft and ultra-soft gluons may still be allowed to factorize in some manner.

Chapter 8

Conclusions

QCD factorization underlies most predictions for LHC observations. In collinear factorization, the parton distribution functions are factorized out, and fixed-order calculations of the hard scattering function can then be performed. In more complicated situations near phase space boundaries, e.g. at low p_T or near the partonic center-of-mass threshold, the hard scattering function is further factorized, and evolution equations can be used to resum large logarithms in the hard scattering function to all orders in α_s.

QCD factorization was first proved in the Collins-Soper-Sterman formalism, using a range of techniques including the Landau equations, reduced diagrams, Libby-Sterman IR power counting, diagrammatic Ward identities and unitarity, and momentum-space contour deformations. Given the apparent complexity of hadron collisions, it is remarkable that the factorization proofs have been established from first principles, with a high degree of rigor. QCD factorization was subsequently re-formulated in soft collinear effective theory (SCET) using the language of EFT and path integrals. This is not surprising, given that some aspects of QCD factorization have strong analogies with EFTs. For example, it was observed long ago [25] that the separation of hard, collinear and soft contributions by a "floating" scale is analogous to "matching conditions" in effective field theories. SCET is distinguished from conventional EFTs in allowing the IR degrees of freedom to have inhomogeneous momentum scalings, but otherwise re-uses conventional EFT techniques including power counting, symmetry constraints on interaction terms, field re-definitions, RG running, and so on.

Some other aspects of QCD factorization proofs have so far eluded SCET. An example is the cancellation of the Glauber region in the Sudakov form factor, by contour deformation. It is an interesting problem how this can be achieved in a non-diagrammatic manner by manipulations of the SCET path integral. A solution would have to go beyond conventional EFT techniques, because conventional EFTs have a single IR region, instead of multiple IR regions that are connected by contour deformations. The Glauber region in the Drell-Yan process would present an even greater challenge.

But in most real-world applications of leading-power factorization, for sufficiently inclusive observables, SCET and "direct" QCD (dQCD) methods agree perfectly. For threshold resummation, this thesis made a detailed comparison of threshold resummation via SCET and dQCD. The fundamental factorization and evolution equations are essentially the same. It turns out that the real discrepancy in the published literature using these two methods is a rather minor one, i.e. the choice of soft scale. The SCET literature uses a single "global"

soft scale obtained from minimizing loop-corrections to the soft function, while the dQCD literature uses a dynamical soft scale depending on the Mellin moment N. The behavior of realistic parton luminosity functions underlies the close agreement between numerical predictions resulting from the two scale choices.

Threshold resummation effects are modest in typical LHC processes, because the parton luminosity function does not fall off that steeply when the Bjorken variables of the two partons are small. This is especially true when the process is mainly initiated by quarks rather than gluons. For example, for W^+W^- production from proton collisions, we observe an increase of the cross section by at most a few percent after threshold resummation is carried out.

However, p_T resummation can have more dramatic effects, because the low p_T region can be easily accessed in colliders. The resummed p_T spectrum in electroweak production is qualitatively different from the fixed-order p_T spectrum, as the former does not show an unphysical divergence as $p_T \to 0$. Parton shower programs, widely relied upon in experimental analyses, give a p_T spectrum that is correct to the leading logarithmic (LL) order, but a dedicated resummation calculation is needed to give accurate NNLL predictions. We performed p_T resummation for W^+W^- pair production at the LHC, and used the results to reweight events generated by parton shower programs. The reweighting changed the jet veto efficiency by $3-7\%$, and reduced tension between theory and experiment. The wider lesson is that there are often substantial, and possibly poorly understood, uncertainties in radiative corrections within the SM, which need to be taken into account in interpreting new physics signatures.

Both our threshold resummation and p_T resummation studies for W^+W^- production, and the jet veto resummation study for this process in [114], have been performed using 1-loop soft, hard, and collinear functions, matched to NLO fixed-order result, in the approximation that the W bosons are produced on-shell. There is obviously room for improvement. First, the narrow width approximation may be lifted for one or both of the W bosons. Second, the 2-loop virtual correction for fully off-shell W^+W^- production has recently been computed by two groups [342, 343], from which we should be able to extract the 2-loop hard function. The improved resummation result should be matched to the NNLO fixed-order result. Taking these steps would help resolve lingering uncertainties in the W^+W^- production cross section at the LHC.

Transverse momentum resummation for electroweak production and threshold resummation for general processes are on very firm theoretical footings, as the relevant factorization theorems have been established to all orders in α_s. But resummation for other observables, for example electroweak production subject to a jet veto, has not been completely understood. From our analysis of factorization-violating effects, we expect the current jet veto resummation methods to break down at sufficiently high logarithmic orders, due to Glauber gluons that fail to cancel. The physics is closely connected with forward scattering and multi-parton interactions. A future phenomenological study, e.g. for Higgs production and W^+W^- production under jet vetoes, is warranted.

With the LHC finding no "smoking gun" signals for resonant new physics, higher-dimensional operators have gained prominence as a model-independent way to parameterize possible deviations from the SM. We studied Higgs-gluon operators and their impacts on the Higgs p_T spectrum resulting from gluon fusion. The differential distribution at high p_T is

sensitive to many new physics models that otherwise have little effect on the total cross section. We find that in most realistic scenarios, the operator hG^2 alone gives a good description of the effects of new physics on the Higgs p_T spectrum. We recommend a two-parameter fit of the Higgs p_T spectrum, involving the matching coefficient of the hG^2 operator and the Higgs-top Yukawa coupling strength. Yet higher-dimensional operators only contribute significantly when we get into the kinematic region in which the non-covergent nature of the EFT power expansion becomes apparent. This is a generic problem when applying EFT methods beyond the leading power.

At smaller p_T, below 200 GeV, it is also useful to integrate out the top quark and absorb the effects into Higgs-gluon effective operators. A large number of theoretical predictions in the literature uses the hG^2 operator only, corresponding to the limit $m_t \to \infty$. We find that studying yet higher dimensional operators produce useful insights into the accuracy of the $m_t \to \infty$ approximation for the Higgs p_T distribution. For example, the high accuracy of this approximation for the gg channel, compared with quark channels, is explained by the fact that the hG^3 amplitudes do not interfere with hG^2 amplitudes in certain kinematic limits. However, again due to the non-convergent nature of the EFT power expansion, it would be of great interest to calculate the $H + j$ production cross section to NLO with full dependence on m_t, which may become possible given the rapid theoretical progress in 2-loop massive Feynman integrals.

Appendix A

Threshold resummation technicalities

A.1 Relating different forms of the non-leading resummation function

At first sight, the moment space form of the resummed exponent, Eq. (2.34) looks rather different than the exponent in Eq. (2.18), found by solving the soft function evolution equation. To leading power in N, however, the Mellin expression in Eq. (2.34) can be rewritten as a double integral in which N appears only in the limits of integration, acted upon by an infinite series of derivatives,

$$\begin{aligned} E\left(N,M\right) &= -\int_0^1 dz \frac{z^{N-1}-1}{1-z}\left[4\int_{(1-z)M}^{M}\frac{d\mu'}{\mu'}A\left(\alpha_s\left(\mu'\right)\right) - D\left(\alpha_s\left((1-z)M\right)\right)\right] \\ &= \sum_{k=0}^{\infty}\frac{\Gamma^{(k)}(1)}{k!}\frac{d^k}{d\ln^k\frac{1}{N}}\int_0^{1-1/N}\frac{dz}{1-z}\left[4\int_{(1-z)M}^{M}\frac{d\mu'}{\mu'}A\left(\alpha_s\left(\mu'\right)\right) - D\left(\alpha_s\left((1-z)M\right)\right)\right] \\ &\quad + \mathcal{O}\left(\frac{1}{N}\right) \\ &\equiv \Gamma\left(1+2\frac{d}{d\ln\frac{1}{N^2}}\right)\int_0^{1-1/N}\frac{dz}{1-z}\left[4\int_{(1-z)M}^{M}\frac{d\mu'}{\mu'}A\left(\alpha_s\left(\mu\right)\right) - D\left(\alpha_s\left((1-z)M\right)\right)\right], \end{aligned} \tag{A.1}$$

where we have set $\mu_f = M$ for simplicity. In the second equality we have replaced the explicit Mellin moment by a modified upper limit in the z integral, using the identity,

$$\int_0^1 dz\, z^{N-1}\left[\frac{\ln^p(1-z)}{1-z}\right]_+ = -\sum_{k=0}^{p+1}\frac{\Gamma^{(k)}(1)}{k!}\frac{d^k}{d\ln^k\frac{1}{N}}\int_0^{1-1/N}dz\,\frac{\ln^p(1-z)}{1-z} + \mathcal{O}\left(\frac{1}{N}\right). \tag{A.2}$$

This relation holds for any power of $\ln(1-z)$, up to inverse powers of N as indicated. It therefore applies to the full μ' integral in (A.1), which is an expansion in logarithms of $1-z$ only. A proof of (A.2) follows from using $(1-z)^\delta$ as a generating function for powers of $\ln(1-z)$, as in Ref. [344]. Following Refs. [70] and [71], we now go on to review how the action of the derivatives can be absorbed into a modified function $D(\alpha_s)$, as in Eq. (2.40).

To make closer contact with the alternate form of the exponent, we change variables in Eq. (A.1) to $\mu = (1-z)M$, giving

$$E(N,M) = \Gamma\left(1 + 2\frac{\partial}{\partial \ln\left(\frac{M}{N}\right)^2}\right) \int_{M/N}^{M} \frac{d\mu}{\mu} \left[4\int_{\mu}^{M} \frac{d\mu'}{\mu'} A\left(\alpha_s\left(\mu'\right)\right) - D\left(\alpha_s\left(\mu\right)\right)\right], \quad \text{(A.3)}$$

again, up to power corrections in N. Here, we have converted the derivative with respect to $\ln N$ to a derivative with respect to $\ln(M/N)$, treating M and M/N as independent. To streamline subsequent expressions, we define a function that represents the integrals on which the derivatives in Eq. (A.2) act,

$$I\left(\rho, M\right) = \int_{\rho}^{M} \frac{d\mu}{\mu} \left[\int_{\mu}^{M} \frac{d\mu'}{\mu'} 4A\left(\alpha_s\left(\mu'\right)\right) - D\left(\alpha_s\left(\mu\right)\right)\right], \quad \text{(A.4)}$$

where in (A.3), $\rho = M/N$. We now introduce the notation [71],

$$\nabla \equiv \frac{d}{d\ln\rho^2} = \frac{\beta\left(\alpha_s\left(\mu'\right)\right)}{2} \frac{d}{d\alpha_s(\mu')}, \quad \text{(A.5)}$$

and use $2e^{\gamma_E \nabla}$ to translate the lower limit of the μ integral in Eq. (A.4),

$$\begin{aligned} E\left(\frac{M}{N}, M\right) &= \Gamma\left(1+2\nabla\right) I\left(\frac{M}{N}, M\right) \\ &= \left[e^{\gamma_E 2\nabla}\Gamma\left(1+2\nabla\right)\right] e^{-\gamma_E 2\nabla} I\left(\frac{M}{N}, M\right) \\ &= \left[e^{\gamma_E 2\nabla}\Gamma\left(1+2\nabla\right)\right] I\left(\frac{M}{\bar{N}}, M\right), \end{aligned} \quad \text{(A.6)}$$

where, as above, $\bar{N} \equiv e^{\gamma_E} N$. The expansion

$$\begin{aligned} e^{2\gamma_E\nabla}\Gamma\left(1+2\nabla\right) &= 1 + \frac{\pi^2}{12}(2\nabla)^2 - \frac{1}{3}\zeta\left(3\right)(2\nabla)^3 \ + \ \cdots \\ &\equiv 1 + \sum_{k=2}^{\infty} a_k (2\nabla)^k \end{aligned} \quad \text{(A.7)}$$

has no linear term in ∇. Carrying out the derivatives of Eq. (A.3) in this notation, we find

$$\begin{aligned} e^{2\gamma_E\nabla}\Gamma\left(1+2\nabla\right) I\left(\frac{M}{\bar{N}}, M\right) &= I\left(\frac{M}{\bar{N}}, M\right) \\ &\quad + \sum_{k=2}^{\infty} a_k \left[4\nabla^{k-2} A\left(\alpha_s\left(M/\bar{N}\right)\right) + \nabla^{k-1} D\left(\alpha_s\left(M/\bar{N}\right)\right)\right], \end{aligned} \quad \text{(A.8)}$$

which depends on M only through the running coupling $\alpha_s(M/N)$. The derivatives ∇ may therefore also be converted to derivatives with respect to the coupling, as in (A.5) above.

With these results in hand, we rewrite the derivative terms in (A.8) in a way that reintroduces an integral over the scale of the running coupling,

$$4\nabla^{k-2}A\left(\alpha_s\left(M/\bar{N}\right)\right)+\nabla^{k-1}D\left(\alpha_s\left(M/\bar{N}\right)\right)=4\nabla^{k-2}A\left(\alpha_s\left(M\right)\right)+\nabla^{k-1}D\left(\alpha_s\left(M\right)\right)$$
$$+\int_{M/\bar{N}}^{M}\frac{d\mu'}{\mu'}\left[-4\nabla^{k-1}A\left(\alpha_s\left(\mu'\right)\right)-\nabla^{k}D\left(\alpha_s\left(\mu'\right)\right)\right]. \qquad \text{(A.9)}$$

In this expression, of course, the M dependence of the constant term is canceled by the upper limit of the integral. Thus, up to an $\bar{N}$-independent constant that only affects the overall cross section, substituting Eq. (A.9) into the final expression for the exponent E in Eq. (A.6) gives

$$E\left(\frac{M}{N},M\right)\cong\int_{M/\bar{N}}^{M}\frac{d\mu}{\mu}\left[\int_{\mu}^{M}\frac{d\mu'}{\mu'}4A\left(\alpha_s\left(\mu'^2\right)\right)-\hat{D}\left(\alpha_s\left(\mu^2\right)\right)\right]$$
$$=\int_{M/\bar{N}}^{M}\frac{d\mu}{\mu}\left[-4A\left(\alpha_s\left(\mu\right)\right)\left(\ln\frac{M}{N\mu}\right)-\hat{D}\left(\alpha_s\left(\mu\right)\right)\right], \qquad \text{(A.10)}$$

where we drop the "constant" terms that depend only on $\alpha_s(M)$, and where in the second expression we first perform the μ integral, and then relabel μ' as μ. A modified D term, $\hat{D}$, has been introduced to absorb the effects of all derivatives ∇^k, $k\geq 2$ in the expansion of Eq. (A.6), where

$$\hat{D}\left(\alpha_s\left(\mu\right)\right)\equiv e^{2\gamma_E\nabla}\Gamma\left(1+2\nabla\right)D\left(\alpha_s\left(\mu\right)\right)+\frac{e^{2\gamma_E\nabla}\Gamma\left(1+2\nabla\right)-1}{\nabla}A\left(\alpha_s\left(\mu\right)\right), \qquad \text{(A.11)}$$

the result given in Ref. [70] .

A.2 The single power approximation with model parton distributions

In this appendix, we confirm explicitly the single-power expansion for parton distributions of the general form, $x^{-\delta}(1-x)^{\beta}$, $\delta,\ \beta>0$. As mentioned in Section 2.5.1, the convolution of two such parton distribution functions, gives a parton luminosity function of the form

$$\mathcal{L}(\tau)=C^2\tau^{-\delta}(1-\tau)^{2\beta+1}F(\beta+1,\beta+1;2\beta+2;1-\tau), \qquad \text{(A.12)}$$

where the constant C is independent of τ. We will study the behavior of this luminosity first in the small-τ limit and then for τ of order unity.

For $\tau\ll 1$ we use the expansion

$$F(a,b;a+b;u)=\frac{\Gamma(a+b)}{\Gamma(a)\Gamma(b)}\sum_{n=0}^{\infty}\frac{(a)_n(b)_n}{(n!)^2}$$
$$\times\ \left[2\psi(n+1)-\psi(a+n)-\psi(b+n)-\ln(1-u)\right](1-u)^n, \qquad \text{(A.13)}$$

in terms of the Polchhammer symbol $(a)_n = \Gamma(a+n)/\Gamma(a)$. For small τ, we can approximate the hypergeometric function simply by the first term in its expansion Eq. (A.13), and

$$\mathcal{L}(\tau) = C^2 \tau^{-\delta} \left(\ln \frac{1}{\tau} - 2\psi(\beta+1) - 2\gamma_E \right) , \tag{A.14}$$

which implies, for the logarithmic derivatives of the luminosity, Eq. (2.64),

$$\begin{aligned} s_1(\tau) &= \delta + \left(\ln \frac{1}{\tau} - 2\psi(\beta+1) - 2\gamma_E \right)^{-1} , \\ s_n(\tau) &= (n-1)! \left(\ln \frac{1}{\tau} - 2\psi(\beta+1) - 2\gamma_E \right)^{-n} . \end{aligned} \tag{A.15}$$

In the limit $\tau \to 0$, $s_1(\tau) \to \delta$ while $s_n(\tau)$ vanishes like $[\ln(1/\tau)]^{-n}$, confirming the validity of the single power approximation, even when the power δ is not large.

For large values of τ, it is convenient to use the integral form of the luminosity function,

$$\begin{aligned} \mathcal{L}(\tau) &\propto \int_\tau^1 \frac{dz}{z} z^{-\delta} (1-z)^\beta \left(\frac{\tau}{z} \right)^{-\delta} \left(1 - \frac{\tau}{z} \right)^\beta \\ &= \tau^{-\delta} \int_\tau^1 \frac{dz}{z} (1-z)^\beta \left(1 - \frac{\tau}{z} \right)^\beta , \end{aligned} \tag{A.16}$$

so that we have

$$\begin{aligned} s_1(\tau) &= -\frac{1}{\mathcal{L}(\tau)} \tau \frac{d}{d\tau} \mathcal{L}(\tau) \\ &= \delta + \frac{\beta\, \tau \int_\tau^1 \frac{dz}{z^2} (1-z)^\beta \left(1 - \frac{\tau}{z} \right)^{\beta-1}}{\int_\tau^1 \frac{dz}{z} (1-z)^\beta \left(1 - \frac{\tau}{z} \right)^\beta} . \end{aligned} \tag{A.17}$$

In the large β limit, both the integral in the numerator and the integral in the denominator can be performed using the saddle point approximation. Both integrands reach their maxima at approximately $z = \sqrt{\tau}$ and have nearly the same peak width. The ratio of the two integrals is then well approximated by the ratio of the integrands at $z = \sqrt{\tau}$,

$$\begin{aligned} s_1(\tau) &\approx \delta + \left. \frac{\beta\, \tau}{z \left(1 - \frac{\tau}{z} \right)} \right|_{z=\sqrt{\tau}} \\ &= \delta + \beta \frac{\sqrt{\tau}}{(1-\sqrt{\tau})} , \end{aligned} \tag{A.18}$$

and

$$s_n(\tau) = \beta \left(\frac{d}{d \ln \tau} \right)^{n-1} \frac{\sqrt{\tau}}{(1-\sqrt{\tau})} . \tag{A.19}$$

Therefore, $s_1(\tau) = \delta + \beta\sqrt{\tau} + \mathcal{O}(\sqrt{\tau})$ and $(1/n!)\, s_n(\tau) / [s(\tau)]^n = O(\beta^{-(n-1)}) << 1$, suggesting that the single power approximation is valid for τ large as well as small.

Appendix B

W^+W^- production

B.1 Fixed Order Results

B.1.1 Lowest Order Results

The coefficients of Eq. (3.8) are [116]

$$\begin{aligned}
c_q^{tt} &= \frac{\pi^2\alpha_{EM}^2}{s_W^2} \\
c_q^{ts}(s) &= \frac{4\pi^2\alpha_{EM}^2}{s_W^2}\frac{1}{s}\left(Q_q + \frac{s}{s-M_Z^2}\frac{1}{s_W^2}(T_{3,q}-Q_q s_W^2)\right) \\
c_q^{ss}(s) &= \frac{16\pi^2\alpha_{EM}^2}{s^2}\left\{\left(Q_q + \frac{1}{2s_W^2}(T_{3,q}-2Q_q s_W^2)\frac{s}{s-M_Z^2}\right)^2 + \left(\frac{T_{3,q}}{2s_W^2}\frac{s}{s-M_Z^2}\right)^2\right\} \qquad \text{(B.1)}
\end{aligned}$$

with $T_{3,q} = \pm\frac{1}{2}$ and $s_W = \sin\theta_W$. The functions occurring in the lowest order amplitudes are,

$$\begin{aligned}
F_u^0(s,t) &= F_d^0(s,u) \\
&= 16\left(\frac{ut}{M_W^4}-1\right)\left(\frac{1}{4}+\frac{M_W^4}{t^2}\right)+16\frac{s}{M_W^2} \\
J_u^0(s,t) &= -J_d^0(s,u) \\
&= 16\left(\frac{ut}{M_W^4}-1\right)\left(\frac{s}{4}-\frac{M_W^2}{2}-\frac{M_W^4}{t}\right)+16s\left(\frac{s}{M_W^2}-2+\frac{2M_W^2}{t}\right) \\
K_u^0(s,t) &= K_d^0(s,u) \\
&= 8\left(\frac{ut}{M_W^4}-1\right)\left(\frac{s^2}{4}-sM_W^2+3M_W^4\right)+8s^2\left(\frac{s}{M_W^2}-4\right). \qquad \text{(B.2)}
\end{aligned}$$

B.1.2 NLO Results

The functions occurring in the one-loop virtual amplitude are[116],

$$
\begin{aligned}
F_u^1(s,t) &= \frac{4(80t^2+73st-140M_W^2t+72M_W^4)}{t^2}-\frac{4(4t+s)^2}{s\beta^2t}-\frac{128(t+2s)}{M_W^2}\\
&+\frac{64(t+s)}{M_W^4}-\left(\frac{32(t^2-3st-3M_W^4)}{t^2}+\frac{128s}{t-M_W^2}\right)\log\left(\frac{-t}{M_W^2}\right)\\
&+\left(\frac{8(6t^2+8st-19M_W^2t+12M_W^4)}{t^2}-\frac{32t^2-128st-26s^2}{s\beta^2t}+\frac{6(4t+s)^2}{s\beta^4t}\right)\log\left(\frac{s}{M_W^2}\right)\\
&+32s\left(\frac{2M_W^4}{t}-u\right)I_4-64(t-M_W^2)\left(\frac{2M_W^4}{t^2}-\frac{u}{t}\right)I_{3t}\\
&+\left(\frac{16t(4M_W^2-u)-49s^2+72M_W^2s-48M_W^4}{2t}+\frac{2(8t^2-14st-3s^2)}{\beta^2t}-\frac{3(4t+s)^2}{2\beta^4t}\right)I_{3l}\\
&+\frac{32\pi^2}{3}\left(\frac{2(t+2s)}{M_W^2}-\frac{3t+2s-4M_W^2}{t}-\frac{t(t+s)}{M_W^4}\right)\\
J_u^1(s,t) &= -\frac{128(t^2+2st+2s^2)}{M_W^2}-\frac{16(t^2-21st-26M_W^2t+34M_W^2s+17M_W^4)}{t}\\
&+\frac{64st(t+s)}{M_W^4}+\frac{32s^2}{t-M_W^2}\\
&+\left(16(t-5s+2M_W^2)-\frac{48M_W^2(2s+M_W^2)}{t}+\frac{64s(2t+s)}{t-M_W^2}-\frac{32s^2t}{(t-M_W^2)^2}\right)\log\left(\frac{-t}{M_W^2}\right)\\
&+\left(\frac{16(4t+s)}{\beta^2}-16(3t-2s)+\frac{48M_W^2(2t-2s-M_W^2)}{t}\right)\log\left(\frac{s}{M_W^2}\right)\\
&+16s\left(t(2s+u)-2M_W^2(2s+M_W^2)\right)I_4+32(t-M_W^2)\left(\frac{2M_W^2(2s+M_W^2)}{t}-2s-u\right)I_{3t}\\
&+\left(32st-12s^2+32M_W^4-16M_W^2(2t+7s)-\frac{4s(4t+s)}{\beta^2}\right)I_{3l}\\
&+\frac{32\pi^2}{3}\left(\frac{2(t^2+2st+2s^2)}{M_W^2}-\frac{st(t+s)}{M_W^4}-\frac{2M_W^2(2t-2s-M_W^2)}{t}-t-4s\right)\\
K_u^1(s,t) &= 16\Bigg\{12t^2+20st-24M_W^2t+17s^2-4M_W^2s+12M_W^4+\frac{s^2t(t+s)}{M_W^4}\\
&-\frac{2s(2t^2+3st+2s^2)}{M_W^2}\Bigg\}(2-\frac{\pi^2}{3})
\end{aligned}
\tag{B.3}
$$

with $F_d^1(s,t) = F_u^1(s,u)$, $J_d^1(s,t) = -J_u^2(s,u)$, and $K_d^1(s,t) = K_u^1(s,u)$. The integrals are given by

$$\begin{aligned} I_4 &= \frac{1}{st}\left(2\log^2\left(\frac{-t}{M_W^2}\right) - 4\log\left(\frac{M_W^2-t}{M_W^2}\right)\log\left(\frac{-t}{M_W^2}\right) - 4\mathrm{Li}_2\left(\frac{t}{M_W^2}\right)\right) \\ I_{3t} &= \frac{1}{M_W^2-t}\left(\frac{1}{2}\log^2\left(\frac{M_W^2}{s}\right) - \frac{1}{2}\log^2\left(\frac{-t}{s}\right) - \frac{\pi^2}{2}\right) \\ I_{3l} &= \frac{1}{s\beta}\left(4\mathrm{Li}_2\left(\frac{\beta-1}{1+\beta}\right) + \log^2\left(\frac{1-\beta}{1+\beta}\right) + \frac{\pi^2}{3}\right). \end{aligned} \tag{B.4}$$

B.2 Approximate NNLO Results

The hard scattering kernel is expanded in a power series:

$$\begin{aligned} C(z,M,\cos\theta,\mu) &= C^0(z,M,\cos\theta,\mu) + \frac{\alpha_s}{4\pi}C^1(z,M,\cos\theta,\mu) \\ &\quad + \left(\frac{\alpha_s}{4\pi}\right)^2 C^2(z,M,\cos\theta,\mu).. \end{aligned} \tag{B.5}$$

Similarly, the hard function is expanded in a power series:

$$\begin{aligned} H(M_{WW},\cos\theta,\mu_f) &= H^0(M_{WW},\cos\theta) + \frac{\alpha_s}{4\pi}H^1(M_{WW},\cos\theta,\mu_f) \\ &\quad + \left(\frac{\alpha_s}{4\pi}\right)^2 H^2(M_{WW},\cos\theta,\mu_f), \end{aligned} \tag{B.6}$$

where $H^1 = H^1_{reg} + H^1_{extra}$ where H^1_{reg} and H^1_{extra} are defined in Eq. (3.23).

The approximate NNLO cross section is found by calculating the scale dependent pieces of the leading singular contribution to C^2 and adding this contribution to the total NLO cross section.Using the results for the hard and soft functions to NNLO, an approximate formula for the NNLO piece, C^2, can be determined which includes the leading singular pieces. The result is written as an expansion of C^2 in "plus"-functions:

$$C^2(z,M,\cos\theta,\mu_f) = \sum_{n=0}^{3} D^{(n)}\left[\frac{\ln^n(1-z)}{1-z}\right]_+ + R^{(0)}\delta(1-z), \tag{B.7}$$

where

$$D^{(3)} = 64H^0 s^{(2,4)} \tag{B.8}$$

$$D^{(2)} = 24H^0\left[s^{(2,3)} + 4L_s s^{(2,4)}\right] \tag{B.9}$$

$$D^{(1)} = 8H^0\left[s^{(2,2)} + 3L_s s^{(2,3)} + 6\left(L_s^2 - \frac{2\pi^2}{3}\right)s^{(2,4)}\right] + 8H^{(1)}s^{(1,2)} \tag{B.10}$$

$$\begin{aligned} D^{(0)} &= 2H^0\left[s^{(2,1)} + 2L_s s^{(2,2)} + 3\left(L_s^2 - \frac{2\pi^2}{3}\right)s^{(2,3)} + 4\left(L_s^3 - 2L_s\pi^2 + 16\zeta_3\right)s^{(2,4)}\right] \\ &\quad + 2H^1\left[s^{(1,1)} + 2L_s s^{(1,2)}\right] \end{aligned} \tag{B.11}$$

and

$$\begin{aligned} R^{(0)} &= H^0\left[s^{(2,0)} + L_M s^{(2,1)} + \left(L_M^2 - \frac{2\pi^2}{3}\right) s^{(2,2)}\right. \\ &\quad + \left(L_M^3 - 2L_M\pi^2 + 16\zeta_3\right) s^{(2,3)} \qquad \text{(B.12)} \\ &\quad \left. + \left(L_M^4 - 4L_M^2\pi^2 + \frac{4\pi^4}{15} + 64L_M\zeta_3\right) s^{(2,4)}\right] \\ &\quad + H^1\left[s^{(1,0)} + L_M s^{(1,1)} + \left(L_M^2 - \frac{2\pi^2}{3}\right) s^{(1,2)}\right] + H^2\,. \qquad \text{(B.13)} \end{aligned}$$

The logarithms are defined as

$$\begin{aligned} L_M &= \log\left(\frac{M^2}{\mu_f^2}\right) \\ L_s &= \log\left(\frac{s}{\mu_f^2}\right) \qquad \text{(B.14)} \end{aligned}$$

The soft contributions are found from the RG evolution and explicit calculation of the soft function [71],

$$\begin{aligned} s^{(1,0)} &= \frac{C_F\pi^2}{3} \\ s^{(2,0)} &= C_F\left[C_F\frac{\pi^4}{18} + C_A\left(\frac{2428}{81} + \frac{67\pi^2}{54} - \frac{\pi^4}{3} - \frac{22}{9}\zeta_3\right) - T_F n_f\left(\frac{656}{81} + \frac{10\pi^2}{27} - \frac{8}{9}\zeta_3\right)\right] \\ s^{(1,2)} &= \frac{\Gamma_0}{2} \\ s^{(1,1)} &= \gamma_0^s \\ s^{(2,4)} &= \frac{\Gamma_0^2}{8} \\ s^{(2,3)} &= \frac{\Gamma_0}{6}(3\gamma_0^s - \beta_0) \\ s^{(2,2)} &= \frac{1}{2}\left(\Gamma_0 s^{(1,0)} + \Gamma_1 + (\gamma_0^s)^2 - \beta_0\gamma_0^s\right) \\ s^{(2,1)} &= s^{(1,0)}(\gamma_0^s - \beta_0) + \gamma_1^s, \qquad \text{(B.15)} \end{aligned}$$

where $C_F = 4/3$, $C_A = 3$, $T_F = 1/2$, $n_f = 5$, and ζ_3 is a Riemann zeta function. Expressions for $\Gamma_0, \Gamma_1, \gamma_0^s, \gamma_1^s$ and β_0 can be found in Ref. [71] (where the soft anomalous dimension is written as γ^W instead of γ^s).

Similarly, the hard coefficients can be expanded as a power series in logs,

$$\begin{aligned} H^0(M_{WW}, \cos\theta) &= h^{(0,0)}(M_{WW}, \cos\theta) \qquad \text{(B.16)} \\ H^1(M_{WW}, \cos\theta, \mu_f) &= \sum_{n=0}^{2} h^{(1,n)}\left(M_{WW}, \cos\theta, \frac{M_{WW}}{Q_h}\right) L_Q^n \\ H^2(M_{WW}, \cos\theta, \mu_f) &= \sum_{n=0}^{4} h^{(2,n)}\left(M_{WW}, \cos\theta, \frac{M_{WW}}{Q_h}\right) L_Q^n\,, \end{aligned}$$

and

$$L \equiv \ln\left(\frac{Q_h^2}{\mu_f^2}\right). \tag{B.17}$$

We have introduced an additional arbitrary scale Q_h. Using the RGEs of the hard function, we can solve for the hard coefficients:

$$\begin{aligned}
h^{(1,2)} &= -\frac{\Gamma_0}{2} h^{(0,0)} \\
h^{(1,1)} &= -\left(\gamma_0^V + \Gamma_0 \ln\frac{M_{WW}^2}{Q_h^2}\right) h^{(0,0)} \\
h^{(2,4)} &= \frac{\Gamma_0^2}{8} h^{(0,0)} \\
h^{(2,3)} &= \frac{\Gamma_0}{6}\left[3\gamma_0^V + \beta_0 + 3\Gamma_0 \ln\frac{M_{WW}^2}{Q_h^2}\right] h^{(0,0)} \\
h^{(2,2)} &= \frac{1}{2}\left[-\Gamma_0 h^{(1,0)} - \Gamma_1 h^{(0,0)} + \left(\gamma_0^V + \Gamma_0 \ln\frac{M_{WW}^2}{Q_h^2}\right)\left(\gamma_0^V + \beta_0 + \Gamma_0 \ln\frac{M_{WW}^2}{Q_h^2}\right) h^{(0,0)}\right] \\
h^{(2,1)} &= -\left(\gamma_0^V + \beta_0 + \Gamma_0 \ln\frac{M_{WW}^2}{Q_h^2}\right) h^{(1,0)} - \left(\gamma_1^V + \Gamma_1 \ln\frac{M_{WW}^2}{Q_h^2}\right) h^{(0,0)},
\end{aligned} \tag{B.18}$$

where the arguments of the hard coefficients have been suppressed. The anomalous dimension of the hard Wilson coefficient C_V, γ^V, can be found in Ref. [71]. The coefficients $h^{(0,0)}$ and $h^{(1,0)}$ can be calculated from the known LO and NLO hard functions given in Eqs. (3.22) and (3.23). Additionally, since an additional arbitrary scale Q_h was introduced, the Q_h dependence of $h^{(1,0)}$ and $h^{(2,0)}$ can be solved for:

$$\begin{aligned}
h^{(1,0)} &= \sum_{n=0}^{2} h^{(1,n)}_{Q_h=M_{WW}} \ln^n \frac{M_{WW}^2}{Q_h^2} \\
h^{(2,0)} &= \sum_{n=0}^{4} h^{(2,n)}_{Q_h=M_{WW}} \ln^n \frac{M_{WW}^2}{Q_h^2},
\end{aligned} \tag{B.19}$$

where the subscript $Q_h = M_{WW}$ indicates the value of Q_h at which the coefficients on the RHS are evaluated at.

Using these coefficients, the NNLO result in Eq. (B.6) is independent of the scale Q_h. However, without a full calculation, it is not possible to know $h^{(2,0)}$. Since the other NNLO coefficients, $h^{(2,n)}$ for $n = 1, 2, 3$, are independent of $h^{(2,0)}$, then $h^{(2,0)}$ can be set to zero and an approximate NNLO result is obtained. The purpose of introducing Q_h is now clear, as discussed in the Section 3.2.4.

Appendix C

NLO $H + j$ results

C.1 Virtual Contributions

Defining V_i, along with the logarithms and dilogarithms, as complex numbers, the one-loop qg virtual contributions proportional to C_1 are [271],

$$\begin{aligned}
V_1 &= -\frac{1}{\epsilon^2}\left[\left(\frac{m_H^2}{-S_{gq}}\right)^{\epsilon} + \left(\frac{m_H^2}{-S_{g\bar{q}}}\right)^{\epsilon}\right] + \frac{13}{6\epsilon}\left(\frac{m_H^2}{-S_{q\bar{q}}}\right)^{\epsilon} \\
&\quad - \log\left(\frac{S_{gq}}{m_H^2}\right)\log\left(\frac{S_{q\bar{q}}}{m_H^2}\right) - \log\left(\frac{S_{g\bar{q}}}{m_H^2}\right)\log\left(\frac{S_{q\bar{q}}}{m_H^2}\right) - 2Li_2\left(1 - \frac{S_{q\bar{q}}}{m_H^2}\right) \\
&\quad - Li_2\left(1 - \frac{S_{gq}}{m_H^2}\right) - Li_2\left(1 - \frac{S_{g\bar{q}}}{m_H^2}\right) + \frac{40}{9} + \frac{\pi^2}{3} - \frac{S_{q\bar{q}}}{2S_{g\bar{q}}} \\
V_2 &= \left[\frac{1}{\epsilon^2} + \frac{3}{2\epsilon}\right]\left(\frac{m_H^2}{-S_{q\bar{q}}}\right)^{\epsilon} + \log\left(\frac{S_{gq}}{m_H^2}\right)\log\left(\frac{S_{g\bar{q}}}{m_H^2}\right) + Li_2\left(1 - \frac{S_{gq}}{m_H^2}\right) \\
&\quad + Li_2\left(1 - \frac{S_{g\bar{q}}}{m_H^2}\right) + 4 - \frac{\pi^2}{6} - \frac{S_{q\bar{q}}}{S_{g\bar{q}}} \\
V_3 &= -\frac{2}{3\epsilon}\left(\frac{m_H^2}{-S_{q\bar{q}}}\right)^{\epsilon} - \frac{10}{9}\,.
\end{aligned} \tag{C.1}$$

These results are in agreement with Ref. [271]. The results must be analytically continued for timelike momentum invariants: $\log(S_{ij}) \to \log(\mid S_{ij} \mid) + i\pi\theta(-S_{ij})$ and $(-1)^{\epsilon} \to 1 + i\pi\epsilon - \frac{\epsilon^2\pi^2}{2}$.

The one-loop qg virtual contributions proportional to C_5 are (with W_i complex),

$$\begin{aligned}
W_1 &= \frac{1}{\epsilon^2}\left[\left(\frac{m_H^2}{-S_{g\bar{q}}}\right)^{\epsilon}+\left(\frac{m_H^2}{-S_{gq}}\right)^{\epsilon}\right]+\frac{1}{\epsilon}\left[\frac{17}{6}\right] \\
&\quad -\log\left(\frac{S_{gq}}{m_H^2}\right)-\frac{33}{18}\log\left(\frac{S_{g\bar{q}}}{m_H^2}\right)+\frac{121}{18}+\frac{1}{6}\frac{S_{g\bar{q}}}{S_{gq}}+\frac{1}{3}\frac{S_{q\bar{q}}}{S_{gq}} \\
W_2 &= -\frac{1}{\epsilon^2}\left(\frac{m_H^2}{-S_{q\bar{q}}}\right)^{\epsilon}+\frac{1}{\epsilon}\left[-\frac{17}{6}\right]+\log\left(\frac{S_{gq}}{m_H^2}\right) \quad +\frac{1}{3}\log\left(\frac{S_{g\bar{q}}}{m_H^2}\right) \\
&\quad +\frac{3}{2}\log\left(\frac{S_{q\bar{q}}}{m_H^2}\right)-\frac{103}{18}+\frac{1}{3}\frac{S_{g\bar{q}}}{S_{gq}}+\frac{1}{6}\frac{S_{q\bar{q}}}{S_{gq}} \qquad \text{(C.2)} \\
W_3 &= \frac{2}{3}\left[\frac{1}{\epsilon}-\log\left(\frac{-S_{q\bar{q}}}{m_H^2}\right)\right]+\frac{10}{9} \quad . \qquad \text{(C.3)}
\end{aligned}$$

This result is in disagreement with that of Ref. [278].

The one-loop gg contribution proportional to C_1 is,

$$\begin{aligned}
U_1 &= -\frac{1}{\epsilon^2}\left[\left(\frac{m_H^2}{-S_{12}}\right)^{\epsilon}+\left(\frac{m_H^2}{-S_{23}}\right)^{\epsilon}+\left(\frac{m_H^2}{-S_{31}}\right)^{\epsilon}\right] \\
&\quad -\log\left(\frac{S_{23}}{m_H^2}\right)\log\left(\frac{S_{31}}{m_H^2}\right)-\log\left(\frac{S_{31}}{m_H^2}\right)\log\left(\frac{S_{12}}{m_H^2}\right) \\
&\quad -\log\left(\frac{S_{12}}{m_H^2}\right)\log\left(\frac{S_{23}}{m_H^2}\right)-2\mathrm{Li}_2\left(1-\frac{S_{12}}{m_H^2}\right) \\
&\quad -2\mathrm{Li}_2\left(1-\frac{S_{23}}{m_H^2}\right)-2\mathrm{Li}_2\left(1-\frac{S_{31}}{m_H^2}\right),
\end{aligned}$$

which agrees with Eq. (11) of Ref. [271].

The one-loop gg contribution proportional to C_3 is,

$$U_3 = -\frac{3}{\epsilon^2\,(1-2\epsilon)}\left[\left(\frac{m_H^2}{-S_{12}}\right)^{\epsilon}+\left(\frac{m_H^2}{-S_{23}}\right)^{\epsilon}+\left(\frac{m_H^2}{-S_{31}}\right)^{\epsilon}\right]+O(\epsilon). \qquad \text{(C.4)}$$

C.2 NLO Real Emission - Quark Amplitudes

C.2.1 $q\bar{q}ggh$ amplitudes

The contribution from O_3, to be multiplied by C_3, is

$$im^{O_3}(q_-(1),g_-(2),g_-(3),\bar{q}_+(4),h) = -3ig_s\frac{\langle 12\rangle\langle 23\rangle\langle 31\rangle}{\langle 14\rangle}, \qquad \text{(C.5)}$$

$$im^{O_3}(q_-(1),g_-(2),g_+(3),\bar{q}_+(4),h) = 0, \qquad \text{(C.6)}$$

$$im^{O_3}(q_-(1),g_+(2),g_-(3),\bar{q}_+(4),h) = 0, \qquad \text{(C.7)}$$

$$\qquad \text{(C.8)}$$

Just like the $ggggh$ amplitudes in Section 5.6, Eq. (C.6) demonstrates non-interference with the O_1 amplitude in the soft Higgs limit. The O_4 operator contains two pairs of quark

bilinears, so does not contribute to the $q\bar{q}ggh$ tree amplitude. The O_5 operator is easily shown to satisfy the operator relation

$$O_5 = O_4 + \partial^\alpha h G^A_{\alpha\nu} D^\beta G^{A\,\nu}_\beta, \tag{C.9}$$

up to total derivatives, which leads to the following contributions proportional to p_H, to be multiplied by C_5,

$$\begin{aligned}
&im^{O_5}\left(q_-(1), g_+(2), g_-(3), \bar{q}_+(4), h\right) \\
&= g_s^2 \left[\frac{i\langle 13\rangle\langle 3\not{p}_H 2]\langle 1\not{p}_H 4]}{2\langle 12\rangle S_{23}} - \frac{i[24]\langle 1\not{p}_H 2]\langle 1\not{p}_H 4]}{2\langle 12\rangle[23][34]} + \frac{i[24]\langle 13\rangle^2}{\langle 12\rangle S_{23}} p_H\cdot(p_2+p_3)\right], \qquad \text{(C.10)}\\
&im^{O_5}\left(q_-(1), g_-(2), g_+(3), \bar{q}_+(4), h\right) \\
&= g_s^2 \left[\frac{i\langle 12\rangle[34]}{S_{23}[12]\langle 34\rangle}\left([13]\langle 34\rangle p_H\cdot p_3 - [12]\langle 24\rangle p_H\cdot p_2\right)\right. \\
&\left. -\frac{i}{2}\frac{\langle 2\not{p}_H 3]}{\langle 34\rangle[12]S_{23}}\left(S_{13}S_{34} - S_{24}S_{12} + S_{23}S_{34} - S_{23}S_{12}\right)\right], \qquad \text{(C.11)}\\
&im^{O_5}\left(q_-(1), g_-(2), g_-(3), \bar{q}_+(4), h\right) \\
&= g_s^2 \left[-\frac{i}{2}\frac{(S_{12}+S_{13}+S_{23})\langle 3\not{p}_H 4]}{2[12][23]} - \frac{i\langle 1\not{p}_H 4]\langle 2\not{p}_H 4]}{2[23][34]}\right] \qquad \text{(C.12)}
\end{aligned}$$

C.2.2 $q\bar{q}q\bar{q}$ and $q\bar{q}Q\bar{Q}$ amplitudes

The O_3 amplitude vanishes at tree-level due to the absence of the ggh vertex. For O_4 and O_5, we define

$$\begin{aligned}
f_4(p_1,p_2,p_3,p_4) &= 2i\langle 14\rangle[32], \qquad \text{(C.13)}\\
f_5(p_1,p_2,p_3,p_4) &= \frac{i}{2}\left(\frac{1}{S_{12}} + \frac{1}{S_{34}}\right) \\
&\quad \left[\langle 1\not{p}_H 2]\langle 4\not{p}_H 3] + \langle 14\rangle[23](p_1+p_2)\cdot(p_3+p_4)\right]. \qquad \text{(C.14)}
\end{aligned}$$

The amplitudes for O_i, $i = 4, 5$, are

$$\begin{aligned}
im^{O_i}\left(q_-^{c_1}(1), \bar{q}_+^{c_2}(2), Q_+^{c_3}(3), \bar{Q}_-^{c_4}, h\right) &= im^{O_i}\left(q_-^{c_1}(1), \bar{q}_+^{c_2}(2), q_+^{c_3}(3), \bar{q}_-^{c_4}, h\right) \\
&= g_s^2 f_i(p_1,p_2,p_3,p_4)\sum_A T^A_{c_1c_2}T^A_{c_3c_4}, \qquad \text{(C.15)}\\
im^{O_i}\left(q_-^{c_1}(1), \bar{q}_+^{c_2}(2), q_-^{c_3}(3), \bar{q}_+^{c_4}, h\right) &= g_s^2 f_i(p_1,p_2,p_4,p_3)\sum_A T^A_{c_1c_2}T^A_{c_3c_4}, \\
&\quad + f_i(p_3,p_2,p_4,p_1)\sum_A T^A_{c_3c_2}T^A_{c_1c_4}, \qquad \text{(C.16)}
\end{aligned}$$

where q and Q represent different flavor quarks.

Appendix D

Definition of the beam function using QCD fields

For completeness, we give a definition of the beam function using QCD fields. This appendix is essentially a review and does not contain original work, because the definition agrees with the SCET definition [319] at least at low orders [48, 49, 50, 345]. The *unsubtracted* momentum-space beam function for a scalar parton ϕ with Bjorken variable x_1 and virtuality (ignoring transverse momentum components) $\omega_1 = x_1 P^+ M \tau_R$, for an incoming hadron $|H_1\rangle$ with a large plus momentum component P^+,

$$B_1^{\text{unsubtracted}}(\omega_1, x_1, \mu) = \frac{xP^+}{2} \int \frac{dw^-}{2\pi} \frac{dw^+}{2\pi} e^{-i\left(x_1 P^+ w^- + M\tau_R\, w^+\right)/2} \langle H_1 | \phi^\dagger \left(w^+, w^-, \mathbf{0}_T\right) \mathcal{P} \exp\left[\int_0^{w^-} \frac{dy^-}{2} igA^+\left(0, y^-, \mathbf{0}_T\right)\right] \phi(0) | H_1 \rangle, \tag{D.1}$$

where μ is the UV renormalization scale at which the matrix element is defined. This is directly analogous to Eq. (50) in [319] (with "+" and "−" exchanged), except that the latter reference used the SCET collinear field with zero-bin subtraction.

The eikonal beam function is defined by replacing the incoming hadron and the interpolating field by a Wilson line in the "+" direction,

$$B_1^{\text{eikonal}}(\omega_1, x_1, \mu) = \frac{xP^+}{2} \int \frac{dw^-}{2\pi} \frac{dw^+}{2\pi} e^{-i\left(x_1 P^+ w^- + M\tau_R\, w^+\right)/2} \langle 0 | W_1^\dagger \left(w^+, w^-, \mathbf{0}_T\right) \mathcal{P} \exp\left[\int_0^{w^-} \frac{dy^-}{2} igA^+\left(0, y^-, \mathbf{0}_T\right)\right] W_1(0) | 0 \rangle, \tag{D.2}$$

where we defined

$$W_1\left(w^+, w^-, \boldsymbol{w}_T\right) = \mathcal{P} \exp\left[\int_{-\infty}^{0} \frac{dy^+}{2} igA^-\left(w^+ + y^+, w^-, \boldsymbol{w}_T\right)\right]. \tag{D.3}$$

Finally, we divide the Laplace transform of $B_1^{\text{unsubtracted}}$ with respect to ω, $\tilde{B}_1^{\text{unsubtracted}}$, by the Laplace transform of B_1^{eikonal}, $\tilde{B}_1^{\text{eikonal}}$, to obtain the gauge-invariant moment-space beam

function $\tilde{B}_1(\tilde{\omega}, x_1, \mu)$. The inverse Laplace transform of this result is the momentum-space beam function $B_1(\omega, x_1, \mu)$.

Bibliography

[1] F. Englert and R. Brout, *Broken Symmetry and the Mass of Gauge Vector Mesons*, *Phys.Rev.Lett.* **13** (1964) 321–323.

[2] P. W. Higgs, *Broken symmetries, massless particles and gauge fields*, *Phys.Lett.* **12** (1964) 132–133.

[3] P. W. Higgs, *Broken Symmetries and the Masses of Gauge Bosons*, *Phys.Rev.Lett.* **13** (1964) 508–509.

[4] G. Guralnik, C. Hagen, and T. Kibble, *Global Conservation Laws and Massless Particles*, *Phys.Rev.Lett.* **13** (1964) 585–587.

[5] P. W. Higgs, *Spontaneous Symmetry Breakdown without Massless Bosons*, *Phys.Rev.* **145** (1966) 1156–1163.

[6] T. Kibble, *Symmetry breaking in nonAbelian gauge theories*, *Phys.Rev.* **155** (1967) 1554–1561.

[7] S. Herb, D. Hom, L. Lederman, J. Sens, H. Snyder, et al., *Observation of a Dimuon Resonance at 9.5-GeV in 400-GeV Proton-Nucleus Collisions*, *Phys.Rev.Lett.* **39** (1977) 252–255.

[8] **UA1** Collaboration, G. Arnison et al., *Experimental Observation of Isolated Large Transverse Energy Electrons with Associated Missing Energy at s**(1/2) = 540-GeV*, *Phys.Lett.* **B122** (1983) 103–116.

[9] **UA2** Collaboration, M. Banner et al., *Observation of Single Isolated Electrons of High Transverse Momentum in Events with Missing Transverse Energy at the CERN anti-p p Collider*, *Phys.Lett.* **B122** (1983) 476–485.

[10] **UA1** Collaboration, G. Arnison et al., *Experimental Observation of Lepton Pairs of Invariant Mass Around 95-GeV/c**2 at the CERN SPS Collider*, *Phys.Lett.* **B126** (1983) 398–410.

[11] **UA2** Collaboration, P. Bagnaia et al., *Evidence for Z0 —¿ e+ e- at the CERN anti-p p Collider*, *Phys.Lett.* **B129** (1983) 130–140.

[12] **CDF** Collaboration, F. Abe et al., *Observation of top quark production in $\bar{p}p$ collisions*, *Phys.Rev.Lett.* **74** (1995) 2626–2631, [hep-ex/9503002].

[13] **D0** Collaboration, S. Abachi et al., *Observation of the top quark*, *Phys.Rev.Lett.* **74** (1995) 2632–2637, [hep-ex/9503003].

[14] J. Hewett, *The Standard model and why we believe it*, hep-ph/9810316.

[15] **ATLAS** Collaboration, G. Aad et al., *Observation of a new particle in the search for the Standard Model Higgs boson with the ATLAS detector at the LHC*, *Phys.Lett.* **B716** (2012) 1–29, [arXiv:1207.7214].

[16] **CMS** Collaboration, S. Chatrchyan et al., *Observation of a new boson at a mass of 125 GeV with the CMS experiment at the LHC*, *Phys.Lett.* **B716** (2012) 30–61, [arXiv:1207.7235].

[17] **ATLAS, CMS** Collaboration, G. Aad et al., *Combined Measurement of the Higgs Boson Mass in pp Collisions at $\sqrt{s} = 7$ and 8 TeV with the ATLAS and CMS Experiments*, arXiv:1503.0758.

[18] T. A. collaboration, *Study of the spin and parity of the Higgs boson in HVV decays with the ATLAS detector*, .

[19] **CMS** Collaboration, V. Khachatryan et al., *Constraints on the spin-parity and anomalous HVV couplings of the Higgs boson in proton collisions at 7 and 8 TeV*, arXiv:1411.3441.

[20] S. P. Martin, *A Supersymmetry primer*, *Adv.Ser.Direct.High Energy Phys.* **21** (2010) 1–153, [hep-ph/9709356].

[21] E. A. Baltz, *Dark matter candidates*, *eConf* **C040802** (2004) L002, [astro-ph/0412170].

[22] A. Accardi, J. Albacete, M. Anselmino, N. Armesto, E. Aschenauer, et al., *Electron Ion Collider: The Next QCD Frontier - Understanding the glue that binds us all*, arXiv:1212.1701.

[23] J. Lansberg, R. Arnaldi, S. Brodsky, V. Chambert, J. Didelez, et al., *AFTER@LHC: a precision machine to study the interface between particle and nuclear physics*, *EPJ Web Conf.* **66** (2014) 11023, [arXiv:1308.5806].

[24] J. C. Collins, D. E. Soper, and G. F. Sterman, *Factorization of Hard Processes in QCD*, *Adv.Ser.Direct.High Energy Phys.* **5** (1988) 1–91, [hep-ph/0409313].

[25] G. F. Sterman, *Partons, factorization and resummation, TASI 95*, hep-ph/9606312.

[26] J. Collins, *Foundations of perturbative QCD*, .

[27] L. Landau, *On analytic properties of vertex parts in quantum field theory*, *Nucl.Phys.* **13** (1959) 181–192.

[28] S. Coleman and R. Norton, *Singularities in the physical region*, *Nuovo Cim.* **38** (1965) 438–442.

[29] G. F. Sterman, *Mass Divergences in Annihilation Processes. 1. Origin and Nature of Divergences in Cut Vacuum Polarization Diagrams*, *Phys.Rev.* **D17** (1978) 2773.

[30] S. B. Libby and G. F. Sterman, *Mass Divergences in Two Particle Inelastic Scattering*, *Phys.Rev.* **D18** (1978) 4737.

[31] O. Erdoan and G. Sterman, *Ultraviolet divergences and factorization for coordinate-space amplitudes*, *Phys.Rev.* **D91** (2015), no. 6 065033, [arXiv:1411.4588].

[32] G. T. Bodwin, *Factorization of the Drell-Yan Cross-Section in Perturbation Theory*, *Phys.Rev.* **D31** (1985) 2616.

[33] J. C. Collins, D. E. Soper, and G. F. Sterman, *Factorization for Short Distance Hadron - Hadron Scattering*, *Nucl.Phys.* **B261** (1985) 104.

[34] J. C. Collins, D. E. Soper, and G. F. Sterman, *Soft Gluons and Factorization*, *Nucl.Phys.* **B308** (1988) 833.

[35] G. Altarelli and G. Parisi, *Asymptotic Freedom in Parton Language*, *Nucl.Phys.* **B126** (1977) 298.

[36] V. Gribov and L. Lipatov, *Deep inelastic e p scattering in perturbation theory*, *Sov.J.Nucl.Phys.* **15** (1972) 438–450.

[37] Y. L. Dokshitzer, *Calculation of the Structure Functions for Deep Inelastic Scattering and e+ e- Annihilation by Perturbation Theory in Quantum Chromodynamics.*, *Sov.Phys.JETP* **46** (1977) 641–653.

[38] S. Scherer, *Introduction to chiral perturbation theory*, *Adv.Nucl.Phys.* **27** (2003) 277, [hep-ph/0210398].

[39] M. Neubert, *Heavy quark symmetry*, *Phys.Rept.* **245** (1994) 259–396, [hep-ph/9306320].

[40] C. W. Bauer and I. W. Stewart, *Invariant operators in collinear effective theory*, *Phys.Lett.* **B516** (2001) 134–142, [hep-ph/0107001].

[41] C. W. Bauer, S. Fleming, and M. E. Luke, *Summing Sudakov logarithms in $B \to X_s + \gamma$ in effective field theory*, *Phys.Rev.* **D63** (2000) 014006, [hep-ph/0005275].

[42] C. W. Bauer, S. Fleming, D. Pirjol, and I. W. Stewart, *An Effective field theory for collinear and soft gluons: Heavy to light decays*, *Phys.Rev.* **D63** (2001) 114020, [hep-ph/0011336].

[43] C. W. Bauer, D. Pirjol, and I. W. Stewart, *Soft collinear factorization in effective field theory*, *Phys.Rev.* **D65** (2002) 054022, [hep-ph/0109045].

[44] M. Beneke, A. Chapovsky, M. Diehl, and T. Feldmann, *Soft collinear effective theory and heavy to light currents beyond leading power*, *Nucl.Phys.* **B643** (2002) 431–476, [hep-ph/0206152].

[45] M. Beneke and T. Feldmann, *Multipole expanded soft collinear effective theory with nonAbelian gauge symmetry*, *Phys.Lett.* **B553** (2003) 267–276, [hep-ph/0211358].

[46] R. J. Hill and M. Neubert, *Spectator interactions in soft collinear effective theory*, *Nucl.Phys.* **B657** (2003) 229–256, [hep-ph/0211018].

[47] A. V. Manohar and I. W. Stewart, *The Zero-Bin and Mode Factorization in Quantum Field Theory*, *Phys.Rev.* **D76** (2007) 074002, [hep-ph/0605001].

[48] C. Lee and G. F. Sterman, *Momentum Flow Correlations from Event Shapes: Factorized Soft Gluons and Soft-Collinear Effective Theory*, *Phys.Rev.* **D75** (2007) 014022, [hep-ph/0611061].

[49] A. Idilbi and T. Mehen, *On the equivalence of soft and zero-bin subtractions*, *Phys.Rev.* **D75** (2007) 114017, [hep-ph/0702022].

[50] A. Idilbi and T. Mehen, *Demonstration of the equivalence of soft and zero-bin subtractions*, *Phys.Rev.* **D76** (2007) 094015, [arXiv:0707.1101].

[51] M. Beneke and V. A. Smirnov, *Asymptotic expansion of Feynman integrals near threshold*, *Nucl.Phys.* **B522** (1998) 321–344, [hep-ph/9711391].

[52] S. Dawson, I. M. Lewis, and M. Zeng, *Threshold resummed and approximate next-to-next-to-leading order results for W^+W^- pair production at the LHC*, *Phys.Rev.* **D88** (2013), no. 5 054028, [arXiv:1307.3249].

[53] G. Sterman and M. Zeng, *Quantifying Comparisons of Threshold Resummations*, *JHEP* **1405** (2014) 132, [arXiv:1312.5397].

[54] P. Meade, H. Ramani, and M. Zeng, *Transverse momentum resummation effects in W^+W^- measurements*, *Phys. Rev.* **D90** (2014), no. 11 114006, [arXiv:1407.4481].

[55] S. Dawson, I. Lewis, and M. Zeng, *Effective Field Theory for Higgs Plus Jet Production*, arXiv:1409.6299.

[56] S. Dawson, I. M. Lewis, and M. Zeng, *Usefulness of effective field theory for boosted Higgs production*, *Phys. Rev.* **D91** (2015) 074012, [arXiv:1501.0410].

[57] M. Zeng, *Drell-Yan process with jet vetoes: breaking of generalized factorization*, arXiv:1507.0165.

[58] G. Parisi, *Summing Large Perturbative Corrections in QCD*, *Phys.Lett.* **B90** (1980) 295.

[59] G. Curci and M. Greco, *Large Infrared Corrections in QCD Processes*, *Phys.Lett.* **B92** (1980) 175.

[60] P. Chiappetta, T. Grandou, M. Le Bellac, and J. Meunier, *THE ROLE OF SOFT GLUONS IN LEPTON PAIR PRODUCTION*, *Nucl.Phys.* **B207** (1982) 251.

[61] G. F. Sterman, *Summation of Large Corrections to Short Distance Hadronic Cross-Sections*, *Nucl.Phys.* **B281** (1987) 310.

[62] S. Catani and L. Trentadue, *Resummation of the QCD Perturbative Series for Hard Processes*, *Nucl.Phys.* **B327** (1989) 323.

[63] S. Catani and L. Trentadue, *Comment on QCD exponentiation at large x*, *Nucl.Phys.* **B353** (1991) 183–186.

[64] H. Contopanagos, E. Laenen, and G. F. Sterman, *Sudakov factorization and resummation*, *Nucl.Phys.* **B484** (1997) 303–330, [hep-ph/9604313].

[65] S. Catani, M. L. Mangano, and P. Nason, *Sudakov resummation for prompt photon production in hadron collisions*, *JHEP* **9807** (1998) 024, [hep-ph/9806484].

[66] G. Korchemsky and G. Marchesini, *Structure function for large x and renormalization of Wilson loop*, *Nucl.Phys.* **B406** (1993) 225–258, [hep-ph/9210281].

[67] G. Korchemsky and G. Marchesini, *Resummation of large infrared corrections using Wilson loops*, *Phys.Lett.* **B313** (1993) 433–440.

[68] A. V. Belitsky, *Two loop renormalization of Wilson loop for Drell-Yan production*, *Phys.Lett.* **B442** (1998) 307–314, [hep-ph/9808389].

[69] S. Catani, D. de Florian, and M. Grazzini, *Higgs production in hadron collisions: Soft and virtual QCD corrections at NNLO*, *JHEP* **0105** (2001) 025, [hep-ph/0102227].

[70] S. Catani, D. de Florian, M. Grazzini, and P. Nason, *Soft gluon resummation for Higgs boson production at hadron colliders*, *JHEP* **0307** (2003) 028, [hep-ph/0306211].

[71] T. Becher, M. Neubert, and G. Xu, *Dynamical Threshold Enhancement and Resummation in Drell-Yan Production*, *JHEP* **0807** (2008) 030, [arXiv:0710.0680].

[72] V. Ahrens, T. Becher, M. Neubert, and L. L. Yang, *Renormalization-Group Improved Prediction for Higgs Production at Hadron Colliders*, *Eur.Phys.J.* **C62** (2009) 333–353, [arXiv:0809.4283].

[73] C. W. Bauer, N. D. Dunn, and A. Hornig, *Factorization of Boosted Multijet Processes for Threshold Resummation*, *Phys.Rev.* **D82** (2010) 054012, [hep-ph/1002.1307].

[74] C. W. Bauer, N. D. Dunn, and A. Hornig, *On the effectiveness of threshold resummation away from hadronic endpoint*, arXiv:1010.0243.

[75] M. Bonvini, S. Forte, M. Ghezzi, and G. Ridolfi, *Threshold Resummation in SCET vs. Perturbative QCD: An Analytic Comparison*, *Nucl.Phys.* **B861** (2012) 337–360, [arXiv:1201.6364].

[76] M. Bonvini, S. Forte, M. Ghezzi, and G. Ridolfi, *The scale of soft resummation in SCET vs perturbative QCD*, *Nucl.Phys.Proc.Suppl.* **241-242** (2013) 121–126, [arXiv:1301.4502].

[77] T. Becher, M. Neubert, and B. D. Pecjak, *Factorization and Momentum-Space Resummation in Deep-Inelastic Scattering*, *JHEP* **0701** (2007) 076, [hep-ph/0607228].

[78] J. C. Collins and D. E. Soper, *Back-To-Back Jets in QCD*, *Nucl.Phys.* **B193** (1981) 381.

[79] L. G. Almeida, S. D. Ellis, C. Lee, G. Sterman, I. Sung, et al., *Comparing and Counting Logs in Direct and Effective Methods of Resummation*, arXiv:1401.4460.

[80] G. P. Korchemsky and G. F. Sterman, *Nonperturbative corrections in resummed cross-sections*, *Nucl.Phys.* **B437** (1995) 415–432, [hep-ph/9411211].

[81] G. F. Sterman, *Infrared divergences in perturbative QCD. (talk)*, *AIP Conf. Proc.* **74** (1981) 22–40.

[82] J. Gatheral, *Exponentiation of Eikonal Cross-sections in Nonabelian Gauge Theories*, *Phys.Lett.* **B133** (1983) 90.

[83] J. Frenkel and J. Taylor, *Nonabelian eikonal exponentiation*, *Nucl.Phys.* **B246** (1984) 231.

[84] E. Laenen, L. Magnea, and G. Stavenga, *On next-to-eikonal corrections to threshold resummation for the Drell-Yan and DIS cross sections*, *Phys.Lett.* **B669** (2008) 173–179, [hep-ph/0807.4412].

[85] E. Laenen, G. F. Sterman, and W. Vogelsang, *Recoil and threshold corrections in short distance cross-sections*, *Phys.Rev.* **D63** (2001) 114018, [hep-ph/0010080].

[86] H. Contopanagos and G. F. Sterman, *Normalization of the Drell-Yan cross-section in QCD*, *Nucl.Phys.* **B400** (1993) 211–224.

[87] S. Catani, M. L. Mangano, P. Nason, and L. Trentadue, *The Resummation of soft gluons in hadronic collisions*, *Nucl.Phys.* **B478** (1996) 273–310, [hep-ph/9604351].

[88] V. Ahrens, A. Ferroglia, M. Neubert, B. D. Pecjak, and L.-L. Yang, *RG-improved single-particle inclusive cross sections and forward-backward asymmetry in $t\bar{t}$ production at hadron colliders*, *JHEP* **1109** (2011) 070, [hep-ph/1103.0550].

[89] A. Vogt, *Next-to-next-to-leading logarithmic threshold resummation for deep inelastic scattering and the Drell-Yan process*, *Phys.Lett.* **B497** (2001) 228–234, [hep-ph/0010146].

[90] T. O. Eynck, E. Laenen, and L. Magnea, *Exponentiation of the Drell-Yan cross-section near partonic threshold in the DIS and MS-bar schemes*, *JHEP* **0306** (2003) 057, [hep-ph/0305179].

[91] E. Laenen and L. Magnea, *Threshold resummation for electroweak annihilation from DIS data*, *Phys.Lett.* **B632** (2006) 270–276, [hep-ph/0508284].

[92] M. Bonvini, S. Forte, and G. Ridolfi, *The Threshold region for Higgs production in gluon fusion*, *Phys.Rev.Lett.* **109** (2012) 102002, [arXiv:1204.5473].

[93] A. Martin, W. Stirling, R. Thorne, and G. Watt, *Parton distributions for the LHC*, *Eur.Phys.J.* **C63** (2009) 189–285, [arXiv:0901.0002].

[94] D. Appell, G. F. Sterman, and P. B. Mackenzie, *Soft Gluons and the Normalization of the Drell-Yan Cross-section*, *Nucl.Phys.* **B309** (1988) 259.

[95] D. de Florian and J. Zurita, *Soft-gluon resummation for pseudoscalar Higgs boson production at hadron colliders*, *Phys.Lett.* **B659** (2008) 813–820, [arXiv:0711.1916].

[96] V. Ahrens, A. Ferroglia, M. Neubert, B. D. Pecjak, and L. L. Yang, *Renormalization-Group Improved Predictions for Top-Quark Pair Production at Hadron Colliders*, *JHEP* **1009** (2010) 097, [arXiv:1003.5827].

[97] C. Anastasiou, C. Duhr, F. Dulat, E. Furlan, T. Gehrmann, et al., *Higgs boson gluon-fusion production at threshold in N3LO QCD*, arXiv:1403.4616.

[98] **CMS** Collaboration, *Evidence for a particle decaying to W+W- in the fully leptonic final state in a standard model Higgs boson search in pp collisions at the LHC*, .

[99] **ATLAS** Collaboration, *Measurements of the properties of the Higgs-like boson in the $WW^{(*)} \to \ell\nu\ell\nu$ decay channel with the ATLAS detector using 25 fb^{-1} of proton-proton collision data*, .

[100] **CDF** Collaboration, T. Aaltonen et al., *Measurement of the W+ W- Production Cross Section and Search for Anomalous WW gamma and WWZ Couplings in p p-bar Collisions at s**(1/2) = 1.96-TeV*, .

[101] **D0** Collaboration, V. Abazov et al., *Measurement of the WW production cross section with dilepton final states in p anti-p collisions at s**(1/2) = 1.96-TeV and limits on anomalous trilinear gauge couplings*, *Phys.Rev.Lett.* **103** (2009) 191801, [arXiv:0904.0673].

[102] **ATLAS** Collaboration, G. Aad et al., *Measurement of W^+W^- production in pp collisions at $\sqrt{s} = 7$ TeV with the ATLAS detector and limits on anomalous WWZ and $WW\gamma$ couplings*, *Phys.Rev.* **D87** (2013) 112001, [arXiv:1210.2979].

[103] T. A. collaboration, *Measurement of the W^+W^- production cross section in proton-proton collisions at $\sqrt{s} = 8$ TeV with the ATLAS detector*, .

[104] **CMS** Collaboration, S. Chatrchyan et al., *Measurement of W+W- and ZZ production cross sections in pp collisions at sqrt(s) = 8 TeV*, *Phys.Lett.* **B721** (2013) 190–211, [arXiv:1301.4698].

[105] **CMS** Collaboration, S. Chatrchyan et al., *Measurement of the W+W- cross section in pp collisions at sqrt(s) = 7 TeV and limits on anomalous WW gamma and WWZ couplings*, arXiv:1306.1126.

[106] **CMS** Collaboration, C. Collaboration, *Measurement of the W^+W^- cross section in pp collisions at sqrt(s) = 8 TeV and limits on anomalous gauge couplings*, .

[107] J. M. Campbell, R. K. Ellis, and C. Williams, *Vector boson pair production at the LHC*, *JHEP* **1107** (2011) 018, [arXiv:1105.0020].

[108] B. Feigl, H. Rzehak, and D. Zeppenfeld, *New Physics Backgrounds to the $H \to WW$ Search at the LHC?*, *Phys.Lett.* **B717** (2012) 390–395, [arXiv:1205.3468].

[109] D. Curtin, P. Jaiswal, and P. Meade, *Charginos Hiding In Plain Sight*, *Phys.Rev.* **D87** (2013) 031701, [arXiv:1206.6888].

[110] D. Curtin, P. Jaiswal, P. Meade, and P.-J. Tien, *Casting Light on BSM Physics with SM Standard Candles*, arXiv:1304.7011.

[111] K. Rolbiecki and K. Sakurai, *Light stops emerging in WW cross section measurements?*, *JHEP* **1309** (2013) 004, [arXiv:1303.5696].

[112] D. Curtin, P. Meade, and P.-J. Tien, *Natural SUSY in Plain Sight*, *Phys.Rev.* **D90** (2014), no. 11 115012, [arXiv:1406.0848].

[113] J. S. Kim, K. Rolbiecki, K. Sakurai, and J. Tattersall, *'Stop' that ambulance! New physics at the LHC?*, *JHEP* **1412** (2014) 010, [arXiv:1406.0858].

[114] P. Jaiswal, K. Kopp, and T. Okui, *Higgs Production Amidst the LHC Detector*, *Phys.Rev.* **D87** (2013), no. 11 115017, [arXiv:1303.1181].

[115] T. Gehrmann, M. Grazzini, S. Kallweit, P. Maierhfer, A. von Manteuffel, et al., *W^+W^- Production at Hadron Colliders in Next to Next to Leading Order QCD*, *Phys.Rev.Lett.* **113** (2014), no. 21 212001, [arXiv:1408.5243].

[116] S. Frixione, *A Next-to-leading order calculation of the cross-section for the production of W+ W- pairs in hadronic collisions*, *Nucl.Phys.* **B410** (1993) 280–324.

[117] J. Ohnemus, *An Order $\alpha^- s$ calculation of hadronic W^-W^+ production*, *Phys.Rev.* **D44** (1991) 1403–1414.

[118] L. J. Dixon, Z. Kunszt, and A. Signer, *Helicity amplitudes for O(alpha-s) production of W^+W^-, $W^\pm Z$, ZZ, $W^\pm\gamma$, or $Z\gamma$ pairs at hadron colliders*, *Nucl.Phys.* **B531** (1998) 3–23, [hep-ph/9803250].

[119] D. A. Dicus, C. Kao, and W. Repko, *GLUON PRODUCTION OF GAUGE BOSONS*, *Phys.Rev.* **D36** (1987) 1570.

[120] E. N. Glover and J. van der Bij, *VECTOR BOSON PAIR PRODUCTION VIA GLUON FUSION*, *Phys.Lett.* **B219** (1989) 488.

[121] T. Binoth, M. Ciccolini, N. Kauer, and M. Kramer, *Gluon-induced W-boson pair production at the LHC*, *JHEP* **0612** (2006) 046, [hep-ph/0611170].

[122] T. Binoth, M. Ciccolini, N. Kauer, and M. Kramer, *Gluon-induced WW background to Higgs boson searches at the LHC*, *JHEP* **0503** (2005) 065, [hep-ph/0503094].

[123] T. Melia, P. Nason, R. Rontsch, and G. Zanderighi, *W+W-, WZ and ZZ production in the POWHEG BOX*, *JHEP* **1111** (2011) 078, [arXiv:1107.5051].

[124] K. Hamilton, *A positive-weight next-to-leading order simulation of weak boson pair production*, *JHEP* **1101** (2011) 009, [arXiv:1009.5391].

[125] S. Hoche, F. Krauss, M. Schonherr, and F. Siegert, *Automating the POWHEG method in Sherpa*, *JHEP* **1104** (2011) 024, [arXiv:1008.5399].

[126] A. Bierweiler, T. Kasprzik, H. Kuhn, and S. Uccirati, *Electroweak corrections to W-boson pair production at the LHC*, *JHEP* **1211** (2012) 093, [arXiv:1208.3147].

[127] J. Baglio, L. D. Ninh, and M. M. Weber, *Massive gauge boson pair production at the LHC: a next-to-leading order story*, *Phys.Rev.* **D88** (2013) 113005, [arXiv:1307.4331].

[128] M. Grazzini, *Soft-gluon effects in WW production at hadron colliders*, *JHEP* **0601** (2006) 095, [hep-ph/0510337].

[129] T. Becher and M. Neubert, *Threshold resummation in momentum space from effective field theory*, *Phys.Rev.Lett.* **97** (2006) 082001, [hep-ph/0605050].

[130] V. Ahrens, T. Becher, M. Neubert, and L. L. Yang, *Origin of the Large Perturbative Corrections to Higgs Production at Hadron Colliders*, *Phys.Rev.* **D79** (2009) 033013, [arXiv:0808.3008].

[131] V. Ahrens, T. Becher, M. Neubert, and L. L. Yang, *Updated Predictions for Higgs Production at the Tevatron and the LHC*, *Phys.Lett.* **B698** (2011) 271–274, [arXiv:1008.3162].

[132] S. Dawson, T. Han, W. Lai, A. Leibovich, and I. Lewis, *Resummation Effects in Vector-Boson and Higgs Associated Production*, *Phys.Rev.* **D86** (2012) 074007, [arXiv:1207.4207].

[133] T. Becher and M. D. Schwartz, *Direct photon production with effective field theory*, *JHEP* **1002** (2010) 040, [arXiv:0911.0681].

[134] A. Broggio, M. Neubert, and L. Vernazza, *Soft-gluon resummation for slepton-pair production at hadron colliders*, *JHEP* **1205** (2012) 151, [arXiv:1111.6624].

[135] V. Ahrens, A. Ferroglia, M. Neubert, B. D. Pecjak, and L. L. Yang, *Precision predictions for the t+t(bar) production cross section at hadron colliders*, *Phys.Lett.* **B703** (2011) 135–141, [arXiv:1105.5824].

[136] N. Kidonakis, *Next-to-next-to-leading soft-gluon corrections for the top quark cross section and transverse momentum distribution*, *Phys.Rev.* **D82** (2010) 114030, [arXiv:1009.4935].

[137] M. Beneke, M. Czakon, P. Falgari, A. Mitov, and C. Schwinn, *Threshold expansion of the gg(qq-bar) —¿ QQ-bar + X cross section at O(alpha(s)**4)*, *Phys.Lett.* **B690** (2010) 483–490, [arXiv:0911.5166].

[138] S. M. Aybat and G. F. Sterman, *Soft-Gluon Cancellation, Phases and Factorization with Initial-State Partons*, *Phys.Lett.* **B671** (2009) 46–50, [arXiv:0811.0246].

[139] W. Giele and E. N. Glover, *Higher order corrections to jet cross-sections in e+ e- annihilation*, *Phys.Rev.* **D46** (1992) 1980–2010.

[140] Z. Kunszt, A. Signer, and Z. Trocsanyi, *Singular terms of helicity amplitudes at one loop in QCD and the soft limit of the cross-sections of multiparton processes*, *Nucl.Phys.* **B420** (1994) 550–564, [hep-ph/9401294].

[141] S. Catani and M. Seymour, *The Dipole formalism for the calculation of QCD jet cross-sections at next-to-leading order*, *Phys.Lett.* **B378** (1996) 287–301, [hep-ph/9602277].

[142] S. Catani and M. Seymour, *A General algorithm for calculating jet cross-sections in NLO QCD*, *Nucl.Phys.* **B485** (1997) 291–419, [hep-ph/9605323]. [Erratum-ibid. B **510**, 503 (1998)].

[143] S. Catani, *The Singular behavior of QCD amplitudes at two loop order*, *Phys.Lett.* **B427** (1998) 161–171, [hep-ph/9802439].

[144] T. Becher and M. Neubert, *Infrared singularities of scattering amplitudes in perturbative QCD*, *Phys.Rev.Lett.* **102** (2009) 162001, [arXiv:0901.0722].

[145] T. Becher and M. Neubert, *On the Structure of Infrared Singularities of Gauge-Theory Amplitudes*, *JHEP* **0906** (2009) 081, [arXiv:0903.1126].

[146] A. V. Manohar, *Deep inelastic scattering as $x \to 1$ using soft collinear effective theory*, *Phys.Rev.* **D68** (2003) 114019, [hep-ph/0309176].

[147] T. A. collaboration, *Measurement of the W^+W^- production cross section in proton-proton collisions at $\sqrt{s} = 8$ TeV with the ATLAS detector*, .

[148] **CMS** Collaboration, C. Collaboration, *Measurement of WW production rate*, .

[149] **CMS** Collaboration, C. Collaboration, *Measurement of WW production rate*, .

[150] **CMS** Collaboration, S. Chatrchyan et al., *Measurement of Higgs boson production and properties in the WW decay channel with leptonic final states*, *JHEP* **1401** (2014) 096, [arXiv:1312.1129].

[151] **ATLAS** Collaboration, G. Aad et al., *Measurements of Higgs boson production and couplings in diboson final states with the ATLAS detector at the LHC*, *Phys.Lett.* **B726** (2013) 88–119, [arXiv:1307.1427].

[152] G. Davatz, G. Dissertori, M. Dittmar, M. Grazzini, and F. Pauss, *Effective K factors for gg —¿ H —¿ WW —¿ l nu l nu at the LHC*, *JHEP* **0405** (2004) 009, [hep-ph/0402218].

[153] N. Kauer and G. Passarino, *Inadequacy of zero-width approximation for a light Higgs boson signal*, *JHEP* **1208** (2012) 116, [arXiv:1206.4803].

[154] N. Kauer, *Interference effects for $H \to WW/ZZ \to \ell\bar{\nu}_\ell\bar{\ell}\nu_\ell$ searches in gluon fusion at the LHC*, *JHEP* **1312** (2013) 082, [arXiv:1310.7011].

[155] F. Campanario, M. Rauch, and S. Sapeta, *W^+W^- production at high transverse momenta beyond NLO*, *Nucl.Phys.* **B879** (2014) 65–79, [arXiv:1309.7293].

[156] F. Campanario and S. Sapeta, *WZ production beyond NLO for high-pT observables*, *Phys.Lett.* **B718** (2012) 100–104, [arXiv:1209.4595].

[157] F. Cascioli, S. Hche, F. Krauss, P. Maierhfer, S. Pozzorini, et al., *Precise Higgs-background predictions: merging NLO QCD and squared quark-loop corrections to four-lepton + 0,1 jet production*, *JHEP* **1401** (2014) 046, [arXiv:1309.0500].

[158] M. Bonvini, F. Caola, S. Forte, K. Melnikov, and G. Ridolfi, *Signal-background interference effects for $ggHW^+W^-$ beyond leading order*, *Phys.Rev.* **D88** (2013), no. 3 034032, [arXiv:1304.3053].

[159] F. Cascioli, T. Gehrmann, M. Grazzini, S. Kallweit, P. Maierhfer, et al., *ZZ production at hadron colliders in NNLO QCD*, *Phys.Lett.* **B735** (2014) 311–313, [arXiv:1405.2219].

[160] L. Magnea and G. F. Sterman, *Analytic continuation of the Sudakov form-factor in QCD*, *Phys.Rev.* **D42** (1990) 4222–4227.

[161] Y. Wang, C. S. Li, Z. L. Liu, D. Y. Shao, and H. T. Li, *Transverse-Momentum Resummation for Gauge Boson Pair Production at the Hadron Collider*, *Phys.Rev.* **D88** (2013) 114017, [arXiv:1307.7520].

[162] **D0** Collaboration, V. M. Abazov et al., *Measurement of the W boson mass with the D0 detector*, *Phys.Rev.* **D89** (2014), no. 1 012005, [arXiv:1310.8628].

[163] D. de Florian, G. Ferrera, M. Grazzini, and D. Tommasini, *Transverse-momentum resummation: Higgs boson production at the Tevatron and the LHC*, *JHEP* **1111** (2011) 064, [arXiv:1109.2109].

[164] A. Banfi, G. P. Salam, and G. Zanderighi, *NLL+NNLO predictions for jet-veto efficiencies in Higgs-boson and Drell-Yan production*, *JHEP* **1206** (2012) 159, [arXiv:1203.5773].

[165] A. Banfi, P. F. Monni, G. P. Salam, and G. Zanderighi, *Higgs and Z-boson production with a jet veto*, *Phys.Rev.Lett.* **109** (2012) 202001, [arXiv:1206.4998].

[166] C. F. Berger, C. Marcantonini, I. W. Stewart, F. J. Tackmann, and W. J. Waalewijn, *Higgs Production with a Central Jet Veto at NNLL+NNLO*, *JHEP* **1104** (2011) 092, [arXiv:1012.4480].

[167] F. J. Tackmann, J. R. Walsh, and S. Zuberi, *Resummation Properties of Jet Vetoes at the LHC*, *Phys.Rev.* **D86** (2012) 053011, [arXiv:1206.4312].

[168] I. W. Stewart, F. J. Tackmann, J. R. Walsh, and S. Zuberi, *Jet p_T resummation in Higgs production at $NNLL' + NNLO$*, *Phys.Rev.* **D89** (2014), no. 5 054001, [arXiv:1307.1808].

[169] T. Becher and M. Neubert, *Factorization and NNLL Resummation for Higgs Production with a Jet Veto*, *JHEP* **1207** (2012) 108, [arXiv:1205.3806].

[170] T. Becher, M. Neubert, and L. Rothen, *Factorization and N^3LL_p+NNLO predictions for the Higgs cross section with a jet veto*, *JHEP* **1310** (2013) 125, [arXiv:1307.0025].

[171] I. Moult and I. W. Stewart, *Jet Vetoes interfering with $H \to WW$*, *JHEP* **1409** (2014) 129, [arXiv:1405.5534].

[172] Y. L. Dokshitzer, D. Diakonov, and S. Troian, *On the Transverse Momentum Distribution of Massive Lepton Pairs*, *Phys.Lett.* **B79** (1978) 269–272.

[173] G. Parisi and R. Petronzio, *Small Transverse Momentum Distributions in Hard Processes*, *Nucl.Phys.* **B154** (1979) 427.

[174] G. Curci, M. Greco, and Y. Srivastava, *QCD Jets From Coherent States*, *Nucl.Phys.* **B159** (1979) 451.

[175] J. C. Collins and D. E. Soper, *Back-To-Back Jets: Fourier Transform from B to K-Transverse*, *Nucl.Phys.* **B197** (1982) 446.

[176] J. Kodaira and L. Trentadue, *Summing Soft Emission in QCD*, *Phys.Lett.* **B112** (1982) 66.

[177] J. Kodaira and L. Trentadue, *Single Logarithm Effects in electron-Positron Annihilation*, *Phys.Lett.* **B123** (1983) 335.

[178] G. Altarelli, R. K. Ellis, M. Greco, and G. Martinelli, *Vector Boson Production at Colliders: A Theoretical Reappraisal*, *Nucl.Phys.* **B246** (1984) 12.

[179] J. C. Collins, D. E. Soper, and G. F. Sterman, *Transverse Momentum Distribution in Drell-Yan Pair and W and Z Boson Production*, *Nucl.Phys.* **B250** (1985) 199.

[180] S. Catani, D. de Florian, and M. Grazzini, *Universality of nonleading logarithmic contributions in transverse momentum distributions*, *Nucl.Phys.* **B596** (2001) 299–312, [hep-ph/0008184].

[181] G. Bozzi, S. Catani, D. de Florian, and M. Grazzini, *Transverse-momentum resummation and the spectrum of the Higgs boson at the LHC*, *Nucl.Phys.* **B737** (2006) 73–120, [hep-ph/0508068].

[182] G. Bozzi, S. Catani, G. Ferrera, D. de Florian, and M. Grazzini, *Production of Drell-Yan lepton pairs in hadron collisions: Transverse-momentum resummation at next-to-next-to-leading logarithmic accuracy*, *Phys.Lett.* **B696** (2011) 207–213, [arXiv:1007.2351].

[183] T. Becher and M. Neubert, *Drell-Yan Production at Small q_T, Transverse Parton Distributions and the Collinear Anomaly*, *Eur.Phys.J.* **C71** (2011) 1665, [arXiv:1007.4005].

[184] A. Vogt, *Efficient evolution of unpolarized and polarized parton distributions with QCD-PEGASUS*, *Comput.Phys.Commun.* **170** (2005) 65–92, [hep-ph/0408244].

[185] E. Laenen, G. F. Sterman, and W. Vogelsang, *Higher order QCD corrections in prompt photon production*, *Phys.Rev.Lett.* **84** (2000) 4296–4299, [hep-ph/0002078].

[186] G. Bozzi, S. Catani, D. de Florian, and M. Grazzini, *The q(T) spectrum of the Higgs boson at the LHC in QCD perturbation theory*, *Phys.Lett.* **B564** (2003) 65–72, [hep-ph/0302104].

[187] P. Nason, *A New method for combining NLO QCD with shower Monte Carlo algorithms*, *JHEP* **0411** (2004) 040, [hep-ph/0409146].

[188] S. Frixione, P. Nason, and C. Oleari, *Matching NLO QCD computations with Parton Shower simulations: the POWHEG method*, *JHEP* **0711** (2007) 070, [arXiv:0709.2092].

[189] S. Alioli, P. Nason, C. Oleari, and E. Re, *A general framework for implementing NLO calculations in shower Monte Carlo programs: the POWHEG BOX*, *JHEP* **1006** (2010) 043, [arXiv:1002.2581].

[190] J. Alwall, R. Frederix, S. Frixione, V. Hirschi, F. Maltoni, et al., *The automated computation of tree-level and next-to-leading order differential cross sections, and their matching to parton shower simulations*, *JHEP* **1407** (2014) 079, [arXiv:1405.0301].

[191] M. Bahr, S. Gieseke, M. Gigg, D. Grellscheid, K. Hamilton, et al., *Herwig++ Physics and Manual*, *Eur.Phys.J.* **C58** (2008) 639–707, [arXiv:0803.0883].

[192] T. Sjostrand, S. Mrenna, and P. Z. Skands, *PYTHIA 6.4 Physics and Manual*, *JHEP* **0605** (2006) 026, [hep-ph/0603175].

[193] J. Pumplin, D. Stump, J. Huston, H. Lai, P. M. Nadolsky, et al., *New generation of parton distributions with uncertainties from global QCD analysis*, *JHEP* **0207** (2002) 012, [hep-ph/0201195].

[194] **DELPHES 3** Collaboration, J. de Favereau et al., *DELPHES 3, A modular framework for fast simulation of a generic collider experiment*, *JHEP* **1402** (2014) 057, [arXiv:1307.6346].

[195] S. Frixione and B. R. Webber, *Matching NLO QCD computations and parton shower simulations*, *JHEP* **0206** (2002) 029, [hep-ph/0204244].

[196] G. Bozzi, S. Catani, G. Ferrera, D. de Florian, and M. Grazzini, *Transverse-momentum resummation: A Perturbative study of Z production at the Tevatron*, *Nucl.Phys.* **B815** (2009) 174–197, [arXiv:0812.2862].

[197] P. Jaiswal and T. Okui, *Explanation of the WW excess at the LHC by jet-veto resummation*, *Phys.Rev.* **D90** (2014), no. 7 073009, [arXiv:1407.4537].

[198] **ATLAS** Collaboration, *Updated coupling measurements of the Higgs boson with the ATLAS detector using up to 25 fb^{-1} of proton-proton collision data*, tech. rep., CERN.

[199] **CMS** Collaboration, *Precise determination of the mass of the Higgs boson and studies of the compatibility of its couplings with the standard model*, Tech. Rep. CMS-PAS-HIG-14-009, CERN, Geneva, 2014.

[200] **LHC Higgs Cross Section Working Group** Collaboration, S. Dittmaier et al., *Handbook of LHC Higgs Cross Sections: 1. Inclusive Observables*, arXiv:1101.0593.

[201] S. Dittmaier, S. Dittmaier, C. Mariotti, G. Passarino, R. Tanaka, et al., *Handbook of LHC Higgs Cross Sections: 2. Differential Distributions*, arXiv:1201.3084.

[202] B. A. Kniehl and M. Spira, *Low-energy theorems in Higgs physics*, *Z.Phys.* **C69** (1995) 77–88, [hep-ph/9505225].

[203] M. Spira, A. Djouadi, D. Graudenz, and P. Zerwas, *Higgs boson production at the LHC*, *Nucl.Phys.* **B453** (1995) 17–82, [hep-ph/9504378].

[204] S. Dawson, *Radiative corrections to Higgs boson production*, *Nucl.Phys.* **B359** (1991) 283–300.

[205] N. Arkani-Hamed, A. Cohen, E. Katz, and A. Nelson, *The Littlest Higgs*, *JHEP* **0207** (2002) 034, [hep-ph/0206021].

[206] R. Contino, Y. Nomura, and A. Pomarol, *Higgs as a holographic pseudoGoldstone boson*, *Nucl.Phys.* **B671** (2003) 148–174, [hep-ph/0306259].

[207] I. Low and A. Vichi, *On the production of a composite Higgs boson*, *Phys.Rev.* **D84** (2011) 045019, [arXiv:1010.2753].

[208] M. Carena, S. Heinemeyer, O. Stl, C. Wagner, and G. Weiglein, *MSSM Higgs Boson Searches at the LHC: Benchmark Scenarios after the Discovery of a Higgs-like Particle*, *Eur.Phys.J.* **C73** (2013) 2552, [arXiv:1302.7033].

[209] M. Carena, S. Gori, N. R. Shah, C. E. Wagner, and L.-T. Wang, *Light Stops, Light Staus and the 125 GeV Higgs*, *JHEP* **1308** (2013) 087, [arXiv:1303.4414].

[210] C. Grojean, E. Salvioni, M. Schlaffer, and A. Weiler, *Very boosted Higgs in gluon fusion*, *JHEP* **1405** (2014) 022, [arXiv:1312.3317].

[211] A. Azatov and A. Paul, *Probing Higgs couplings with high p_T Higgs production*, *JHEP* **1401** (2014) 014, [arXiv:1309.5273].

[212] I. Low, R. Rattazzi, and A. Vichi, *Theoretical Constraints on the Higgs Effective Couplings*, *JHEP* **1004** (2010) 126, [arXiv:0907.5413].

[213] M. Buschmann, C. Englert, D. Goncalves, T. Plehn, and M. Spannowsky, *Resolving the Higgs-Gluon Coupling with Jets*, *Phys.Rev.* **D90** (2014) 013010, [arXiv:1405.7651].

[214] M. Schlaffer, M. Spannowsky, M. Takeuchi, A. Weiler, and C. Wymant, *Boosted Higgs Shapes*, arXiv:1405.4295.

[215] A. Azatov and J. Galloway, *Light Custodians and Higgs Physics in Composite Models*, *Phys.Rev.* **D85** (2012) 055013, [arXiv:1110.5646].

[216] S. Dawson and E. Furlan, *A Higgs Conundrum with Vector Fermions*, *Phys.Rev.* **D86** (2012) 015021, [arXiv:1205.4733].

[217] M. Gillioz, R. Grober, C. Grojean, M. Muhlleitner, and E. Salvioni, *Higgs Low-Energy Theorem (and its corrections) in Composite Models*, *JHEP* **1210** (2012) 004, [arXiv:1206.7120].

[218] S. Dawson, E. Furlan, and I. Lewis, *Unravelling an extended quark sector through multiple Higgs production?*, *Phys.Rev.* **D87** (2013) 014007, [arXiv:1210.6663].

[219] A. Banfi, A. Martin, and V. Sanz, *Probing top-partners in Higgs + jets*, arXiv:1308.4771.

[220] D. Neill, *Two-Loop Matching onto Dimension Eight Operators in the Higgs-Glue Sector*, arXiv:0908.1573.

[221] R. V. Harlander and T. Neumann, *Probing the nature of the Higgs-gluon coupling*, *Phys.Rev.* **D88** (2013) 074015, [arXiv:1308.2225].

[222] R. V. Harlander and W. B. Kilgore, *Next-to-next-to-leading order Higgs production at hadron colliders*, *Phys.Rev.Lett.* **88** (2002) 201801, [hep-ph/0201206].

[223] V. Ravindran, J. Smith, and W. L. van Neerven, *NNLO corrections to the total cross-section for Higgs boson production in hadron hadron collisions*, *Nucl.Phys.* **B665** (2003) 325–366, [hep-ph/0302135].

[224] C. Anastasiou and K. Melnikov, *Higgs boson production at hadron colliders in NNLO QCD*, *Nucl.Phys.* **B646** (2002) 220–256, [hep-ph/0207004].

[225] C. Anastasiou, K. Melnikov, and F. Petriello, *Fully differential Higgs boson production and the di-photon signal through next-to-next-to-leading order*, *Nucl.Phys.* **B724** (2005) 197–246, [hep-ph/0501130].

[226] S. Catani and M. Grazzini, *An NNLO subtraction formalism in hadron collisions and its application to Higgs boson production at the LHC*, *Phys.Rev.Lett.* **98** (2007) 222002, [hep-ph/0703012].

[227] V. Ravindran, J. Smith, and W. Van Neerven, *Next-to-leading order QCD corrections to differential distributions of Higgs boson production in hadron hadron collisions*, *Nucl.Phys.* **B634** (2002) 247–290, [hep-ph/0201114].

[228] R. V. Harlander and K. J. Ozeren, *Finite top mass effects for hadronic Higgs production at next-to-next-to-leading order*, *JHEP* **0911** (2009) 088, [arXiv:0909.3420].

[229] A. Pak, M. Rogal, and M. Steinhauser, *Finite top quark mass effects in NNLO Higgs boson production at LHC*, *JHEP* **1002** (2010) 025, [arXiv:0911.4662].

[230] K. Chetyrkin, B. A. Kniehl, and M. Steinhauser, *Decoupling relations to O (α_s^3) and their connection to low-energy theorems*, *Nucl.Phys.* **B510** (1998) 61–87, [hep-ph/9708255].

[231] Y. Schroder and M. Steinhauser, *Four-loop decoupling relations for the strong coupling*, *JHEP* **0601** (2006) 051, [hep-ph/0512058].

[232] K. Chetyrkin, J. H. Kuhn, and C. Sturm, *QCD decoupling at four loops*, *Nucl.Phys.* **B744** (2006) 121–135, [hep-ph/0512060].

[233] M. Kramer, E. Laenen, and M. Spira, *Soft gluon radiation in Higgs boson production at the LHC*, *Nucl.Phys.* **B511** (1998) 523–549, [hep-ph/9611272].

[234] R. K. Ellis, I. Hinchliffe, M. Soldate, and J. van der Bij, *Higgs Decay to tau+ tau-: A Possible Signature of Intermediate Mass Higgs Bosons at the SSC*, *Nucl.Phys.* **B297** (1988) 221.

[235] U. Baur and E. N. Glover, *Higgs Boson Production at Large Transverse Momentum in Hadronic Collisions*, *Nucl.Phys.* **B339** (1990) 38–66.

[236] D. de Florian, M. Grazzini, and Z. Kunszt, *Higgs production with large transverse momentum in hadronic collisions at next-to-leading order*, *Phys.Rev.Lett.* **82** (1999) 5209–5212, [hep-ph/9902483].

[237] C. J. Glosser and C. R. Schmidt, *Next-to-leading corrections to the Higgs boson transverse momentum spectrum in gluon fusion*, *JHEP* **0212** (2002) 016, [hep-ph/0209248].

[238] R. V. Harlander, T. Neumann, K. J. Ozeren, and M. Wiesemann, *Top-mass effects in differential Higgs production through gluon fusion at order alpha s4*, *JHEP* **1208** (2012) 139, [arXiv:1206.0157].

[239] M. Grazzini and H. Sargsyan, *Heavy-quark mass effects in Higgs boson production at the LHC*, *JHEP* **1309** (2013) 129, [arXiv:1306.4581].

[240] E. Bagnaschi, G. Degrassi, P. Slavich, and A. Vicini, *Higgs production via gluon fusion in the POWHEG approach in the SM and in the MSSM*, *JHEP* **1202** (2012) 088, [arXiv:1111.2854].

[241] T. Neumann and M. Wiesemann, *Finite top-mass effects in gluon-induced Higgs production with a jet-veto at NNLO*, arXiv:1408.6836.

[242] W.-Y. Keung and F. J. Petriello, *Electroweak and finite quark-mass effects on the Higgs boson transverse momentum distribution*, *Phys.Rev.* **D80** (2009) 013007, [arXiv:0905.2775].

[243] R. Boughezal, F. Caola, K. Melnikov, F. Petriello, and M. Schulze, *Higgs boson production in association with a jet at next-to-next-to-leading order in perturbative QCD*, *JHEP* **1306** (2013) 072, [arXiv:1302.6216].

[244] T. Becher, G. Bell, C. Lorentzen, and S. Marti, *The transverse-momentum spectrum of Higgs bosons near threshold at NNLO*, arXiv:1407.4111.

[245] T. Becher, G. Bell, C. Lorentzen, and S. Marti, *Transverse-momentum spectra of electroweak bosons near threshold at NNLO*, *JHEP* **1402** (2014) 004, [arXiv:1309.3245].

[246] F. P. Huang, C. S. Li, H. T. Li, and J. Wang, *Renormalization-group improved predictions for Higgs boson production at large p_T*, arXiv:1406.2591.

[247] V. Del Duca, W. Kilgore, C. Oleari, C. Schmidt, and D. Zeppenfeld, *Higgs + 2 jets via gluon fusion*, *Phys.Rev.Lett.* **87** (2001) 122001, [hep-ph/0105129].

[248] V. Del Duca, W. Kilgore, C. Oleari, C. Schmidt, and D. Zeppenfeld, *Gluon fusion contributions to H + 2 jet production*, *Nucl.Phys.* **B616** (2001) 367–399, [hep-ph/0108030].

[249] F. Campanario and M. Kubocz, *Higgs boson production in association with three jets via gluon fusion at the LHC: Gluonic contributions*, *Phys.Rev.* **D88** (2013), no. 5 054021, [arXiv:1306.1830].

[250] H. van Deurzen, N. Greiner, G. Luisoni, P. Mastrolia, E. Mirabella, et al., *NLO QCD corrections to the production of Higgs plus two jets at the LHC*, *Phys.Lett.* **B721** (2013) 74–81, [arXiv:1301.0493].

[251] G. Cullen, H. van Deurzen, N. Greiner, G. Luisoni, P. Mastrolia, et al., *Next-to-Leading-Order QCD Corrections to Higgs Boson Production Plus Three Jets in Gluon Fusion*, *Phys.Rev.Lett.* **111** (2013), no. 13 131801, [arXiv:1307.4737].

[252] L. J. Dixon, *Calculating scattering amplitudes efficiently*, hep-ph/9601359.

[253] M. E. Peskin, *Simplifying Multi-Jet QCD Computation*, arXiv:1101.2414.

[254] W. Buchmuller and D. Wyler, *Effective Lagrangian Analysis of New Interactions and Flavor Conservation*, *Nucl.Phys.* **B268** (1986) 621–653.

[255] S. Dawson and R. Kauffman, *QCD corrections to Higgs boson production: nonleading terms in the heavy quark limit*, *Phys.Rev.* **D49** (1994) 2298–2309, [hep-ph/9310281].

[256] J. Gracey, *Classification and one loop renormalization of dimension-six and dimension-eight operators in quantum gluodynamics*, *Nucl.Phys.* **B634** (2002) 192–208, [hep-ph/0204266].

[257] K. Melnikov and T. v. Ritbergen, *The Three loop relation between the MS-bar and the pole quark masses*, *Phys.Lett.* **B482** (2000) 99–108, [hep-ph/9912391].

[258] R. Pasechnik, O. Teryaev, and A. Szczurek, *Scalar Higgs boson production in a fusion of two off-shell gluons*, *Eur.Phys.J.* **C47** (2006) 429–435, [hep-ph/0603258].

[259] J. C. Collins, F. Wilczek, and A. Zee, *Low-Energy Manifestations of Heavy Particles: Application to the Neutral Current*, *Phys.Rev.* **D18** (1978) 242.

[260] W. B. Kilgore, *One-Loop Single-Real-Emission Contributions to $pp \to H + X$ at Next-to-Next-to-Next-to-Leading Order*, *Phys.Rev.* **D89** (2014) 073008, [arXiv:1312.1296].

[261] T. Gehrmann, M. Jaquier, E. Glover, and A. Koukoutsakis, *Two-Loop QCD Corrections to the Helicity Amplitudes for $H \to 3$ partons*, *JHEP* **1202** (2012) 056, [arXiv:1112.3554].

[262] H. Kluberg-Stern and J. Zuber, *Ward Identities and Some Clues to the Renormalization of Gauge Invariant Operators*, *Phys.Rev.* **D12** (1975) 467–481.

[263] R. Tarrach, *The Renormalization of Ff*, *Nucl.Phys.* **B196** (1982) 45.

[264] B. Grinstein and L. Randall, *The Renormalization of g^2*, *Phys.Lett.* **B217** (1989) 335.

[265] L. Abbott, *The Background Field Method Beyond One Loop*, *Nucl.Phys.* **B185** (1981) 189.

[266] A. Alloul, N. D. Christensen, C. Degrande, C. Duhr, and B. Fuks, *FeynRules 2.0 - A complete toolbox for tree-level phenomenology*, *Comput.Phys.Commun.* **185** (2014) 2250–2300, [arXiv:1310.1921].

[267] T. Hahn, *Generating Feynman diagrams and amplitudes with FeynArts 3*, *Comput.Phys.Commun.* **140** (2001) 418–431, [hep-ph/0012260].

[268] T. Hahn and M. Perez-Victoria, *Automatized one loop calculations in four-dimensions and D-dimensions*, *Comput.Phys.Commun.* **118** (1999) 153–165, [hep-ph/9807565].

[269] R. Mertig, M. Bohm, and A. Denner, *FEYN CALC: Computer algebraic calculation of Feynman amplitudes*, *Comput.Phys.Commun.* **64** (1991) 345–359.

[270] R. K. Ellis and G. Zanderighi, *Scalar one-loop integrals for QCD*, *JHEP* **0802** (2008) 002, [arXiv:0712.1851].

[271] C. R. Schmidt, *$H \to ggg(gq\bar{q})$ at two loops in the large M_t limit*, *Phys.Lett.* **B413** (1997) 391–395, [hep-ph/9707448].

[272] B. Harris and J. Owens, *The Two cutoff phase space slicing method*, *Phys.Rev.* **D65** (2002) 094032, [hep-ph/0102128].

[273] W. Beenakker, H. Kuijf, W. van Neerven, and J. Smith, *QCD Corrections to Heavy Quark Production in p anti-p Collisions*, *Phys.Rev.* **D40** (1989) 54–82.

[274] S. Dawson and R. Kauffman, *Higgs boson plus multi - jet rates at the SSC*, *Phys.Rev.Lett.* **68** (1992) 2273–2276.

[275] R. P. Kauffman, S. V. Desai, and D. Risal, *Production of a Higgs boson plus two jets in hadronic collisions*, *Phys.Rev.* **D55** (1997) 4005–4015, [hep-ph/9610541].

[276] L. J. Dixon and Y. Shadmi, *Testing gluon self-interactions in three jet events at hadron colliders*, *Nucl.Phys.* **B423** (1994) 3–32, [hep-ph/9312363].

[277] L. J. Dixon, E. N. Glover, and V. V. Khoze, *MHV rules for Higgs plus multi-gluon amplitudes*, *JHEP* **0412** (2004) 015, [hep-th/0411092].

[278] D. Neill, *Analytic Virtual Corrections for Higgs Transverse Momentum Spectrum at $\mathcal{O}(\alpha_s^2/M_t^3)$ via Unitarity Methods*, arXiv:0911.2707.

[279] J. Broedel and L. J. Dixon, *Color-kinematics duality and double-copy construction for amplitudes from higher-dimension operators*, *JHEP* **1210** (2012) 091, [arXiv:1208.0876].

[280] F. Cachazo, P. Svrcek, and E. Witten, *MHV vertices and tree amplitudes in gauge theory*, *JHEP* **0409** (2004) 006, [hep-th/0403047].

[281] C. Degrande, C. Duhr, B. Fuks, D. Grellscheid, O. Mattelaer, et al., *UFO - The Universal FeynRules Output*, *Comput.Phys.Commun.* **183** (2012) 1201–1214, [arXiv:1108.2040].

[282] J. Owens, A. Accardi, and W. Melnitchouk, *Global parton distributions with nuclear and finite-Q^2 corrections*, *Phys.Rev.* **D87** (2013), no. 9 094012, [arXiv:1212.1702].

[283] K. Hagiwara, S. Ishihara, R. Szalapski, and D. Zeppenfeld, *Low-energy effects of new interactions in the electroweak boson sector*, *Phys.Rev.* **D48** (1993) 2182–2203.

[284] S. Alam, S. Dawson, and R. Szalapski, *Low-energy constraints on new physics revisited*, *Phys.Rev.* **D57** (1998) 1577–1590, [hep-ph/9706542].

[285] B. Henning, X. Lu, and H. Murayama, *How to use the Standard Model effective field theory*, arXiv:1412.1837.

[286] G. Giudice, C. Grojean, A. Pomarol, and R. Rattazzi, *The Strongly-Interacting Light Higgs*, *JHEP* **0706** (2007) 045, [hep-ph/0703164].

[287] T. Corbett, O. Eboli, J. Gonzalez-Fraile, and M. Gonzalez-Garcia, *Constraining anomalous Higgs interactions*, *Phys.Rev.* **D86** (2012) 075013, [arXiv:1207.1344].

[288] A. Falkowski and F. Riva, *Model-independent precision constraints on dimension-6 operators*, arXiv:1411.0669.

[289] J. Ellis, V. Sanz, and T. You, *Complete Higgs Sector Constraints on Dimension-6 Operators*, *JHEP* **1407** (2014) 036, [arXiv:1404.3667].

[290] C.-Y. Chen, S. Dawson, and C. Zhang, *Electroweak Effective Operators and Higgs Physics*, *Phys.Rev.* **D89** (2014) 015016, [arXiv:1311.3107].

[291] A. V. Manohar and M. B. Wise, *Modifications to the properties of the Higgs boson*, *Phys.Lett.* **B636** (2006) 107–113, [hep-ph/0601212].

[292] M. Buschmann, D. Goncalves, S. Kuttimalai, M. Schonherr, F. Krauss, et al., *Mass Effects in the Higgs-Gluon Coupling: Boosted vs Off-Shell Production*, arXiv:1410.5806.

[293] D. Ghosh and M. Wiebusch, *The Dimension Six Triple Gluon Operator in Higgs+Jet Observables*, arXiv:1411.2029.

[294] P. L. Cho and E. H. Simmons, *Searching for G3 in $t\bar{t}$ production*, *Phys.Rev.* **D51** (1995) 2360–2370, [hep-ph/9408206].

[295] R. Bonciani, G. Degrassi, and A. Vicini, *Scalar particle contribution to Higgs production via gluon fusion at NLO*, *JHEP* **0711** (2007) 095, [arXiv:0709.4227].

[296] C. Arnesen, I. Z. Rothstein, and J. Zupan, *Smoking Guns for On-Shell New Physics at the LHC*, *Phys.Rev.Lett.* **103** (2009) 151801, [arXiv:0809.1429].

[297] G. D. Kribs and A. Martin, *Enhanced di-Higgs Production through Light Colored Scalars*, *Phys.Rev.* **D86** (2012) 095023, [arXiv:1207.4496].

[298] R. Boughezal and F. Petriello, *Color-octet scalar effects on Higgs boson production in gluon fusion*, *Phys.Rev.* **D81** (2010) 114033, [arXiv:1003.2046].

[299] S. Gori and I. Low, *Precision Higgs Measurements: Constraints from New Oblique Corrections*, *JHEP* **1309** (2013) 151, [arXiv:1307.0496].

[300] L. Lavoura and J. P. Silva, *Bounds on the mixing of the down type quarks with vector - like singlet quarks*, *Phys.Rev.* **D47** (1993) 1117–1126.

[301] J. Aguilar-Saavedra, *Effects of mixing with quark singlets*, *Phys.Rev.* **D67** (2003) 035003, [hep-ph/0210112].

[302] J. Aguilar-Saavedra, R. Benbrik, S. Heinemeyer, and M. Perez-Victoria, *A handbook of vector-like quarks: mixing and single production*, arXiv:1306.0572.

[303] M. B. Popovic and E. H. Simmons, *Weak singlet fermions: Models and constraints*, *Phys.Rev.* **D62** (2000) 035002, [hep-ph/0001302].

[304] **ATLAS** Collaboration, G. Aad et al., *Search for pair and single production of new heavy quarks that decay to a Z boson and a third-generation quark in pp collisions at $\sqrt{s} = 8$ TeV with the ATLAS detector*, *JHEP* **1411** (2014) 104, [arXiv:1409.5500].

[305] **CMS** Collaboration, S. Chatrchyan et al., *Inclusive search for a vector-like T quark with charge $\frac{2}{3}$ in pp collisions at $\sqrt{s} = 8$ TeV*, *Phys.Lett.* **B729** (2014) 149–171, [arXiv:1311.7667].

[306] C. Grojean, E. E. Jenkins, A. V. Manohar, and M. Trott, *Renormalization Group Scaling of Higgs Operators and $\Gamma_{H\to\gamma\gamma}$*, *JHEP* **1304** (2013) 016, [arXiv:1301.2588].

[307] C. Englert and M. Spannowsky, *Effective Theories and Measurements at Colliders*, *Phys.Lett.* **B740** (2014) 8–15, [arXiv:1408.5147].

[308] J. C. Collins and G. F. Sterman, *Soft Partons in QCD*, *Nucl.Phys.* **B185** (1981) 172.

[309] C. W. Bauer, B. O. Lange, and G. Ovanesyan, *On Glauber modes in Soft-Collinear Effective Theory*, *JHEP* **1107** (2011) 077, [arXiv:1010.1027].

[310] J. F. Donoghue, B. K. El-Menoufi, and G. Ovanesyan, *Regge behavior in effective field theory*, *Phys.Rev.* **D90** (2014), no. 9 096009, [arXiv:1405.1731].

[311] J. C. Collins and A. Metz, *Universality of soft and collinear factors in hard-scattering factorization*, *Phys.Rev.Lett.* **93** (2004) 252001, [hep-ph/0408249].

[312] T. Becher and G. Bell, *Analytic Regularization in Soft-Collinear Effective Theory*, *Phys.Lett.* **B713** (2012) 41–46, [arXiv:1112.3907].

[313] J.-Y. Chiu, A. Jain, D. Neill, and I. Z. Rothstein, *A Formalism for the Systematic Treatment of Rapidity Logarithms in Quantum Field Theory*, *JHEP* **1205** (2012) 084, [arXiv:1202.0814].

[314] J. C. Collins, *Fragmentation of transversely polarized quarks probed in transverse momentum distributions*, *Nucl.Phys.* **B396** (1993) 161–182, [hep-ph/9208213].

[315] J.-w. Qiu and G. F. Sterman, *Power corrections to hadronic scattering. 2. Factorization*, *Nucl.Phys.* **B353** (1991) 137–164.

[316] Z.-B. Kang, Y.-Q. Ma, J.-W. Qiu, and G. Sterman, *Heavy Quarkonium Production at Collider Energies: Factorization and Evolution*, *Phys.Rev.* **D90** (2014), no. 3 034006, [arXiv:1401.0923].

[317] A. Papaefstathiou, J. M. Smillie, and B. R. Webber, *Resummation of transverse energy in vector boson and Higgs boson production at hadron colliders*, *JHEP* **1004** (2010) 084, [arXiv:1002.4375].

[318] M. Grazzini, A. Papaefstathiou, J. M. Smillie, and B. R. Webber, *Resummation of the transverse-energy distribution in Higgs boson production at the Large Hadron Collider*, *JHEP* **1409** (2014) 056, [arXiv:1403.3394].

[319] I. W. Stewart, F. J. Tackmann, and W. J. Waalewijn, *Factorization at the LHC: From PDFs to Initial State Jets*, *Phys.Rev.* **D81** (2010) 094035, [arXiv:0910.0467].

[320] I. W. Stewart, F. J. Tackmann, and W. J. Waalewijn, *The Beam Thrust Cross Section for Drell-Yan at NNLL Order*, *Phys.Rev.Lett.* **106** (2011) 032001, [arXiv:1005.4060].

[321] D. Kang, O. Z. Labun, and C. Lee, *Equality of hemisphere soft functions for e^+e^-, DIS and pp collisions at $\mathcal{O}(\alpha_s^2)$*, arXiv:1504.0400.

[322] J. R. Gaunt, *Glauber Gluons and Multiple Parton Interactions*, *JHEP* **1407** (2014) 110, [arXiv:1405.2080].

[323] C. Bomhof, P. Mulders, and F. Pijlman, *Gauge link structure in quark-quark correlators in hard processes*, *Phys.Lett.* **B596** (2004) 277–286, [hep-ph/0406099].

[324] A. Bacchetta, C. Bomhof, P. Mulders, and F. Pijlman, *Single spin asymmetries in hadron-hadron collisions*, *Phys.Rev.* **D72** (2005) 034030, [hep-ph/0505268].

[325] C. Bomhof, P. Mulders, and F. Pijlman, *The Construction of gauge-links in arbitrary hard processes*, *Eur.Phys.J.* **C47** (2006) 147–162, [hep-ph/0601171].

[326] W. Vogelsang and F. Yuan, *Hadronic Dijet Imbalance and Transverse-Momentum Dependent Parton Distributions*, *Phys.Rev.* **D76** (2007) 094013, [arXiv:0708.4398].

[327] T. C. Rogers, *Extra spin asymmetries from the breakdown of transverse-momentum-dependent factorization in hadron-hadron collisions*, *Phys.Rev.* **D88** (2013), no. 1 014002, [arXiv:1304.4251].

[328] J. Collins and J.-W. Qiu, *k_T factorization is violated in production of high-transverse-momentum particles in hadron-hadron collisions*, *Phys.Rev.* **D75** (2007) 114014, [arXiv:0705.2141].

[329] J. Collins, *2-soft-gluon exchange and factorization breaking*, arXiv:0708.4410.

[330] T. C. Rogers and P. J. Mulders, *No Generalized TMD-Factorization in Hadro-Production of High Transverse Momentum Hadrons*, *Phys.Rev.* **D81** (2010) 094006, [arXiv:1001.2977].

[331] S. Gangal, M. Stahlhofen, and F. J. Tackmann, *Rapidity-Dependent Jet Vetoes*, *Phys.Rev.* **D91** (2015), no. 5 054023, [arXiv:1412.4792].

[332] J. R. Forshaw, A. Kyrieleis, and M. Seymour, *Super-leading logarithms in non-global observables in QCD*, *JHEP* **0608** (2006) 059, [hep-ph/0604094].

[333] J. Forshaw, A. Kyrieleis, and M. Seymour, *Super-leading logarithms in non-global observables in QCD: Colour basis independent calculation*, *JHEP* **0809** (2008) 128, [arXiv:0808.1269].

[334] S. Catani, D. de Florian, and G. Rodrigo, *Space-like (versus time-like) collinear limits in QCD: Is factorization violated?*, *JHEP* **1207** (2012) 026, [arXiv:1112.4405].

[335] J. R. Forshaw, M. H. Seymour, and A. Siodmok, *On the Breaking of Collinear Factorization in QCD*, *JHEP* **1211** (2012) 066, [arXiv:1206.6363].

[336] H. T. Li, C. S. Li, D. Y. Shao, L. L. Yang, and H. X. Zhu, *Top quark pair production at small transverse momentum in hadronic collisions*, *Phys.Rev.* **D88** (2013) 074004, [arXiv:1307.2464].

[337] S. Catani, M. Grazzini, and A. Torre, *Transverse-momentum resummation for heavy-quark hadroproduction*, *Nucl.Phys.* **B890** (2014) 518–538, [arXiv:1408.4564].

[338] A. Banfi, G. P. Salam, and G. Zanderighi, *Phenomenology of event shapes at hadron colliders*, *JHEP* **1006** (2010) 038, [arXiv:1001.4082].

[339] G. F. Sterman, *Energy flow observables*, hep-ph/0501270.

[340] J. Labastida and G. F. Sterman, *Inclusive Hadron - Hadron Scattering in the Feynman Gauge*, *Nucl.Phys.* **B254** (1985) 425.

[341] T. Hahn, *The CUBA library*, *Nucl.Instrum.Meth.* **A559** (2006) 273–277, [hep-ph/0509016].

[342] T. Gehrmann, A. von Manteuffel, and L. Tancredi, *The two-loop helicity amplitudes for $q\bar{q}' \to V_1 V_2 \to 4$ leptons*, arXiv:1503.0481.

[343] F. Caola, J. M. Henn, K. Melnikov, A. V. Smirnov, and V. A. Smirnov, *Two-loop helicity amplitudes for the production of two off-shell electroweak bosons in gluon fusion*, arXiv:1503.0875.

[344] S. Forte and G. Ridolfi, *Renormalization group approach to soft gluon resummation*, *Nucl.Phys.* **B650** (2003) 229–270, [hep-ph/0209154].

[345] I. Feige, M. D. Schwartz, and K. Yan, *Removing phase-space restrictions in factorized cross sections*, *Phys.Rev.* **D91** (2015) 094027, [arXiv:1502.0541].